Department of Aerospace and Mechanical Engineering
Multibody and Mechatronic Systems Laboratory

Nonlinear analysis of compliant deployable structures:

modelling, simulation and experimental validation

Thesis submitted in fulfilment of the requirements for the degree of
Doctor in Engineering Sciences

by

Florence Dewalque
F.R.S.-FNRS Research Fellow

August 2017

AUTHOR'S CONTACT DETAILS

Ir. Florence Dewalque

Multibody and Mechatronic Systems Laboratory
Department of Aerospace and Mechanical Engineering
Université de Liège

Allée de la Découverte 13A (B52/3)
B-4000 Liège
Belgium

Professional e-mail: f.dewalque@ulg.ac.be
Private e-mail: florencedewalque@hotmail.com

Phone: +32 (0)4 366 92 13

EXAMINATION COMMITTEE

Prof. Olivier Brüls – *Advisor*
Université de Liège (Liège, Belgium)

Prof. Pierre Rochus – *Co-advisor*
Université de Liège (Liège, Belgium)
Centre Spatial de Liège (Liège, Belgium)

Prof. Stéphane Bourgeois
École Centrale Marseille (Marseille, France)

Ir. Jean-Paul Collette
Walopt (Embourg, Belgium)

Prof. Dirk Vandepitte
Katholieke Universiteit Leuven (Leuven, Belgium)

Prof. Gaëtan Kerschen
Université de Liège (Liège, Belgium)

Prof. Jean-Philippe Ponthot – *President of the jury*
Université de Liège (Liège, Belgium)

FINANCIAL SUPPORT

This Ph.D. thesis was financially supported by the Belgian National Fund for Scientific Research (F.R.S.-FNRS) from October 2013 to September 2017.

ABSTRACT

Compliant mechanisms are flexible components which can store elastic energy when deformed and then passively release it to produce a motion. Their scope of applications encompasses various domains from robotic orthoses to microscopes and grippers. In this work, the developments focus on compliant mechanisms called tape springs used in deployable space structures.

Tape springs, due to their autonomous deployment capacity from a compact folded configuration, their high stiffness in the deployed equilibrium state and their simplicity of integration, represent efficient alternatives to common motorised hinges for space applications. Thus, they are currently used to deploy appendices on satellites such as solar panels or telescopes and are considered as valuable components in the design of future applications such as solar sails, deployable optics and inflatable structures. However, their structural behaviour is highly nonlinear and quite sensitive to the design parameters and to the various constraints encountered on Earth and in a space environment. The objective of this thesis is thus to develop validated high-fidelity dynamic models of tape springs which can be used to support the design process. The methodology involves the development of advanced finite element models and experimental tests based on an original set-up.

First, a quasi-static model based on shell finite elements is established and used to investigate the nonlinear response of tape springs as well as the influence of various geometric parameters. This model is then exploited for the design of tape springs deploying a reflector based on an automatic optimisation procedure. The study is further extended to dynamic analyses, which are characterised by a self-locking of the tape springs in their final deployed configuration. In order to accurately capture these phenomena, the importance of a suitable representation of the physical structural dissipation in the model is demonstrated and, for metallic tape springs, a Kelvin-Voigt model is retained.

An experimental set-up is then designed in order to validate the model and its capacity to represent the nonlinear phenomena inherent to tape springs which occur during quasi-static and dynamic tests. The experimental data are acquired by the means of an innovative 3D motion analysis system and a force plate. The reproducibility of the tests is assessed and a procedure, involving several elementary tests, is proposed to identify the parameters of the finite element model, in particular, the structural damping. In the end, a fair correlation between the experimental and numerical results is achieved. The proposed methodology, which relies on numerical and experimental methods, thus leads to a dynamic model of tape springs which can be used to predict their behaviour in various conditions.

ACKNOWLEDGEMENTS

This Ph.D. thesis is the achievement of four years of research at the University of Liège during which fruitful collaborations with a number of people helped to the fulfilment of this final manuscript.

First of all, I would like to acknowledge my advisor Professor Olivier Brüls who convinced me to embark on this long journey. His encouragements, guidance and insightful ideas punctuated each step of this work.

I am also thankful to the research teams who allowed me to use their laboratory and infrastructures to perform my experimental tests: Dr. Cédric Schwartz, Profs. Vincent Denoël, Jean-Louis Croisier and Bénédicte Forthomme from the Laboratory of Human Motion Analysis (LAMH), and Ir. Laura Zorzetto and Prof. Davide Ruffoni from the Mechanics of Biological and Bioinspired Materials Laboratory (MBBM).

Then, I would like to express my gratitude to my co-advisor Prof. Pierre Rochus for allowing me to collaborate with the Centre Spatial de Liège (CSL), Ir. Jean-Paul Collette for offering me the possibility to work on a project commissioned by the ESA and the members of the examination committee Profs. Stéphane Bourgeois, Dirk Vandepitte, Gaëtan Kerschen and Jean-Philippe Ponthot for accepting to take part in the final evaluation.

I am thankful to my colleagues from the Multibody and Mechatronic Systems Laboratory and from the Department of Aerospace and Mechanical Engineering for welcoming me and creating a friendly working environment.

Finally, I would like to thank my parents, my brother and Donatienne for their unconditional support and love.

CONTENTS

LIST OF FIGURES

LIST OF TABLES

CHAPTER 1

INTRODUCTION

Compliant mechanisms rely on the deformation of flexible structural components to produce motion. Based on this behaviour, several advantageous characteristics can be put forward compared to the use of common kinematic joints. When deformed, a compliant mechanism stores some elastic energy which creates a restoring force. This force can be exploited to bring the mechanism back to its undeformed equilibrium state autonomously and passively without the need of any external action. Thus, the guiding and motor functions are naturally integrated in the mechanism. Its design usually involves a small number of mechanical components, sometimes limited to a single one, which simplifies the assembly procedure. It represents then an efficient solution to build systems with a high positioning accuracy thanks to the absence of gap and backlash between components. Finally, since the motion of compliant mechanisms relies on their elastic deformation, the influence of friction can be considerably reduced or even completely removed. Thus, these elements present a long operational life as the impact of wear is limited and they can be used without any form of lubrication [42].

In terms of applications, compliant elements can be found in various domains: in constant-force mechanisms applying a constant reaction force despite being deformed [16, 105] (Figure 1.1a), in electrical contacts to ensure a reliable connection between moving parts [71] (Figure 1.1b), in robotic orthoses to design safe lightweight structures for the rehabilitation of neurological impaired patients [43], in grippers able to adapt to the different sizes and shapes of the handled objects [61], in the auto-focusing mechanism of cameras leading thus to better performance and quality [52], in atomic force microscopes to improve their accuracy [9] (Figure 1.1c) and in deployable structures [80] which are the main applications covered in this thesis. Let us also mention that compliant mechanisms can be efficiently designed using topology optimisation methods [42, 61, 98].

As it can be seen, compliant mechanisms are used in a broad range of applications and can take many forms. This thesis addresses the study of a special class of mechanisms called *tape springs* and their application in deployable space structures.

1.1 Tape springs: properties, applications and analysis tools

Tape springs are defined as thin strips curved along their width. They are commonly known as Carpenter tapes and used in the everyday life as measuring tapes. Before presenting their properties, their geometry and some fundamental concepts are defined. Their geometric characteristics are illustrated in Figure 1.2 where L is the length, t is the thickness, α is the subtended angle, R is the transverse radius of curvature, h is the height of the cross-section and w is the width of the

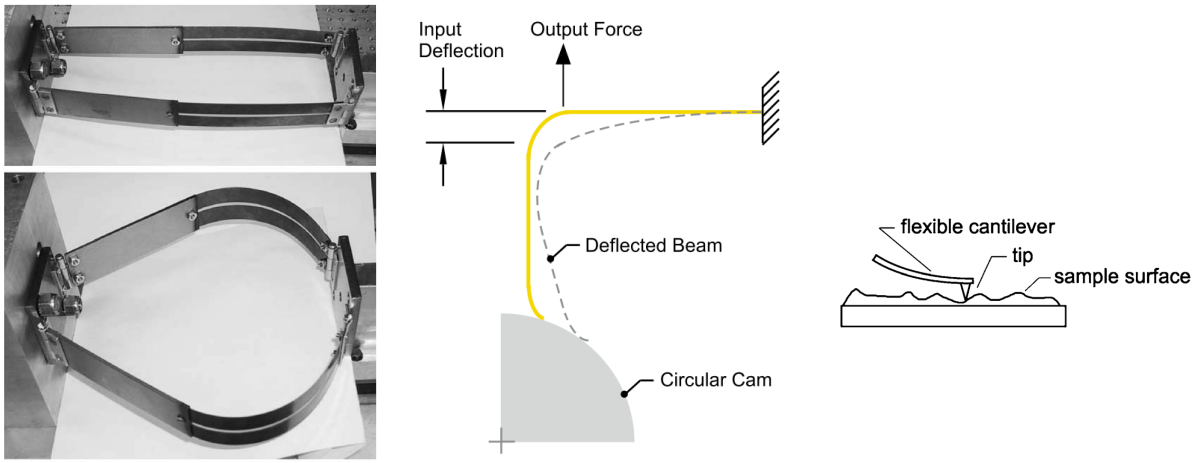

(a) Compliant constant force mechanism [16].

(b) Basic architecture of a compliant constant force electrical contact [71].

(c) Schematic representation of an atomic force microscope [42].

Figure 1.1: Compliant mechanisms.

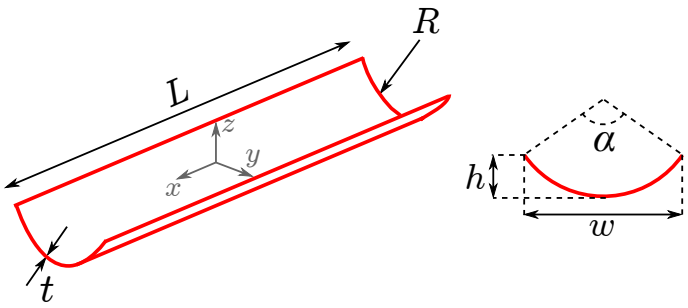

Figure 1.2: Geometric characteristics of tape springs with the length L, the thickness t, the subtended angle α, the transverse radius of curvature R, the height of the cross-section h, the width of the cross-section w and the reference coordinate system (x, y, z).

cross-section. The associated reference coordinate system (x, y, z) is defined such that the x-axis corresponds to the longitudinal direction, the y-axis corresponds to the transversal direction and the z-axis corresponds to the vertical direction unless otherwise specified. When the tape spring is straight as in Figure 1.2, it shall be referred to as the *undeformed configuration*, the *deployed configuration* or the *equilibrium state*. Starting from this configuration, it is possible, by for example applying bending moments at its extremities, to force the tape spring to buckle. It leads thus to a *folded configuration*, as illustrated in Figure 1.3, which is characterised by a fold in the middle, undeformed parts near the extremities and away from the fold, and transition regions between the fold and the undeformed parts.

The initial transverse curvature of tape springs is responsible for their nonlinear behaviour which leads to the following properties, in addition to the general characteristics of compliant mechanisms presented previously. First of all, when deformed to reach their folded configuration, the deformations may stay in the elastic regime, provided that the geometric and material parameters satisfy a design constraint [93]. When released from the folded configuration, a small but non-zero residual bending moment allows a passive and self-actuated deployment until the tape spring reaches its equilibrium state which, in the context of this work, is the straight stress-free configuration. In some other applications, several stable configurations may coexist [51, 80].

Figure 1.3: Folded configuration of a tape spring.

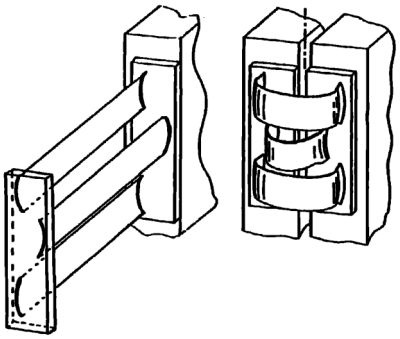

Figure 1.4: MAEVA hinge [33].

Furthermore, compared to kinematic joints which usually imply some sliding between contact surfaces while in motion, the deployment of tape springs only leads to the deformation of structural elements. The use of lubricant is then irrelevant in this case and the risks of outgassing or contamination are thus limited in space environments. The structural simplicity of tape springs is also a strong asset since it greatly improves the robustness and limits the possibilities of failure during the folding and deployment stages. Moreover, they represent an efficient alternative to reduce the weight of the support structure as they combine the support, guiding and motor functions in a single element. Finally, due to the formation of a fold which is localised in a small region of the tape springs when they are bent, high packaging ratios can be achieved in order to fit large structures in the confined space available in the fairing of launch vehicles.

Several tape springs can easily be combined to form a compliant hinge and meet the requirements of the application at hand with a high versatility. For example, the MAEVA hinge is composed of three tape springs with alternate orientations [33] (Figure 1.4) and Boesch *et al.* designed a hinge with four pairs of tape springs, each one being composed of a long and a short element [14] (Figure 1.5). The assets of tape springs can also be found in hinges consisting of thin walled tubes with longitudinal holes which are called *integral slotted hinges* [63, 74] (Figure 1.6).

The main applications for tape springs are the deployment of space structures around satellites. Successful ones can be found in several space missions such as the six MYRIADE microsatellites for the deployment of solar arrays, antennas and masts [97], the ALOUETTE spacecraft for the deployment of a mast called *Storable Tubular Extendible Member* (STEM) [35] or the MARS EXPRESS spacecraft for the deployment of a long wavelength antenna [74]. They will be found in future missions such as SOLAR ORBITER for the deployment of a radio and plasma wave antenna, NORSAT-1 for the deployment of an AIS (Automatic Identification System) receiver

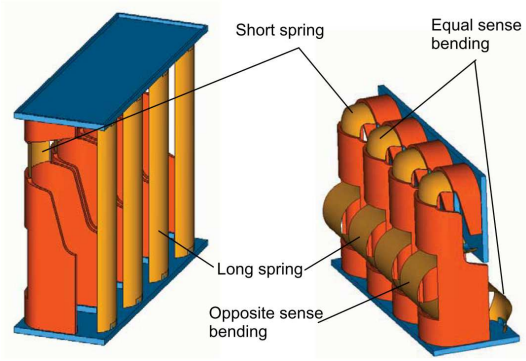

Figure 1.5: Hinge designed by Boesch *et al.* [14].

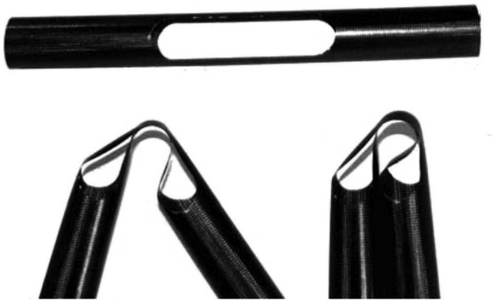

Figure 1.6: Integral slotted hinge [63].

and they are considered as support structures for the deployment of Cassegrain telescopes composed of two mirrors (primary and secondary) connected by tape springs [11], for the deployment of inflatable structures [26] and for the deployment of solar sails [46, 96].

The complexity of tape springs comes from their highly nonlinear mechanical behaviour whose major features are presented here and will be described in detail in Chapter 2. First of all, according to the sense of bending, different deformed configurations are encountered. For example, by submitting a tape spring to pure bending at its extremities, the opposite sense bending leads to the formation of a symmetric fold, while in equal sense bending, an instability in torsion leads first to an asymmetric deformed configuration before, in some cases, forming a symmetric fold. These folds are induced by the buckling of the tape spring. This phenomenon represents the transition from a configuration withstanding a large bending moment and characterised by a high stiffness to a folded configuration associated with a small residual bending moment and a very low stiffness. Because of the low post-buckling stiffness, large motion amplitudes can be encountered and have to be constrained and accurately evaluated in order to avoid collisions with other components. Likewise, the shocks created by the formation and the disappearance of folds have to be monitored to limit the interferences with other sensitive instruments. Finally, the loading and unloading evolutions of a tape spring are not identical. The quasi-static and dynamic responses are then affected by some energy dissipation. In the case, for example, of a deployment, this phenomenon of hysteresis helps bringing the tape spring back to its equilibrium state after a limited number of cycles.

For the pure bending of a single tape spring, Wüst [111], Rimrott [86] and Mansfield [66] were the first to derive the theoretical relationship between the applied rotation angle and the associated bending moment. Various analytical models were developed afterwards: in [94], since the fold after buckling is localised and the regions near the extremities remain straight, tape

springs are represented as two rigid bodies of variable length interconnected by a mobile hinge (Figure 1.7); in [92], a variational approach expressed in terms of potential energy is used to perform quasi-static analyses; in [37, 81], a one-dimensional planar rod model with a flexible cross-section is investigated (Figure 1.8); in [18], a viscoelastic analytical model representing three aspects (stowage, stability and deployment) of bistable tape springs is developed; in [53, 54], the equations of motion for the deployment of solar panels with tape springs are derived through a path-dependent path identification method combined with dynamic equations (Figure 1.9) and based on a rigid multi-body theory in [57]. Numerous examples of finite element analyses exploiting models defined by shells can also be found. For example, comprehensive static analyses were performed in order to understand the impact of geometric and material parameters on the relationship linking the bending moment to the rotation angle in the case of a single tape spring [93] or of integral slotted hinges [65]. Nonlinear dynamic analyses focusing on the nonlinear phenomena are available in [41] and on the three-dimensional folding and deployment of tape springs in [106]. The compliance of tape springs is generally high during the deployment and the oscillations about the final equilibrium configuration may involve strongly nonlinear phenomena as the local folds may get released and/or reversed during the motion. In such simulations, the dynamic response thus appears extremely sensitive to the physical and numerical parameters of the model.

So far in the majority of these works, the dynamic simulations of tape springs were performed without any physical representation of the structural damping with few notable exceptions such as in [54, 57] where it is represented by a diagonal damping matrix with constant damping elements chosen to fit directly the experimental deployment, in [74] where the damping factors of the proportional damping model are functions of the natural frequency of the studied tape spring hinge and in [18, 58] where the parameters of a Prony series are fitted on the experimental evolution of the relaxation modulus of the tape springs at different temperatures. Clearly, structural damping significantly affects the deployment of tape springs which calls for further investigations related with damping models and their experimental characterisation.

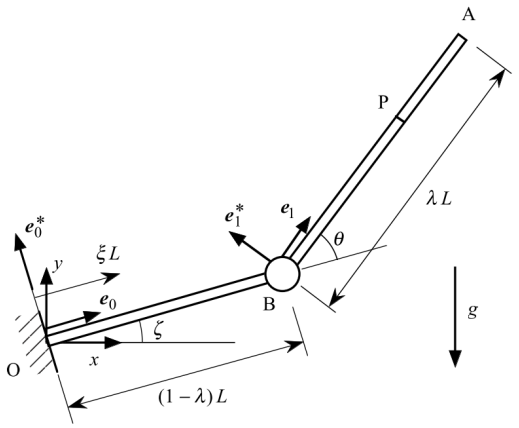

Figure 1.7: Representation of tape springs as two rigid bodies of variable length interconnected by a mobile hinge [94].

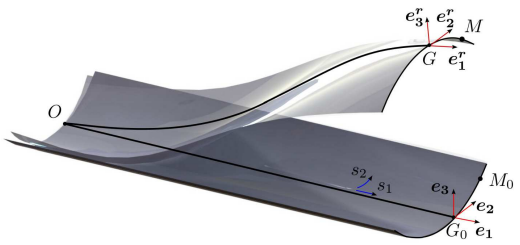

Figure 1.8: Representation of tape springs as one-dimensional planar rods with a flexible cross-section [37, 81].

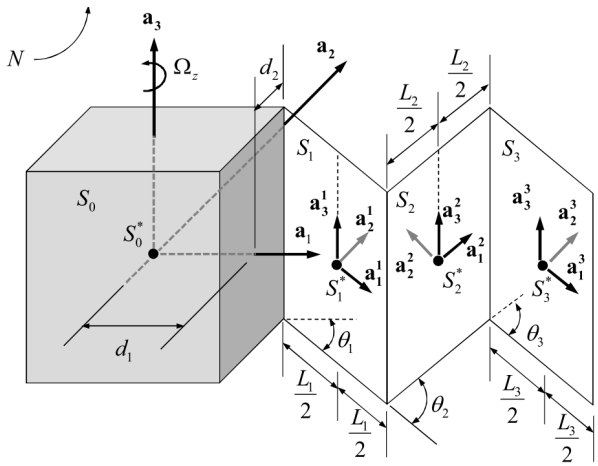

Figure 1.9: Model used for the deployment of solar panels in [53, 54].

One of the first experimental tests on tape springs was performed by Fischer [31] and reproduced by Seffen [94, 95]. The apparatus, illustrated in Figure 1.10, is used to measure the quasi-static bending moment at the extremities of the tape spring while controlling the rotation by the means of gear boxes. More recent experimental tests, usually combined with finite element models used for the initial design or the correlation of the full deployment simulations, can be found in [94, 107] for single tape springs in the case of planar and three-dimensional folding (Figure 1.11) respectively, in [14, 33, 102] for hinges composed of multiple tape springs (Figure 1.12), in [63, 64, 65, 74] for the deployment of integral slotted hinges (Figure 1.13), in [2, 11] for simultaneous deployments of multiple separated tape springs used as support structures for optical devices (Figure 1.14) and in [26] where tape springs are used as structural stiffeners for inflatable structures. In these works, the bending moment is estimated by the means of strain gauges without any correlated information on the configuration [107], or of load cells while the rotation angle is controlled and the motion kept planar [33, 45, 102]. Regarding displacements, the most common solution is to capture the dynamic motion using high-speed cameras and then post-treat the images [14, 65, 93, 94], which limits the experimental results to planar motions unless several cameras are used at the same time. Finally, in [33, 97], the dynamic tests had the particularity to be performed either on an air cushion table or during 0-g flights to reach microgravity conditions. To the best of our knowledge, the accurate measurement of complete 3D motions and loads during dynamic deployment tests has not yet been achieved for the quantitative analysis of the structural response of tape springs and for the validation of detailed numerical

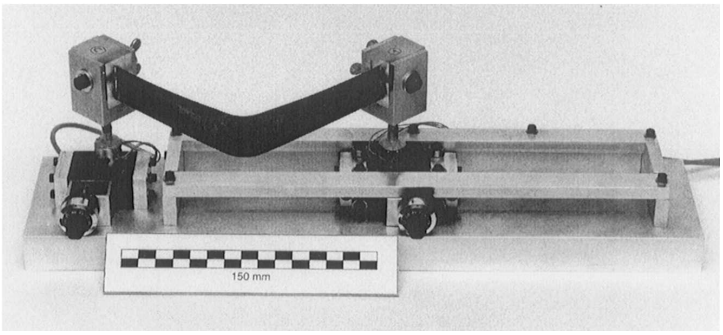

Figure 1.10: Apparatus used to measure the quasi-static relationship between the bending moment and the applied bending angle [95].

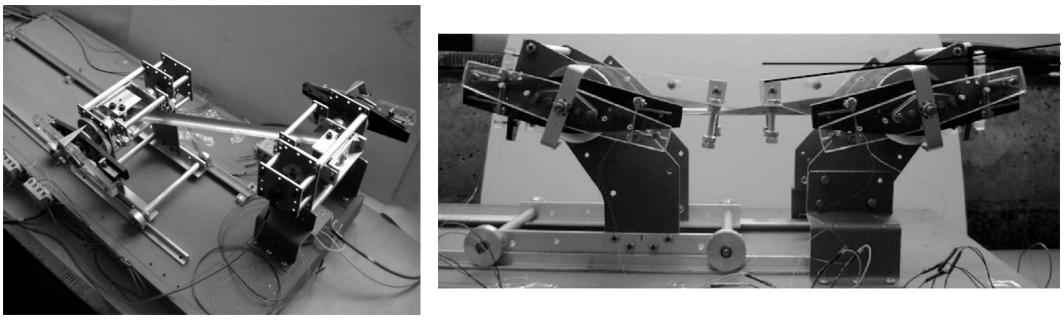

Figure 1.11: Experimental quasi-static folding of tape springs in three dimensions [107].

models. Furthermore, large campaigns of tests assessing the precision and the reproducibility of experimental results could not be found.

1.2 Objective and methodology

To summarise the state of the art regarding tape springs analysis, it can be concluded that only a very limited number of studies focusing on dynamic models were found, the large majority of the simulations being performed under static or quasi-static conditions. In terms of dynamic experimental tests, most of them were captured with cameras limiting thus the results to planar motions from which only qualitative data were extracted. Finally, only a few correlations between dynamic models and dynamic tests could be found in the literature.

The main objective of this thesis is then to develop dynamic models of tape springs able to predict a complete folding and deployment process. Based on this model, several properties of the system could be checked. In particular, the simulation should correctly predict the kinematics of the motion so as to confirm the absence of collision between the deployable appendices and the main body of the satellite. The vibration amplitudes and their decay time have to be evaluated in order to ensure that the sought configuration is reached in a reasonable time lapse and with sufficient accuracy. Furthermore, the forces and vibration frequencies transmitted to the rest of the satellite during the deployment sequence have to be quantified and compared to the requirements. Finally, the models and simulations should also give information on the mechanical stresses affecting the structures, allowing thus to check the absence of irreversible damage.

To reach this objective, the appropriate representation of the structural damping and the experimental validation of the model are essential. A three-step methodology is thus proposed. First, a detailed analysis of the tape spring quasi-static behaviour is performed based on a basic,

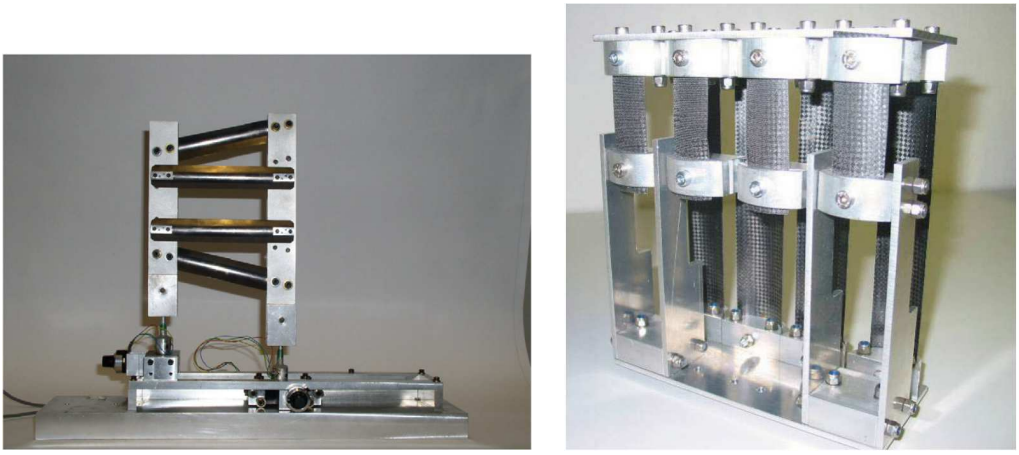

(a) Test rig from [102]. (b) Breadboard model from [14].

Figure 1.12: Experimental hinges composed of multiple tape springs.

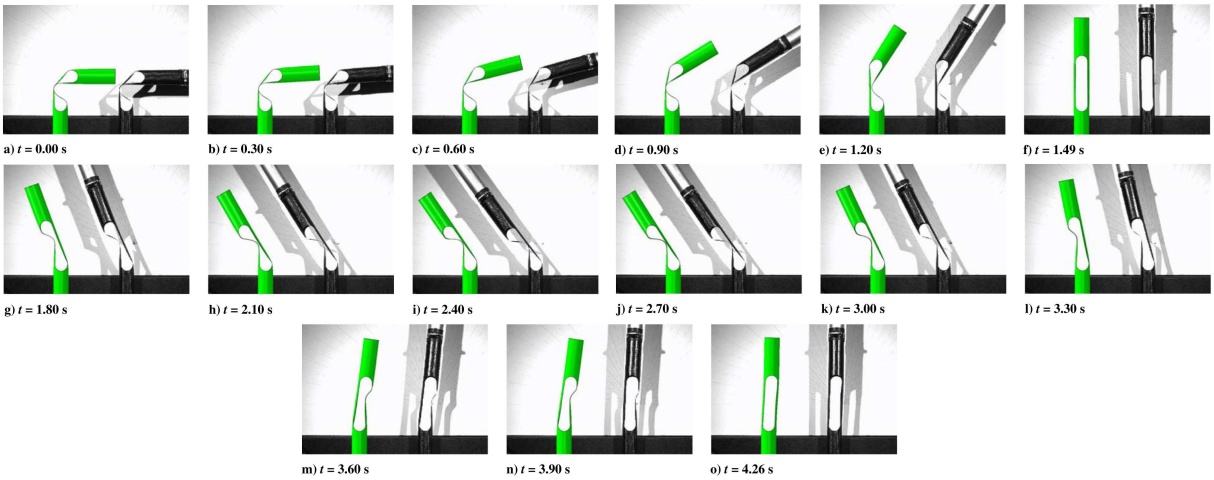

Figure 1.13: Experimental deployment of an integral slotted hinge (in black) and associated finite element model (in green) [64].

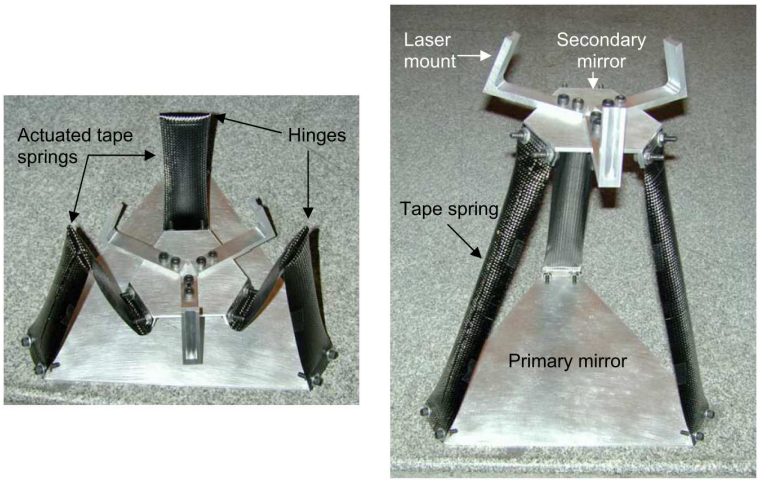

Figure 1.14: Prototype of optical devices supported by tape springs [11].

yet representative, finite element model. Then, an experimental set-up is designed and a large campaign of experimental tests is performed. The data collected based on specific tests, namely quasi-static and linear vibration tests, are thus used to identify the parameters of the associated model. Finally, the validation relies on a comparison between experimental and numerical deployment tests.

This manuscript is structured as follows. First, in order to clearly understand the behaviour of tape springs and the impact of the structural damping, the fundamental concepts that are necessary for their analysis are first defined, as well as the general characteristics of the finite element models used to represent them throughout this work (Chapter 2). Then, the impact of the geometric parameters on the nonlinear response in pure bending is investigated in terms of bending moment, deformed configuration and modal characteristics (Chapter 3). Thereafter, an optimisation procedure is developed in order to automatically determine the geometric parameters which meet the requirements of a specific deployable reflector application (Chapter 4). These analyses are performed by the means of finite element models which play a growing role in the creation, the design, the development and the testing of new devices or configurations of known components since they offer a large range of possibilities in terms of modelling and solvers often associated with a reasonable computational cost.

The impact of the structural damping in the finite element models is clarified with the help of dedicated analyses. They show the necessity of an accurate representation of physical damping phenomena in order to numerically capture all the physical characteristics of tape springs. A first simple model of structural damping characterised by a single parameter is proposed (Chapters 5 and 6).

Then, an experimental set-up is designed in order to collect experimental data on the nonlinear phenomena inherent to tape springs such as buckling, the formation of folds and hysteresis, and to perform dynamic deployment tests (Chapter 7). An optoelectronic acquisition equipment which triangulates the position of active markers is exploited, along with a synchronised force plate. The procedures of experimental testing are validated by confirming the reproducibility of the tests.

In parallel, the finite element model of the set-up is developed while taking into consideration all the aspects presented previously. To determine the geometric and physical parameters of the model, specific experimental tests are undertaken and divided into two main categories: quasi-static tests (Chapter 8) and dynamic tests (Chapter 9). The final step is then to validate the model based on the experimental results. Since the parameters of the model are not determined by directly fitting the deployment evolutions, but rather by the means of dedicated experimental tests, the quality of the correlation is an indicator of the model robustness. Thus, the proposed model could be used to predict the behaviour of the system under different conditions such as in vacuum or zero-gravity environments which cannot be experimentally reproduced with the infrastructures available in the laboratory.

CHAPTER 2

FUNDAMENTAL CONCEPTS FOR TAPE SPRINGS ANALYSIS

In this chapter, fundamental concepts for the analysis of tape springs are presented. First of all, the general theoretical behaviour is described before summarising the analytical developments which led to the first quasi-static relationships between the applied bending angle and the resulting bending moment. Then, the characteristics of the finite element models used throughout this thesis are defined.

2.1 Theoretical behaviour

2.1.1 General behaviour

The general quasi-static behaviour of a single tape spring in pure bending is first described here based on intuitive concepts before going into more details in the next sections.

The advantageous characteristics of tape springs result from their highly nonlinear mechanical behaviour which is theoretically illustrated in Figure 2.1. This figure describes the evolution of the bending moment M determined at the clamped extremity of the tape spring when the bending angle θ is imposed at the other end. Similar descriptions can be found in [93, 94, 95], while a simplified diagram is available in [102].

First of all, the sense of bending has a significant impact on the behaviour and on the deformed configuration of the tape spring. The two senses of bending are defined and described as follows: the *opposite sense bending* ($M, \theta > 0$) leads to longitudinal and transverse curvatures in opposite sense which induce tensile stresses along the longitudinal edges, while the *equal sense bending* ($M, \theta < 0$) leads to longitudinal and transverse curvatures in the same sense which induce compressive stresses along the longitudinal edges [111].

In opposite sense bending, starting from point O, the evolution of the bending moment M is linear for small bending angles. The corresponding deformed configuration is characterised by a constant longitudinal curvature. As the rotation angle θ increases, the region located in the middle of the tape spring flattens and the associated bending moment continues to increase until it reaches a maximum $M_+^{\max}$ called *peak moment*. Shortly after, the moment undergoes a sharp drop (AB) which is due to the buckling of the structure leading to the formation of a fold. In this configuration, only the middle part of the tape spring is deformed due to the fold, while the rest of the structure remains almost straight. Regarding the radius of curvature of the fold, it can be considered as a first approximation as equal to the transverse radius of curvature of the non-deformed structure [20, 111]. However, finite element analyses showed that

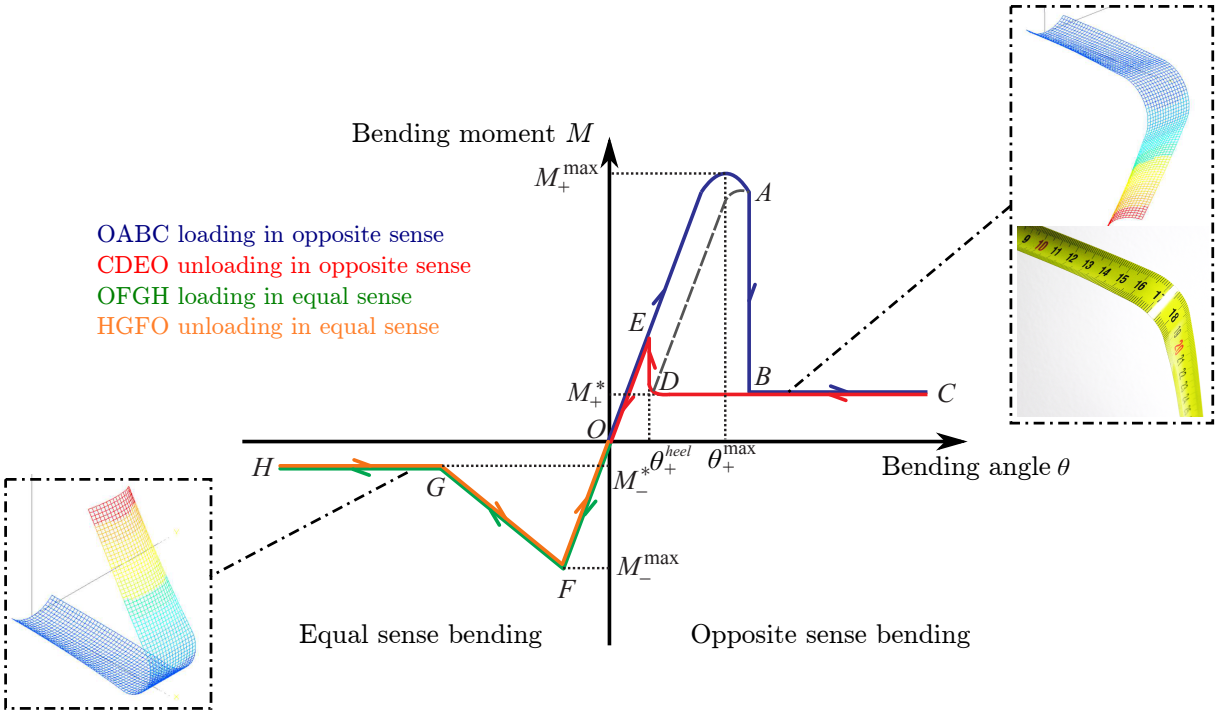

Figure 2.1: General evolution of the bending moment M with respect to the bending angle θ in pure bending (inspired from [93]).

a difference exists [91], although marginal. Once buckling occurred, larger rotation angles induce in theory no change in the bending moment (BC) which is defined as the *steady-state* or *residual moment* M_+^*. Regarding the deformed configuration, only the arc-length of the fold is affected by the variations of the bending angle. All this description is representative of the quasi-static loading or folding of a tape spring in opposite sense.

Regarding the controlled unloading of this loaded configuration, the first part of the curve (CB) is superimposed on the loading path. However, at point B, the red curve remains equal to M_+^* until point D, associated to the heel angle θ_{heel}, is reached before jumping back on the loading curve at point E which corresponds to a deformed configuration without any fold. For the last part (EO), a linear evolution is recovered.

The fact that the fold does not disappear at the same rotation angle as the one at which it is formed is responsible for a hysteresis phenomenon. Every time that a fold is formed and then disappears, some energy is transferred to the high-frequency modes of deformation leading thus to some dissipation [41], which can be quantified by computing the difference of areas under the loading and unloading curves. In the case of a dynamic deployment, this results first in a decrease of the motion amplitude until the amount of energy in the system becomes too small to go beyond the maximum bending moment and trigger buckling. The tape spring vibrates then around its equilibrium state characterised by a higher stiffness. This abrupt increase in the stiffness from a configuration with a fold to an unfolded one is called *self-locking*.

The jumps AB and DE are part of the stable evolution of the tape spring. Nonetheless, an unstable path of the static equilibrium exists between points A and D. It can be captured by the means of continuation methods as in [41, 93] leading to the superposition of the loading and unloading paths, however, experimentally only the stable behaviour can be measured.

In the equal sense bending, starting again from O, the relationship between the bending moment and the rotation angle is linear (OF) and characterised by the same stiffness as in opposite sense. The peak moment is reached for a relatively small angle which implies that $|M_-^{\max}| < |M_+^{\max}|$. It is directly followed by buckling which, in this case, is due to asymmetric torsional folds converging from the extremities of the tape spring to its middle where they combine to form a symmetric fold. Then, as in opposite sense, the behaviour after buckling (GH) is defined by a constant steady-state or residual moment M_-^* such that $|M_-^*| < |M_+^*|$. Finally, it is commonly accepted that, in theory, the unloading path in equal sense coincides with the folding sequence, although in practice and in finite element models the adequacy is not perfect [94].

After this qualitative description of tape springs behaviour and of the main features of their response, such as buckling, the creation of folds and the hysteresis phenomenon, more detailed analytic developments which led to these results are described in the following section.

2.1.2 Analytical developments

In the early developments of the plate theory, a large number of works was dedicated to the understanding of their elastic behaviour in the case of small deformations. Since the twentieth century and the advent of aeronautics, the need for a theory taking into account large deflections increased substantially, mainly because these structures consist of large surfaces with a thickness relatively small in comparison with the other two dimensions. The pioneers were well known mathematicians such as Von Kármán and Reissner who, respectively, derived the governing nonlinear equations in the case of large deflections and studied the bending and torsion of long strips of constant thickness.

In the case of initially curved plates, three main authors developed the mathematical background that is used nowadays. Chronologically, Wüst [111] was the first to exploit equilibrium considerations starting from the theory of linear shell structures to determine the relation between the bending moment and the resulting longitudinal curvature. Then, Rimrott [86] managed to obtain the same results through energetic considerations. Finally, Mansfield [66] created his own model based on a variational method and, most importantly, he was the first to include the effects of torsion observed in equal sense bending in his theory.

Wüst's general theory [111] The main hypothesis of Wüst's theory is to consider that a tape spring with a small initial transversal curvature κ_t subtending a small angle α can be studied as a slightly distorted axisymmetric cylindrical shell submitted to pure bending (Figure 2.2). Furthermore, the length L of the tape spring is considered infinitely long to be free of end effects by the principle of Saint-Venant. Finally, the deformed configuration is induced by two identical end moments M which create a uniform longitudinal curvature κ_l of corresponding radius r_l. The remaining parameters are the transverse radius of curvature $R = 1/\kappa_t$, the thickness t and Poisson's ratio ν.

By starting from the theory of shells from Calladine [19, 94] and linking the bending moment per unit length to the out of plane displacement of the axisymmetric shell, Wüst defines a nonlinear relationship between the applied bending moment M and the longitudinal curvature κ_l:

$$M = \frac{\alpha R t^3}{12} \frac{E}{R(1-\nu^2)} \left[(\nu + R\kappa_l) - \nu(1+\nu R\kappa_l)P_1 + (1+\nu R\kappa_l)^2 \frac{P_2}{\kappa_l R} \right] \tag{2.1}$$

with

- $P_1 = \dfrac{2}{\lambda} \dfrac{\cosh\lambda - \cos\lambda}{\sinh\lambda + \sin\lambda}$

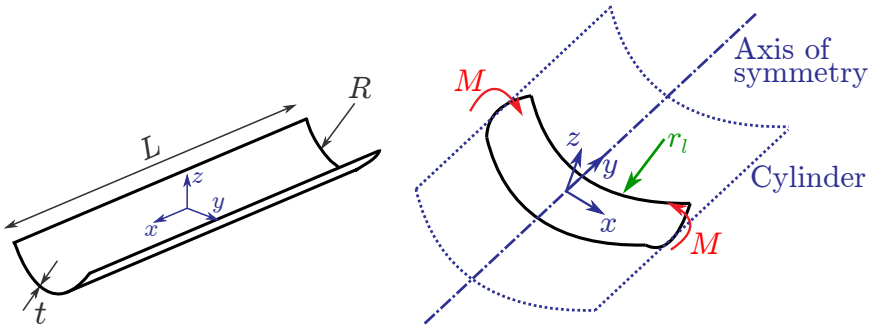

(a) Undeformed configuration. (b) Deformed configuration and cylinder.

Figure 2.2: Representation of the Wüst's theory based on an axisymmetric cylinder and coordinate reference system (x, y, z) [111].

$$\triangleright\ P_2 = \frac{1}{2\lambda}\frac{\cosh\lambda - \cos\lambda}{\sinh\lambda + \sin\lambda} - \frac{\sinh\lambda\sin\lambda}{(\sinh\lambda + \sin\lambda)^2}$$

$$\triangleright\ \lambda = \sqrt[4]{3(1-\nu^2)}\sqrt{\frac{\kappa_l R^2\alpha^2}{t}}$$

This result is only valid in opposite sense bending since it is only characterised by flexural deformations. Indeed, this analytical model does not take torsional deformations into account which appear in the case of equal sense bending. Furthermore, due to the hypotheses, Eq. (2.1) leads to a deformed tape spring with uniform longitudinal curvature κ_l. Wüst's general theory can then be used to evaluate the maximum bending moment in opposite sense and the residual moment, as it will be detailed later in this section. The main steps leading to these results are detailed in Appendix A.

Wüst's simplified theory [94, 111] As mentioned in the general characteristics of tape springs, it is commonly assumed that in the region of a well defined fold, the transversal curvature κ_t is equal to zero and the longitudinal curvature κ_l is equivalent to the initial transversal curvature of the undeformed tape spring R^{-1}. This region can then be approximately represented by a cylinder. Furthermore, the Gaussian curvature of the undeformed $(\kappa_l = 0, \kappa_t \neq 0)$ and the deformed $(\kappa_l \neq 0, \kappa_t = 0)$ configurations, defined as the product of the longitudinal and transversal curvatures $\kappa_l.\kappa_t$, remain the same. Based on these considerations, for a bending angle large enough between the extremities of the tape spring which forms a well defined fold in opposite or equal sense, Wüst derives simplified expressions for the residual moment in opposite sense:

$$M_+^* = (1+\nu)D\alpha \tag{2.2}$$

and for the residual moment in equal sense:

$$M_-^* = -(1-\nu)D\alpha \tag{2.3}$$

These results were also obtained by Rimrott [86].

Mansfield's theory [66] The theory developed by Mansfield exploits the nonlinear equations describing the evolution of large deflections in long strips with a transverse curvature characterised by either a lenticular or constant thickness profile. Only the second situation is of interest in the case of the tape springs considered in this work. This theory also captures the bending and, unlike Wüst's theory, the torsion characterising the deformation of tape springs.

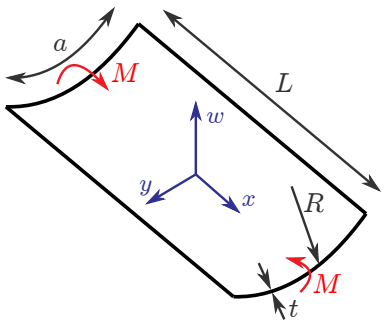

Figure 2.3: Coordinate reference system (x, y, w) for Mansfield's theory and characteristics of the tape spring [66].

The hypotheses that guarantee the validity of this theory are the following. First of all, the rotations and the slopes are assumed small everywhere as it is commonly done in the theory of plates submitted to large deflections. The *everywhere* condition can be relaxed to *a length equal to the width of the plate* in particular cases when all the sections behave in the same manner. Furthermore, as in the theory developed by Wüst, the tape spring is considered infinitely long in order to avoid taking end effects into account. Finally, the reference coordinate system and the characteristics of the tape spring used in these developments are given in Figure 2.3.

Based on the evolution of the total strain energy with respect to the deflection of the strip, Mansfield derives the following expression of the non-dimensional bending moment:

$$\bar{M} = \bar{\kappa}_x + \frac{\lambda}{1-\nu^2}\left(\mu\Phi_1(\bar{\kappa}_x) - \lambda\bar{\kappa}_x\Phi_2(\bar{\kappa}_x)\right) \tag{2.4}$$

with the parameters:

- $\bar{M} = \dfrac{3a\sqrt{3(1-\nu^2)}}{Et^4}M$
- $\lambda = \bar{\kappa}_{xy}^2 + \bar{\kappa}_x(\nu\bar{\kappa}_x - \bar{\kappa}_{y,0})$
- $\mu = 2\nu\bar{\kappa}_x - \bar{\kappa}_{y,0}$
- $\Phi_1(\bar{\kappa}_x \neq 0) = \dfrac{1}{\bar{\kappa}_x^2}\left[1 - \dfrac{1}{\sqrt{\bar{\kappa}_x}}\dfrac{\cosh(2\sqrt{\bar{\kappa}_x}) - \cos(2\sqrt{\bar{\kappa}_x})}{\sinh(2\sqrt{\bar{\kappa}_x}) + \sin(2\sqrt{\bar{\kappa}_x})}\right]$
- $\Phi_1(\bar{\kappa}_x = 0) = \dfrac{4}{45}$
- $\Phi_2(\bar{\kappa}_x \neq 0) = \dfrac{1}{\bar{\kappa}_x^4}\left[1 + \dfrac{\sinh(2\sqrt{\bar{\kappa}_x})\sin(2\sqrt{\bar{\kappa}_x})}{(\sinh(2\sqrt{\bar{\kappa}_x}) + \sin(2\sqrt{\bar{\kappa}_x}))^2} - \dfrac{5}{4\sqrt{\bar{\kappa}_x}}\dfrac{\cosh(2\sqrt{\bar{\kappa}_x}) - \cos(2\sqrt{\bar{\kappa}_x})}{\sinh(2\sqrt{\bar{\kappa}_x}) + \sin(2\sqrt{\bar{\kappa}_x})}\right]$
- $\Phi_2(\bar{\kappa}_x = 0) = \dfrac{32}{2835}$
- $\{\bar{\kappa}_{y,0}, \bar{\kappa}_x, \bar{\kappa}_{xy}\} = \dfrac{a^2\sqrt{3(1-\nu^2)}}{4t}\{\kappa_{y,0}, \kappa_x, \kappa_{xy}\}$

where $\kappa_x, \kappa_{y,0}$ and κ_{xy} are respectively the longitudinal curvature, the initial transverse curvature and the twisting curvature, a is the arc length of the tape spring cross-section and non-dimensional quantities are marked by the symbol $(\bar{.})$. Contrary to Wüst's theory, the effect of torsion is taken into account through the twisting curvature κ_{xy}. As for the previous theory, more detailed developments are available in Appendix A.

t	α	R
0.1 mm	1.92 rad	14 mm

Table 2.1: Geometric characteristics of the tape spring (thickness t, subtended angle α and transverse radius of curvature R).

E	ν	ρ
131000 MPa	0.3	8100 kg/m^3

Table 2.2: Material properties of beryllium copper (Young's modulus E, Poisson's ratio ν and density ρ) [93].

Comparison and numerical results In order to compare the two analytical theories, the evolution of the bending moment with respect to the longitudinal curvature (denoted as κ_l in the first case and as κ_x in the second one) is computed based on Eqs. (2.1) and (2.4) for the opposite sense bending. The geometric and material characteristics of the considered tape spring are given in Tables 2.1 and 2.2 respectively. Since the analytical developments are only valid in the case of infinitely long tape springs, the value of the length L is not fixed at this point of the comparison.

The bending moment in opposite sense obtained in Wüst's theory is illustrated in Figure 2.4. This curve represents the evolution of M in the case of a uniform longitudinal bending of the whole tape spring before and after the maximum peak, while in the general behaviour presented in Section 2.1.1 and in practice, the longitudinal curvature is not uniform after buckling because of the creation of a fold. Based on this curve, it is then possible to identify the initial stiffness as the tape spring is truly defined by a constant and uniform longitudinal curvature in this first phase, the subsequent maximum bending moment $M_+^{\max}$ and finally the residual bending moment M_+^* by applying concepts from the propagating instabilities theory [22, 94]. This latter is obtained *by searching for a horizontal line such that the area above this line, but under the peak of the curve is equal to the area below this line and above the trough (Maxwell construction)* [94, 95]. This horizontal line is represented in Figure 2.4, as well as the intersection point at which the residual moment is measured. A summary of all these results is given in Table 2.3.

Mansfield's theory leads to a curve with a similar evolution illustrated in Figure 2.5. Compared to the results from Wüst's theory (Table 2.3), it can be seen that the three considered features, the maximum bending moment $M_+^{\max}$, the associated bending angle $\theta_+^{\max}$ and the residual moment M_+^* in opposite sense, are smaller of 1.52 %, 0.43 % and 5.88 % respectively. It can be concluded, as expected, that both theories give similar results [94].

Furthermore, the expression of the residual moment in opposite sense Eq. (2.2), which comes from Wüst's simplified theory, leads to a good approximation of the value in Wüst's general theory with a difference of 4.80 % and of the value in Mansfield's theory with a difference of 11.34 %.

Finally, preliminary tests were performed with finite element models which will be described in detail in the next section. It can be seen in Table 2.3 that the characteristics of the maximum bending moment are close to the analytical developments in the case of long tape springs since, in the theories, tape springs with an infinite length are considered. However, for shorter tape springs, the increasing impact of end effects leads to larger bending moments and smaller associated bending angles. Nonetheless, the residual moment remains weakly affected.

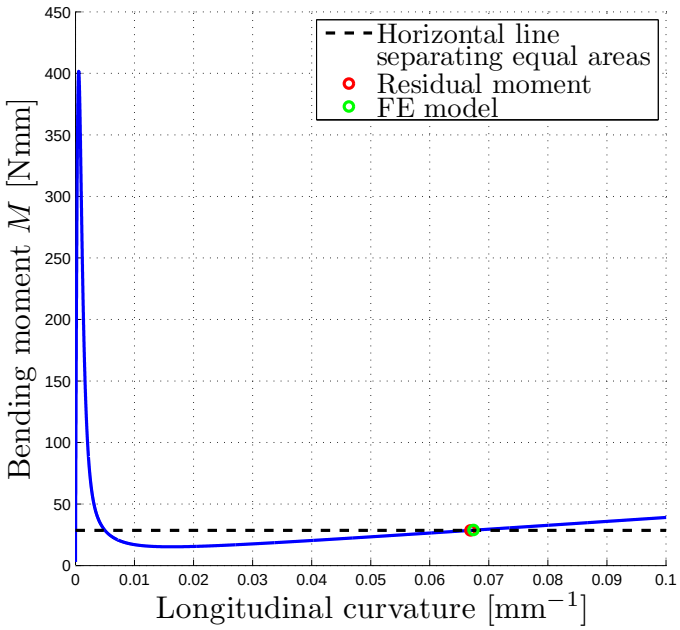

Figure 2.4: Wüst's theory: evolution of the bending moment with respect to the longitudinal curvature Eq. (2.1).

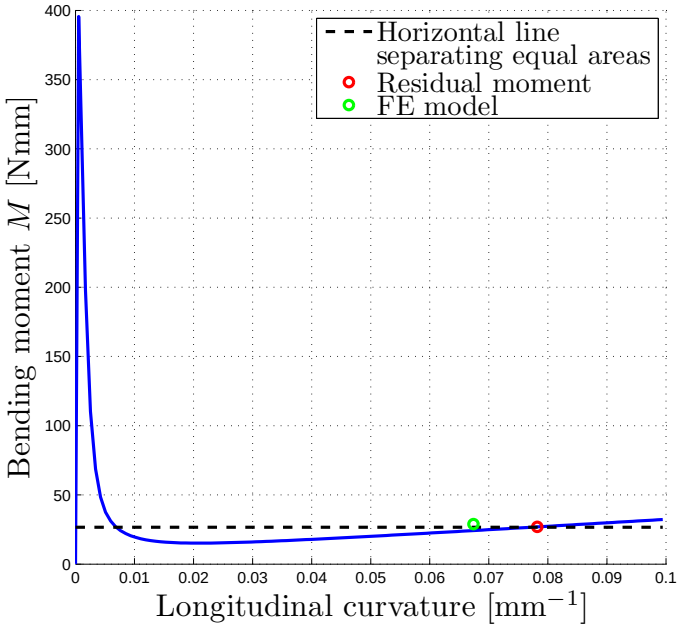

Figure 2.5: Mansfield's theory: evolution of the bending moment with respect to the longitudinal curvature Eq. (2.4).

	$M_+^{\max}$ [Nmm]	$\theta_+^{\max}$ [deg]	M_+^* [Nmm]	M_-^* [Nmm]
Wüst's theory	401.72	13.81	28.57	–
Mansfield's theory	395.62	13.75	26.89	–
$M_+^* = (1+\nu)D\alpha$	–	–	29.94	–
$M_-^* = -(1-\nu)D\alpha$	–	–	–	−16.12
FE model ($L = 440$ mm)	416.32	13.78	29.77	–
FE model ($L = 220$ mm)	469.61	7.56	28.93	−16.90
FE model ($L = 110$ mm)	758.42	5.76	30.85	−15.95

Table 2.3: Comparison of the results from Wüst's theory, Mansfield's theory, simplified expressions of the residual bending moments in both senses and finite element models for the maximum bending moment in opposite sense $M_+^{\max}$, the associated bending angle $\theta_+^{\max}$, the residual moments in opposite sense M_+^* and in equal sense M_-^*.

L	t	α	R
100 mm	0.1 mm	1.57 rad	10 mm

Table 2.4: Geometric characteristics of the tape spring for the description of the finite element models (length L, thickness t, subtended angle α and transverse radius of curvature R).

A further comparison between the finite element model and both theories relies on the evaluation of the longitudinal curvature of the fold. To this end, a circle is fitted on three points located within the fold of a tape spring model with the characteristics defined in Tables 2.1 and 2.2 and a length of 220 mm. A mean curvature is computed between 50° and 90° where the fold is assumed to be well defined. The resulting data $(\kappa_l^{FEM}, M_+^*) = (0.0674\ \text{mm}^{-1}, 28.93\ \text{Nmm})$ are represented in Figures 2.4 and 2.5 by a green circle where it can be seen that the numerical model is in good agreement with Wüst's theory, but is further from Mansfield's. Furthermore, it confirms that the longitudinal curvature of the fold can be approximated by the initial transverse curvature since $1/\kappa_l^{FEM} = 14.8$ mm, that is a difference of 5.7 % with respect to $1/\kappa_t = R = 14$ mm.

Regarding the residual moment in equal sense M_-^* given in Table 2.3, the finite element models with a length of 220 mm and 110 mm are also close to the simplified expression from Eq. (2.3). In the case of a length of 440 mm, no value could be extracted from the model as it does not buckle to form a symmetric fold in equal sense. The impact of the length on the results of the finite element models briefly presented here will be confirmed and studied in depth in Section 3.2.2.

2.2 Finite element models

Throughout this thesis, finite element models of tape springs are used to perform parametric analyses, to develop optimisation procedures, to study the validity of different forms of damping and to reproduce experimental tests. In this section, the main characteristics of these finite element models are defined, while features specific to the considered application will be indicated in their dedicated sections.

All the finite element models are developed in the commercial software Samcef [89]. The results presented in this section were obtained for a tape spring defined by the geometric parameters from Table 2.4 and the material properties from Table 2.2.

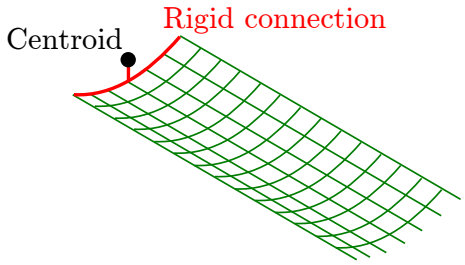

Figure 2.6: Additional node at the centroid of the cross-section located at the extremity of the tape spring used for the definition of boundary conditions.

2.2.1 Element type

In tape springs, the thickness is commonly several orders of magnitude smaller that the other dimensions. Modelling them by the means of flexible linear shell elements based on the Mindlin-Reissner theory represents then an efficient solution. For information, parabolic shells were also tested, but using them had a negligible impact on the results while unnecessarily increasing the computational cost.

This plate theory is an extension from the Kirchhoff-Love theory [60], in which the equations of motion of two dimensional thin plates are derived, taking the effects of shear deformations through the thickness of the plates into account [73]. This theory considers that straight lines initially normal to the middle surface of the plate remain straight and undeformed, but not necessarily normal to the deformed middle surface. This implies that the shear deformations are responsible for a linear variation of the displacement field along the thickness, but this latter is assumed to remain constant [78]. The plate theories developed by Mindlin [73] and Reissner [84] are based on different hypotheses. The main one is that Reissner's theory starts with an assumed stress field, while Mindlin's starts with an assumed linear displacement field [10, 108].

If no structural dissipation is taken into account in the model, a linear, isotropic and elastic material law is defined in the shell model by introducing the Young's modulus, the Poisson's ratio and the density of the considered material. Otherwise, the dissipation will be represented by the means of a viscoelastic material law which will be discussed later.

2.2.2 Boundary conditions

In order to facilitate the definition of boundary conditions, two additional nodes are created at the centroids of the cross-sections located at the extremities of the tape spring (Figure 2.6). These nodes are rigidly connected to their corresponding cross-sections which are themselves considered as rigid. At these nodes, it is either possible to evaluate the bending moment by the means of a clamp, impose a loading or unloading sequence by controlling the bending angle, connect the tape spring to other elements or leave them free of constraint.

2.2.3 Quasi-static analyses

Solver In the case of quasi-static analyses involving the folding and the controlled unloading of tape springs, the damped Newmark method [79] of first-order accuracy is used. To respect the quasi-static conditions, the deformation is performed at a slow rate, usually by prescribing an evolution of the bending angle of $1°/s$.

Purely static analyses taking the form of continuation methods may be exploited to solve these problems and capture the unstable part of the equilibrium path. However, this latter is of

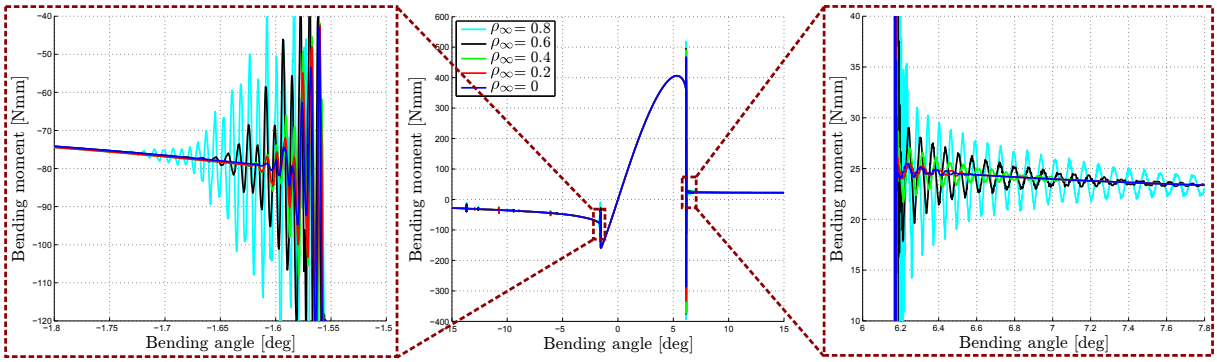

Figure 2.7: Impact of the numerical damping ρ_∞ on the nonlinear behaviour of tape springs in quasi-static analyses, zooms on the oscillations after buckling.

little practical interest in the present work and the continuation algorithms turn out to be quite sensitive to the associated numerical parameters while severely increasing the computational costs. Furthermore, a comparison between static and quasi-static results can be found in [41] which shows that the two approaches give very close solutions in the stable evolution of tape spring behaviour. As a consequence, continuation methods are not used in this work.

When using the Newmark method for a quasi-static analysis, the dynamic phenomena can be filtered out from the response by introducing some numerical damping. This latter is defined by two parameters γ and β. They can be linked to the spectral radius at infinite frequencies ρ_∞ belonging to the interval $[0, 1]$, as [34]:

$$\gamma = \frac{3 - \rho_\infty}{2(1 + \rho_\infty)} \qquad \beta = \frac{1}{(1 + \rho_\infty)^2} \tag{2.5}$$

where $\rho_\infty = 0$ leads to a complete annihilation of the high-frequency content and $\rho_\infty = 1$ to the absence of numerical damping. The impact of ρ_∞ on the quasi-static behaviour of a tape spring is illustrated in Figure 2.7. It can be seen that modifying the amount of numerical damping in the solver only affects the time required to damp out the artificial oscillations after buckling due to the numerical solver, while the other main features remain stable. The most representative curve of the quasi-static behaviour is then obtained with the numerical damping fixed to $\rho_\infty = 0$ which leads to results weakly affected by numerical oscillations.

Mesh size The choice of the mesh size is based on a convergence analysis of the maximum bending moment in both senses. Considering the evolutions described in Figure 2.8, the element size is fixed to 2 mm, even though the convergence is less marked in opposite sense than in equal sense. Indeed, a smaller element size leads to higher computation times, especially for 1 mm, and as the amplitude of the maximum bending moment is always larger in opposite sense, the mesh size should be primarily determined to accurately capture the behaviour in equal sense. In the end, the differences between mesh sizes of 2 mm and 1 mm for $M_+^{\max}$ and $M_-^{\max}$ are respectively 1.52 % and 2.08 %. Finally, the similarity of the results for meshes of 3.5 mm and 4 mm is due to the same number of shell elements used in both cases to mesh the tape spring along the width.

Time step The time step h is determined by an adaptive time stepping procedure available in SAMCEF: if the Newton-Raphson solver does not converge in a prescribed number of iterations or if the local error estimate is above the selected tolerance, the time step is reduced at most by half, convergence being achieved when the norm of the residues in relative value is below 10^{-3}. A lower limit of the time step, under which it is considered that convergence is impossible, is fixed to 10^{-6} s. Thus, the nonlinear phenomena such as buckling can be accurately captured

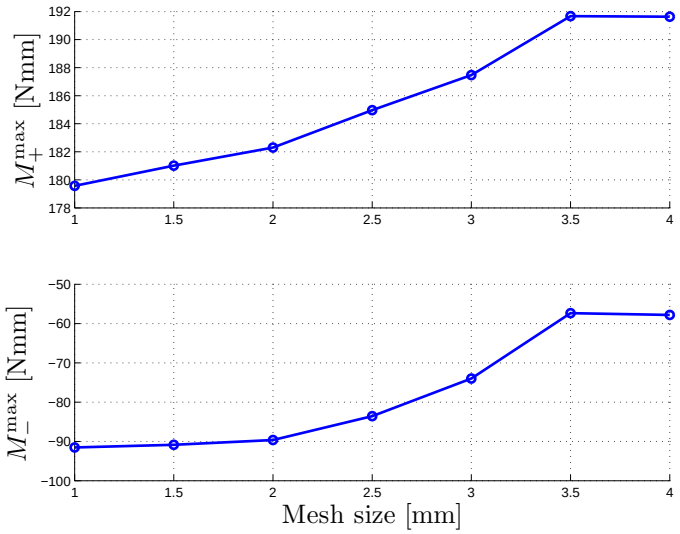

Figure 2.8: Impact of the mesh size on the maximum bending moment in opposite sense $M_+^{\max}$ and in equal sense $M_-^{\max}$.

by reducing the time step, while the computational cost can be limited otherwise. However, a maximum limit $h_{\max}$ has to be defined in order to avoid the truncation of the maximum bending moment in opposite sense due to the interpolation of a small number of computed points (Figure 2.9). In Figure 2.9a and the rest of this thesis, the following convention is used: loading curves are represented by full lines and have to be read from small to large bending angles (in absolute values), while unloading curves are represented by dashed lines and have to be read from large to small bending angles (in absolute values).

Regarding the other features characterising the tape spring, such as the instant of buckling, the residual moment or the heel angle, the choice of the maximum time step has a weak impact on their value either because they are computed with smaller steps defined by the adaptive procedure or because they are less sensitive to that numerical parameter.

Considering the convergence of the maximum bending moment in opposite sense $M_+^{\max}$ illustrated in Figure 2.10, the maximum time step is fixed to 0.1 s which leads to a difference of 0.002 % with respect to the maximum bending moment obtained with a time step ten times smaller. Notice that in this last figure, the direction of the abscissa axis is reversed.

Results The complete quasi-static evolution of the bending moment with respect to the bending angle in both senses of bending along the loading and unloading paths is given in Figure 2.11. Compared to the general behaviour presented in Figure 2.1, it can be seen that for the loading in opposite sense, all the characteristic features are well captured by the model: the linear behaviour for small rotations, the peak moment $M_+^{\max}$ followed by the buckling of the structure and a steady-state moment M_+^*. During the unloading, the bending moment jumps back on the loading curve for a smaller bending angle than the one at which buckling occurred. Thus, the hysteresis phenomenon is well captured. The only discrepancies are the vertical peaks visible when a fold is created or disappears. They are purely numerical and are due to the transient behaviour of the Newmark solver and the lack of filtering of the dynamic phenomena.

Regarding the loading and unloading paths in equal sense, they are also characterised by a peak moment $M_-^{\max}$ and a steady-state moment M_-^* for larger rotations. Furthermore, the slope in the linear zone is equivalent to the one created in opposite sense bending. However, contrary

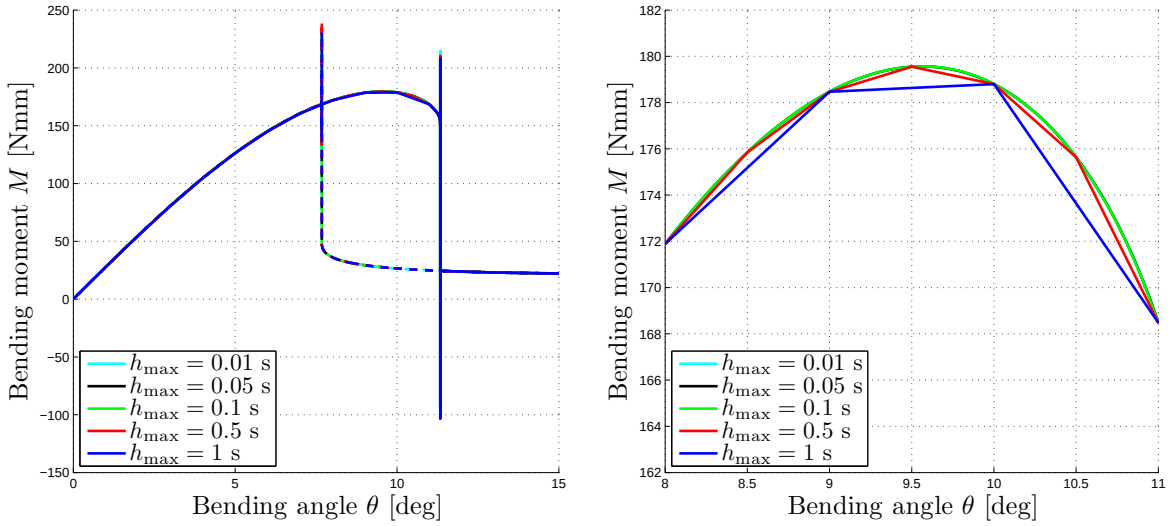

(a) Loading (full lines) and unloading (dashed lines) paths.

(b) Zoom on the maximum bending moment.

Figure 2.9: Impact of the maximum time step $h_{\max}$ on the evolution of the bending moment with respect to the bending angle in opposite sense.

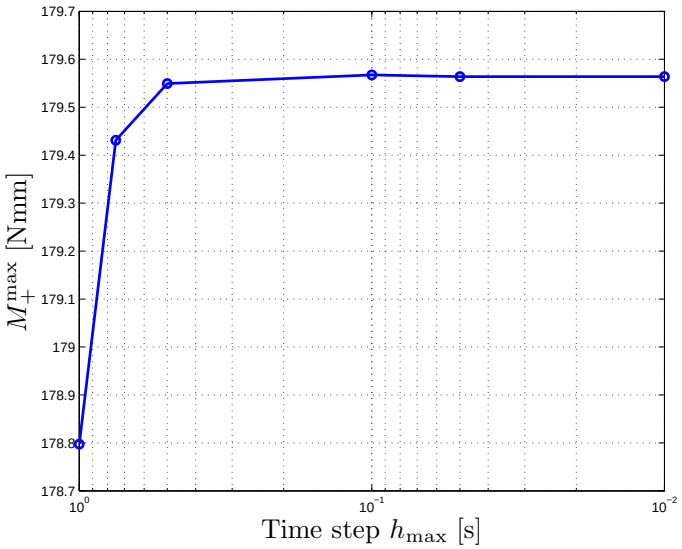

Figure 2.10: Impact of the maximum time step $h_{\max}$ on the maximum bending moment in opposite sense $M_+^{\max}$.

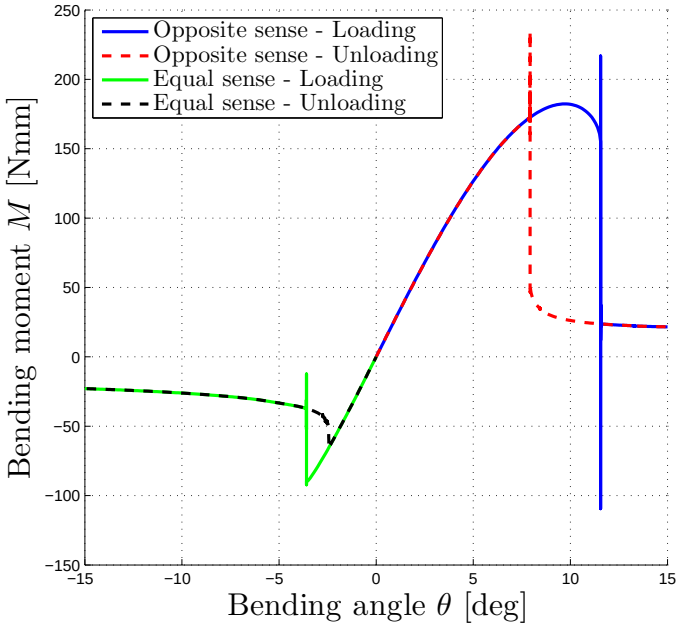

Figure 2.11: Quasi-static evolution of the bending moment with respect to the bending angle obtained with the Newmark method (full lines = loading, dashed lines = unloading).

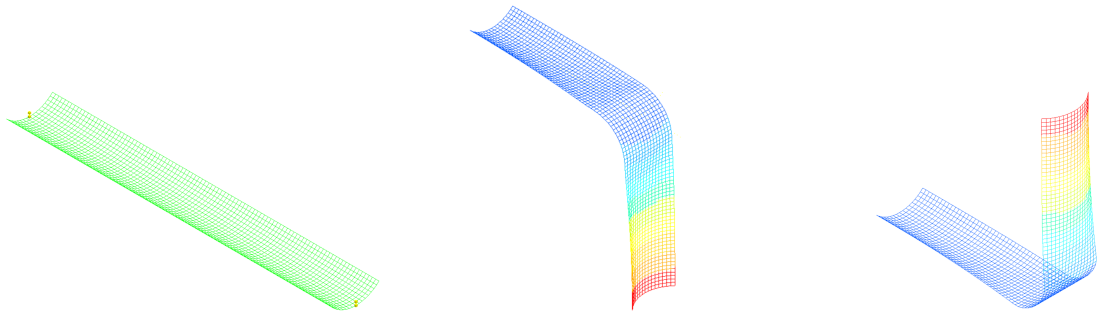

(a) Undeformed configuration.

(b) Deformed configuration in opposite sense.

(c) Deformed configuration in equal sense.

Figure 2.12: Finite element model.

to what was presented in the general behaviour, a difference exists between the two curves which leads, as in opposite sense, to a dissipation of energy through hysteresis. The complexity of the equal sense bending due to the formation of asymmetric torsional folds will be studied in depth by the means of more detailed analyses in Chapter 3.

Regarding the quantitative accuracy of the software, the results displayed in Figure 2.11 fairly reproduce those numerically obtained in [93]. The results on long tape springs are validated by the comparison with the analytical results presented in Table 2.3. Finally, compared to experimental investigations in [107], the average peak moment and steady-state moment in opposite sense bending are obtained with a difference of 5.34 % and 1.91 % respectively.

Finally, an illustration of the undeformed finite element model is given in Figure 2.12a and of deformed configurations in opposite and equal sense at a bending angle of 90° in Figures 2.12b and 2.12c respectively.

2.2.4 Dynamic analyses

Solvers In the case of dynamic analyses, the generalised-α method [24] is used for its second-order accuracy. The numerical damping in this solver is directly imposed through the spectral radius at infinite frequencies ρ_∞. The characteristics of this method will be covered in detail in Chapter 6. For information, it was also observed that the Hilber-Hughes-Taylor (HHT) method gives similar results for the dynamic behaviour of tape springs [41].

Mesh size At this stage of the thesis, due to the complexity of the dynamic models, the mesh size is assumed to be the same as in quasi-static analyses. In the following chapters, this hypothesis will be reconsidered if necessary when all the required concepts will be introduced.

Time step For dynamic analyses, the time step selection strategy is similar to the one presented in the quasi-static case.

2.3 Summary

This chapter introduced the general nonlinear behaviour of tape springs. In particular, the asymmetry of the bending moment with respect to the bending angle, the differences in the deformed configurations, the existence of nonlinear phenomena such as buckling, the formation of folds and the dissipation through hysteresis were described. Furthermore, some analytical formulations for the analysis of tape springs were presented and compared to each other.

The general characteristics of the finite element models used throughout this thesis were introduced. These models are developed in the commercial software Samcef with flexible linear shell elements, an adaptive time stepping procedure, a mesh size fixed to 2 mm and solved by either the Newmark or the generalised-α method whether the analysis is quasi-static or dynamic.

CHAPTER 3

NUMERICAL ANALYSIS OF TAPE SPRINGS: QUASI-STATIC AND MODAL BEHAVIOUR

The general nonlinear behaviour of tape springs illustrated in Figure 2.1 results from their geometry and more precisely from their transverse curvature. In order to reach a detailed understanding of the influence of the geometric parameters on this quasi-static behaviour and accurately describe the nonlinear phenomena, such as the formation of folds and the fundamental differences between the two senses of bending, parametric studies on a single tape spring are performed by the means of finite element models. Compared to the theoretical developments presented in Section 2.1.1 which rely on the hypothesis of an infinite length and thus do not take any boundary conditions into account, numerical analyses allow the definition of more realistic tape spring models characterised by a finite length and boundary conditions. Furthermore, finite element models offer the possibility to perform a large battery of tests that can be automated while limiting development costs.

The investigated parameters are the length L, the thickness t and the transverse radius of curvature R. Regarding the latter, in order to compare similar models, the width of the tape spring is kept constant and the subtended angle α is then modified accordingly. Since in the remaining of this thesis, only straight tape springs are involved in the various analyses and applications, the impact of the initial longitudinal radius of curvature R_L is not covered here, but dedicated analyses can be found in [95]. Finally, to complete these parametric studies, the impact of the geometric features on the modal characteristics of tape springs is investigated in terms of eigenfrequencies and mode shapes.

3.1 Definition of the finite element model

For the parametric studies, the finite element model is kept as simple as possible. In addition to the characteristics described in Section 2.2, the nominal model is defined by the geometric and material properties given in Tables 3.1 and 3.2 respectively. The parametric studies are based on variations around this nominal configuration.

L	t	α	R
100 mm	0.1 mm	$\pi/2$ rad	10 mm

Table 3.1: Geometric characteristics of the tape springs (length L, thickness t, subtended angle α and transverse radius of curvature R).

E	ν	ρ	σ_y
131000 MPa	0.3	8100 kg/m^3	1175 MPa

Table 3.2: Material properties of beryllium copper (Young's modulus E, Poisson's ratio ν, density ρ and yield strength σ_y) [93].

Regarding the boundary conditions, one centroid is clamped and the evolution of the bending moment during the deformation of the tape spring is collected at the clamping point. At the other extremity, the bending angle is imposed and the lateral displacements of the centroid are blocked in order to guide the deformation without restraining the torsion in equal sense. The folding sequence is as follows: starting from the deployed configuration, the tape spring is bent up to an angle of 45° (resp. $-45°$) in opposite sense (resp. equal sense), then the structure is brought back to its straight configuration at the same deformation rate which is fixed at a maximum value of 1° per second in order to have quasi-static loading and unloading behaviours.

As presented in Section 2.2, the Newmark method is used to solve this quasi-static problem and the numerical damping is set to a high value filtering the high-frequency oscillations after buckling ($\rho_\infty = 0$).

Finally, the definition of the different finite element models is automated by means of a MATLAB script which modifies the required parameter or parameters in a nominal model, creates the new model, launches the simulation, extracts the results and post-processes them to obtain the figures presented in the following sections.

3.2 Quasi-static analyses

3.2.1 Impact of the thickness

The influence of the thickness on the evolution of the bending moment when the folding and unfolding of the tape spring are quasi-static is summarised in Figure 3.1, where the abscissa axis spans from $-35°$ to 35° for the sake of visibility. The full lines correspond to the loading sequence, while the dashed lines correspond to the controlled unloading of the tape spring. As can be expected, structures with a larger thickness are stiffer. In Figure 3.1, this behaviour is illustrated by the larger slopes at the origin which lead to higher peak moments in both senses, as well as larger residual moments. Accordingly, the phenomenon of buckling is triggered for higher absolute bending angles.

As it can be seen in Figure 3.1, the curves obtained in equal sense can be divided into two categories depending on the existence of a clear jump in the amplitude of the bending moment. To clearly understand their behaviour, a tape spring with a thickness of 0.15 mm is folded up to an angle of $-90°$ and then brought back to its deployed state. In parallel, its deformed configuration is given at several points of interest (Figure 3.2).

For small values of the thickness ($t = 0.1$ mm and $t = 0.15$ mm), the behaviour is as follows. During the folding, a first large peak is encountered which, in terms of deformation, corresponds to the formation of two torsional folds (configuration 2). Then, for higher bending angles, these folds move towards the middle of the tape springs. Due to the meshing, these displacements are not perfectly smooth and can create vertical peaks along the curve. These latter are numerical and can be avoided by refining the mesh. Then, the torsional folds combine themselves to form a symmetric one which is noticeable by the last jump before finally reaching the quasi-constant residual moment (configuration 3). During unloading, a similar procedure is followed in the re-

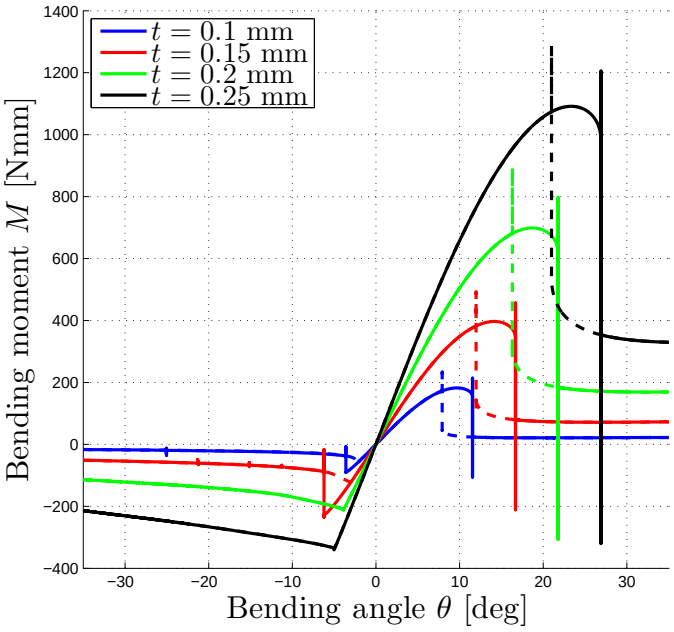

Figure 3.1: Impact of the thickness t on the evolution of the bending moment with respect to the bending angle in opposite and equal senses (full lines = loading from 0° to ±45°, dashed lines = unloading from ±45° to 0°).

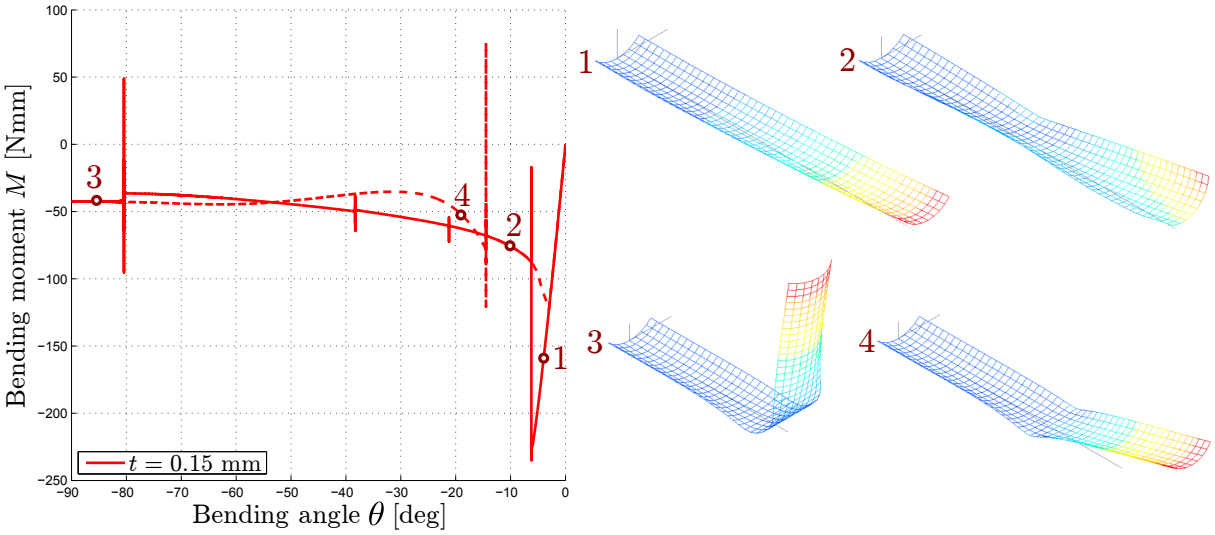

Figure 3.2: Focus on the behaviour in equal sense for a thin tape spring (full lines = loading from 0° to −90°, dashed lines = unloading from −90° to 0°).

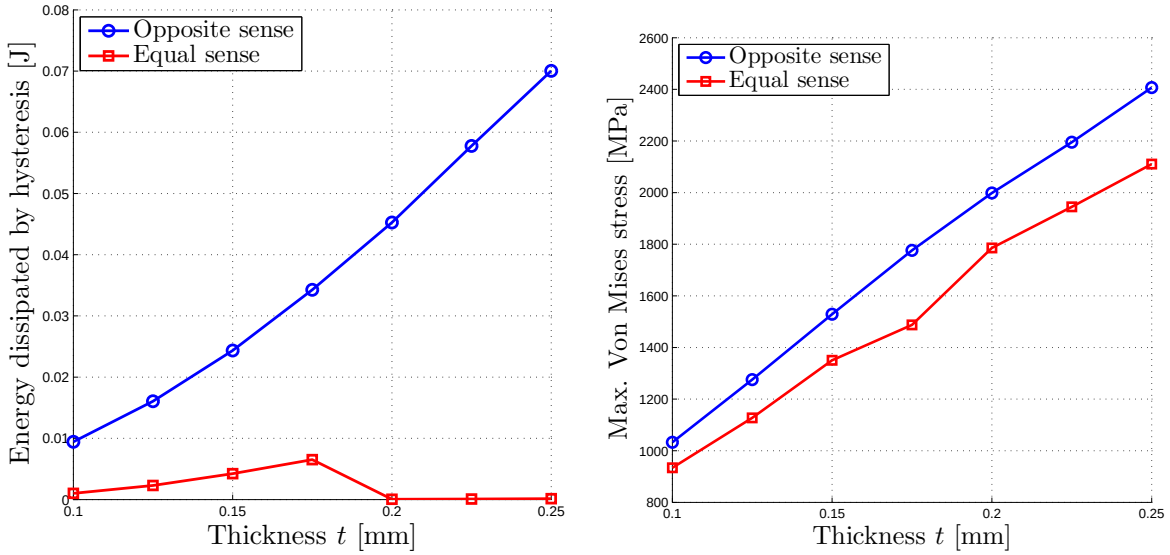

(a) Amount of energy dissipated by hysteresis.

(b) Maximum Von Mises stresses.

Figure 3.3: Impact of the thickness t in both senses of bending for a loading from $0°$ to $\pm 45°$ and an unloading from $\pm 45°$ to $0°$.

verse order: the symmetric fold divides itself into two torsional folds, then these latter move away from each other to finally disappear as the bending angle is reduced. However, compared to the loading procedure, the symmetric fold is preserved on a larger range of bending angles (configuration 4). All these elements lead to the non-superposition of the loading and unloading paths. Finally, by comparing the curves simulated up to an angle of $-45°$ and $-90°$ in Figures 3.1 and 3.2 respectively, it can be seen that the loading history has an impact on the unloading paths. Indeed, the jump due to the separation of the symmetric fold into torsional folds is not visible in the $-45°$-case since the two torsional folds remain separated during the whole loading phase. Nonetheless, the first peak due to the formation of the torsional folds is clearly present.

For larger values of the thickness (0.2 mm to 0.25 mm), the formation of torsional folds is more progressive and the associated jumps in the bending moment reach amplitudes of less than 10 Nmm on the loading and unloading curves (Figure 3.1). Thus, if no symmetric fold is formed, as it is the case for the nominal folding from $0°$ to $-45°$, both paths are almost superimposed.

When comparing the areas subtended by the loading and unloading curves in opposite sense, larger differences are visible for stiffer tape springs. It implies that the dissipation of energy by hysteresis has a stronger impact on the behaviour of the structure as the thickness increases (Figure 3.3a). In equal sense, the dissipated energy first follows a similar evolution from $t = 0.1$ mm to $t = 0.175$ mm, but at a lower amplitude. Then, for larger values of the thickness, the loading and unloading paths remain very close during the whole quasi-static bending procedure. It leads to a low dissipation by hysteresis, but tends nonetheless to again increase with the thickness.

The last critical parameter, on which the impact of the thickness is analysed, is the maximum Von Mises stress reached in the structure throughout its folding and controlled deployment. In the case of the present quasi-static analyses, the results in opposite and equal senses are given in Figure 3.3b where it can be seen that the stresses increase almost linearly with the thickness. In practical applications, it is then necessary to fix an upper limit to this geometric parameter in order to keep the deformations in the elastic regime.

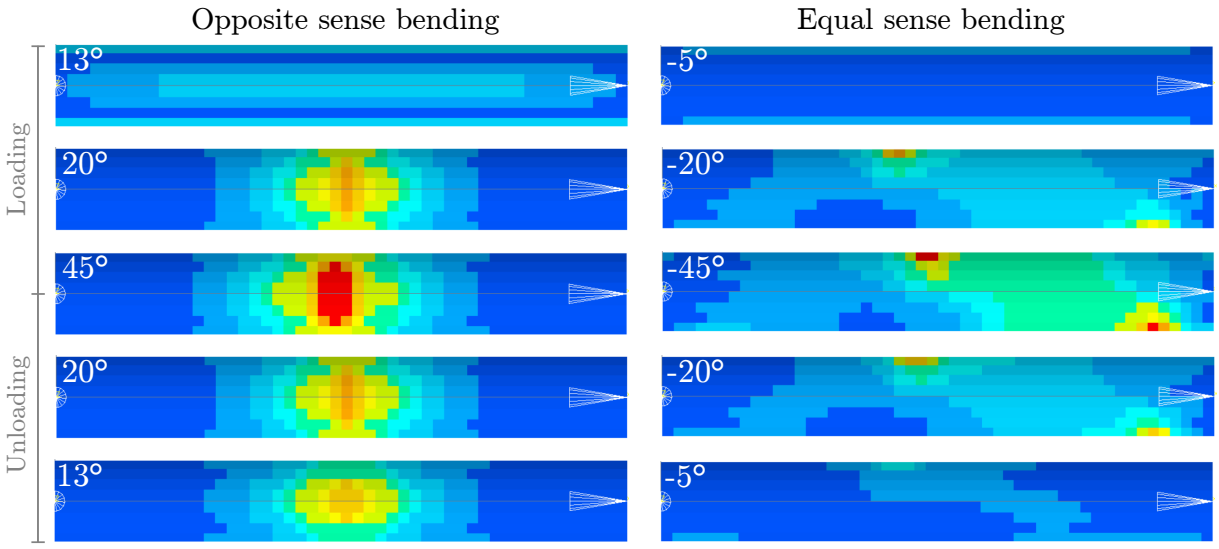

Figure 3.4: Qualitative evolution of the Von Mises stresses for a loading from 0° to ±45° and an unloading from ±45° to 0° for a thickness of 0.15 mm (blue = small stresses, red = large stresses).

A qualitative evolution of the Von Mises stresses during the loading and unloading phases is illustrated in Figure 3.4 in the case of a thickness of 0.15 mm and a maximum bending angle of 45° in both senses. The understanding of these evolutions is facilitated by putting them in relation with the $M - \theta$ curve in Figure 3.1. The first configuration in opposite sense corresponds to a tape spring characterised by a constant longitudinal curvature. The stresses are then almost uniformly distributed along the length, the largest ones being encountered along the median and the longitudinal sides ($\theta_{load} = 13°$). As soon as the tape spring buckles, the stresses are concentrated in the region of the fold and are smaller at the extremities by one to two orders of magnitude ($\theta_{load} = 20°$). They increase with the bending angle in the loading phase ($\theta_{load} = 20° \rightarrow 45°$) and inversely in the unloading one ($\theta_{unload} = 45° \rightarrow 20°$). Finally, as expected from the curve in Figure 3.1, the evolution is not symmetric since a fold is still present in the last configuration shown here ($\theta_{unload} = 13°$).

In equal sense, the first configuration without any fold is characterised by larger stresses along the longitudinal sides ($\theta_{load} = -5°$). After buckling, due to the two torsional folds, the largest stresses are found at two different locations on these longitudinal sides, while the rest of the tape spring is also affected by non-negligible stresses ($\theta_{load} = -20°$). Then, as in opposite sense, increasing the bending angle leads to larger stresses ($\theta_{load} = -20° \rightarrow -45°$) up to a maximum before decreasing in the unloading phase ($\theta_{unload} = -45° \rightarrow -20°$). Finally, the asymmetry of the tape spring behaviour is again visible by comparing the first ($\theta_{load} = -5°$) and last configurations ($\theta_{unload} = -5°$).

In the case of the formation of a symmetric fold in equal sense, which was described in terms of bending angle, bending moment and deformed configuration in Figure 3.2, the qualitative evolution of the Von Mises stresses is illustrated in Figure 3.5. Compared to the symmetric fold in opposite sense, it can be seen that in this case, the largest stresses are always located along the longitudinal sides. Furthermore, the maximum stress is not associated to the largest bending angle, but is reached during the unloading phase for $\theta_{unload} = -33.7°$ in this particular case. Compared to the maximum in the nominal 45°-case (Figure 3.3b), an increase of almost 25 % is noticed. The loading history has then also an impact on the maximum Von Mises stress in equal sense.

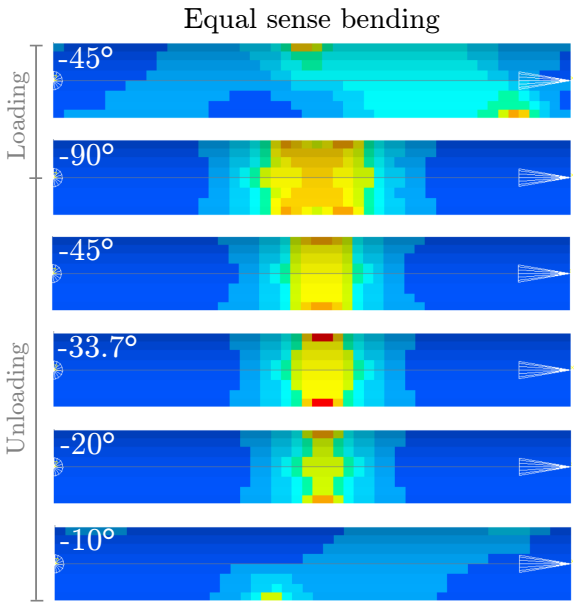

Figure 3.5: Qualitative evolution of the Von Mises stresses in equal sense for a loading from 0° to −90° and an unloading from −90° to 0° for a thickness of 0.15 mm (blue = small stresses, red = large stresses).

3.2.2 Impact of the length

The impact of the length on the behaviour of tape springs is illustrated in Figure 3.6. In opposite sense, increasing the length leads to smaller maximum bending moments, while the associated bending angle keeps increasing. On the contrary, the residual moment is weakly affected by the value of the length. This behaviour was confirmed by Seffen [94] by comparing experimental tests and numerical simulations performed on tape springs of different lengths. Furthermore, it also respects the analytical theories developed by Wüst and Mansfield and presented in Section 2.1.2: the impact of end effects are more significant in small tape springs which leads to an increase of the maximum bending moment and a reduction of the associated bending angle. As the length increases, the maximum bending moment tends to converge towards the value given by the theoretical models defined by an infinite length. Finally, the residual moment remains mainly unaffected and can be estimated by Eq. (2.2) which yields $M_+^* = 24.5$ Nmm.

In equal sense, the value of the residual moment is more sensitive to the length, while the maximum bending moment remains more stable, but not the associated bending angle. Furthermore, contrary to the deformed configuration in opposite sense for which increasing the bending angle always leads to the formation of a symmetric fold by buckling, the deformed configuration in equal sense can follow three types of evolution according to the length (Figure 3.7). For $L = 50$ mm, a symmetric fold is progressively formed without being initiated by torsional folds and disappears by following almost the same path. It implies that the associated $M - \theta$ curves of loading and unloading (Figure 3.6) are almost superimposed and that the amount of energy dissipated by hysteresis is close to zero (Figure 3.8a). For $L = 75$ mm, torsional folds are initiated and combine themselves into a symmetric one. The bending angles for which the two kinds of folds are created or disappear are different, as it was shown in Figure 3.2, which implies that the loading and unloading paths are not superimposed and that the dissipation by hysteresis is more significant (Figure 3.8a). Finally, for $L = 100$ mm, the deformed configuration is only characterised by torsional folds in the case of a maximum bending angle of −45° (this case is the nominal one already discussed in Section 3.2.1). The amount of dissipated energy is then smaller than in the previous case, but tends to increase with the length.

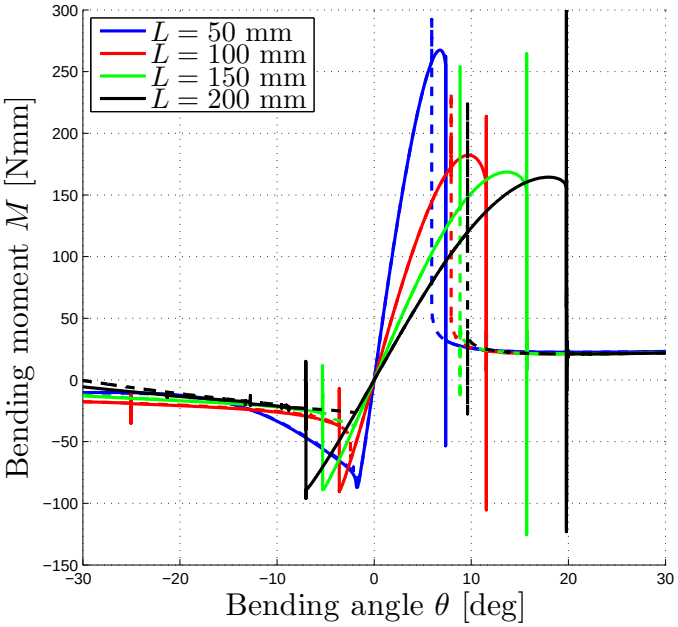

Figure 3.6: Impact of the length L on the evolution of the bending moment with respect to the bending angle in opposite and equal senses (full lines = loading from 0° to ±45°, dashed lines = unloading from ±45° to 0°).

Regarding the maximum Von Mises stresses (Figure 3.8b), the two senses of bending have distinct evolutions. In opposite sense, the maximum stress converge towards a minimum as the length increases, while in equal sense the maximum stress is minimal for a specific value of the length. In a design process involving the length as a design parameter, a compromise should be found between these two behaviours in order to limit the stresses within the tape spring in both senses.

3.2.3 Impact of the radius of curvature

In order to understand the influence of the radius of curvature R on the behaviour of tape springs, similar models must be compared. To do so, the width w, defined as the chord joining the extremities of the tape spring cross-section, is fixed to the value obtained with the geometric parameters in Table 3.1. It implies then that the subtended angle α shall evolve with the radius of curvature R based on the equation:

$$w = 2R \sin\left(\frac{\alpha}{2}\right) \tag{3.1}$$

Furthermore, only a specific interval of radii can be studied in order to keep geometries representative of tape springs. Indeed, if the subtended angle exceeds 180°, the structure becomes tubular and some contacts on the internal surface occur during folding. Extensive analyses of tubular compliant hinges can be found in [63, 74], but these geometries are beyond the scope of the present study. On the other hand, if the radius of curvature is too large and accordingly the subtended angle too small, all the attractive properties in terms of dissipation, self-locking and self-actuation in tape springs are lost, since the structure tends to behave like a flat plate.

The evolution of the bending moment for four different radii of curvature is given in Figure 3.9, where the interval of the bending angle spans from −20° to 20° for the sake of clarity. Increasing the radius of curvature leads to the diminution of the absolute value of the maximum

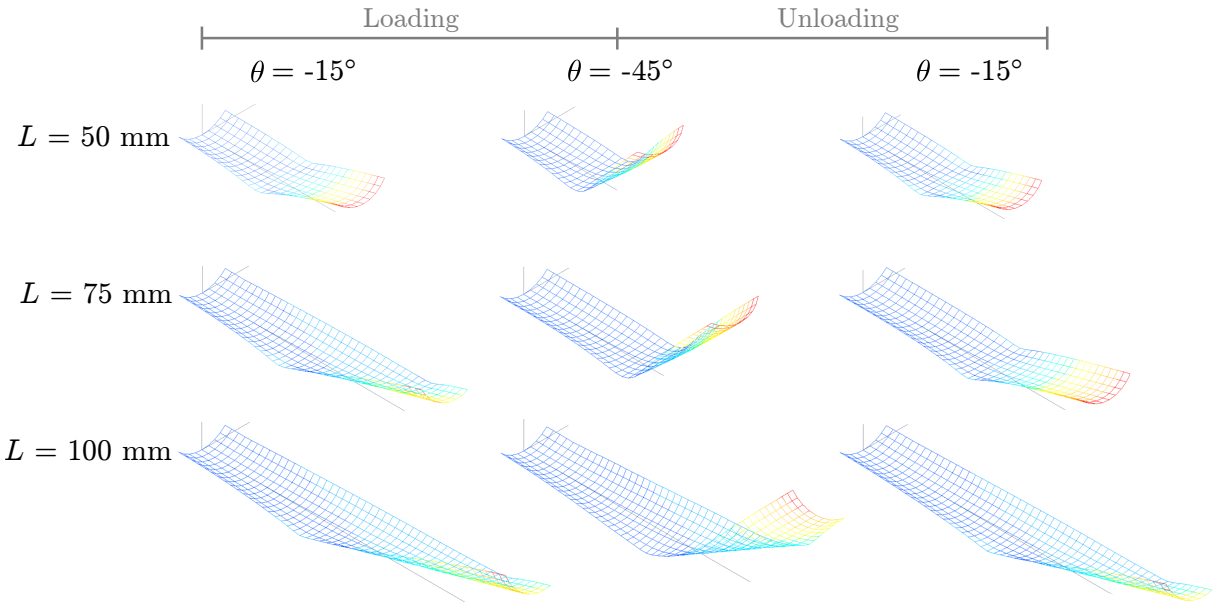

Figure 3.7: Impact of the length L on the evolution of the deformed configuration in equal sense.

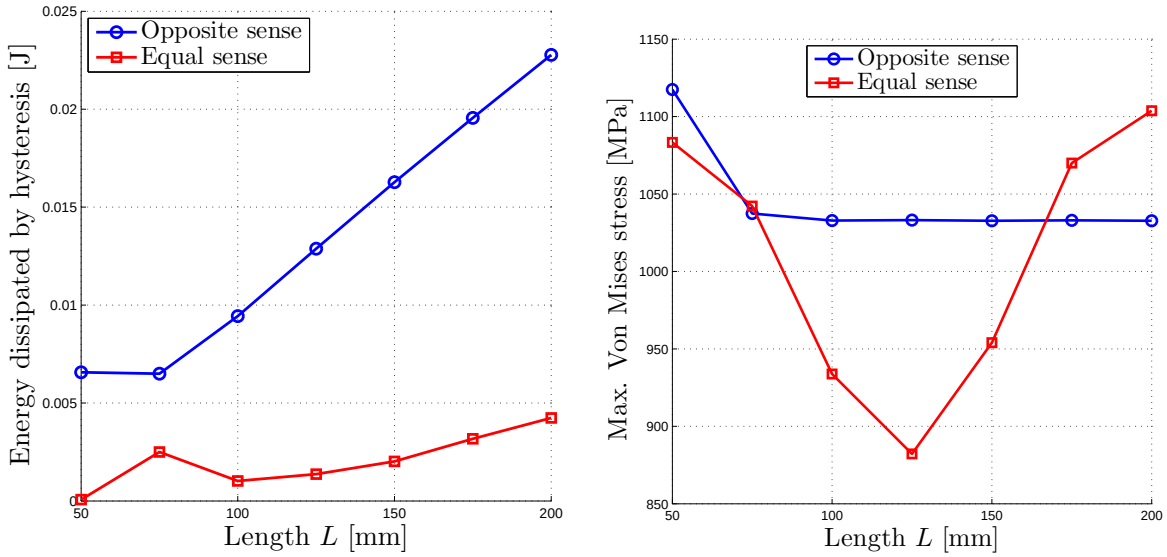

(a) Amount of energy dissipated by hysteresis.

(b) Maximum Von Mises stresses.

Figure 3.8: Impact of the length L in both senses of bending.

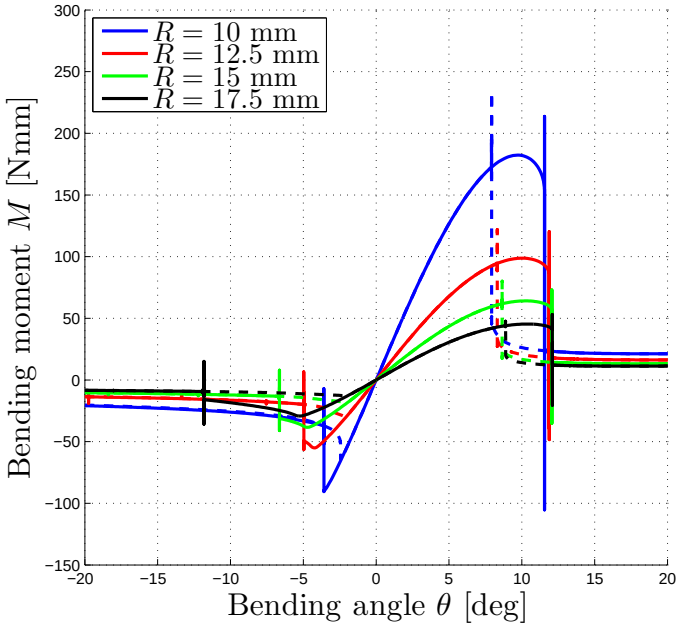

Figure 3.9: Impact of the radius R on the evolution of the bending moment with respect to the bending angle in opposite and equal senses (full lines = loading from 0° to ±45°, dashed lines = unloading from ±45° to 0°).

bending moments in both senses. Indeed, since the tape spring becomes flatter, its stiffness decreases and the required moment to bend it is naturally reduced. However, unlike in the previous parametric studies, the associated bending angle in opposite sense does not vary significantly. Regarding the residual moments reached after the formation of the fold, stiffer tape springs are logically characterised by larger residual moments.

Focusing on the opposite sense bending, since the bending angles corresponding to buckling and the disappearance of the fold are similar for each model, the highest dissipation by hysteresis is encountered in the tape spring with the smallest radius of curvature (Figure 3.10a). On the other hand, as mentioned in the previous sections, the behaviour in equal sense bending is intrinsically more complex and does not allow an evolution as clear as in the opposite sense, but the general decrease is preserved.

Finally, compared to the thickness (Figure 3.3b), the radius of curvature has the opposite effect on the evolution of the maximum Von Mises stress. Indeed, increasing this parameter leads to a less stiff tape spring and logically the stresses are reduced when it is deformed (Figure 3.10b). In terms of values, the maximum Von Mises stress is almost always higher in opposite sense, except for really small radii of curvature defining tape springs with a geometry close to a half circle.

The fact that the highest Von Mises stresses are encountered in opposite sense is not always true and depends both on the geometry of the tape spring and on the maximum bending angle reached before unloading. Similar parametric studies performed in [30] showed that for a tape spring of 150 mm in length, 0.1 mm in thickness, 20 mm in radius of curvature, 90° in subtended angle and quasi-static tests reaching a bending angle of ±60°, the highest Von Mises stress is encountered in equal sense when the thickness and the radius of curvature are the varying parameters (Figures 3.11a and 3.11b respectively).

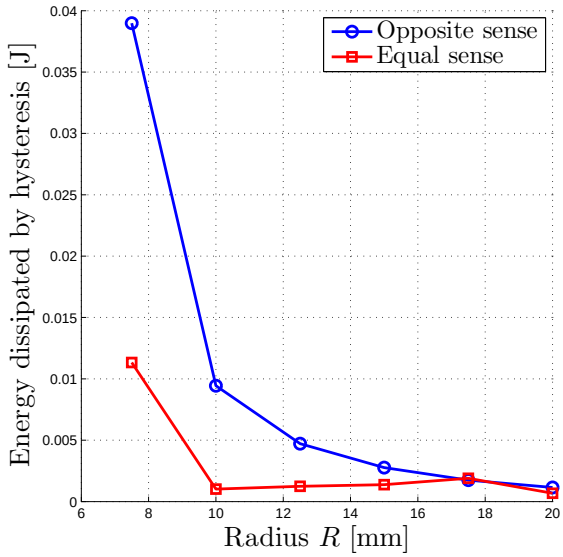

(a) Amount of energy dissipated by hysteresis.

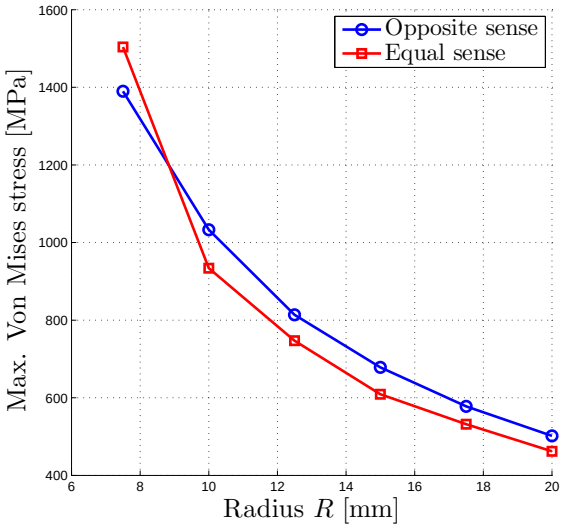

(b) Maximum Von Mises stresses.

Figure 3.10: Impact of the radius R in both senses of bending.

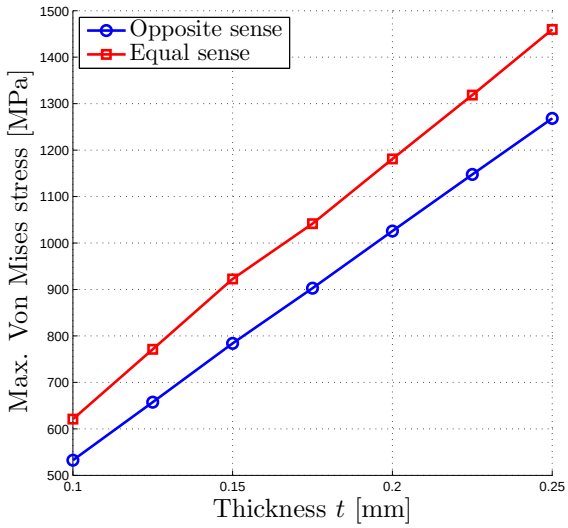

(a) Parametric study on the thickness.

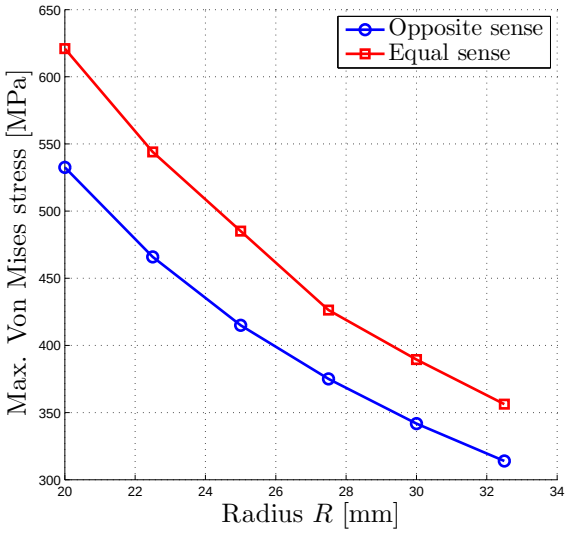

(b) Parametric study on the radius of curvature.

Figure 3.11: Maximum Von Mises stresses for a tape spring of 150 mm in length, 0.1 mm in thickness, 20 mm in radius of curvature, 90° in subtended angle and quasi-static tests reaching a bending angle of ±60° from [30].

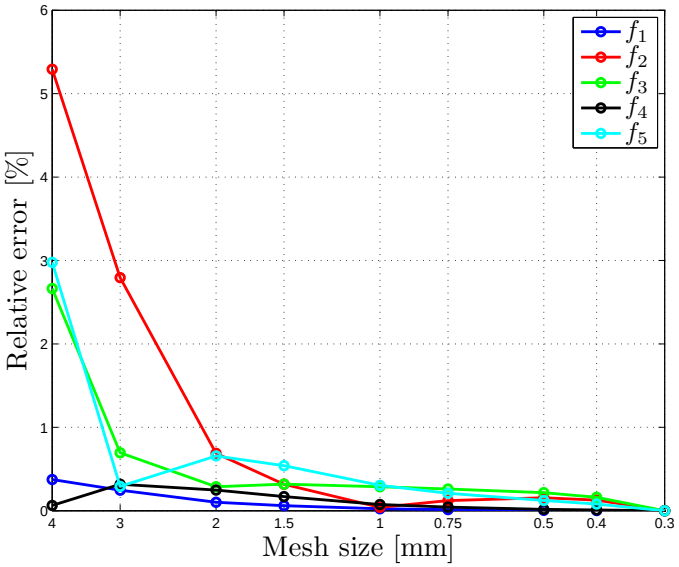

Figure 3.12: Relative error on the first five eigenfrequencies with respect to the mesh size compared to the reference case of 0.3 mm.

	Mode 1	Mode 2	Mode 3	Mode 4	Mode 5
Shape	M_{y1}	T_{x1}	T_{x2}	$M_{x1} - M_{y2}$	T_{x3}
Frequency [Hz]	197.3	274.9	618.0	1120.1	1280.5

Table 3.3: Mode shapes and eigenfrequencies in the nominal case; M_y = bending mode around the y-axis, T_x = torsion mode around the x-axis, M_x = bending mode around the x-axis.

3.3 Modal analysis

3.3.1 Mesh verification

In order to assess the accuracy of the finite element model for a linear modal analysis around the underformed configuration of the tape spring, a convergence analysis is performed on the first five eigenfrequencies f_i $(i = 1, ..., 5)$ with respect to the mesh size. The finite element model is characterised by the same boundary conditions as in the previous parametric studies: one extremity is clamped, while the transverse displacements are locked at the other end through additional nodes rigidly connected to the cross-sections. In Figure 3.12, the evolution of the relative errors on the eigenfrequencies compared to a reference case corresponding to a mesh size of 0.3 mm is given. Notice that the logarithmic axis used for the abscissae increases from right to left.

It can be concluded that, as expected, reducing the mesh size leads to the convergence of the eigenfrequencies. Furthermore, this convergence analysis shows that, as it was the case for the previous parametric studies, a mesh size of 2 mm is sufficiently accurate to capture the modal characteristics of a tape spring, since the relative error is below 1 % in each case.

3.3.2 Mode shapes in the nominal case

In the nominal case defined by the geometry and the material properties in Tables 3.1 and 3.2, the eigenmodes and the associated eigenfrequencies are given in Table 3.3. As a reminder, the reference coordinate system is illustrated in Figure 1.2.

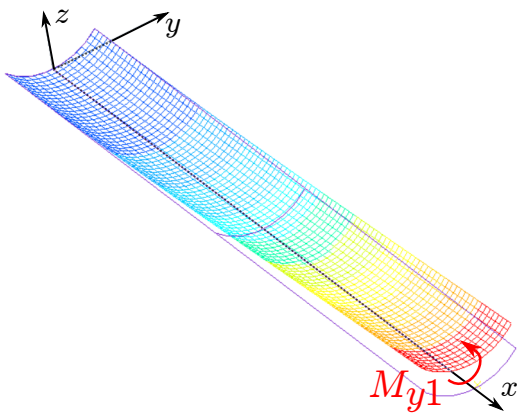

Figure 3.13: First mode shape in the nominal case: first bending mode around the y-axis M_{y1}, 197.3 Hz.

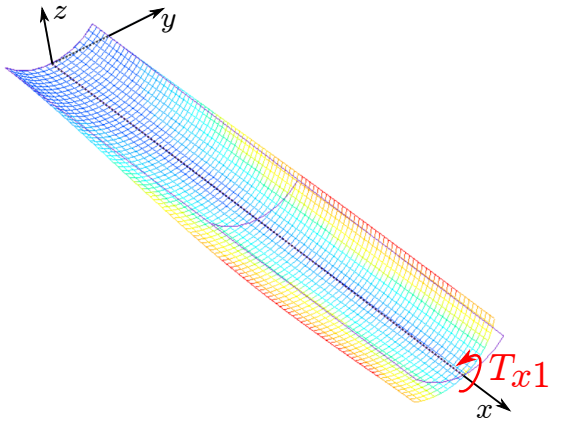

Figure 3.14: Second mode shape in the nominal case: first torsion mode around the x-axis T_{x1}, 274.9 Hz.

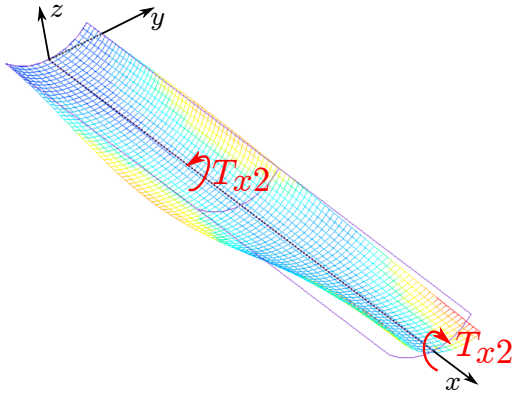

Figure 3.15: Third mode shape in the nominal case: second torsion mode around the x-axis T_{x2}, 618.0 Hz.

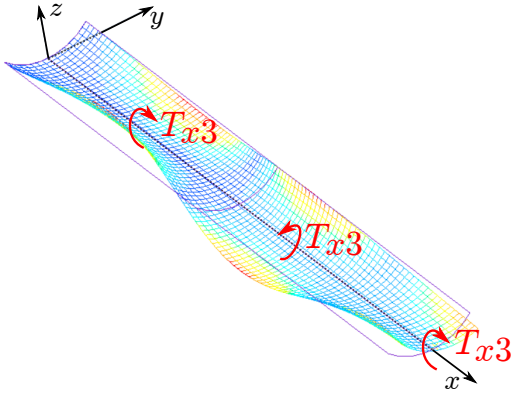

Figure 3.16: Fifth mode shape in the nominal case: third torsion mode around the x-axis T_{x3}, 1280.5 Hz.

The first mode corresponds to the first bending mode around the y-axis M_{y1} illustrated in Figure 3.13. Then, for higher frequencies, torsion modes around the x-axis T_x of increasing order are triggered (Figures 3.14 to 3.16), except for the fourth mode. The deformed configuration of this latter is the combination of two modes, the evolution of which will be covered in more details in the next sections.

3.3.3 Impact of the length

The impact of the length on the evolution of the first five eigenmodes is illustrated in Figure 3.17 where their eigenfrequencies are computed between 50 mm and 200 mm with a step of 1 mm. In each case, an increase in the length yields a decrease in the eigenfrequencies as it is the case for beams and flat plates.

The evolution of the mode shapes was checked at seven different lengths marked by a circle in Figure 3.17. It was concluded that the modes remain affected by the same types of deformation as the length increases, except for the fourth mode. This latter evolves from the first bending mode around the x-axis M_{x1} to the second bending mode around the y-axis M_{y2} as the tape spring becomes longer, a length of 100 mm having the particularity to be characterised by an intermediate shape between these two cases. Indeed, a comparison of the mode shapes for the

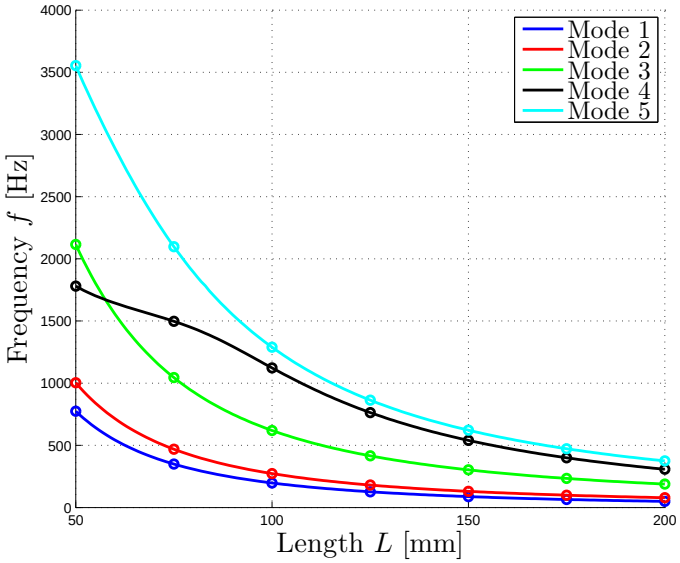

Figure 3.17: Impact of the length L on the eigenmodes and eigenfrequencies of the tape spring.

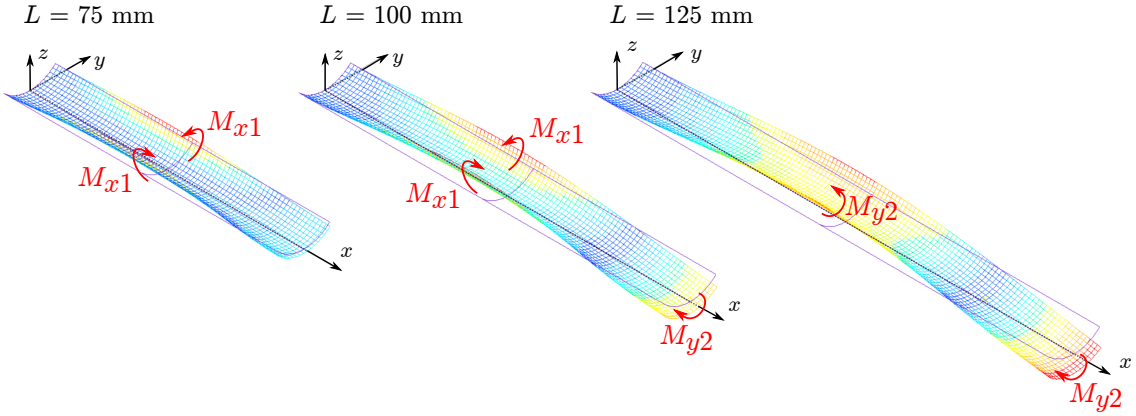

Figure 3.18: Comparison of the fourth mode shape for the lengths 75 mm (first bending mode around the x-axis M_{x1}), 100 mm (combination of M_{x1} and M_{y2}) and 125 mm (second bending mode around the y-axis M_{y2}).

lengths 75 mm, 100 mm and 125 mm (Figure 3.18) shows that, as the length increases, the bending around the x-axis M_{x1} that alternatively brings closer and pulls away the longitudinal sides of the tape spring decreases in intensity, while the vertical displacement of the median increases due to the bending around the y-axis M_{y2}. For a length of 125 mm, the impact of M_{x1} is negligible on the shape of the cross-section and the mode shape is fully formed by the second bending mode around the y-axis M_{y2}. This behaviour is further illustrated in Figure 3.19 which shows the front and side views of the same tape springs: for a length of 75 mm, the cross-sections are significantly deformed and the median almost coincides with the x-axis, for a length of 125 mm, the transverse curvature remains close to its undeformed value all along the tape spring and the vertical position of the median varies, and for a length of 100 mm, the mode shape presents an intermediate configuration between the two previous ones.

Finally, a mode crossing between the third and fourth modes is visible in Figure 3.17 where the two curves intersect for a length of 57.5 mm. At this point, the order of the eigenfrequencies is exchanged. This phenomenon is quite common when varying the parameters of a system [6] and, in the case of tape springs, tends to occur more often when higher modes are considered.

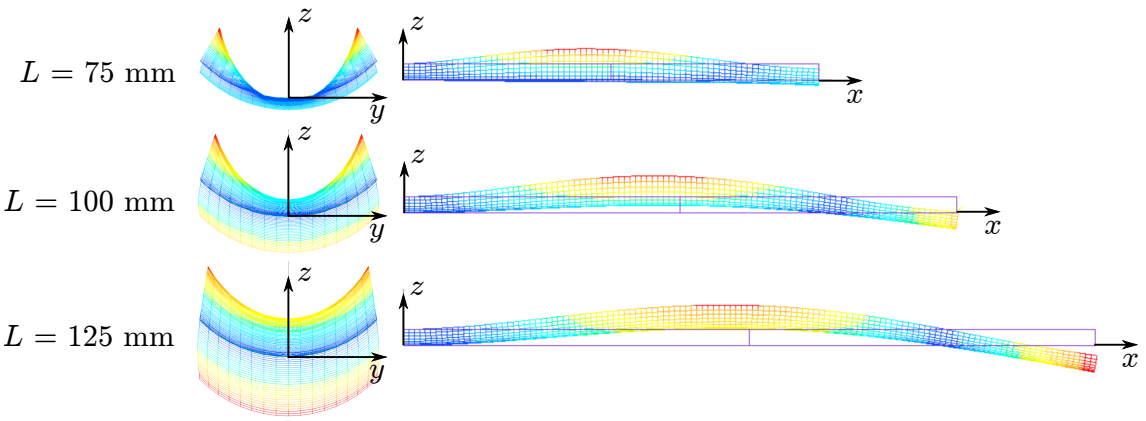

Figure 3.19: Front and side views of the fourth mode shape for the lengths 75 mm (first bending mode around the x-axis M_{x1}), 100 mm (combination of M_{x1} and M_{y2}) and 125 mm (second bending mode around the y-axis M_{y2}).

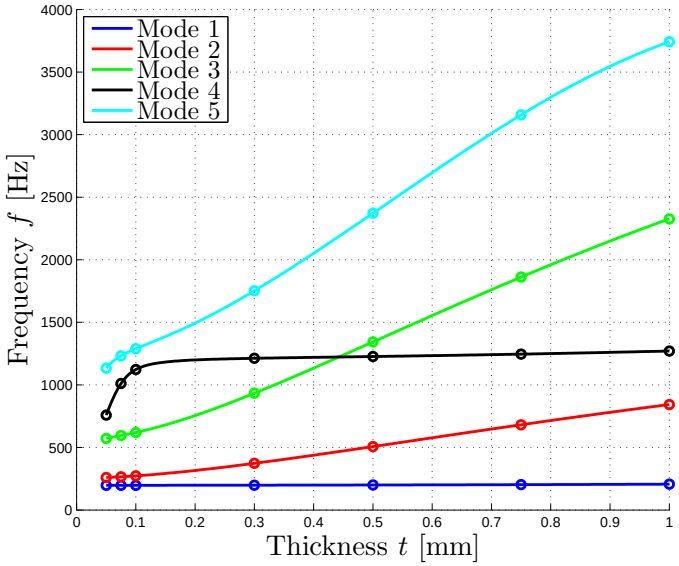

Figure 3.20: Impact of the thickness t on the eigenmodes and eigenfrequencies of the tape spring.

3.3.4 Impact of the thickness

As it is the case for beams and flat plates, the eigenfrequencies of a tape spring increase with its thickness. This evolution is given in Figure 3.20 for the first five eigenmodes obtained with a step of 0.005 mm between each computed point.

As in the previous section, the shape of the eigenmodes was checked at seven values of the thickness which are marked by circles in Figure 3.20. They present the same evolution as described previously, including the particularity of the fourth mode. Furthermore, the third and fourth modes are still affected by a mode crossing occurring when the tape spring has a thickness of 0.46 mm.

3.3.5 Impact of the radius of curvature

As it was the case in Section 3.2.3, in order to determine the impact of the radius of curvature R on the eigenmodes and the eigenfrequencies of a tape spring, similar models must be compared. It implies then that the width w has to be kept constant and that the subtended

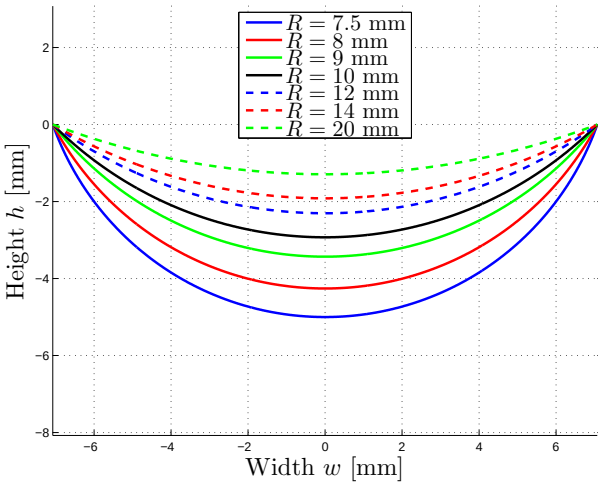

Figure 3.21: Cross-sections of the tape spring for several radii of curvature R when the width w is fixed.

	Mode 1	Mode 2	Mode 3	Mode 4	Mode 5
Half circle	M_{y1}	T_{x1}	T_{x2}	$M_{x1} - M_{y2}$	T_{x3}
Nominal case	M_{y1}	T_{x1}	T_{x2}	$M_{x1} - M_{y2}$	T_{x3}
Flat plate	M_{y1}	M_{y2}	T_{x1}	M_{y3}	M_{y4}

Table 3.4: Mode shapes associated to a tape spring with a half circle cross-section, the nominal case and a flat plate; M_y = bending mode around the y-axis, T_x = torsion mode around the x-axis, M_x = bending mode around the x-axis.

angle α has to be computed based on Eq. (3.1). For this analysis, the width w is again fixed to the value obtained with the radius of curvature R and the subtended angle α defined in Table 3.1.

The seven cross-sections considered in detail in this analysis are illustrated in Figure 3.21 where it can be seen that for large radii of curvature, the models tend to behave like a flat plate, while on the opposite, small radii of curvature define cross-sections that tend to take the form of a half circle.

The evolutions of the first five eigenmodes are given in Figure 3.22 where the seven detailed cases are marked by circles, while the main curves are obtained with a step of 0.01 mm before $R = 7.5$ mm and of 0.1 mm afterwards. The mode crossing between the third and fourth modes is associated to a radius of 8.6 mm.

By comparing the mode shapes associated to a half circle, a flat plate and the nominal tape spring (Table 3.4), it can be seen that, in the case of the first five modes considered here, the eigenmodes of strips with curved cross-sections are mainly submitted to torsion deformations, while in flat plates, bending modes are dominant. It is then likely that by further increasing the radius of curvature R in Figure 3.22, the eigenmodes would evolve until reaching those mentioned in the last entry of Table 3.4 and additional mode crossing phenomena could be visible.

3.4 Summary

Based on a shell finite element model, the impact of geometric parameters (the length L, the thickness t and the transverse radius of curvature R) on the quasi-static nonlinear behaviour of tape springs is investigated. The formation of a symmetric fold by buckling is observed in

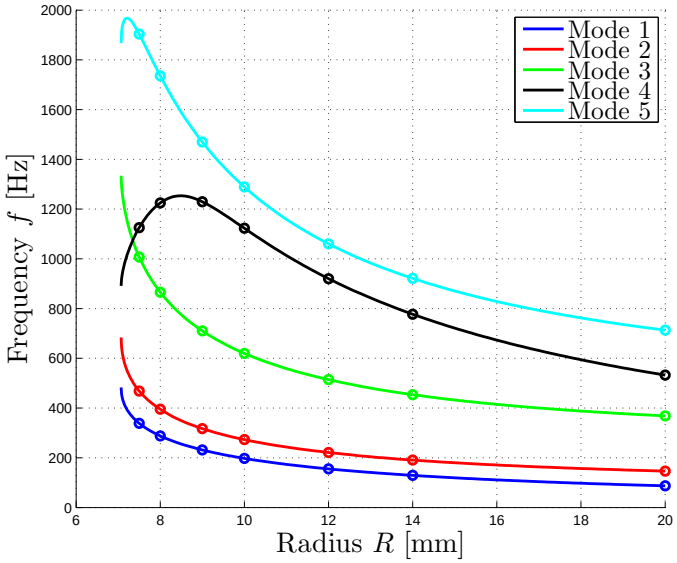

Figure 3.22: Impact of the radius of curvature R on eigenmodes and the eigenfrequencies of the tape spring for a fixed width w.

opposite sense, while in equal sense several evolutions of the deformed configuration can be encountered whether or not torsional folds are formed, whether or not they involve a significant jump in the amplitude of the bending moment and whether or not the bending angle is large enough to lead to the formation of a symmetric fold.

These characteristics have a direct impact on the amount of energy dissipated by hysteresis since they condition the superposition of the loading and unloading paths. Nevertheless, the dissipation associated with the formation of folds in opposite sense is always higher than in equal sense. The maximum Von Mises stress affecting the tape spring during its deformation depends both on its geometry and on the maximum bending angle reached before unloading. The proposed model is thus useful to verify if the tape spring stays in an elastic regime.

Finally, the impact of the same geometric parameters on the modal content of tape springs is analysed. It shows the complexity of the mode shapes evolution with the considered parameters and the existence of particular phenomena such as mode crossing.

CHAPTER 4

APPLICATION TO THE DESIGN OF A DEPLOYABLE REFLECTOR

After investigating the nonlinear behaviour of tape springs and the influence of geometric parameters, the quasi-static finite element model is exploited for the design of a deployable reflector around a solar panel and extended to perform dynamic simulations representing the deployment sequence.

The choice of this application was made by taking into consideration the growing interest in the development of technologies for small satellites of less than 200 kg. The intended purpose is the launch of numerous missions requiring both a low budget and a short period of design. Regarding the on-board power consumption of the electronic equipment, solar cells are used to supply the required energy, but it is generally not possible or enough to cover all the external surfaces of the satellite. The most common solution is then to deploy solar panels on the sides of the satellite once it is jettisoned from the launcher. Adding reflectors along the solar panels concentrates the sunlight on the solar cells and thus, in theory, doubles the geometric concentration factor and the area of the solar panels can be consecutively reduced. This solution, however, requires the folding of the panels and the reflectors in order to integrate the satellite inside the confined space of the fairing. Tape springs represent an attractive solution in this context thanks to their passive deployment capacity from a compact folded configuration, their high stiffness in their deployed equilibrium state and their simplicity of integration.

For space systems, the use of reflectors has been investigated since the nineties [101]. The V-trough concentrators were first integrated on the solar panels of the PanAmSat Galaxy XI satellite and, a few years later, they were exploited on the Boeing BSS-702 Satellite Bus with limited success due to the contamination of the reflecting surfaces and the shrinkage of the reflectors alignment system [13]. More recently, JAXA launched the small spacecraft REIMEI equipped with single lateral reflectors on each solar panel (Figure 4.1) which gave satisfactory results according to their last report [88].

The use of reflectors is then not unusual to increase the performance of solar panels and deploying them with tape springs shows promising advantages. A particular deployment procedure exploiting the self-actuated and the self-locking properties of tape springs can be found in [103] where they provide the driving torques to classical hinges mounted in parallel.

In the present case, the connection between the reflectors and the solar panels consists only of tape springs which are not combined to any additional classical hinges. An extensive analysis is then required to prove their efficiency for this type of applications. During folding and then deployment, the most critical parameters are the maximum stresses affecting the structure and

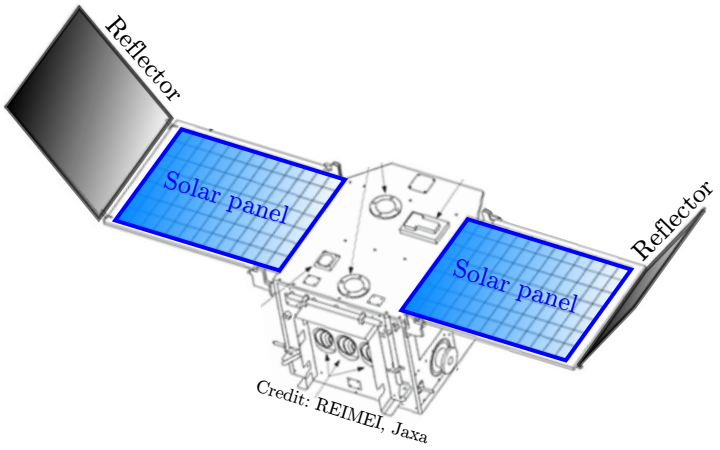

Figure 4.1: Deployed configuration of the reflectors on the spacecraft REIMEI (modified illustration from [88]).

the maximum motion amplitude. Regarding the former, its value must be kept under the yield limit in order to remain in the elastic regime and prevent irreversible deformations, while for the latter, which is only relevant during deployment, any collision with the other elements of the spacecraft must be avoided. To fulfil these requirements, the geometry of the tape springs has to be adapted to the specific situation. Since several parameters can be modified, it is proposed in this work to address this problem by the means of an optimisation procedure relying on the simulation of finite element models.

The developments presented here were used as a basis during a collaboration with the WalOpt company (Belgium). The project, called *Feasibility Study and Pre-Test of a Low Cost Concentrator Solar Array*, is commissioned by the European Space Agency (ESA) and sponsored by the Belgian Federal Science Policy Office (Belspo). The other partners are the CRM Group (Belgium) and the ONERA (France). The objective is the design of a breadboard composed of a solar panel and two reflectors being deployed by different systems, one consisting of tape springs. A feasibility study is presented here, however, the project is still ongoing and an experimental validation of the deployable mechanism should be performed in the future.

4.1 Definition of the problem

The problem under study is the deployment of a single reflector around a fixed solar panel. In its folded configuration, it is located on top of the panel and the reflective membrane is a square of sides 200 mm supported by a frame. The reflector, including the membrane and the frame, has a mass of 0.4 kg. At this stage of the design, the mass inertia of the reflector is unknown. In its deployed configuration, the angle formed with the solar panel reaches 120° as recommended in [103]. The reflector is connected to the panel by two tape springs in order to limit the impact of the torsion in equal sense and ensure that the motion remains mainly planar. Their orientation will be determined in the last part of this study. Indeed, three configurations are possible: both tape springs initially bent in opposite sense, both tape springs initially bent in equal sense and the alternate configuration in which both senses of bending are present, each case being characterised by different quasi-static and dynamic behaviours.

In a spacecraft, the available space is strictly limited and the one devoted to the tape springs of the reflector is most likely determined at an early stage of the spacecraft design. In order to solve a relevant problem, their length L is then fixed to 50 mm, while for their cross-section, the

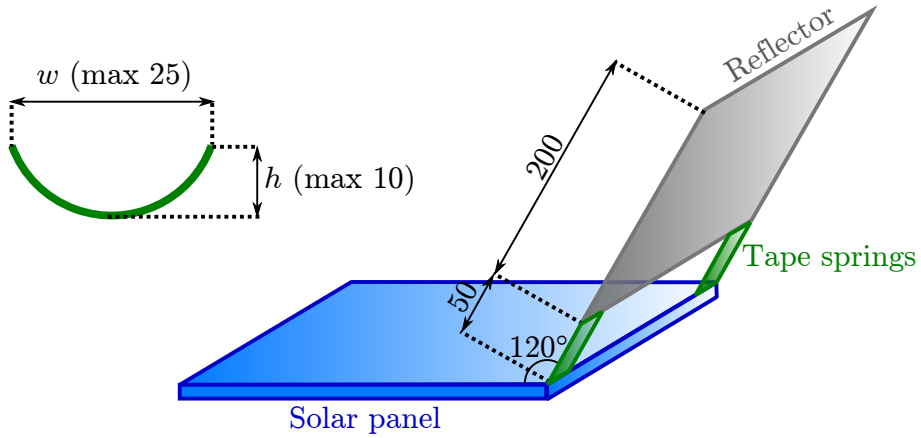

Figure 4.2: Deployed configuration of the reflector and maximum dimensions (in millimetres) of the tape springs.

width w and the height h have to respect the following design constraints:

$$w = 2R\sin\frac{\alpha}{2} \leq 25 \text{ mm} \tag{4.1}$$

$$h = R\left(1-\cos\frac{\alpha}{2}\right) \leq 10 \text{ mm} \tag{4.2}$$

where R is the radius of curvature and α is the subtended angle of the tape spring cross-section. A schematic representation of the deployed reflector is given in Figure 4.2, along with the maximum dimensions accepted for the tape springs. Even though the following results are specific to this problem, the developments remain representative of any design procedure that could be undertaken to determine the geometry of tape springs used for the deployment of solar panels or reflectors.

The thickness t, the radius of curvature R and the subtended angle α are the design variables which have to be determined in order to respect the geometric constraints in Eqs. (4.1) and (4.2), while minimising the objective function consisting of the maximum Von Mises stress $\sigma_{\max}$ and/or the maximum motion amplitude $\beta_{\max}$ that will be clearly defined in the following sections.

Regarding the material composing the tape springs, its properties are fixed *a priori* in order to limit the complexity of the design problem in these first analyses. In space applications, the choice of materials is anyway limited due to restricting requirements on contamination. The chosen material used throughout this application is the beryllium copper, as in the previous chapters. Its properties are given in Table 3.2 where E is the Young's modulus, ν the Poisson's ratio, ρ the density and σ_y the yield limit.

4.2 Optimisation on a single tape spring

In order to determine the most efficient tape springs which meet the requirements for the deployment of the reflector defined in Section 4.1, an optimisation procedure is proposed. The selection of the geometric parameters is first performed on a single tape spring connected to a lumped mass representing half of the reflector mass, both in opposite and equal senses. However, as mentioned in Section 4.1, the final deployable system in this practical application is composed of two tape springs in order to restrain the lateral displacements due to torsion and guide the deployment motion. Even though limited torsional effects and three-dimensional motions could

	t [mm]	R [mm]	α [deg]
lb	0.08	10	60
ub	0.25	32.5	135

Table 4.1: Lower and upper bounds of the design variables.

be expected, the results obtained for one tape spring have then to be confirmed for the complete system *a posteriori*.

4.2.1 Optimisation procedure

The optimisation procedure exploits the active-set algorithm available in the MATLAB software through the `fmincon` function which allows solving constrained nonlinear multivariable problems of medium scale [70]. The optimisation problem to solve can be expressed as:

$$\min_x f(x) \text{ such that } \begin{cases} c(x) \leq 0 \\ lb \leq x \leq ub \end{cases} \tag{4.3}$$

where $f(x)$ is the objective function to be minimised with respect to the vector of design variables x, $c(x)$ contains the nonlinear inequality constraints, and lb and ub are the vectors containing respectively the lower and upper bounds of the design variables. The vector of design variables is defined as:

$$x = [t \;\; R/10 \;\; \alpha] \tag{4.4}$$

in order to have elements with the same order of magnitude and define single values for the maximum and minimum allowed changes between two iterations. They are fixed to 0.5 mm or rad and 10^{-3} mm or rad respectively. A termination tolerance of 10^{-4} is chosen on the variation of the objective function and the design variables, while the tolerance on the constraints violation is also set to 10^{-4}. Notice that the optimisation function `fmincon` only determines local minima. The initial guess of the design parameters has then an impact on the solution and has to be chosen with care by the designer. To this end, the information collected in Chapter 3 on the nonlinear behaviour of tape springs is exploited to determine the characteristics of the initial geometry whenever possible and by trial and error otherwise.

The nonlinear inequality constraints are the two limits imposed on the width and the height of the tape spring cross-section (Eqs. (4.1) and (4.2)). They are expressed as:

$$\begin{cases} c_1(\alpha, R) &= 2R\sin\dfrac{\alpha}{2} - w_{\max} &\leq 0 \\ c_2(\alpha, R) &= R\left(1 - \cos\dfrac{\alpha}{2}\right) - h_{\max} &\leq 0 \end{cases} \tag{4.5}$$

with $w_{\max} = 25$ mm and $h_{\max} = 10$ mm as it was decided in Section 4.1.

Regarding the lower and upper bounds of the design variables, they are defined in Table 4.1 based on our experience acquired during the numerical quasi-static analyses in Chapter 3 such that even in the extreme cases, the tape spring still preserves its advantageous features such as self-actuation, self-locking and dissipation by hysteresis.

The optimisation procedure is performed automatically as follows. Starting from an initial geometry, the design variables are introduced in the SAMCEF software which creates the corresponding finite element model and then solves it. The results are post-treated in order to extract the value of the objective function and the nonlinear equality constraints. They are then

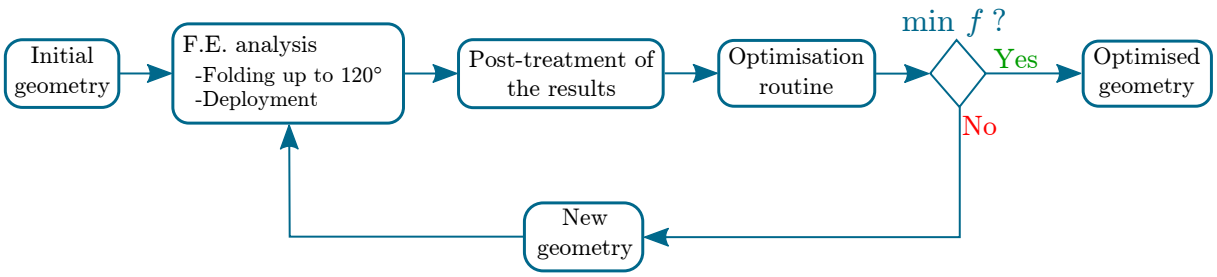

Figure 4.3: Optimisation procedure for a single tape spring.

sent back to the optimisation routine in MATLAB which checks the validity of the constraints and the stationarity of $f(x)$. If these two conditions are respected, the optimised geometry is found, otherwise, the optimisation routine automatically determines the next configuration to be analysed and a new cycle is carried out. This procedure is schematically represented in Figure 4.3.

The finite element model is similar to those presented in Chapters 2 and 3: one extremity is clamped, at the other one the bending angle is controlled when necessary, the mesh size is fixed to 2 mm and an adaptive time stepping procedure is used. The main differences come from the existence of a rigid body representing half of the reflector mass rigidly connected to the second extremity and the locking of the transverse displacements along the whole median of the tape spring. Indeed, in the analyses in Chapter 3, only the lateral displacements of the extremity were constrained in order to guide to motion without affecting the formation of the torsional folds. In that case, it was shown that these latter do not always converge to create a symmetric fold depending on the geometry of the tape spring. However, in this application, tests show that the simultaneous folding of two tape springs always leads to the formation of symmetric folds whatever the sense of bending and the optimised geometry. This behaviour is then simulated on the single tape spring model by transversally locking its median.

In the finite element analyses, the simulation is performed in two steps. Starting from the straight undeformed configuration, the tape spring is first folded until the bending angle reaches 120°, which corresponds to the initial position of the reflector on top of the solar panel. For this stage, a quasi-static simulation is performed with a maximum bending velocity fixed to half a degree per second, reaching thus a simulation time of 240 s. Once the tape spring reaches its folded configuration, the rotation constraint is removed and the deployment is studied for 30 s through a dynamic analysis. Due to this second phase, the generalised-α method is preferred to the Newmark method, nonetheless the spectral radius at infinite frequencies is still set to zero so that the numerical dissipation is maximised. The choice of this value and the absence of a form of physical dissipation will be reconsidered in the next chapter.

This procedure is followed for the two senses of bending since each one is characterised by a distinct behaviour and a specific deformed configuration. Furthermore, as already mentioned, it implies that for the complete system composed of two tape springs, three configurations are possible: both tape springs initially folded at an angle of 120° in opposite sense, both tape springs initially folded in equal sense and the alternate configuration in which both senses of bending are present. The choice of the final orientation is performed after the optimisation procedure summarised in Figure 4.3. Finally, for symmetry reasons, both tape springs will have the same optimised geometry.

Sense	Geometry	t [mm]	R [mm]	α [deg]	$\sigma_{\max}$ [MPa]	$\lvert\beta_{\max}\rvert$ [deg]	Nbr. of func. eval.
Opposite/Equal	Initial	0.08	17.5	90	–	–	–
Opposite	Optimised	0.08	10	60	**861.68**	205.95	8
Equal	Optimised	0.08	15.79	60	**647.33**	57.05	61

Table 4.2: Results for the minimisation of the maximum Von Mises stress $\sigma_{\max}$.

4.2.2 Minimisation of the maximum Von Mises stress

In this first case, the optimisation procedure aims at minimising the maximum Von Mises stress $\sigma_{\max}$ reached in the whole tape spring during folding and deployment, while the maximum motion amplitude $\beta_{\max}$ is left free of constraint. It means then that in the expression of the problem Eq. (4.3), the objective function is defined as $f(x) = \sigma_{\max}$.

The results of the optimisation procedure are given in Table 4.2, along with the initial geometry. Notice that for this latter, the thickness is already set to its lowest bound, since, as it was shown in Figure 3.3b, increasing this parameter only leads to higher values of the maximum Von Mises stress.

Starting from the same geometry, the optimised results are different according to the sense of bending in terms of radius of curvature R, this latter being larger in equal sense, while it is set to the lowest bound in opposite sense. Regarding the subtended angle α, the lowest bound is also the optimised value and as expected, the smallest allowed thickness t is retained. Finally, it can be seen that the optimised geometry in opposite sense was obtained after 8 function evaluations, meaning that 8 successive finite element models were solved before reaching the one described in Table 4.2, while 61 function evaluations were performed in equal sense.

Regarding the objective function, the maximum Von Mises stresses $\sigma_{\max}$ for the optimised geometries are, as required, below the yield limit $\sigma_y = 1175$ MPa in both senses so that the deformations are kept in the elastic regime. Nonetheless, larger stresses are encountered in opposite sense, the maximum value being 33.11 % larger than in equal sense. The stress values given in Table 4.2 and in the following analyses are the maximum of both the quasi-static folding and the dynamic deployment. In this case, the maxima are reached right after triggering the deployment.

The evolutions of the displacements at the extremity of the tape spring are given in Figure 4.4a for the two types of initial foldings and focuses on the deployment stage. It can be seen that even though the starting points at 240 s are almost the same (the small discrepancies being due to the different deformed configurations depending on the sense of bending), the motion amplitude is much smaller in equal sense. However, even after 30 s, the tape spring keeps oscillating in both cases. This design is then not efficient in a space environment where a weak motion damping yields a long waiting period before the stabilisation of the spacecraft. In the next section, it will be shown that minimising the motion amplitude may help in improving this behaviour.

To quantify the motion amplitude β, Figures 4.5a and 4.5b which show the complete deployment of the reflector and the tape spring in the xz-plane are used. In both figures, the straight green line represents the non-deformed tape spring, the straight black line represents the deployed reflector and the straight blue line represents the fixed solar panel. As usual, the orientation of the frame is aligned on the non-deformed tape spring: the x-axis corresponds to its longitudinal direction, the y-axis to its transverse direction and the z-axis to its vertical direction. The quasi-circular arcs show the position of the tape spring extremity and of the lumped mass (located at

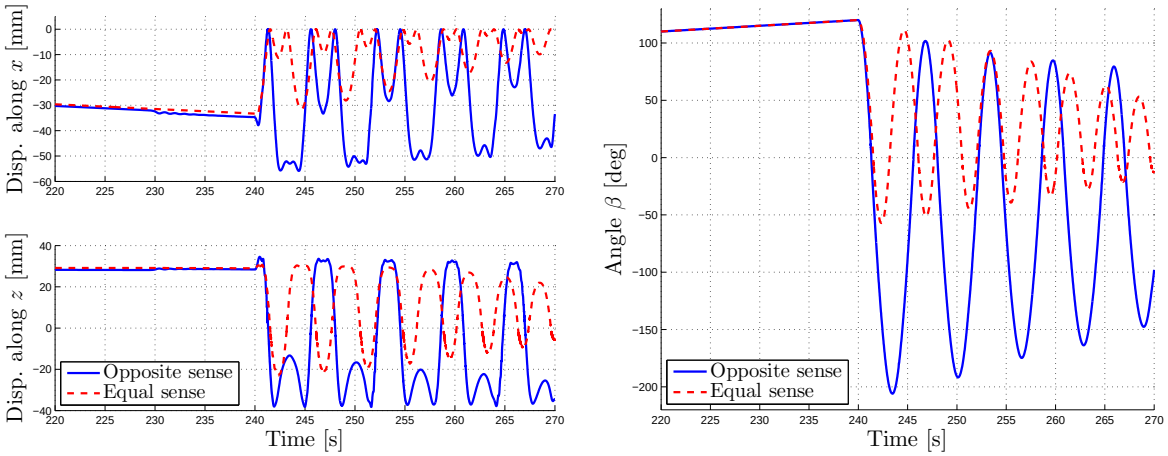

(a) Displacements at the extremity.

(b) Motion amplitude (β angle).

Figure 4.4: Evolution of the tape spring in both senses of bending in the case $f(x) = \sigma_{\max}$.

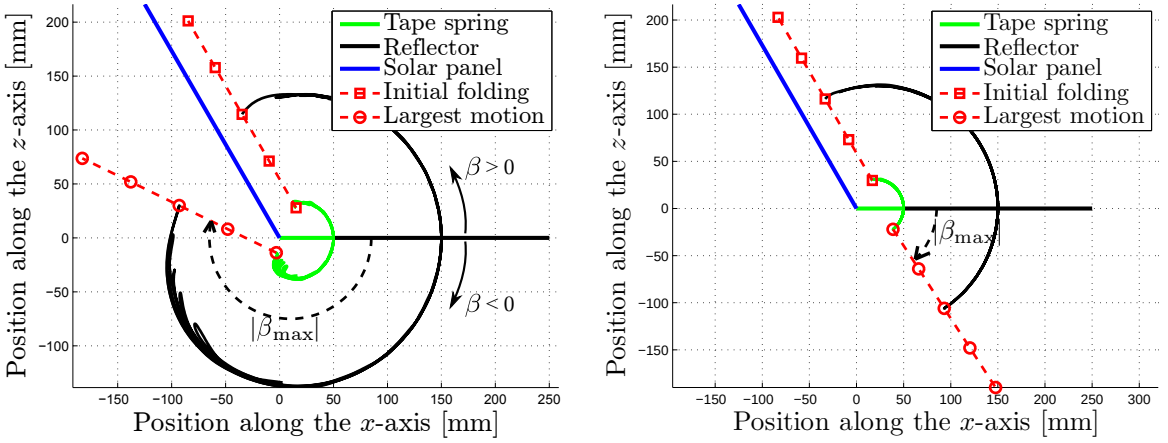

(a) In opposite sense.

(b) In equal sense.

Figure 4.5: Deployment of the tape spring in the case $f(x) = \sigma_{\max}$.

the reflector centre of mass) during the different time steps of the dynamic analysis. Finally, the red squares correspond to the position of the reflector when the tape spring is folded up to an angle of 120°, the reflector is then parallel to the solar panel; and the red circles correspond to the position of the reflector in the most extreme configuration reached in the transient phase. The maximum motion amplitude $\beta_{\max}$ is then defined as the maximum angle between this last line and the reflector in its deployed configuration (straight black line). Finally, these figures can be used to visually confirm the absence of collision between the reflector and the solar panel.

The complete evolution of the angle β is given in Figure 4.4b where the fully folded configuration corresponds to $\beta = 120°$ and the stabilised deployed configuration corresponds to $\beta = 0°$ (not reached here due to the slow damping of the oscillations). The sign of this angle is defined as illustrated in Figure 4.5a. Since the amount of potential energy inside a tape spring folded up to an angle of 120° in opposite sense is almost twice the amount in equal sense, a larger motion amplitude is logically encountered in the deployment of a tape spring initially bent in opposite sense.

Sense	Geometry	t [mm]	R [mm]	α [deg]	$\sigma_{\max}$ [MPa]	$\lvert\beta_{\max}\rvert$ [deg]	Nbr. of func. eval.
Opposite	Initial	0.08	10	131	–	–	–
	Optimised	0.08	10.03	130.72	2545.7	**114.71**	38
Equal	Initial	0.25	10	135	–	–	–
	Optimised	0.085	10.11	124.10	1448.7	**6.17**	57

Table 4.3: Results for the minimisation of the maximum motion amplitude $\beta_{\max}$.

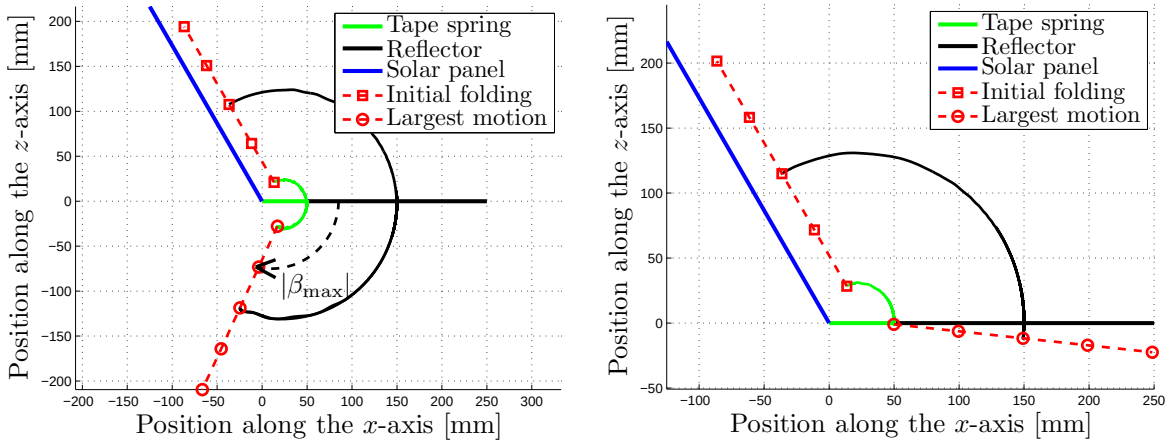

(a) In opposite sense.

(b) In equal sense.

Figure 4.6: Deployment of the tape spring in the case $f(x) = \beta_{\max}$.

4.2.3 Minimisation of the maximum motion amplitude

In this second case, the aim is to minimise the maximum motion amplitude $\beta_{\max}$, while the maximum Von Mises stress $\sigma_{\max}$ is left free to vary. The objective function in Eq. (4.3) is then defined as $f(x) = \beta_{\max}$.

The optimised results, given in Table 4.3, are obtained in opposite and equal senses after 38 and 57 function evaluations respectively. Notice that two different initial geometries have to be used to reach the minimum motion amplitude since, as mentioned in Section 4.2.1, the optimisation procedure determines only local minima. The optimised geometry of the tape springs are similar for both senses: the thickness t and the radius of curvature R are equal or close to their lowest limit, while a large subtended angle α is required.

The maximum motion amplitude $\beta_{\max}$ is obviously reduced compared to the results obtained after solely minimising the maximum Von Mises stress as it can be seen quantitatively in Table 4.3 and qualitatively in Figures 4.6a and 4.6b, which illustrate the deployment sequence in the xz-plane for an initial folding in opposite and equal sense respectively. These figures also validate the absence of geometric interference between the reflector and the solar panel.

The evolution of the displacements at the extremity of the tape spring are given in Figure 4.7a where the abscissa axis spans from 220 s to 250 s. As could be expected, minimising the maximum motion amplitude leads to smaller displacements after deployment. Regarding the oscillations, they are characterised by a higher frequency and they are quickly damped out after ~ 6 s in opposite and equal senses, while previously 30 s were not nearly enough. Obviously, this behaviour is also apparent in the evolution of the angle β with respect to time (Figure 4.7b).

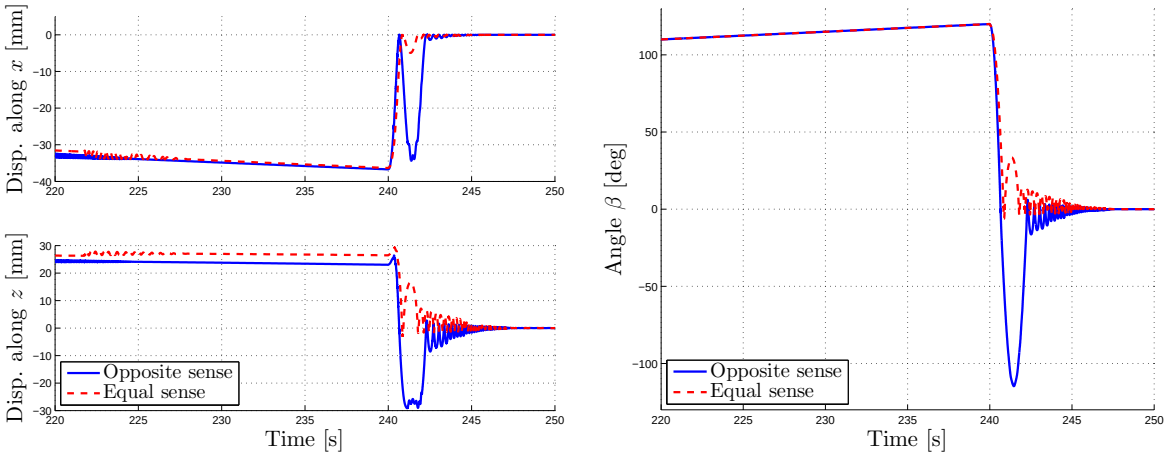

(a) Displacements at the extremity.

(b) Motion amplitude (β angle).

Figure 4.7: Evolution of the tape spring in both senses of bending in the case $f(x) = \beta_{\max}$.

Sense	Geometry	t [mm]	R [mm]	α [deg]	$\sigma_{\max}$ [MPa]	$\lvert\beta_{\max}\rvert$ [deg]	Nbr. of func. eval.
Opposite/Equal	Initial	0.2	20	60	–	–	–
Opposite	Optimised	0.08	10	60	**861.68**	**205.95**	23
Equal	Optimised	0.08	10	60	**824.34**	**39.67**	30

Table 4.4: Results for the minimisation of the weighted objective function Eq. (4.6).

However, minimising the maximum motion amplitude comes with an increase of the Von Mises stresses for which the maximum clearly exceeds the yield limit of the beryllium copper, whatever the initial sense of folding (Table 4.3). The deformations are then such that, after deployment, a straight configuration might not be recovered due to irreversible deformations and/or damage of the tape spring. Notice that in this work, the finite element models do not take plastic deformations into account.

4.2.4 Minimisation of a weighted objective function

In this third case, the objective function is a combination of the two previous problems. It is then defined as a weighted sum of the maximum Von Mises stress $\sigma_{\max}$ and the maximum motion amplitude $\beta_{\max}$ such that:

$$f(x) = w_1\sigma_{\max} + w_2|\beta_{\max}| \tag{4.6}$$

where w_1 and w_2 are weights respectively expressed in [deg] and [MPa]. In this optimisation procedure, the choice is made to use $w_1 = 0.1w_2$ in order to sum two terms with a similar order of magnitude. Notice that the previous objective functions can be recovered by setting alternatively one of the two weights to zero.

The results are given in Table 4.4 along with the number of function evaluations required to reach them. Starting from the same model, the optimised geometry is the same for the two different folding senses. For an initial folding in equal sense, it corresponds to a tape spring which achieves a compromise between the performances obtained by minimising the two objective functions separately. However, in opposite sense, the geometry minimising the maximum Von Mises stress $\sigma_{\max}$ is recovered.

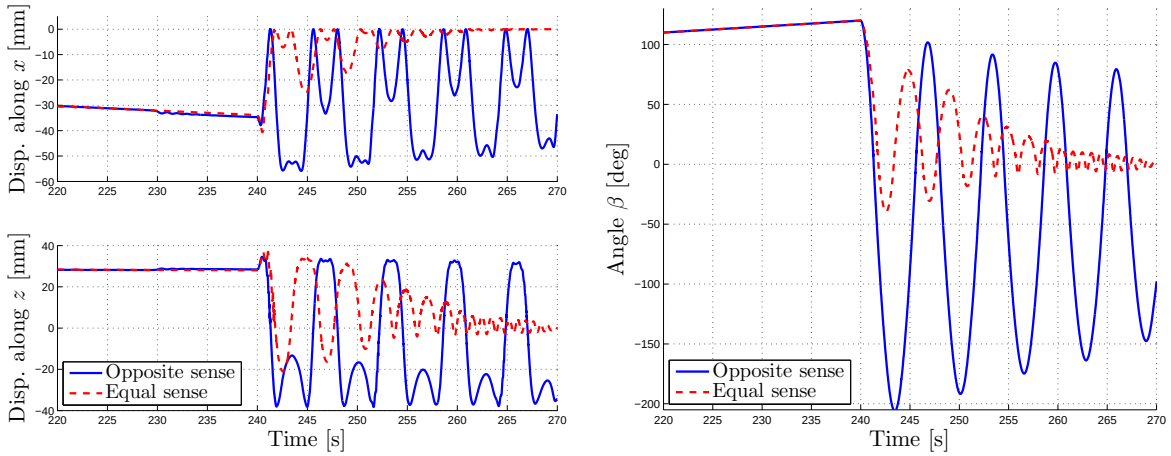

(a) Displacements at the extremity.

(b) Motion amplitude (β angle).

Figure 4.8: Evolution of the tape spring in both senses of bending in the case Eq. (4.6).

Regarding the evolutions of the displacements at the extremity of the tape spring and of the angle β (Figures 4.8a and 4.8b respectively), the results are also between the two previous extreme cases in equal sense, both in terms of frequency of oscillations and time of damping, while in opposite sense the curves are the same as those presented in Figures 4.4a and 4.4b respectively. In opposite sense, the results are thus characterised by the same drawback in terms of damping time.

In conclusion, these analyses lead to two tape springs which stay in the elastic regime throughout the folding and the deployment sequence, and avoid any collision between the reflector and the solar panel. However, compared with the case in opposite sense, the structure starting with a fold in equal sense is stabilised in a much shorter period of time.

The objective function defined by a weighted sum and used in this section is a pragmatic approach to solve a multi-objective problem. However, its results are directly influenced by the selected values of the weights w_1 and w_2 in Eq. (4.6). It is thus relevant to determine the Pareto front of the multi-objective optimisation problem. The Pareto front represents all the possible compromises which minimise the multi-objective function while respecting the constraints. For each point on the Pareto front, it is not possible to improve one term of the objective function without degrading the result of the others (*e.g.*, in this case it is not possible to reduce to value of the maximum Von Mises stress $\sigma_{\max}$ without increasing the value of the maximum motion amplitude $\beta_{\max}$, and *vice versa*).

A number of points of the Pareto front for both senses of folding have been computed and are given in Figure 4.9 where all the optimised results summarised in Tables 4.2, 4.3 and 4.4 can easily be recovered. In the remaining parts of this work, the results given in Table 4.4 will be exploited as it represents a fair compromise between the maximum Von Mises stress $\sigma_{\max}$ and the maximum motion amplitude $\beta_{\max}$. Furthermore, the optimised geometry is conveniently the same in both senses of folding.

4.3 Deployment of the reflector

Based on the optimal geometry obtained in the previous section, the 3D deployment of the complete system including the reflector and the two tape springs is now investigated. A schematic

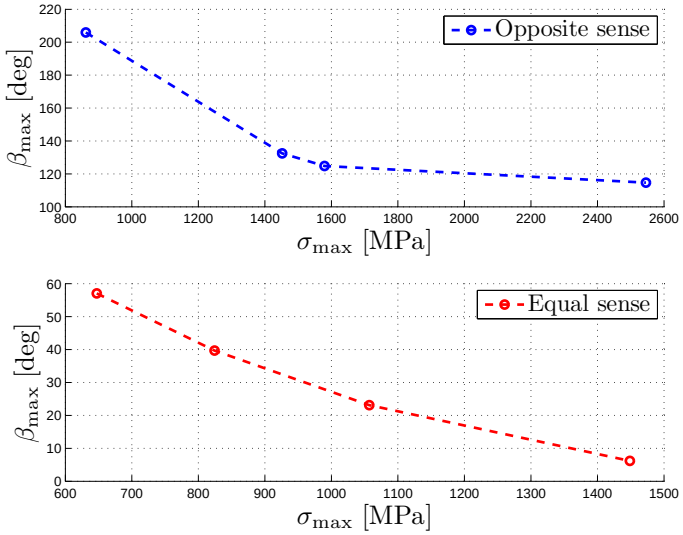

Figure 4.9: Pareto front in opposite and equal senses for a multi-objective function on the maximum Von Mises stress $\sigma_{\max}$ and the maximum motion amplitude $\beta_{\max}$.

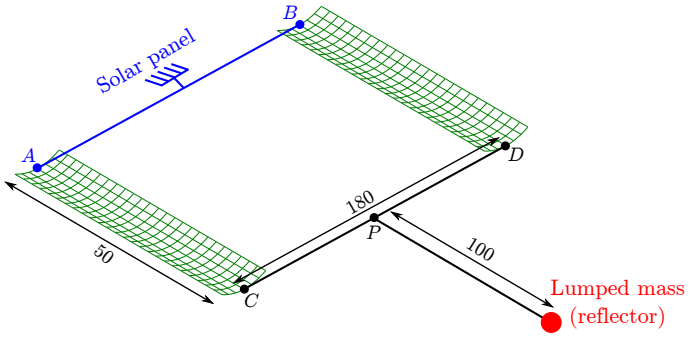

Figure 4.10: Illustration of the finite element model of the hinge (dimensions in millimetres, not to scale).

illustration of the finite element model is given in Figure 4.10. Regarding the boundary conditions, as mentioned previously, the solar panel is considered as already deployed and fixed, the tape springs are then clamped at these extremities, while this time the transverse displacements are not constrained. The reflector is represented as a lumped mass (red dot) located at its centre of mass and rigidly connected to the extremities of the tape springs through an intermediate point P. Finally, the distance between these latter is chosen as large as possible while keeping a margin of 5 mm on each lateral sides of the reflector.

As it was proven for a single tape spring, an initial folding in equal sense leads to smaller values of maximum Von Mises stress $\sigma_{\max}$ and maximum motion amplitude $\beta_{\max}$ compared to an initial folding in opposite sense. Furthermore, the amount of time required to damp out the oscillations of the motion is also reduced. The selected solution is then based on the two tape springs initially bent in equal sense with the optimised geometry defined in Table 4.4.

The evolution of the angle β from the fully folded configuration of the reflector and its transient position during the deployment is given in Figure 4.11 where the results for initial foldings in opposite sense and the alternate configuration (one tape spring folded in opposite sense and the other one folded in equal sense) are also shown for the sake of completeness. As expected, the selected solution has a smaller motion amplitude and is more quickly stabilised than the two other configurations.

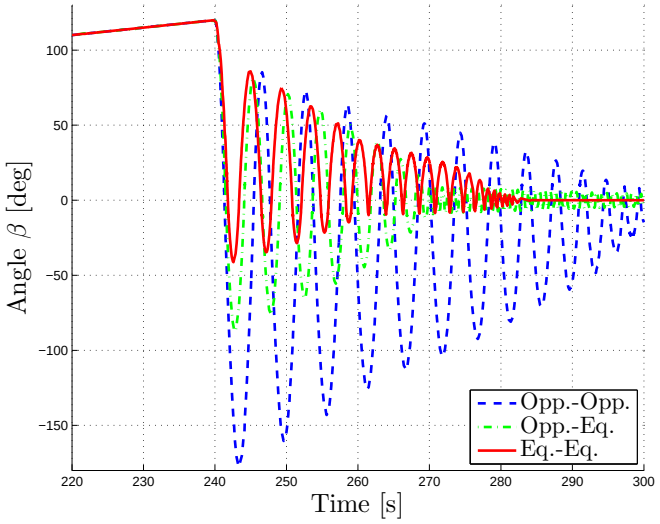

Figure 4.11: Evolution of the angle β for the hinge at point P.

	$\sigma_{\max}$ [MPa]	$\lvert\beta_{\max}\rvert$ [deg]	$\lvert Y_{\max}\rvert$ [mm]	$\gamma_{\max}$ [deg]
Eq.-Eq.	827.78	41.29	0.44	4.15
Opp.-Eq.	895.61	87.21	0.83	3.36
Opp.-Opp.	908.26	177.75	0.35	3.50

Table 4.5: Maximum values for the three configurations of the tape springs ($\sigma_{\max}$ maximum Von Mises stress, $\beta_{\max}$ maximum motion amplitude, $Y_{\max}$ maximum lateral displacement, $\gamma_{\max}$ maximum torsion angle).

Furthermore, the maximum Von Mises stress $\sigma_{\max}$, the maximum motion amplitude $|\beta_{\max}|$, the maximum lateral displacement $|Y_{\max}|$ and the maximum torsion angle $\gamma_{\max}$ are given in Table 4.5, where Eq.-Eq. (resp. Opp.-Opp.) is the case with the two tape springs initially folded in equal sense (resp. opposite sense) and Opp.-Eq. is the alternate configuration. In terms of $\sigma_{\max}$ and $|\beta_{\max}|$, the small differences compared to Table 4.4 are due to the fact that the lateral displacements of the tape spring medians are now left free while previously they were blocked. For the alternate configuration, the values are logically between the two other cases. Regarding the lateral displacements, as expected, they remain small which validates *a posteriori* the choice of the boundary conditions in the optimisation procedure based on a single tape spring.

The effect of the torsion around the longitudinal axis is quantified by the means of the torsion angle $\gamma_{\max}$ defined as the maximum acute angle between the two skew lines AB, representing the solar panel, and CD, representing the reflector, in a 3D-space (Figure 4.10). By considering the deformed configurations of the tape springs associated to $\gamma_{\max}$ (Figure 4.12), it can be seen that the maximum torsion angles are linked to an asymmetry in the location of the folds, this phenomenon being accentuated when both folds are formed in equal sense during deployment. The alternate configuration (Opp.-Eq.) is then more stable with respect to torsion. The small values of $\gamma_{\max}$ further confirm the characteristics of the optimisation procedure.

To conclude these last results, the optimised geometry of the tape springs leads to a deployment of the reflector avoiding any collision with the solar panel, stresses such that the deformations stay in the elastic regime, and limited lateral displacements and torsional effects. The reflector can then be safely folded and deployed.

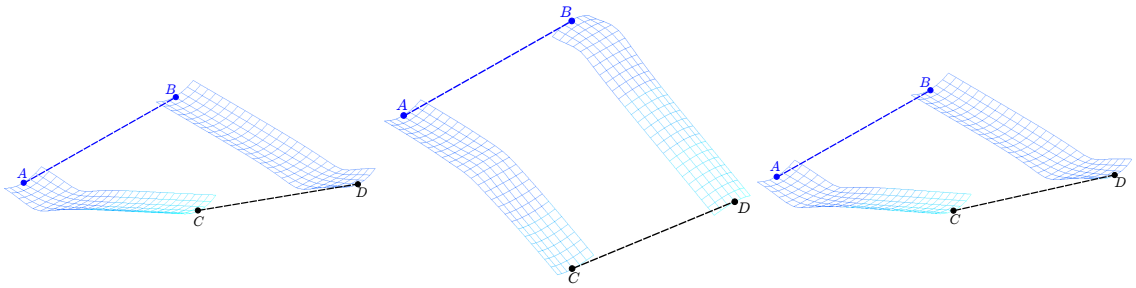

(a) Equal-Equal. (b) Opposite-Equal. (c) Opposite-Opposite.

Figure 4.12: Deformed configurations of the tape springs associated to the maximum torsion angle $\gamma_{\max}$.

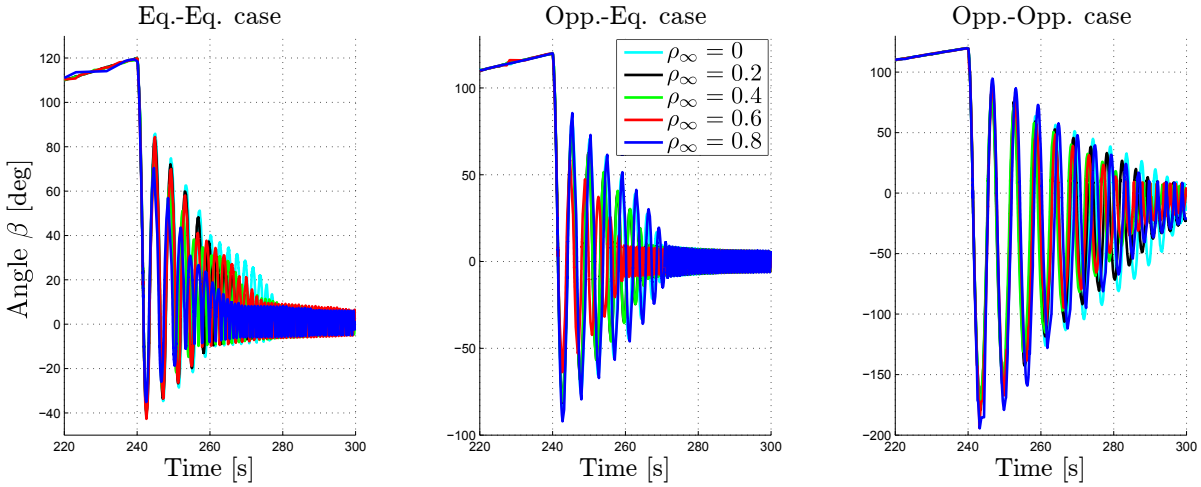

Figure 4.13: Impact of the numerical damping ρ_∞ on the deployment of the reflector in the three configurations.

4.4 Further analyses on the finite element models

So far in this application and the previous parametric studies, the numerical damping introduced in the solver of the Newmark method or the generalised-α method is fixed to a large value by setting the spectral radius parameter ρ_∞ to 0. Thus, the influence of the high-frequency transient disturbances, due to the representation of the tape springs by finite element models, is kept to a minimum, which helps in the convergence of the solver. Furthermore, as it was presented in Section 2.2.3, the resulting quasi-static behaviour is weakly affected by numerical phenomena since the artificial oscillations after buckling are damped in a small number of time steps.

However, by performing several simulations of the deployment of the reflector with different values of ρ_∞ as illustrated in Figure 4.13 where the evolution of the angle β is given for the three configurations of the tape springs, it can be seen that the numerical damping has a clear impact on the oscillations triggered after removing the constraint on the bending angle, both in terms of amplitude and frequency. Furthermore, focusing on the maximum motion amplitude $\beta_{\max}$ in Figure 4.14, it can be seen that decreasing the numerical damping does not lead to the convergence of this feature, which varies significantly. It can then be concluded that reducing the numerical damping is not sufficient to develop robust dynamic models of tape springs in terms of transient dissipation phenomena and therefore, in the case of tape springs, self-locking capacity.

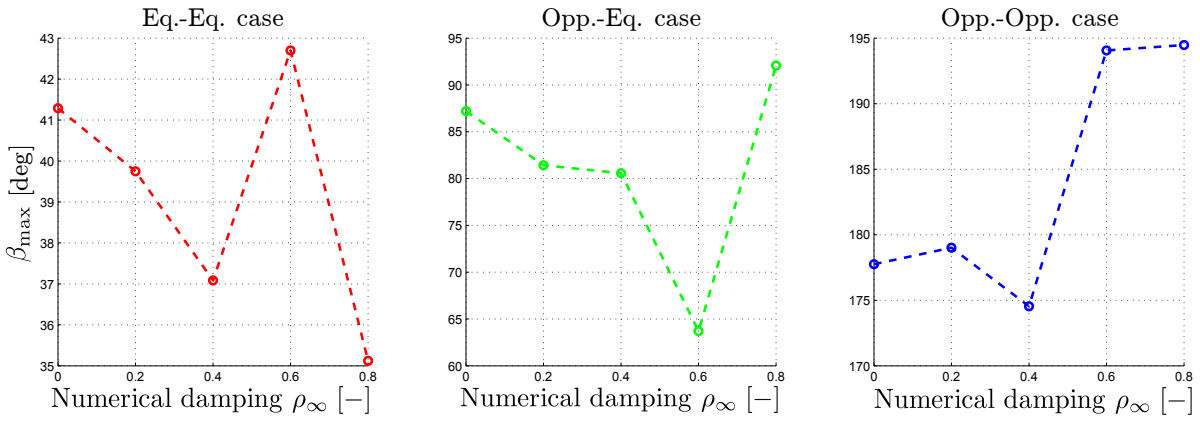

Figure 4.14: Impact of the numerical damping ρ_∞ on the maximum motion amplitude $\beta_{\max}$.

More thorough analyses are then required to fully understand the influence of the numerical damping and investigate physical damping models. To that purpose, a general review of the different sources of damping affecting a structure in motion is proposed in Chapter 5, while a detailed analysis of the impact of the structural and the numerical dampings on the nonlinear behaviour of tape springs is undertaken in Chapter 6.

4.5 Summary

An application consisting in deploying a reflector around a solar panel by the means of two tape springs is studied. The design parameters are the thickness, the transverse radius of curvature and the subtended angle of the tape springs, while the objective is to minimise the maximum Von Mises stresses and the maximum motion amplitude. The purpose of the former constraint is to keep the stresses under the yield limit in order to remain in the elastic regime and thus prevent irreversible deformations, while for the second one, any collision with the solar panel must be avoided. The length and the material of the tape springs are fixed *a priori* and bounds are defined for the design parameters, as well as for the height and the width of tape spring cross-section in order to fulfil space allocation requirements.

As three design parameters have to be determined, an optimisation procedure based an finite element models is proposed in order to find the optimised geometry. The problem is first solved for a single tape spring, the behaviour of the complete hinge being reproduced by blocking the transverse displacements of its median. Each objective function, the maximum Von Mises stress and the maximum motion amplitude, is considered separately, then simultaneously by defining a weighted objective function and the associated Pareto front. In the end, the optimised geometry used to deploy the reflector is the one given in Table 4.4 with the tape springs both initially bent in equal sense.

The finite element models used for the quasi-static folding of the tape springs and their dynamic deployments are further analysed in order to determine the influence of the numerical damping on the dynamic response. It was shown that the amount of numerical damping clearly modifies the deployments. Furthermore, reducing its value does not lead to converged models, for example in terms of the maximum motion amplitude. It is then proposed to further investigate the influence of numerical damping and to introduce structural damping models in the next chapters.

CHAPTER 5

REVIEW OF DAMPING PHENOMENA AND MODELS

In engineering structures, the motion is generally affected by damping which can be seen as a beneficial characteristic or, on the contrary, as a drawback according to the objective to be achieved.

On the one hand, the amplitude of a system characterised by damping is limited when excited at its resonance frequency which can help in preserving the structural integrity of the system, for example, by preventing a building from collapsing during earthquakes. Damping can also be added between different components to avoid transmitting disturbances, or at least reduce their propagation. For example, in satellites, it is often necessary to limit the interference between the vibrations from the reaction wheels, controlling the attitude, and sensitive instruments. In these applications, after setting a structure into motion, damping contributes then to bringing it back to a state free of external perturbation.

On the other hand, damping can sometimes be seen as a major drawback as it induces energy losses. For example, in mechanical transmissions, in order to maintain a desired level of motion or speed at the output, more energy must be introduced in the system to counteract the effects of damping. Furthermore, it can also lead to a degradation of the accuracy in sensitive components. In MEMS (microelectromechanical systems) resonators, air damping affects the quality factor which is fundamental to the development of accurate high-frequency components [114]. In these situations, the objective is then to reduce the impact of the damping on the performances of the system.

In the case of structures deployed by tape springs, damping has clearly a beneficial impact since after triggering the deployment, it is important that the mechanism and the deployed components stabilise themselves in the required configuration as early as possible before starting the acquisition of data in the case of an instrument or to reach the optimal non-vibratory configuration for the operation of solar panels or reflectors.

In a structure, many sources of dissipation can be identified. The most common ones are reviewed in the following of this chapter.

5.1 Friction damping

In every structure composed of several elements which have surfaces in contact, friction damping occurs whether the contact is used to transmit motion such as in gears or belt transmissions, or to assemble two elements by using for example bolted connections. In these situations, friction

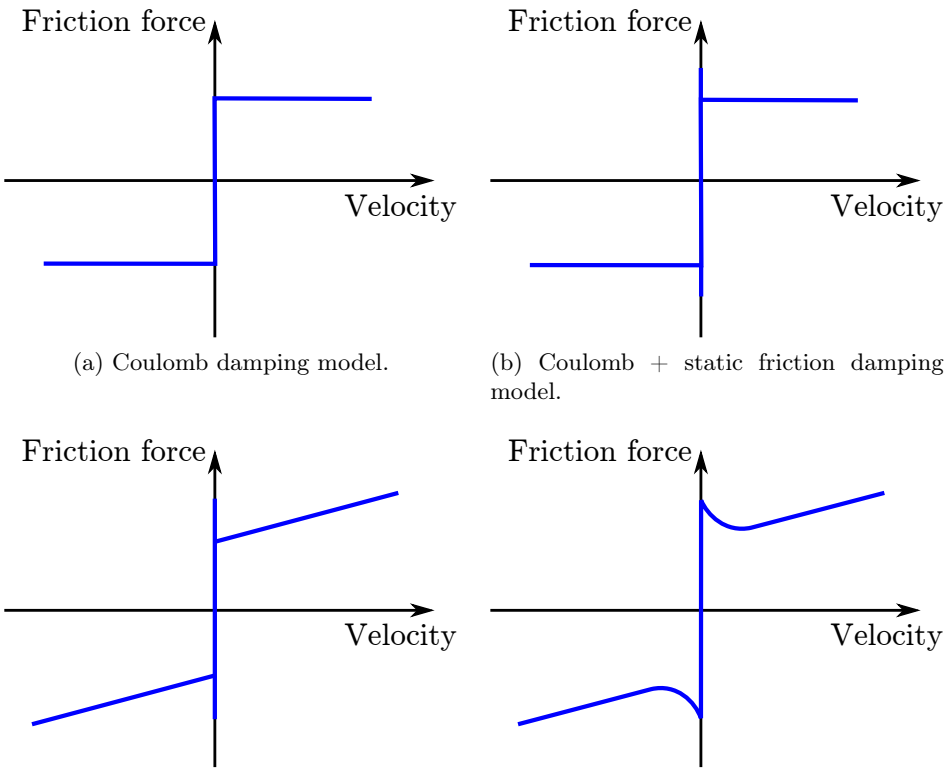

(a) Coulomb damping model.

(b) Coulomb + static friction damping model.

(c) Static friction + viscous damping model.

(d) Stribeck damping model.

Figure 5.1: Evolution of the models for friction damping.

induces both wear and energy losses as the mechanical work is partially transformed into heat.

In this section, the theoretical aspects and the models of friction damping considered as the most relevant ones and allowing to grasp the underlying physical concepts involved in this thesis are presented. For a more comprehensive survey of friction models, the reader is encouraged to refer to [3] which focuses on the impact of friction in the case of controlled machines or to [68] which reviews friction models in the context of multibody system dynamics.

Coulomb developed his famous mathematical model based on a large variety of experimental tests involving different materials with different areas in contact and concluded that the friction force is independent of the surface area, that a minimum applied tangential force is required to set the body into motion, and that the resulting friction force is independent of the velocity and proportional to the normal force [27]. The coefficient of proportionality is defined as the friction coefficient μ and is the single parameter of this model. This relationship between the friction force and the velocity, which involves a discontinuity at the origin, is illustrated in Figure 5.1a.

Coulomb [27] already mentions that the force required to set a body into motion and the one required to maintain a uniform velocity have to be distinguished. A static friction coefficient μ_S larger than the kinetic friction coefficient μ_K involved in the Coulomb damping model is then introduced by Morin [75]. The relationship linking the friction force and the velocity can then be represented as in Figure 5.1b. The values of both coefficients are dependent on the properties of the materials into contact [15, 50], on the surface roughness [50, 72] and on the presence or absence of lubricant [8].

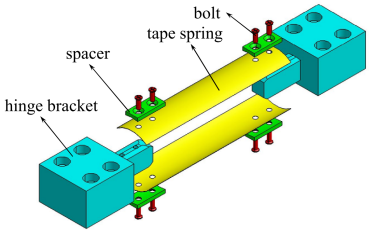

(a) Interfaces in [53].

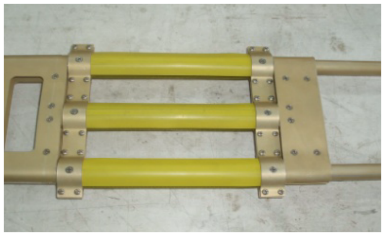

(b) Interfaces in [36].

(c) Interfaces in [113].

Figure 5.2: Source of friction damping: interfaces between the tape springs and other components.

The Coulomb damping model can be further improved to account for the effects of grease or oil lubricant applied at the interface between the two bodies. In machineries, the purpose of using lubricants is twofold: it leads to the reduction of the friction coefficient and limits the impact of wear. While in the first case, a decrease by a factor of 2 to 10 can be perceived, the effects of lubricants are even more noticeable in wear with a reduction factor of 10^2 to 10^4 [32].

This viscous damping was first analysed by Reynolds [85] who observed a linear relationship between the friction force and the velocity (Figure 5.1c), the slope being determined by the viscous coefficient of the lubricant layer. Extensive analyses on a mass – spring system combined with viscous damping can be found in [29, 44] in the case of forced vibrations applied on the mass and in [59] for a support excited system. As lubricants are not used in this thesis, no theoretical development is given here.

The main drawback of the three previously described models is that the transition between the static and kinetic friction coefficients is discontinuous, while in nature such an instantaneous and sharp variation seems unlikely. The evolution of this transition was studied by Stribeck [104] who showed experimentally the existence of a continuous transition between the static and kinetic friction forces (Figure 5.1d).

In the particular case of deployable structures, friction damping can be encountered in the deployment mechanisms when they are composed of several elements revolving around or sliding over each other. Regarding tape springs, alone, they are free of this form of damping. However, they need to be connected to other components by the means of interfaces. In addition to the experimental devices shown in Chapter 1, some of the interfaces that can be found in other works are illustrated in Figure 5.2. Furthermore, tape springs can sometimes be mounted in parallel with common hinges in which friction damping is present [103]. Finally, when tested on the ground, deployable structures are often supported by a gravity compensation system, which is usually composed of rails and/or pulleys, in order to approach the deployment conditions encountered in space (Figure 5.3). In that case, this additional system is affected by friction damping which interferes with the motion of the deployable structure. It is then essential to limit and evaluate the impact of this damping in order to collect relevant experimental results.

5.2 Fluid interaction damping

A second important source of damping results from the interaction between a structure in motion and the surrounding fluid which can correspond to liquids, gases or plasmas.

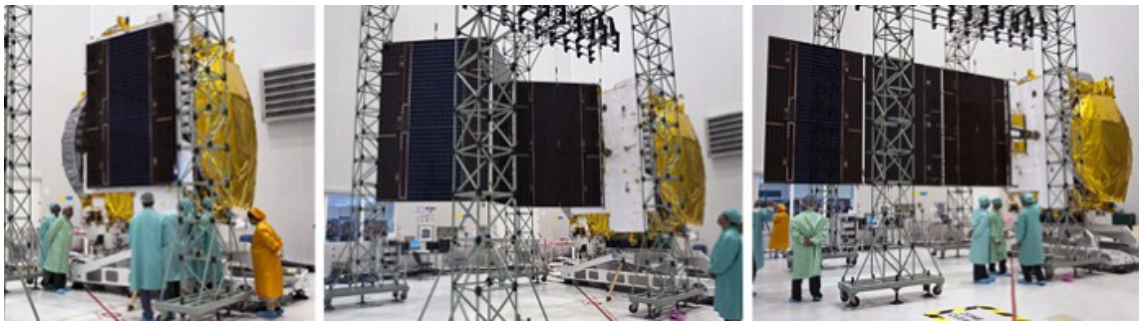

Figure 5.3: On-ground deployment of the solar panels on GSAT-10 with a gravity compensation system [1].

Due to the presence of the fluid, the body in motion has to counteract an additional force opposed to the velocity. In the case of large structures, this phenomenon is referred to as drag and the objective is, in general, to reduce its impact as it induces energy losses. For example, for cars, planes or trains, designing aerodynamic profiles helps limiting the drag. The same concept is applied for boat hulls. In the case of small components such as MEMS, air damping is predominant due to the difference of scaling between the volume and the surface, this latter being the largest [48, 49].

In space applications, air damping is negligible or inexistent depending on the proximity of the spacecraft to the earth atmosphere. However, tests prior to the launch are usually conducted under atmospheric conditions mostly because the deployed configuration of a spacecraft can easily reach several meters and the use of large vacuum chambers is costly and time-consuming. It is then essential to quantify the impact of air damping on the evolution of the deployment with respect to the other types of damping involved in the motion. Indeed, the global damping being higher during on-ground tests, the motion amplitude is reduced, which increases the safety regarding collisions and facilitates the stabilisation of the structure when submitted to vibratory motion. These results need to be extrapolated and confirmed in vacuum, hence the necessity to evaluate and characterise the influence of air damping.

The most common situations encountered in the space domain on which air damping has a significant effect are the deployment of solar panels and masts which can be represented as flat plates and beams respectively. By testing beams of different size and material at different air pressures, air damping appears to be predominant for thin beams submitted to large motion amplitude [5]. This behaviour is also confirmed for thin flat plates in [109, 110].

Furthermore, the impact of air damping is evaluated in [5] by linking the logarithmic decrement to the energy dissipated by drag. In its general definition, the logarithmic decrement δ quantifies damping by computing the ratio of decreasing motion amplitudes X_i over N cycles:

$$\delta = \frac{1}{N} \ln \frac{X_i}{X_{i+N}} \tag{5.1}$$

Using the equation of motion of a free vibrating beam and the commonly accepted definition of the drag force which is quadratic in terms of velocity:

$$F_D = \frac{1}{2} \rho_f C_D S v^2 \tag{5.2}$$

where ρ_f is the density of the fluid, C_D is the drag coefficient, S is the surface area normal to the flow and v is the velocity, the logarithmic decrement due to air damping δ_{AD} can be

Mode n	1	2	3	4	5
β_n	1.473	1.300	1.270	1.252	1.252

Table 5.1: Mode shape contribution factor [5, 110].

approximated assuming that the damping is low, implying that the change of motion amplitude is small over a cycle, by the means of energy methods such that :

$$\delta_{AD} = \frac{4}{3} C_D \beta_n \frac{\rho_f X_n}{\rho_b h} \tag{5.3}$$

$$= \frac{4}{3} C_D \beta_n \frac{\rho_f X_n S}{m} \tag{5.4}$$

where X_n is the tip amplitude of the nth mode of the beam, ρ_b is the beam density, h is the beam thickness, m is the beam mass and β_n is a mode shape contribution factor defined in Table 5.1 for the first five modes of a thin cantilever beam obtained by numerical integrations of the normal mode shape function [5]. The impact of the mode shapes on the amount of damping can be explained by the fact that each mode undergoes specific deformations characterised by different displacements of the structure and therefore different displacements of the surrounding fluid. Experimental tests on plates showing a similar behaviour can be found in [109].

By computing the total damping of a structure with Eq. (5.1), it is then possible to divide it into two contributions:

$$\delta = \delta_{AD} + \delta_{Int} \tag{5.5}$$

where δ_{AD} is the part due to air damping and approximated by Eqs. (5.3) and (5.4), and δ_{Int} contains the internal damping phenomena such as friction and material damping.

Another type of structure – fluid interaction worth mentioning is called gas pumping. Gas pumping is encountered in situations where enclosed gas is submitted to changes of pressure due to the vibration of the containing walls [77] or in structures in which adjacent elements are physically connected at specific points, for example with rivets or bolts, and separated by a thin film of air on the remaining of the surface [62, 77]. In the first case, the containing walls are never perfectly sealed which allows the gas to flow through holes or cracks (Figure 5.4a). The displacement of the gas is responsible for air damping which increases with the entrapped volume, decreases with the atmospheric pressure and has a more significant impact when the containing walls are submitted to excitations at low frequency. In the second situation, spaces between the adjacent surfaces are alternatively created and removed as the elements vibrate (Figure 5.4b). Again, the flow of gas leads to air damping which is proportional to the air pressure and low at high vibration frequencies. This phenomenon is also encountered in MEMS where a vibrating surface close to another one induces damping by squeezing the film of air present between them. In this case, it is referred to as squeeze film air damping [7].

Finally in compressible fluids, beams or plates submitted to vibrations at high frequency can experience acoustic radiation damping due to the emission of noise in the surrounding fluid. The acoustic damping depends on the fluid density, the velocity of the sound waves and the mass and stiffness of the structure [77]. Furthermore, the relationship between this type of damping and the vibration frequency at which the structure is excited is nonlinear as shown experimentally in [47]. The damping tends to vary significantly when the frequency is above a certain value (or similarly when the wavelength is below a certain value) and a maximum is reached at a specific value which depends on the geometry and the dimensions of the cross-section beam. These authors also showed that, in their experimental cases, the maximum acoustic damping can be more than ten times larger than the internal damping.

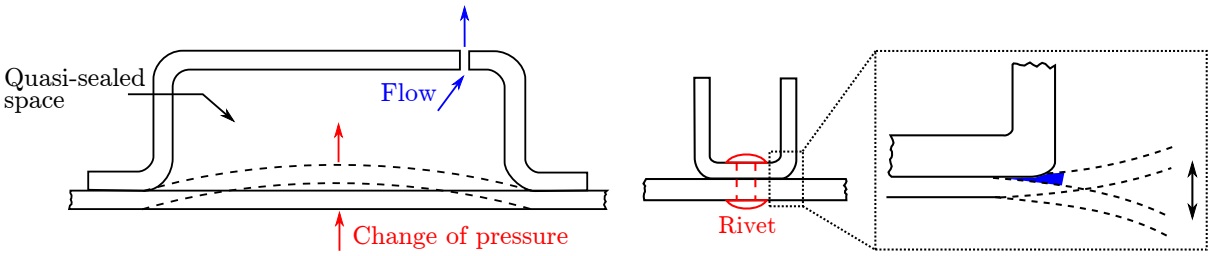

(a) Due to enclosed gas. (b) Due to joints.

Figure 5.4: Gas pumping [77].

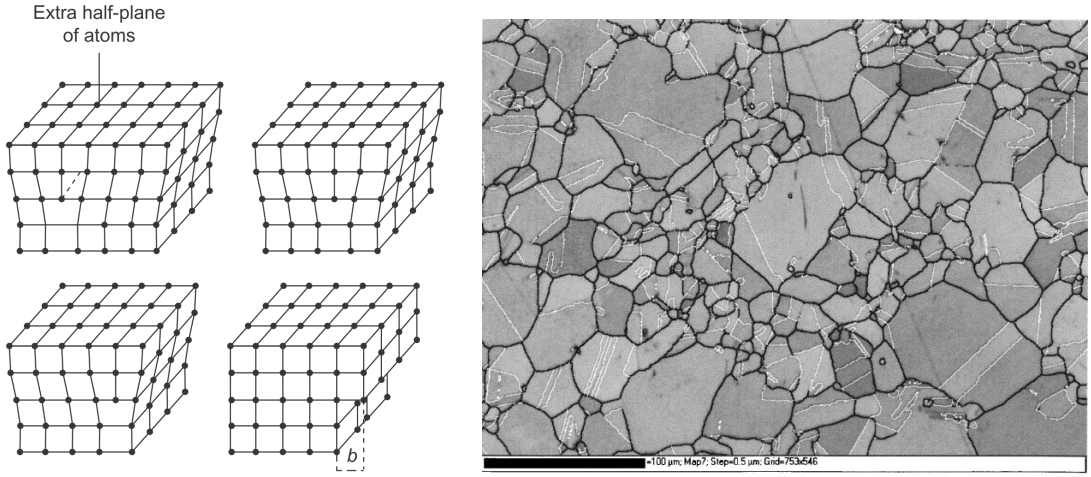

(a) Dislocations [100]. (b) Grain boundaries [83].

Figure 5.5: Defects in metals.

5.3 Material damping

Material damping is a form of dissipation occurring at the microscopic scale or smaller of a material. This section describes the main physical phenomena involved in metals and polymers and some associated elementary models.

In the case of metals, the main source of dissipation is due to the mobility of defects in their polycrystalline structure inducing thus internal frictions. They are commonly divided into three categories according to their dimensions [12, 77]. At the atomic level, defects are due to the absence of atoms (vacancies), the substitution of host atoms by foreign ones, possibly of different size, or the presence of foreign interstitial atoms between the host atoms [38, 56]. Linear defects, called dislocations, consist of lines of atoms being misaligned in the crystal structure of the metal (Figure 5.5a). Their diffusion through the lattice is also responsible for the ductility of metals allowing them to sustain large elastic and plastic deformations before breaking [87, 100]. Finally, since metals are in general polycrystalline materials, they are composed of numerous crystals or grains of different sizes and orientations (Figure 5.5b). The grain boundaries connecting them are 2D defects which can rearrange themselves during the relaxation process in order to reach an equilibrium state [82].

Polymers are made of large molecules, usually combining carbon and hydrogen atoms, connected in chains. Submitting a polymer to an external force leads then to a relative motion of the chains one over the other, and thus to internal friction. The motion amplitude mainly depends on the type of bonds linking the chains. For example, a weak cohesion is obtained when linear

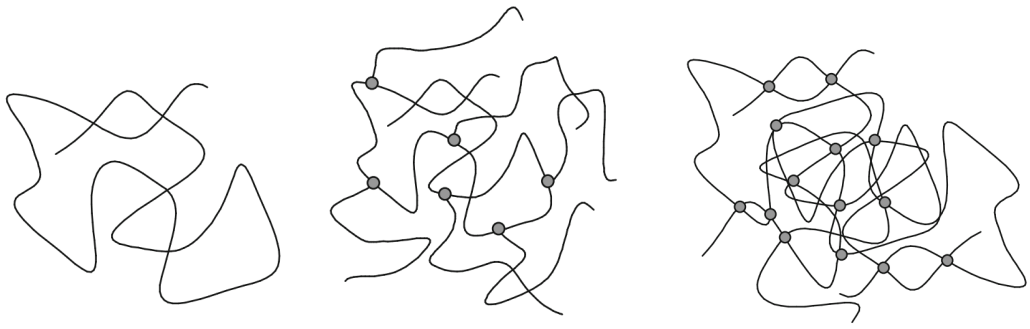

(a) Entanglement. (b) Branched chains. (c) Cross-linked chains.

Figure 5.6: Bonds between chains of polymers [17].

chains are entangled (Figure 5.6a), it increases in the case of branched chains (Figure 5.6b) and stronger bonds are formed by cross-linking the chains (Figure 5.6c) [17].

The simplest representation of these physical behaviours is by the means of one-dimensional rheological models combining springs and dashpots. Springs are ideal elastic elements following Hooke's law and characterised by an elasticity modulus E:

$$\sigma_s(t) = E\varepsilon_s(t) \tag{5.6}$$

where $\sigma(t)$ represents the stresses and $\varepsilon(t)$ the strains, while dashpots are ideal viscous elements respecting the law of newtonian flows and characterised by a viscosity coefficient η:

$$\sigma_d(t) = \eta\dot{\varepsilon}_d(t) \tag{5.7}$$

where $\dot{\varepsilon}(t)$ is the strain rate. A detailed description of the models created by combining these simple elements can be found in [23, 69]. The most common ones and their main characteristics are recalled here.

The Maxwell model combines a spring and a dashpot in series as illustrated in Figure 5.7a. The system equations are:

$$\sigma(t) = \sigma_s(t) = \sigma_d(t) \tag{5.8}$$
$$\varepsilon(t) = \varepsilon_s(t) + \varepsilon_d(t) \tag{5.9}$$

which can be differentiated with the help of the element equations Eqs. (5.6) and (5.7) to obtain the constitutive equation:

$$\dot{\varepsilon}(t) = \frac{\dot{\sigma}(t)}{E} + \frac{\sigma(t)}{\eta} \tag{5.10}$$

from which it can be shown that the Maxwell model behaves like a viscous and compressible fluid. Furthermore, it is characterised by an instantaneous reversible elastic strain and an irreversible unbounded strain in the case of creep (analysis of the strain evolution under a constant stress). On the other hand, in the relaxation process (analysis of the stress evolution under a constant strain), the stress follows an exponential decay which vanishes for $t \to \infty$.

The Kelvin-Voigt model consists of a spring and a dashpot in parallel as illustrated in Figure 5.7b. It is defined by the following equations where this time each element is submitted to the same strain:

$$\sigma(t) = \sigma_s(t) + \sigma_d(t) \tag{5.11}$$
$$\varepsilon(t) = \varepsilon_s(t) = \varepsilon_d(t) \tag{5.12}$$

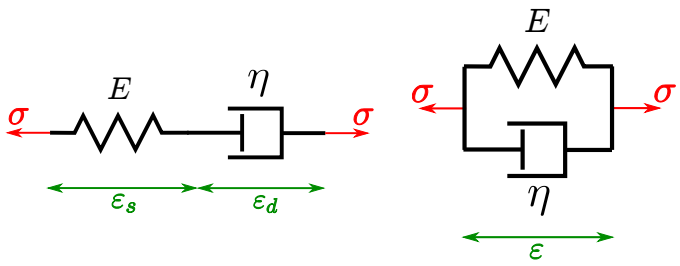

(a) Maxwell model. (b) Kelvin-Voigt model.

Figure 5.7: Rheological models.

The resulting differential equation is:

$$\sigma(t) = E\varepsilon(t) + \eta\dot{\varepsilon}(t) \tag{5.13}$$

which represents the behaviour of a viscous solid. In the case of creep, the strain evolution is bounded by an asymptotic solution depending on the elasticity of the spring. Furthermore, this rheological model leads to the exponential decay of vibratory motions [23].

More complex and generalised models can be achieved by increasing the number of springs and dashpots and connecting them in series and/or parallel. Thus, a larger number of design parameters can be used to fit experimental behaviours [21].

In the case of tape springs, material damping is present and affects their dynamic evolution. To the best of our knowledge, only a few number of works took that phenomenon into account in the developments of tape springs models. In [54, 57], damping is represented by a diagonal damping matrix for which constant damping elements are determined by directly fitting the model evolution on the experimental deployments. In [74], the Rayleigh or proportional damping model is used. This model consists in defining the damping matrix $\mathbf{C}$ as a linear combination of the mass $\mathbf{M}$ and stiffness $\mathbf{K}$ matrices of the system:

$$\mathbf{C} = \alpha\mathbf{M} + \beta\mathbf{K} \tag{5.14}$$

with α and β the mass and stiffness proportional damping factors respectively. In the considered work [74], the material damping is represented by the stiffness term only and the β factor varies with the natural frequency of the system deformed configuration. Finally, in [18, 58], a linear viscoelastic law is defined by a Prony series. In this case, the coefficients are determined by fitting the series on the experimental evolution of the relaxation modulus of the tape springs at different temperatures.

To conclude, in these works, the parameters of the material damping models are identified based on experimental tests, either by fitting the final output (for example, the complete deployment motion) or by fitting the behaviour of a single component of the system (for example, the nonlinear behaviour of a tape spring). In this thesis, the second approach will be preferred in order to develop more robust models which can be used to predict a variety of deployment scenarios.

5.4 Summary

Three types of damping sources are commonly found in engineering structures and, in particular, in deployable structures: friction damping, fluid interaction damping and material damping. Their physical characteristics were exposed here in simple cases and simple representative models were presented.

In the following of this thesis, this review will be used as a basis to identify the most important damping effects affecting the considered experimental set-up and help choosing a representative model.

CHAPTER 6

STRUCTURAL AND NUMERICAL DAMPINGS IN MODELS

In finite element models, the spatial discretisation of structures leads to a poor representation of the high-frequency modes. These modes have to be filtered out in order to improve the quality of the system response and ensure the convergence of the solver, especially in the case of nonlinear problems. To this end, some numerical damping is thus introduced in the solver. At the same time, the low-frequency modes which represent the physical response of the structure should not be affected by this numerical artefact.

In Sections 2.2.3 and 4.4, the models under study did not include any representation of the physical damping, but numerical damping was introduced for convergence reasons. It was shown that, in the case of quasi-static analyses on tape springs, the numerical damping mainly influences the damping of the artificial oscillations after buckling, while the other physical features, such as the stiffness, the maximum and residual moments in both senses of bending, remain unaffected. However, in dynamic analyses, the numerical damping clearly impacts the behaviour of the physical oscillations triggered after deployment, as well as the value of critical characteristics such as the maximum motion amplitude. It can then be concluded that a model in which some numerical damping is introduced, but without any structural damping, is not appropriate for the simulation of the dynamic response.

The objective of this chapter is then to provide a better understanding of the influence of the numerical and structural dampings on the numerical results in order to develop models representative of a real structure. To reach this goal, the impact of both parameters is first investigated at the level of the solver in a simple case study. Then, a detailed analysis on the dynamic behaviour of tape springs is performed.

6.1 Generalised-α method

The equation of motion of the problem can be put under the general form:

$$\mathbf{M}(\mathbf{q})\ddot{\mathbf{q}} + \mathbf{g}(\mathbf{q}, \dot{\mathbf{q}}, t) = \mathbf{0} \tag{6.1}$$

where $\mathbf{M}$ is the mass matrix, $\mathbf{q}$ is the vector of nodal coordinates, the dot symbol ($\dot{}$) indicates a derivation with respect to time, $\mathbf{g}$ is the vector of external forces, t is the time and the initial conditions are:

$$\mathbf{q}(t_0) = \mathbf{q}_0 \tag{6.2}$$

$$\dot{\mathbf{q}}(t_0) = \dot{\mathbf{q}}_0 \tag{6.3}$$

In this thesis, as introduced in Section 2.2.4, this type of dynamic problem is solved by the means of the generalised-α method which is second-order accurate and unconditionally stable when applied to linear problems. It was precisely developed to solve dynamic problems while controlling the numerical dissipation in the high-frequency domain and minimising its impact on the low-frequency content without jeopardising the convergence of the solver [24].

The generalised-α method relies on the following time integration formulae [4]:

$$\begin{aligned}
\mathbf{M}(\mathbf{q}_{n+1})\ddot{\mathbf{q}}_{n+1} + \mathbf{g}(\mathbf{q}_{n+1}, \dot{\mathbf{q}}_{n+1}, t_{n+1}) &= \mathbf{0} && (6.4)\\
\mathbf{q}_{n+1} &= \mathbf{q}_n + h\dot{\mathbf{q}}_n + h^2(0.5-\beta)\mathbf{a}_n + h^2\beta\mathbf{a}_{n+1} && (6.5)\\
h\dot{\mathbf{q}}_{n+1} &= h\dot{\mathbf{q}}_n + h^2(1-\gamma)\mathbf{a}_n + h^2\gamma\mathbf{a}_{n+1} && (6.6)\\
(1-\alpha_m)h^2\mathbf{a}_{n+1} + \alpha_m h^2\mathbf{a}_n &= (1-\alpha_f)h^2\ddot{\mathbf{q}}_{n+1} + \alpha_f h^2\ddot{\mathbf{q}}_n && (6.7)
\end{aligned}$$

where the first equation is the equation of motion, h is the time step, $\mathbf{a}$ is an acceleration-like variable which approximates the physical acceleration $\ddot{\mathbf{q}}$ at an intermediate time as:

$$\mathbf{a}_n \simeq \ddot{\mathbf{q}}(t_n + h(\alpha_m - \alpha_f)) \tag{6.8}$$

with the initial condition $\mathbf{a}_0 = \ddot{\mathbf{q}}_0$ and $\beta, \gamma, \alpha_m, \alpha_f$ are numerical parameters.

For information, the Newmark method [79] is recovered from this system of equations when:

$$\alpha_f = \alpha_m = 0 \tag{6.9}$$

while the Hilber-Hughes-Taylor (HHT) method [39] requires to have:

$$\begin{aligned}
\alpha_m &= 0 && (6.10)\\
\alpha_f &\in [0, 1/3] && (6.11)\\
\gamma &= 0.5 + \alpha_f && (6.12)\\
\beta &= 0.25(\gamma + 0.5)^2 && (6.13)
\end{aligned}$$

In the generalised-α method, the numerical damping is controlled in the high-frequency domain through the spectral radius at infinite frequencies ρ_∞ which belongs to the interval $[0, 1]$. In order to have an optimal solver with the characteristics previously mentioned in terms of accuracy, stability and impacts on the low- and high-frequency modes, the numerical parameters have to respect the following relationships [24]:

$$\begin{aligned}
\alpha_m &= \frac{2\rho_\infty - 1}{\rho_\infty + 1} && (6.14)\\
\alpha_f &= \frac{\rho_\infty}{\rho_\infty + 1} && (6.15)\\
\gamma &= \frac{1}{2} - \alpha_m + \alpha_f && (6.16)\\
\beta &= \frac{1}{4}(1 - \alpha_m + \alpha_f)^2 && (6.17)
\end{aligned}$$

Thus, the numerical dissipation leads to a complete annihilation of the high-frequency content in one step when $\rho_\infty = 0$, while on the opposite, there is no dissipation when $\rho_\infty = 1$.

6.2 Case study: the mass – spring – damper system

The influence of the numerical and structural damping parameters is investigated in a simple case study: the mass – spring – damper system (Figure 6.1) which is solved using the generalised-α

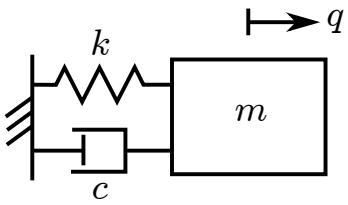

Figure 6.1: Mass m – spring k – damper c system.

method.

The equation of motion of this system when free of external force is:

$$m\ddot{q} + c\dot{q} + kq = 0 \tag{6.18}$$

with q the displacement, m the mass, k the spring stiffness and c the damper damping. The initial conditions on the displacement and the velocity are fixed to q_0 and $\dot{q}_0$ respectively. It is possible to reformulate this equation by introducing the natural pulsation $\omega^2 = \frac{k}{m}$ and the structural damping $\varepsilon = \frac{c}{2\omega m}$ of the system as:

$$\ddot{q} + 2\varepsilon\omega\dot{q} + \omega^2 q = 0 \tag{6.19}$$

6.2.1 Numerical solution

In order to use the generalised-α method, the equation of motion (6.4) is particularised to the present case:

$$\ddot{q}_{n+1} + 2\varepsilon\omega\dot{q}_{n+1} + \omega^2 q_{n+1} = 0 \tag{6.20}$$

which, with the equations Eqs. (6.5)–(6.7), forms the system to be solved. After the elimination of the acceleration $\ddot{q}_{n+1}$, it can be expressed in the following matrix form:

$$\mathbf{E}\mathbf{x}_{n+1} = \mathbf{B}\mathbf{x}_n \tag{6.21}$$

where $\mathbf{x}_n = \begin{pmatrix} q_n & h\dot{q}_n & h^2 a_n \end{pmatrix}^T$ and the 3-by-3 matrices $\mathbf{E}$ and $\mathbf{B}$ are given by:

$$\mathbf{E} = \begin{pmatrix} 1 & 0 & -\beta \\ 0 & 1 & -\gamma \\ (1-\alpha_f)\omega^2 h^2 & (1-\alpha_f)2\varepsilon\omega h & 1-\alpha_m \end{pmatrix} \tag{6.22}$$

$$\mathbf{B} = \begin{pmatrix} 1 & 1 & 0.5-\beta \\ 0 & 1 & 1-\gamma \\ -\alpha_f\omega^2 h^2 & -\alpha_f 2\varepsilon\omega h & -\alpha_m \end{pmatrix} \tag{6.23}$$

These developments lead to the definition of the amplification matrix $\mathbf{A}$ as:

$$\mathbf{x}_{n+1} = \mathbf{A}\mathbf{x}_n = \mathbf{A}^{n+1}\mathbf{x}_0 \quad \text{with} \quad \mathbf{A} = \mathbf{E}^{-1}\mathbf{B} \tag{6.24}$$

The level of dissipation in the solver and its distribution on the frequency ranges are then evaluated by computing the spectral radius ρ defined as:

$$\rho = \max(|\lambda_1|, |\lambda_2|, |\lambda_3|) \tag{6.25}$$

where the λ_i $(i = 1, 2, 3)$ are the eigenvalues of the amplification matrix $\mathbf{A}$ of the system. A value of spectral radius ρ smaller than 1 is an indicator of the presence of dissipation, the smaller the spectral radius, the higher the dissipation.

In order to avoid inverting the matrix $\mathbf{E}$, the eigenvalues of the amplification matrix $\mathbf{A}$ are obtained knowing that the roots of $\det|\mathbf{A}-\lambda\mathbf{I}|$ are the same as those of $\det|\mathbf{B}-\lambda\,\mathbf{E}|$ [34]. After calculations, the following characteristic equation which possesses three roots λ_1, λ_2 and λ_3 is found:

$$\begin{aligned}\det|\mathbf{B}-\lambda\,\mathbf{E}| &= -(1-\lambda)^2[\alpha_m+\lambda(1-\alpha_m)]\\ &\quad +\omega^2h^2[\alpha_f+\lambda(1-\alpha_f)][(1-\lambda)(0.5-\beta+\lambda\beta)-(1-\gamma+\lambda\gamma)]\\ &\quad +2\varepsilon\omega h[\alpha_f+\lambda(1-\alpha_f)](1-\gamma+\lambda\gamma)(1-\lambda)\end{aligned} \tag{6.26}$$

6.2.2 Analytical solution

The amplification matrix $\mathbf{A}$ calculated with the generalised-α method based on Eq. (6.24) can be compared to its exact expression $\mathbf{A}^{exact}$ since the equation of motion Eq. (6.19) possesses an analytical solution. The goal is then to find $\mathbf{A}^{exact}$ such that:

$$\begin{pmatrix} q_{n+1} \\ h\dot{q}_{n+1}\end{pmatrix} = \mathbf{A}^{exact}(h,\omega,\varepsilon)\begin{pmatrix} q_n \\ h\dot{q}_n\end{pmatrix} \tag{6.27}$$

In the case of an underdamped motion ($\varepsilon<1$), the solution of Eq. (6.19) has the following form:

$$q_{n+1} = e^{-\varepsilon\omega h}(C_1\cos\omega_d h + C_2\sin\omega_d h) \tag{6.28}$$

with the following parameters:

$$\omega_d = \omega\sqrt{1-\varepsilon^2} \tag{6.29}$$

$$C_1 = q_n \tag{6.30}$$

$$C_2 = \frac{1}{\omega\sqrt{1-\varepsilon^2}}(\dot{q}_n+\varepsilon\omega q_n) \tag{6.31}$$

After some calculations, the four components of the matrix $\mathbf{A}^{exact}$ are found:

$$A_{11}^{exact} = e^{-\varepsilon\omega h}\left[\cos(\omega h\sqrt{1-\varepsilon^2})+\frac{\varepsilon\sin(\omega h\sqrt{1-\varepsilon^2})}{\sqrt{1-\varepsilon^2}}\right] \tag{6.32}$$

$$A_{12}^{exact} = e^{-\varepsilon\omega h}\frac{\sin(\omega h\sqrt{1-\varepsilon^2})}{\omega h\sqrt{1-\varepsilon^2}} \tag{6.33}$$

$$A_{21}^{exact} = -e^{-\varepsilon\omega h}\frac{\omega h\sin(\omega h\sqrt{1-\varepsilon^2})}{\sqrt{1-\varepsilon^2}} \tag{6.34}$$

$$A_{22}^{exact} = e^{-\varepsilon\omega h}\left[\cos(\omega h\sqrt{1-\varepsilon^2})-\frac{\varepsilon\sin(\omega h\sqrt{1-\varepsilon^2})}{\sqrt{1-\varepsilon^2}}\right] \tag{6.35}$$

In the particular case where the structural damping is equal to $\varepsilon=1$, which corresponds to a critically damped motion, the solution of the equation of motion is:

$$q_{n+1} = e^{-\varepsilon\omega h}(C_1+C_2h) \tag{6.36}$$

with the two constants:

$$C_1 = q_n \tag{6.37}$$

$$C_2 = \dot{q}_n+\omega q_n \tag{6.38}$$

Thus, the components of the new analytical amplification matrix $\mathbf{A}_{\varepsilon=1}^{exact}$ are the following:

$$\mathbf{A}_{\varepsilon=1}^{exact} = e^{-\varepsilon\omega h}\begin{pmatrix}1+\omega h & 1\\ -\omega^2h^2 & 1-2\varepsilon\omega h+\omega h\end{pmatrix} \tag{6.39}$$

These two matrices are characterised by two eigenvalues. The spectral radius of the analytical solution is then given by:

$$\rho = \max(|\lambda_1|, |\lambda_2|) \tag{6.40}$$

Its evolution with respect to the dimensionless product ωh, as well as the evolution of the numerical spectral radius obtained previously, will be studied and compared for several values of the structural damping ε in the following section.

6.2.3 Comparison between the analytical and numerical solutions

In the model of a structure, the frequency content can be commonly divided into three parts. The first one contains the low-frequency domain defined as $\omega h \lesssim 0.5$. In this range of the spectrum, the numerical simulation should be accurate in order to have a good representation of the physical behaviour. It implies that the damping introduced in the model should represent a good approximation of the physical damping. The second part corresponds to the high-frequency domain such that $\omega h \gtrsim 2$. In this case, some dissipation is desirable for purely numerical reasons, since it guarantees the convergence of the solver and improves the accuracy of the numerical solution by removing the poorly represented high-frequency modes. Finally, the last part contains the intermediate frequencies for which a reasonable compromise must be found between the two previous constraints to ensure a smooth transition between the low- and high-frequency domains.

In order to determine how the evolution of the spectral radius is affected by the structural and numerical dampings in the mass – spring – damper system, the numerical and the analytical amplification matrices, defined in Sections 6.2.1 and 6.2.2 respectively, are computed for several combinations of the damping parameters. The resulting spectral radii are given in Figure 6.2.

It can be seen in Figure 6.2a that when no structural damping ($\varepsilon = 0$) is present in the model, the analytical spectral radius stays obviously equal to unity over the whole frequency domain and this behaviour is numerically recovered when there is no numerical damping ($\rho_\infty = 1$). Furthermore, this figure also highlights the previously exposed characteristics of the generalised-α method: the numerical dissipation is active in the high-frequency domain and the spectral radius converges towards the imposed value ρ_∞, while the impact on the low-frequency content is minimised.

If some structural damping ε is now introduced (Figures 6.2b to 6.2d), the comparison between the analytical and numerical spectral radii is divided into the three previously mentioned parts. In the low-frequency domain, the numerical curves first coincide with the analytical one as required. The curves tend to remain superimposed on a larger frequency range when the structural damping is high and the numerical damping is low. In the high-frequency domain, the curves clearly diverge, but most importantly, in the numerical model, the structural damping cannot provide the desired dissipation properties in this part of the spectrum. Finally, the transition between these two ranges is smoother when the structural damping remains low.

It can be observed that the curve related to $\rho_\infty = 0$ is the only one to converge towards the analytical solution at high frequencies. However, other values of ρ_∞ smaller than 1 are also acceptable since accuracy is not sought in this part of the domain. Indeed, the most important point is the presence of dissipation to ensure the convergence of the numerical response.

To conclude, in order to have a valid numerical solution, a correct representation of the structural damping is needed in the low-frequency range and some numerical damping should be introduced to filter the undesired high-frequency spurious modes. These conclusions concern a simple yet representative linear problem, while in tape springs, the nonlinearities give rise to

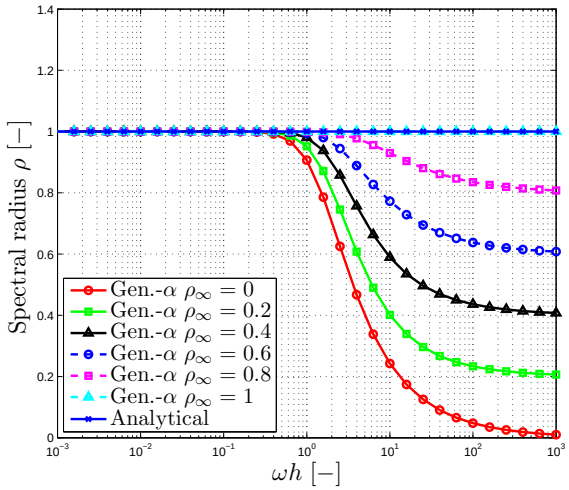

(a) Damping parameters: $\varepsilon = 0, 0 \leq \rho_\infty \leq 1$

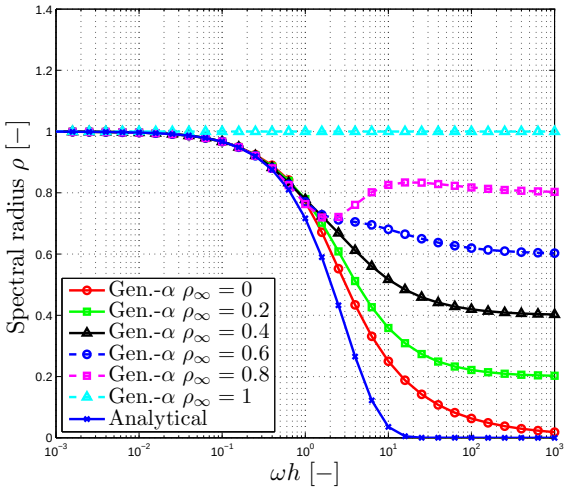

(b) Damping parameters: $\varepsilon = 1/3, 0 \leq \rho_\infty \leq 1$

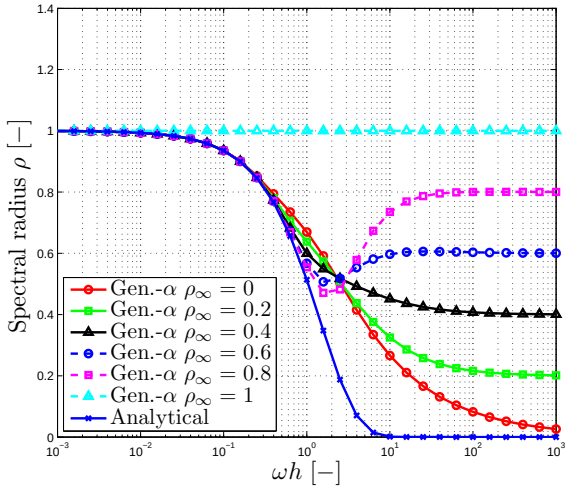

(c) Damping parameters: $\varepsilon = 2/3, 0 \leq \rho_\infty \leq 1$.

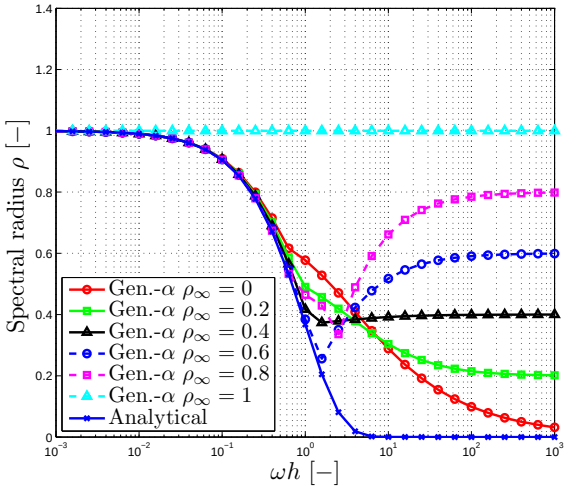

(d) Damping parameters: $\varepsilon = 1, 0 \leq \rho_\infty \leq 1$.

Figure 6.2: Evolution of the spectral radius ρ in the analytical solution and the generalised-α method for several combinations of the structural damping ε and the numerical damping ρ_∞.

more complex behaviours such as couplings and transfers of energy between the low and high frequencies. The objective of the following section is then to extend this analysis to the numerical and structural dampings in tape springs based on finite element simulations.

6.3 Dynamic behaviour of tape springs

In order to understand the importance of the structural damping in the finite element models of tape springs, let us start by recalling the results obtained by Hoffait *et al.* [41]. In this work, the dynamic deployment of a MAEVA hinge is simulated and detailed analyses are dedicated to the understanding of the hysteresis and self-locking phenomena. This type of hinge is composed of three tape springs with alternate orientations as illustrated in Figure 1.4. It implies that when the hinge is bent, at least one tape spring is always folded in opposite sense. The dynamic simulations were performed with the generalised-α method, a numerical damping fixed to $\rho_\infty = 0.9$ and no structural damping.

During a deployment sequence, the relationship between the bending moment and the rotation angle follows successively the evolutions given in Figures 6.3a to 6.3c. Figure 6.3a shows the initial quasi-static folding of the hinge in order to reach the sought deformed configuration with one tape spring folded in opposite sense and two in equal sense, then the deployment and the first backwards motion until a zero rotation angle is reached. Starting from this last point, Figure 6.3b shows the folding of the hinge in the other direction leading to two folds in opposite sense and a single one in equal sense and the subsequent unfolding. Finally, Figure 6.3c shows a new cycle with the same folded configuration as initially. In each figure, the hysteresis phenomenon is visible by the non-superposition of the loading and unloading curves. It implies that some dissipation occurs each time that the folds disappear, the decrease of energy corresponding to the difference of area under the folding and unfolding curves. It can be expected from the analyses performed in Chapter 3 that the main contributions to the dissipation are due to the formation and the disappearance of the folds in opposite sense.

On the associated energy curves of the system (Figure 6.3d), it can be seen that the total energy drops when the kinetic energy is at its highest and the potential energy at its lowest, which corresponds to a zero rotation angle of the hinge. Hoffait *et al.* showed that these decreases of energy are directly due to the hysteresis phenomena encountered during the hinge deployment. In the end, as the motion amplitude decreases, the dissipation leads to the self-locking of the hinge.

In order to show the necessity of introducing some structural damping in the models, the results obtained by Hoffait *et al.* are completed by simulating the deployment of a single tape spring under specific conditions. The simulation is first performed with numerical damping only, then a representation of the structural damping is added.

The finite element model consists of a single tape spring defined by the geometric and material characteristics given in Tables 6.1 and 2.2 and illustrated in Figure 6.4. The same boundary conditions as those used in the optimisation procedure of the reflector (Section 4.2.1) are defined: one extremity is clamped, the other one is rigidly connected to a lumped mass of 0.5 kg and the displacements are blocked along the tape spring median. Regarding the simulation, starting from its unfolded configuration, the tape spring is quasi-statically bent until a 60°-angle in opposite sense is reached, then this rotation constraint is released and the structure is left free to oscillate for 80 s.

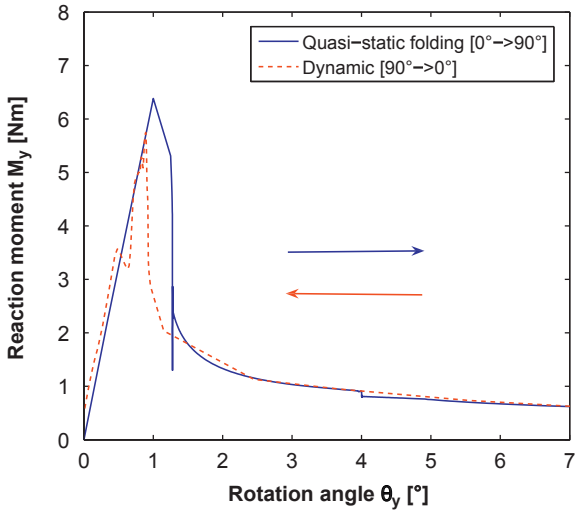

(a) Quasi-static folding (→) and first part of the dynamic deployment (←). Simulation time: folding 0 to 100 s, deployment 100 to ∼ 102 s.

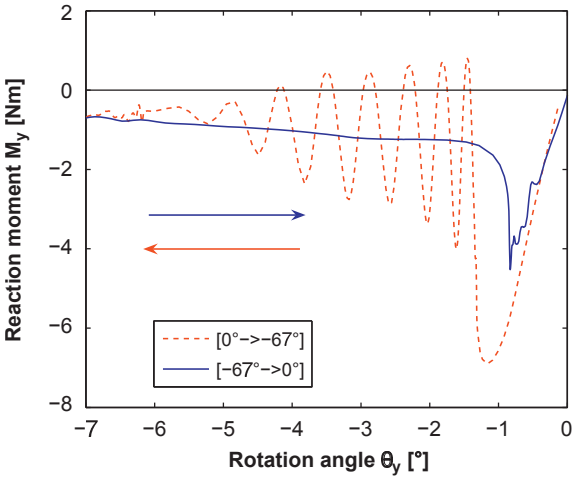

(b) Second part of the deployment: folding (←) and unfolding (→). Simulation time: ∼ 102 to ∼ 105.5 s.

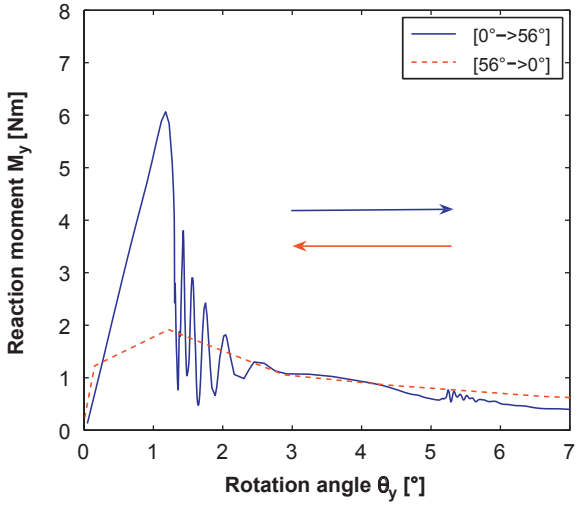

(c) Third part of the deployment: folding (→) and unfolding (←). Simulation time: ∼ 105.5 to ∼ 109 s.

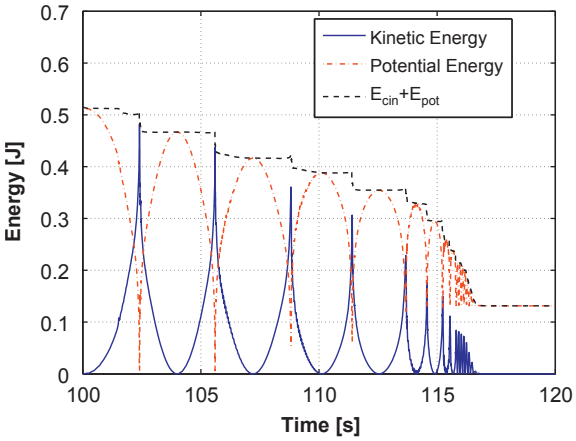

(d) Evolution of the kinetic, potential and total energies during the deployment.

Figure 6.3: Results obtained by Hoffait *et al.* [41] on the deployment of the MAEVA hinge.

L	t	α	R
400 mm	0.1 mm	$\pi/2$ rad	20 mm

Table 6.1: Geometric characteristics.

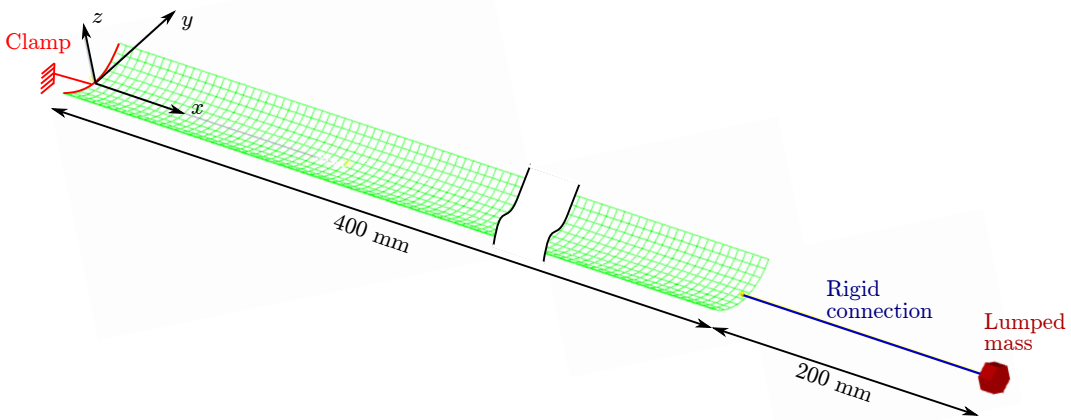

Figure 6.4: Finite element model used to identify the impact of the numerical and structural dampings.

6.3.1 Impact of the numerical damping

When some numerical damping is present in the model ($0 \leq \rho_\infty < 1$), but no physical damping is included, the bending moment behaves as illustrated in Figure 6.5a. In that case, as already shown qualitatively in Section 2.2.3 and represented quantitatively in Figure 6.5b, it can be seen that in the quasi-static part spanning from 0 to 60 s, the numerical damping has almost no impact on the value of the peak moment $M_+^{\max}$ and the residual moment M_+^*. However, a reduction of the numerical damping implies longer periods of artificial oscillations after the buckling around 10.4 s (Figure 6.5c, first plot). Between the two extreme situations corresponding to $\rho_\infty = 0$ and $\rho_\infty = 0.8$, an increase in time of 24.83 % is noticed for these oscillations. It was considered that the artificial oscillations are damped out when the bending moment reaches values smaller than 10 % of the residual bending moment in opposite sense. In the case $\rho_\infty = 0.8$, the associated results were obtained after a CPU time of 153 hours[1] (Figure 6.5c, second plot), therefore simulations for which $\rho_\infty > 0.8$ were not performed.

In the dynamic part of the simulation (from 60 to 140 s), the deployment of the tape spring leads to large asymmetric oscillations submitted to very low damping whatever the chosen value of ρ_∞ (Figure 6.5a). On that same figure, it can be seen that the limits defined by the quasi-static peak moments $M_+^{\max}$ and $M_-^{\max}$ are both exceeded. In order to check whether this leads to the formation of folds in the dynamic response, the flattening of the cross-sections is analysed at each time step by computing their curvature. A fold is then considered created when the curvature of one of the cross-sections is lower than 10^{-2} mm^{-1} which is the value reached at the beginning of the buckling in the quasi-static part. The folded configuration is such that there is never more than one fold in the structure at a given time. The results are represented in Figure 6.5d which shows the evolution of the vertical displacement at the tip of the tape spring during deployment starting from the folded configuration. Superimposed to the black curve, a dot marking the presence or absence of fold is drawn for each time step. It can be seen that, during the oscillations, red dots are only associated with positive vertical displacements (the orientation of the reference coordinate system is illustrated in Figure 6.4), which means that the formation of folds only occurs in the equal sense.

[1] on a computer with 16 GB of RAM and quad core processors Intel(R) Core(TM) i7-2600 CPU (3.40 Hz) running Windows 7.

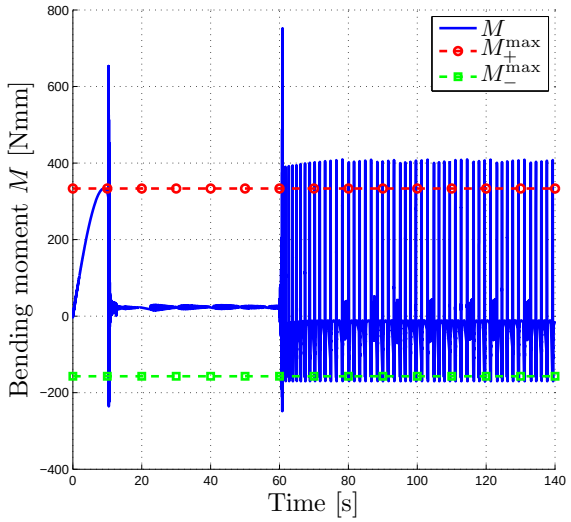

(a) Evolution of the bending moment with $\rho_\infty = 0.2$ and $\varepsilon = 0$.

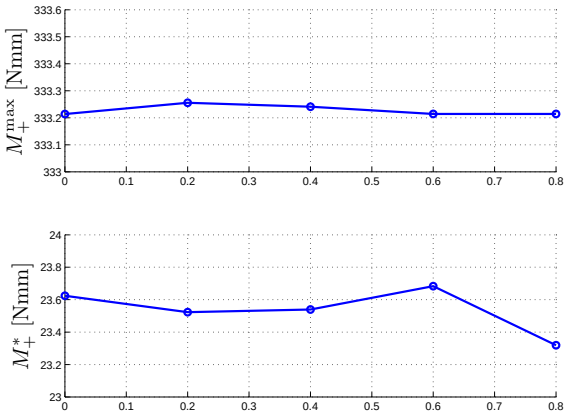

(b) Peak moment $M_+^{\max}$ and residual moment M_+^* with respect to the numerical damping ρ_∞.

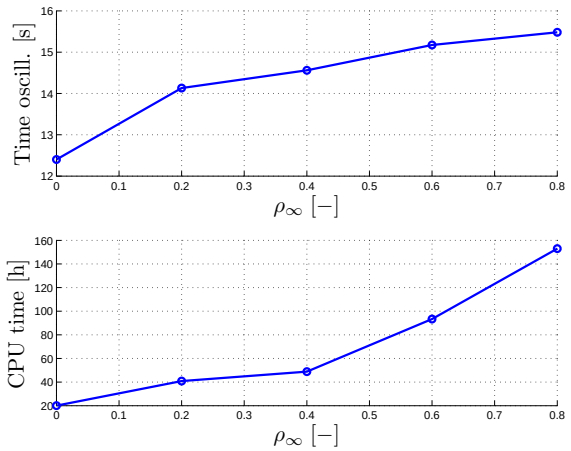

(c) Time at which the oscillations after buckling are damped out and CPU time with respect to the numerical damping ρ_∞.

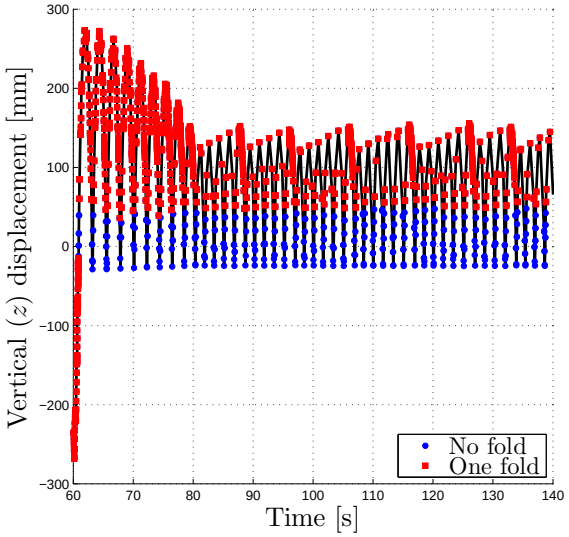

(d) Vertical displacement of the tip of the tape spring with $\rho_\infty = 0.2$ and existence of folds.

Figure 6.5: Impact of the numerical damping ρ_∞ on the dynamic behaviour of tape springs.

Thus, compared to what was obtained by Hoffait *et al.*, the dissipation by hysteresis is inexistent in the dynamic response of the considered model since the motion of the tape spring does not lead to the formation of folds in opposite sense and, for those in equal sense, the loading and unloading curves are superimposed due to the locking of the median transverse displacements. Tape springs with a very low dissipation due to hysteresis are not unrealistic cases. As a reminder, this type of behaviour was observed for specific geometries of tape springs where the transversal displacements of the median were not blocked as it was shown in Figures 3.3a and 3.8a. So, despite the presence of numerical damping, the model cannot predict the stabilisation of the tape spring in the equilibrium state and thus contradicts the experimental results.

It can then be concluded that the numerical damping alone is not always sufficient to develop realistic models as they do not reproduce all the inherent dissipation phenomena that are observed experimentally [94].

6.3.2 Impact of the structural damping

Some structural damping is now added in the finite element model described in Figure 6.4. In order to keep the simulations as simple as possible, the dissipation is represented by a Kelvin-Voigt material model characterised by a viscosity coefficient η and introduced in Chapter 5.

The evolution of the bending moment during the folding and the deployment is given in Figure 6.6a for $\rho_\infty = 0.2$ and $\eta = 10^{-3}$ s. For information, the viscous parameter given here is the one introduced in the SAMCEF software which is normalised by the Young's modulus. Compared to the previous situations without any structural damping, the following elements are noticeable. First, the peak moment $M_+^{\max}$ is barely affected (Figure 6.6b, first plot). Then, right after buckling, the amplitude of the oscillations is much smaller, as well as their duration which is quasi independent from the numerical damping (Figure 6.6c, first plot). After the stabilisation in the folded state, the residual moment M_+^* has a better convergence and is also less dependent on the numerical damping (Figure 6.6b, second plot).

In the dynamic part, the oscillations after deployment are damped out and, although their duration naturally increases when the numerical damping decreases (Figure 6.6c, second plot), the difference between the extreme values of ρ_∞ is only of 9.4 %. The time at which the oscillations are damped out is still defined as the time at which the bending moment reaches values smaller than 10 % of the residual moment in opposite sense. Finally, as it was the case in the previous section, the limits defined by the peak moments $M_+^{\max}$ and $M_-^{\max}$ are both overshot, but only folds in the equal sense bending are formed as it can be seen in Figure 6.6d. Hysteresis dissipation is then again absent. The stabilisation of the motion can then be attributed to the presence of structural damping in the model.

The dynamic response can be divided into two parts based on the evolution of the bending moment. First, from 60 to $\sim$ 80 s (Figure 6.6a), the presence of structural damping during the formation of folds in equal sense leads to a nonlinear damping of the asymmetric oscillations. On the evolution of the vertical tip displacement of the tape spring (Figure 6.6d), it can be seen that the identification procedure only detects folds leading to the complete transverse flattening of the tape spring up to 75 s. Between 75 and 80 s, the presence of partially formed folds was confirmed visually. The behaviour of the tape spring can then be considered as linear after 80 s. In that case, the oscillations are symmetric with an exponential decrease due to the choice of the structural damping model. In the end, the presence of structural damping leads to the stabilisation of the structure in its fully deployed state as expected in experimental applications.

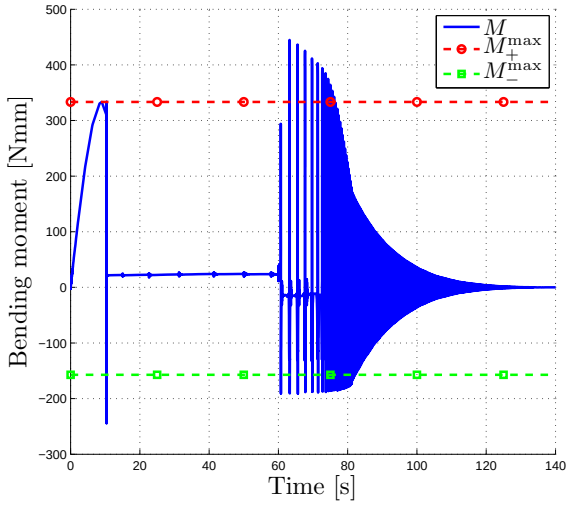

(a) Evolution of the bending moment with $\rho_\infty = 0.2$ and $\eta = 10^{-3}$ s.

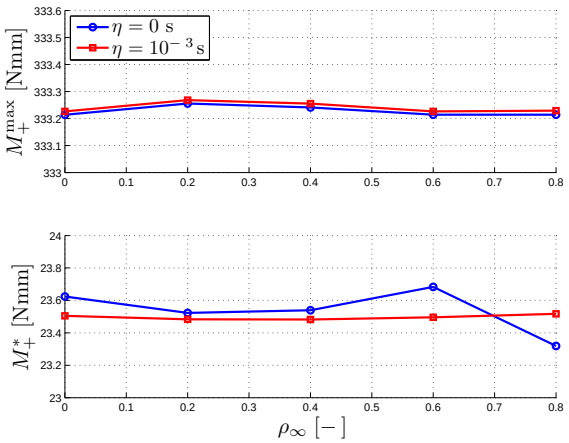

(b) Peak moment $M_+^{\max}$ and residual moment M_+^* with respect to the numerical damping ρ_∞.

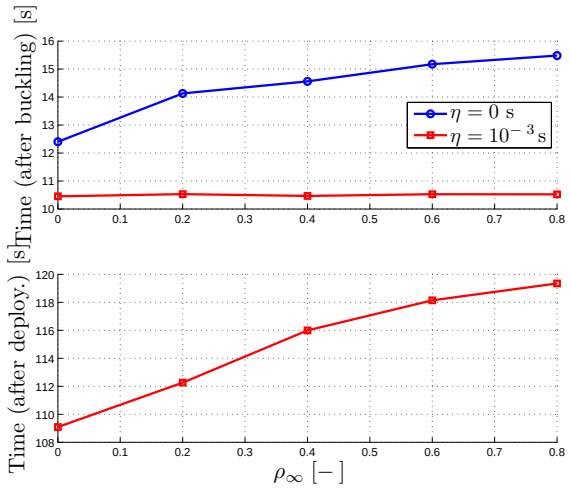

(c) Time at which the oscillations are damped out after buckling and after deployment.

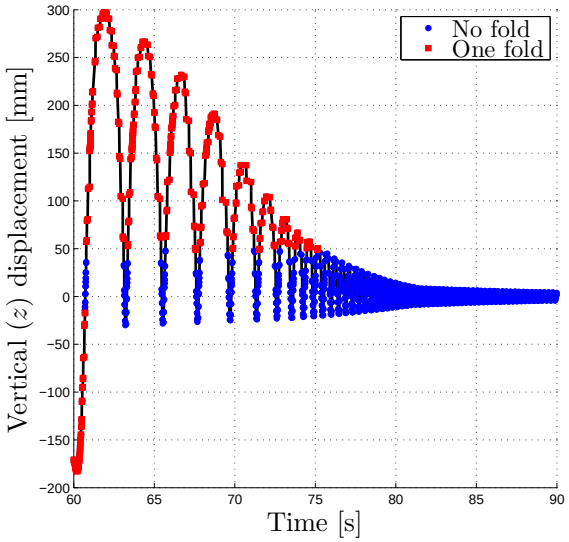

(d) Vertical displacement of the tip of the tape spring with $\rho_\infty = 0.2$ and $\eta = 10^{-3}$ s and existence of folds.

Figure 6.6: Impact of the numerical damping ρ_∞ and the structural damping ε on the dynamic behaviour of tape springs.

6.4 Summary

Based on a simple one-degree-of-freedom system, the impact of the numerical and the structural dampings are investigated in the generalised-α method. The numerical damping introduces some dissipation in the high-frequency domain. Thus, it guarantees the convergence of the solver and a solution that is unaffected by the poorly represented modes in this domain. On the other hand, the structural damping is dominant in the low-frequency domain and is required to have a good representation of the real damping and of the physical behaviour of the system but, in finite element models, it does not contribute to the dissipation of the high-frequency modes. Both numerical and structural dampings are thus needed for a reliable simulation.

Regarding the dynamic behaviour of tape springs, some structural damping is introduced in the finite element model by the means of a Kelvin-Voigt material model. It is shown that the presence of structural damping allows reducing the dependence of the characteristic features to the amount of numerical damping. Furthermore, it ensures a correct representation of the damping of the physical oscillations after deployment leading thus to a fully deployed state, as observed experimentally.

CHAPTER 7

DESIGN OF AN EXPERIMENTAL SET-UP

So far, the general behaviour of tape springs has been studied based on analytical models in Chapter 2 and more detailed quasi-static and modal analyses in Chapter 3. An application in Chapter 4 led to the conclusion that structural damping should be included in the model to represent the dynamic response, which was confirmed by the detailed dynamic analyses performed in Chapter 6. The next step is then the design of an experimental set-up in order to investigate the nonlinear phenomena inherent to tape springs such as buckling, the formation of folds and the dissipation by hysteresis, and to experimentally evaluate the structural damping.

In this chapter, the design process of the experimental set-up is explained, then the acquisition equipment is described and compared to those used by other authors, finally the different types of damping exposed in Chapter 5 are particularised to the present case.

7.1 Geometric characteristics

The proposed experimental set-up is schematically illustrated in Figure 7.1. A dummy appendix is connected to the fixation support by two tape springs which are cut out from a common measuring tape of the brand STANLEY® (Figure 7.2). They have the same orientation so that the initial bending prior to deployment can be performed in opposite or equal sense by turning upside down the whole block composed of the tape springs, the interfaces, the rod and the dummy appendix. Furthermore, using two tape springs allows limiting the impact of torsion while keeping the structure quite simple, as it was shown in the simulation of the deployable reflector (Chapter 4). Each extremity of the tape springs is clamped by interfaces composed of two complementary parts with curved regions fitting the geometry of the tape springs (Figure 7.3).

The different geometric characteristics of the tape springs are given in Table 7.1. Only the length L, the thickness t, the width w and the height h were physically measured using a calliper, while the subtended angle α and the radius of curvature R were recovered with the help of simple trigonometric equations. Regarding the length L, the given value corresponds to the distance between the two interfaces (Figure 7.1b), that is without the parts of the tape springs clamped in the interfaces.

L [mm]	t [mm]	w [mm]	h [mm]	α [deg]	R [mm]
100	0.14	17.8	2.8	69.85	15.55

Table 7.1: Geometric characteristics of the tape springs used in the experimental set-up.

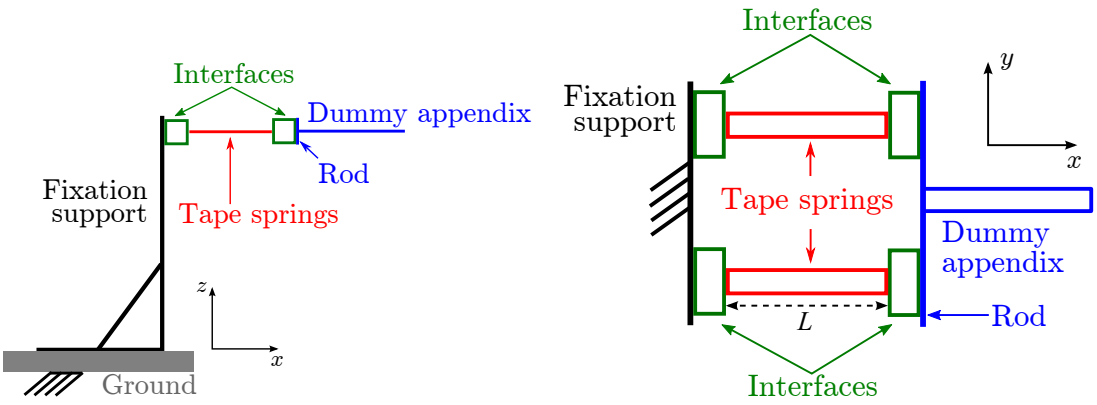

(a) Side view. (b) Top view.

Figure 7.1: Schematic representation of the experimental set-up.

Figure 7.2: Measuring tape STANLEY® FatMax 5 m.

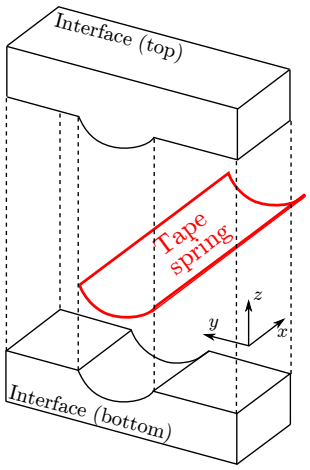

Figure 7.3: Exploded view of the interface.

7.2 Determination of the maximum mass at the free end

One objective of this work is to study the folding followed by the autonomous deployment of the appendix despite the presence of the gravity field. It implies that, when designing the experimental set-up, one must ensure that the mass at the free end (the combination of two interfaces, the rod and the dummy appendix) is limited in order to respect two constraints. First of all, the structure cannot buckle under its own weight, and secondly, when initially folded downwards, the residual moment in the tape springs must be able to passively deploy the structure against gravity until the equilibrium state is recovered, whatever the initial sense of bending. As it can be deduced from the quasi-static relationship between the bending angle θ and the resulting bending moment M (Figure 2.1), the second constraint is the most restrictive one since $|M^*| < |M^{\max}|$. Furthermore, as explained previously, the amplitude of the residual moment is smaller in equal sense ($|M^*_-| < |M^*_+|$). It implies then that in order to use the same set-up in both senses, the maximum mass is constrained by the low value of the residual moment in equal sense bending.

The determination of this maximum mass is complicated by the existence of uncertainties affecting the values of the thickness t and the Young's modulus E. Indeed, regarding only the thickness t, its size is one to three orders of magnitude smaller than all the other dimensions of the tape springs, which limits the accuracy of the value given in Table 7.1 as it was measured with a calliper. But most importantly for both the thickness t and the Young's modulus E, the main source of uncertainties comes from the fact that the tape springs are cut out from a common measuring tape which is made of a metallic layer covered by a wear resistant yellow coating and surrounded on both faces by protective layers of transparent plastic. The material properties of this composite are then hard to assess. Furthermore, the distribution of the thickness is not necessarily constant along the length and the width of the tape spring. A measurement of an uneven distribution of thickness can be found in [58] for tape springs manufactured with a single polymeric material.

The characterisation of an equivalent thickness and Young's modulus is postponed to Section 8.2. Thus, during the design phase of the experimental set-up, some uncertainties were taken into account in order to evaluate the maximum mass allowing a passive deployment and parametric analyses were performed to characterise the impact of the thickness and the Young's modulus on the value of this mass.

Based on a simple finite element model composed of two tape springs under gravity acceleration, the residual moment M^* can be evaluated at an angle of $\theta = 90°$. This angle is expected to be the initial bending angle in the experimental tests and, in that case, it is also the one which leads to the lowest value of the residual moment M^* as it either stays constant or slightly decreases after buckling. On the other hand, the moment due to gravity, which has to be counteracted, is the highest when the tape springs are close to their deployed configuration and is then equal to mgl. A passive deployment is then certainly possible if the following inequality is respected:

$$M^*(\theta = 90°) > mgl \tag{7.1}$$

where m is the mass, g is the gravity and l is the lever arm between the folds in the tape springs and the centre of mass of the mass. As a first estimation, the mass is considered as fixed at the tip of the tape springs and the folds are assumed to be located in the middle of the tape springs leading to $l = L/2$. The maximum masses respecting the inequality are then given in Figure 7.4a for the opposite sense and in Figure 7.4b for the equal sense for different combinations of the thickness t and the Young's modulus E.

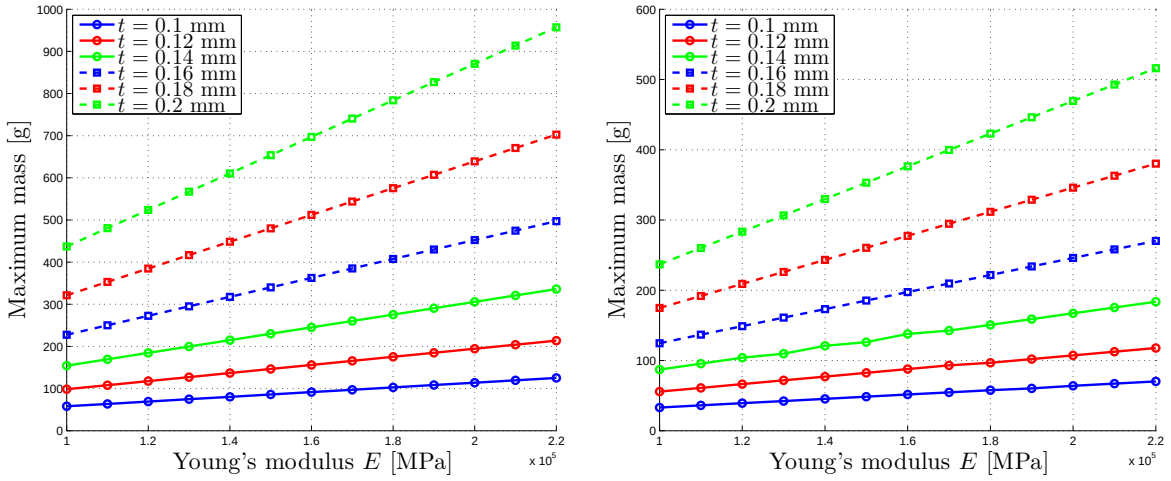

(a) Starting with an initial folding in opposite sense.

(b) Starting with an initial folding in equal sense.

Figure 7.4: Maximum masses allowing a passive deployment.

As anticipated, the larger these parameters, the larger the mass allowing a passive deployment. Furthermore, the residual moments and therefore the masses are proportional to t^3 for a fixed Young's modulus and linear with respect to E for a fixed thickness as expected from the simplified expressions of the residual moments Eqs. (2.2) and (2.3) and [94]. For these parametric studies, instead of solving several finite element models, the simplified expressions of $M_{\pm}^{*}$ could have been exploited as a first approximation. However, compared to the finite element results, they lead to larger admissible masses by up to ~ 9 % in both senses, except for small thicknesses and Young's moduli in equal sense where decreases of up to 3.3 % are noticed. The use of finite element models was then preferred to improve the accuracy of the results.

Starting from these values and iterating on the design of the set-up, the lever arm is re-evaluated and the mass is adjusted accordingly. In the end, the set-up described in the following section is obtained.

7.3 Experimental set-up

According to the previous analysis, the interfaces, the rod and the dummy appendix are designed as light as possible. This objective is achieved by drilling holes in the rod and the dummy appendix, while two types of interfaces are used. On the side of the fixation support, the interfaces are larger and thicker to ensure rigid links and an easy connection with the support. On the other side, to reduce the mass, the interfaces are clamped around the tape springs by means of only one screw going through the tape springs. The resulting experimental set-up is visible in Figure 7.5 where the total mass at the free end reaches 77 g. Its exploded view is given in Figure 7.6.

The deployed configurations of the experimental set-up are given in Figures 7.5 and 7.7 for an initial folding in opposite and equal sense respectively. Compared to each other, the whole block composed of the four interfaces, the two tape springs, the rod and the dummy appendix is just turned upside down in order to start with a downwards initial folded configuration deploying against gravity in both cases.

The orientation of the y and z-axes is different according to the initial folded configuration in opposite (Figure 7.5) or equal sense (Figure 7.7). Thus, the experimental evolution of the bending angle measured positively about the y-axis respects the sign convention defined in Section 2.1.1,

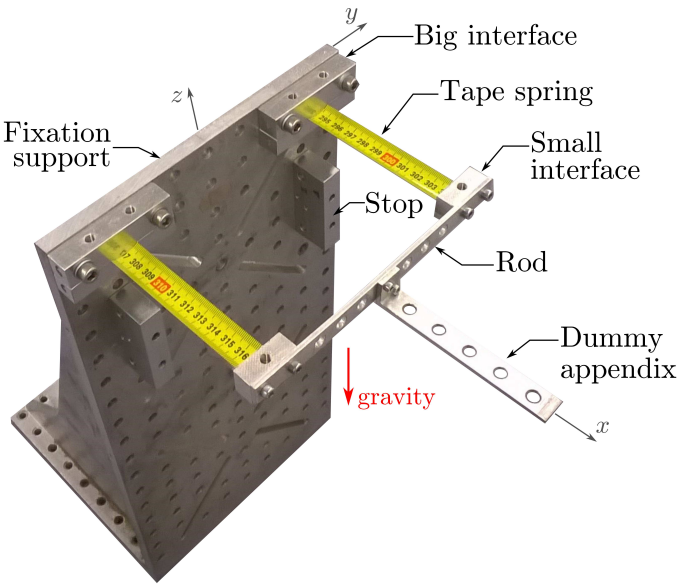

Figure 7.5: Experimental set-up.

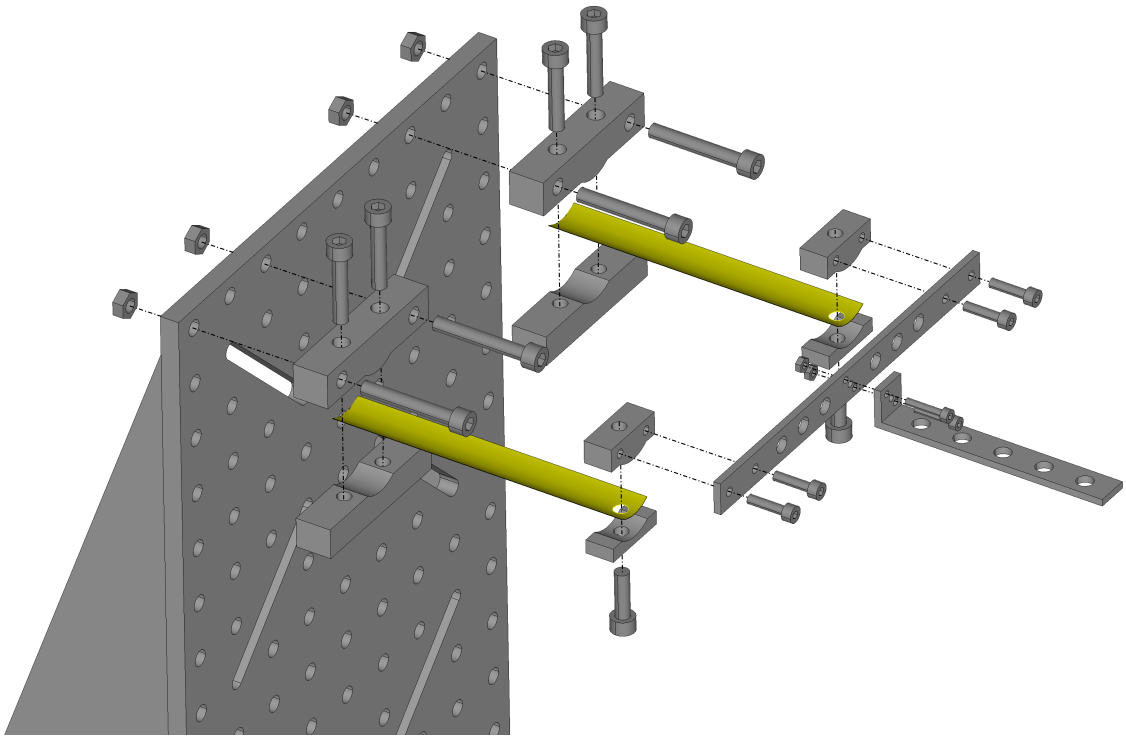

Figure 7.6: Exploded view of the experimental set-up.

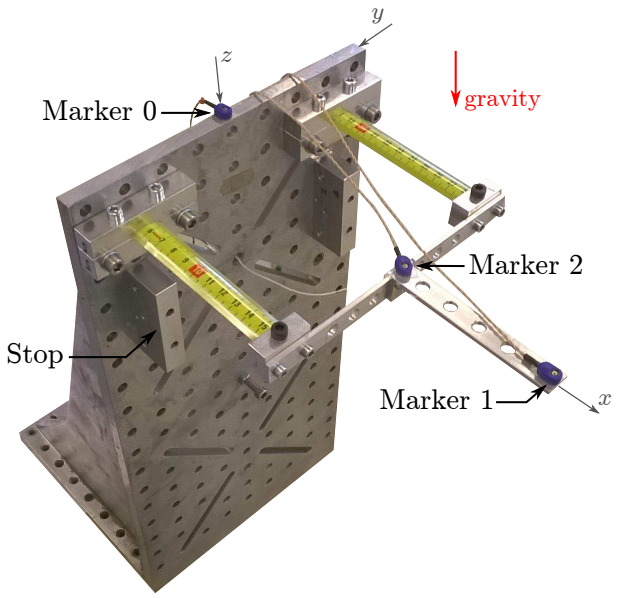

Figure 7.7: Deployed configuration of the experimental set-up in equal sense.

a positive bending angle being associated to folds in opposite sense and a negative bending angle being associated to folds in equal sense. Furthermore, the nominal positions of the markers are given in Figure 7.7 where they are located on the top of the fixation support, at the tip of the dummy appendix and in the middle of the rod. Experimental tests which require a different number of markers or a different layout will be specified in their dedicated sections.

7.4 Acquisition equipment

In this work, the position of active markers fixed on the deployable structure is captured by the means of a 3D motion analysis system from Codamotion [25] (Figure 7.8a). Each CX1 unit, located around the set-up, is able to triangulate the position of the markers as they combine three sensing arrays. Even though one unit would be sufficient, the four at our disposal are used to improve the accuracy which reaches 0.05 mm for the standard deviation in position along the longitudinal and vertical axes and 0.3 mm along the transversal axis when the distance between the markers and scanners is below 3 m. Furthermore, the acquisition frequency is fixed to 800 Hz and the real-time latency is below 10 ms.

To complete this system, a force plate from Kistler (Type 9281E) [55] composed of four built-in piezoelectric sensors is located under the fixation support to collect information on the forces and the moments affecting the set-up during its deployment. The acquisitions with the motion system and the force plate are synchronised. The measuring ranges span from -125 N to 125 N along the three axes. The threshold is less than 250 mN, allowing thus accurate measurements even in the case of low loadings, while the acquisition frequency is 1 kHz.

Thus, this acquisition equipment allows collecting experimental data on the set-up in a broad variety of situations such as in dynamic deployments, quasi-static foldings and small vibrations around the equilibrium configuration on both the displacements and the loads. For information, this equipment is normally devoted to human motion analysis at the University of Liège (Figure 7.9), but is used here in a different context (see for example [90] for a more detailed description of the equipment and the analyses performed in the laboratory or the website `http://labos.ulg.ac.be/lamh/`).

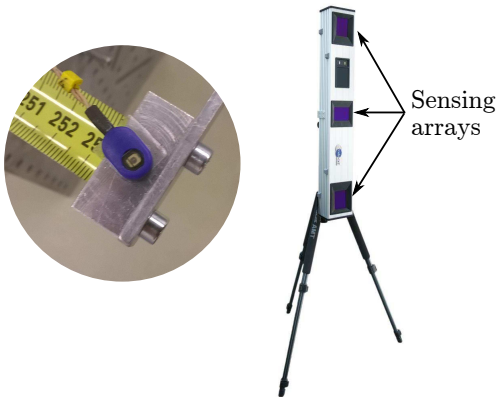

(a) Marker and CX1 scanner from Codamotion [25].

(b) Force plate from Kistler (Type 9281E) [55].

Figure 7.8: Acquisition equipment.

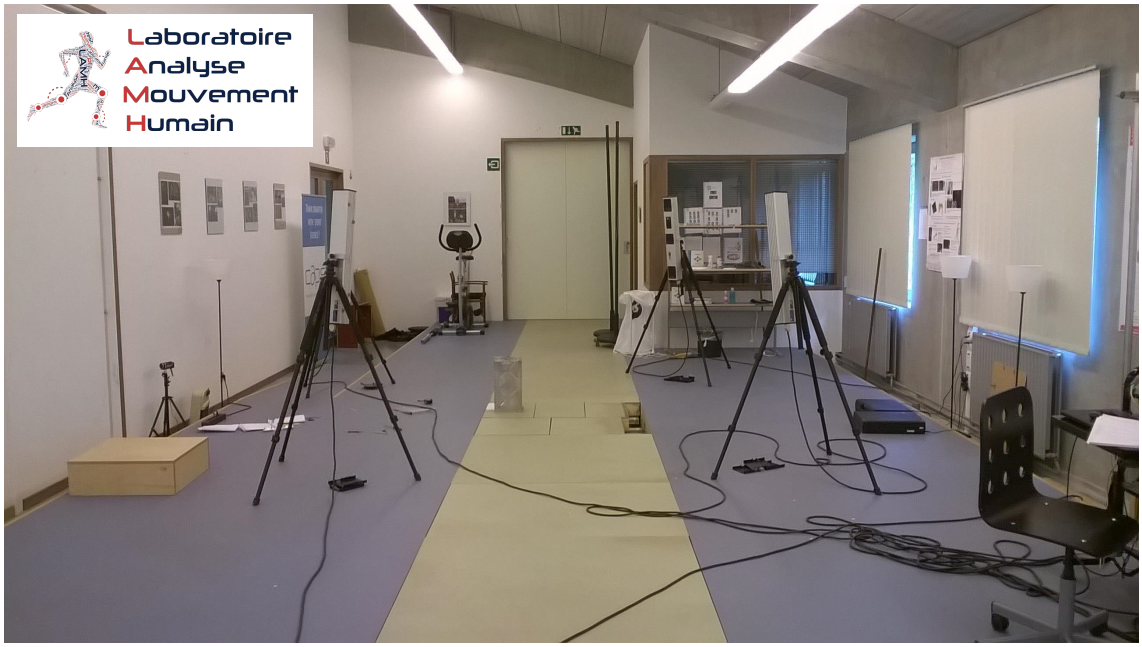

Figure 7.9: Laboratory of Human Motion Analysis at the University of Liège (the force plate is integrated in the floor under the set-up).

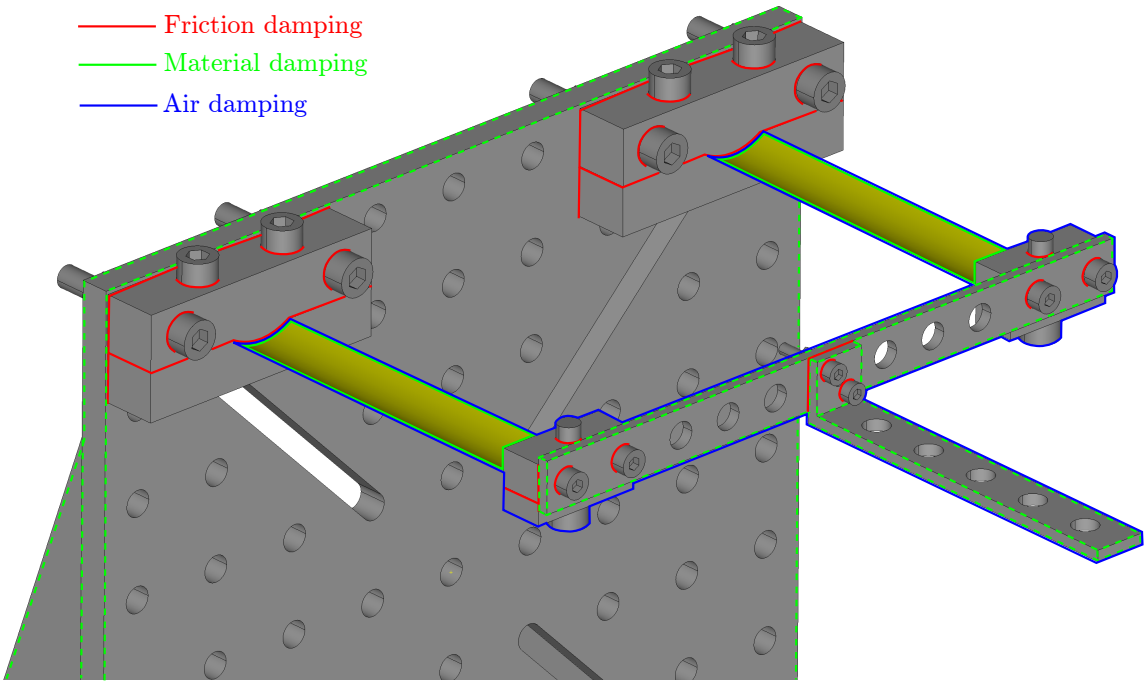

Figure 7.10: Main locations of the different sources of damping on the experimental set-up.

7.5 Damping phenomena present in the set-up

The three damping phenomena described in Chapter 5 are present in the experimental set-up with different levels of impact on the overall motion. The regions of the set-up affected by each type is illustrated in Figure 7.10.

Friction damping is encountered between surfaces in contact: between the different parts of the interfaces, between the fixation support and the big interfaces, between the tape springs and the interfaces, between the rod and the dummy appendix and at each screw. Since in practice these elements are tightly connected, the amount of energy dissipation due to friction is expected to be limited.

Even though every component of the structure is characterised by a certain amount of material damping, the main contribution is expected to be found in the tape springs as they are the most flexible parts and subjected to the largest deformations. At a much lower level, the rod, the dummy appendix and the fixation support also contribute to this type of dissipation. In the interfaces and the screws, material damping is less present due to their small dimensions and high stiffness.

Finally, the experimental tests being performed under atmospheric conditions, air damping affects all the moving parts, the contribution of each one being mainly linked to its surface area normal to the air flow and to the relative velocity of the flow.

7.6 Summary

An experimental set-up is designed in order to investigate the nonlinear phenomena inherent to tape springs. Since they are cut out from a common measuring tape, uncertainties affect the values the Young's modulus and the thickness of the tape springs and the maximum mass allowing a passive deployment is taken into account. The damping phenomena (friction damping,

material damping, air damping) are expected to affect the dynamic response of the set-up.

The acquisition equipment consists of a 3D motion analysis system which triangulates the position of markers on the set-up and of a synchronised force plate capturing the associated forces and moments under the fixation support of the structure.

CHAPTER 8

QUASI-STATIC TESTS

As mentioned in the previous chapter, uncertainties exist on the values of the thickness and the Young's modulus of the tape springs used in the experimental set-up. In order to identify these parameters and develop an accurate finite element model, specific quasi-static experimental tests are performed in this chapter, whereas dynamic tests will be addressed in the next one.

The finite element model used throughout these analyses and in the following chapter is first described. Then, a first simple post-buckling quasi-static test is performed and the experimental results are exploited to determine suitable values for the thickness and the Young's modulus by the means of an optimisation procedure. With these values, the robustness and the predictive capacity of the numerical model is studied for a variety of other quasi-static tests. In each case, the reproducibility of the experimental results is quantified by performing the same tests a large number of times on different tape spring samples.

8.1 Finite element model of the experimental set-up

A finite element model of the experimental set-up is developed in order to reproduce and further investigate quasi-static tests analysed in this chapter and the deployment tests that will be performed in Chapter 9. The characteristics and parameters required to perform both types of tests are given in this section in order to avoid dispersing the informations, even though the dynamic aspects will only be detailed and exploited in the next chapter. Using the commercial software SAMCEF [89], the general model of the experimental set-up illustrated in Figure 8.1 is defined.

The modelling assumptions are the following:

- the tape springs, the rod and the dummy appendix are represented by flexible Mindlin shells characterised by a uniform isotropic material (Section 2.2.1);
- the tape springs, which in reality are multi-layered composites as mentioned in Section 7.2, are simplified as single-layered elements with equivalent thickness and Young's modulus. They are assumed to be characterised by uniform geometric parameters;
- in dynamic analyses, postponed to Chapter 9, the global structural damping of the whole structure is represented by a single equivalent parameter η introduced in the Kelvin-Voigt material model of the tape springs whose impact on finite element models was presented in Chapter 6. Drag effects due to air resistance are included in that parameter as their contribution cannot be precisely separated from the other damping phenomena in the

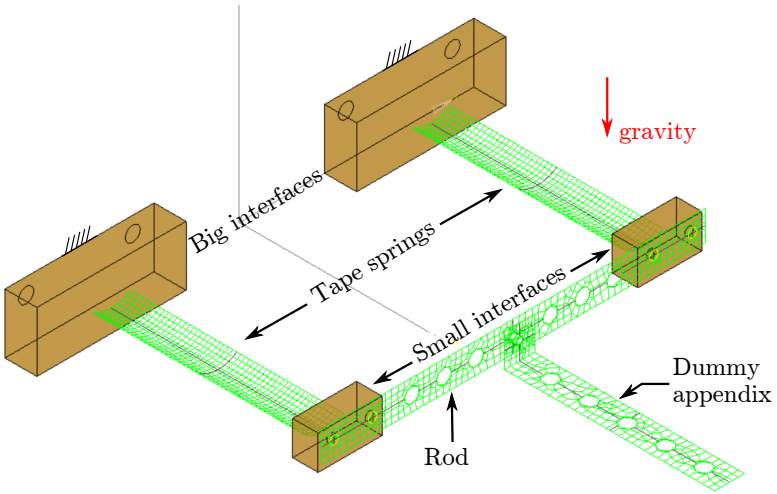

Figure 8.1: General finite element model of the experimental set-up.

present experiments. Nevertheless, the proportion of damping due to the surrounding air will be estimated based on the theoretical model in Eq. (5.4);

- ▷ based on convergence analyses with respect to the mesh size similar to those described in Section 2.2, it is set to 2 mm for the tape springs to accurately capture the large deformations and the nonlinear phenomena, while it is fixed to 3 mm for the rod and the dummy appendix which are expected to be weakly deformed;
- ▷ the four interfaces and their fixation screws are represented by rigid volumes with dimensions corresponding to the interfaces only and characterised by equivalent masses;
- ▷ the connexions at the interfaces and between the rod and the dummy appendix are considered as rigid;
- ▷ the fixation support is not included in the model, implying thus that the structure is assumed to be clamped at the big interfaces;
- ▷ gravity is represented by a global acceleration along the vertical axis applied on the whole model.

Regarding the solver, the second-order accurate generalised-α method is used. The evolution of the time steps is adaptive in order to capture the nonlinear phenomena with precision and to reduce the simulation time otherwise. Finally, the numerical damping defined as the spectral radius at infinite frequencies ρ_∞ is chosen so that its impact on the results is limited, but still allows the solver to converge. It implies that in quasi-static analyses, the model is characterised by a high numerical damping ($\rho_\infty = 0$) as it was concluded from the developments in Sections 2.2.3 and 6.3.1. However, in dynamic analyses, the value of ρ_∞ shall be determined later in Section 9.2.2 in order to limit its impact on the response as it was shown in Section 4.4.

8.2 Identification of the thickness and Young's modulus

8.2.1 Post-buckling tests

Experimental tests The thickness and the Young's modulus are identified based on a configuration of the set-up with two static equilibria: a folded one which characterises the post-buckling behaviour of the tape springs and an unfolded one. For that purpose, an additional weight is fixed to the rod so that, after buckling, the residual moment does not lead to a passive deployment and

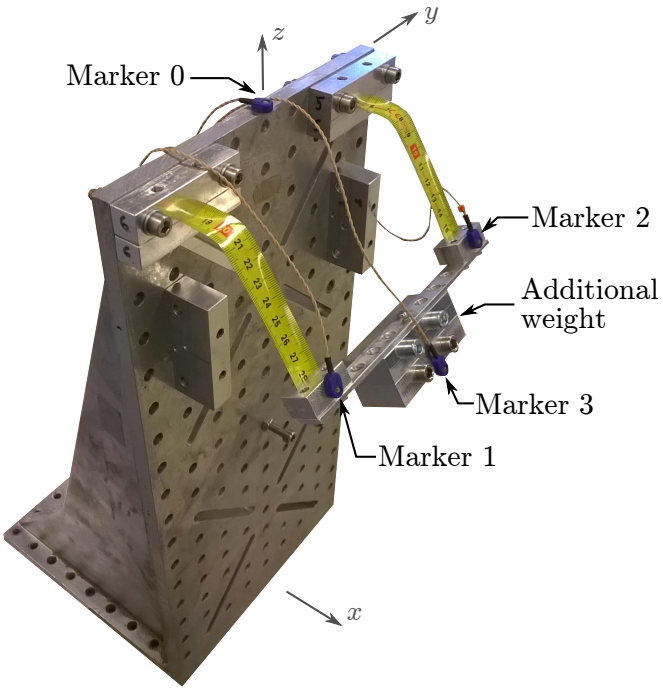

Figure 8.2: Deformed configuration of the experimental set-up used to determine equivalent values of the thickness and the Young's modulus.

	|Displacement| [mm]		
	x	y	z
Marker 0	0.2	0.1	0.1
Markers $1-2$	24.7	0.1	77.9
Marker 3	41.8	0.6	110.9

Table 8.1: Experimental displacements in absolute values of the markers to reach the deformed configuration used to determine equivalent values of the thickness and the Young's modulus.

a new static folded equilibrium configuration exists (Figure 8.2). The measured displacements for the two equilibrium configurations are then used to determine the equivalent thickness and Young's modulus.

The data acquisition is performed with four active markers which are placed on the set-up as follows. Marker 0 is located on the fixation support and is used as a control point as it remains fixed. Displacements measured at markers 1 and 2 on the small interfaces are used to obtain average values at both locations as in theory they should be equal. However, experimentally, some differences might be encountered, for example due to the set-up not being perfectly symmetric or perfectly aligned along the axes. Finally, a last marker is located at the tip of the additional weight. The measured displacements, in absolute values, are given in Table 8.1.

Finite element model To determine the equivalent values of the Young's modulus E and the thickness t to be used in the finite element model of the experimental set-up, a model reproducing the deformed configuration after the formation of the folds is developed.

In this case, the simulation follows two steps: first, a vertical displacement at the tip of the additional weight, considered as rigid, is imposed in order to force buckling, then that displace-

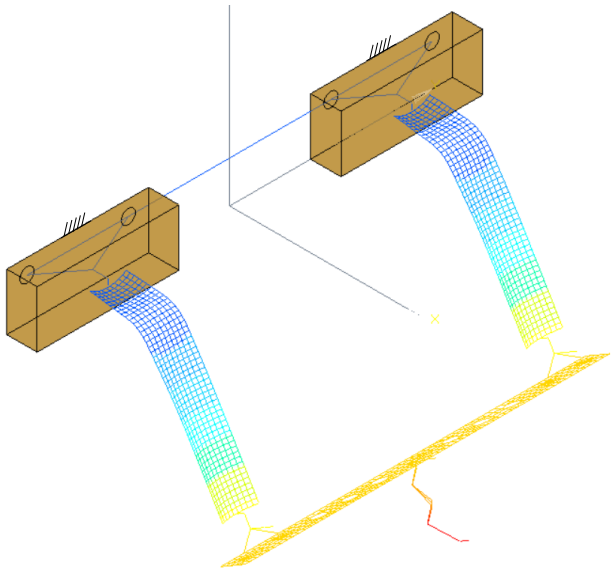

Figure 8.3: Finite element model used to determine equivalent values of the thickness and the Young's modulus (deformed configuration).

ment constraint is removed and the simulation is performed until the structure is stabilised in the sought deformed configuration given in Figure 8.3.

Optimisation procedure The Young's modulus E and the thickness t fitting at best the previous experimental results are obtained by solving an optimisation problem expressed as:

$$\min_{E,t} f(E,t) \text{ such that } \begin{cases} E_{\min} \leq E \leq E_{\max} \\ t_{\min} \leq t \leq t_{\max} \end{cases} \tag{8.1}$$

where $f(E,t)$ is the objective function to be minimised and quantifies the correlation between the numerical and the mean experimental results. To this end, displacements along the x and z-axes are compared, while the displacements along the y-axis are not included in the optimisation problem. The objective function $f(E,t)$ is then the sum of the differences in absolute values, each term being divided by the corresponding mean experimental value in order to sum adimensional terms with the same order of magnitude:

$$f(E,t) = \frac{|d_x^{exp} - d_x^{FEM}|}{|d_x^{exp}|} + \frac{|d_z^{exp} - d_z^{FEM}|}{|d_z^{exp}|} \tag{8.2}$$

where d is the displacement measured experimentally (exp) or obtained with the finite element model (FEM), each one being influenced by E and t.

Regarding the bounds limiting the design variables, the ranges of values allowing a passive deployment of the mass and which are based on the developments in Section 7.2 are used (Table 8.2). This optimisation procedure is similar to, but simpler than the one exploited in Chapter 4 for the deployment of a reflector, since no nonlinear constraint is taken into consideration.

The problem is solved by the means of the interior-point algorithm available through the `fmincon` function in MATLAB which solves large, sparse multivariable problems, as well as small dense ones [70]. This method aims at finding a local minimum of the objective function, which may depend on the initial guess. Therefore, several tests starting at different points of the ranges

Bounds	E [MPa]	t [mm]
min	100000	0.12
max	220000	0.2

Table 8.2: Lower and upper bounds of the design variables in the optimisation procedure.

E [MPa]	t [mm]
151760	0.138

Table 8.3: Identified parameters based on the post-buckling response.

in Table 8.2 are performed before finding a global solution.

The final results of the optimisation procedure are given in Table 8.3, while the comparison of the displacements obtained experimentally and numerically is computed in Table 8.4. Thanks to this latter, it can be concluded that it is reasonable to model each tape spring as an homogeneous structure with an equivalent thickness and an equivalent Young's modulus.

In order to fully define the isotropic material, the Poisson's ratio has to be determined in addition to the Young's modulus. By performing optimisation procedures in which the Poisson's ratio is also a design variable, it was found that both parameters have a similar impact on the tape spring behaviour. The same quasi-static response could then be obtained whether the Poisson's ratio was left free to vary or not. It was then decided, as it was done in this section, to fix the Poisson's ratio *a priori* to a value of 0.3 in order to reduce the number of design variables.

The thickness t and the Young's modulus E identified in this section will be used in the next one in order to check if the finite element model can accurately predict the quasi-static evolution of the experimental set-up when it is submitted to a different kind of test.

8.2.2 Pre-buckling tests

Experimental tests In order to check the capacity of the model with the identified parameters to reproduce the complete static response, other quasi-static experimental tests which focus on the pre-buckling behaviour of the tape springs are performed by pulling vertically, by hand, on a string attached in the middle of the rod. They are performed as slowly as possible and such that, after buckling, the tape springs are folded in opposite sense. Compared to the nominal configuration of the experimental set-up (Figure 7.5), the dummy appendix was removed to avoid contact with the hand of the operator. Experimental data are collected on the maximum vertical force by the means of the force plate and on the associated vertical displacement reached before the buckling of the tape springs with a marker located in the middle of the rod.

		|Displacement|		
		Exp. [mm]	Num. [mm]	Δ [%]
Markers $1-2$	x	24.7	25.7	4.1
	z	77.9	77.9	< 0.1
Marker 3	x	41.8	43.7	4.6
	z	110.9	111.6	0.6

Table 8.4: Comparison between the results of the experimental tests and the numerical model after the identification based on the post-buckling response.

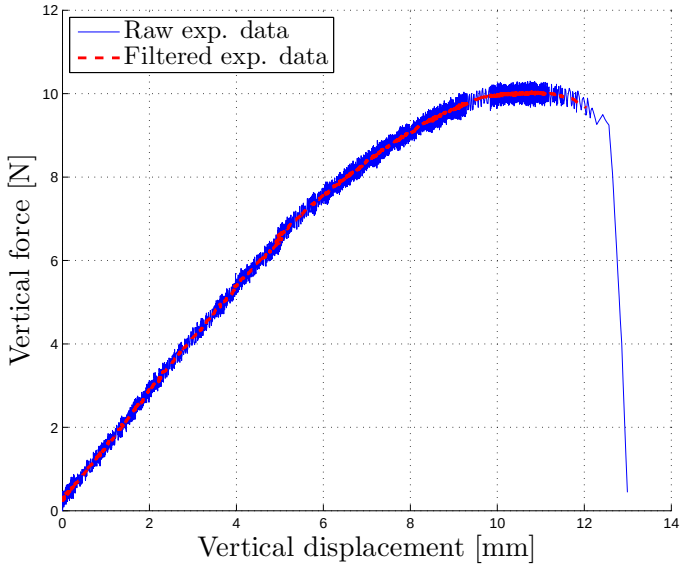

Figure 8.4: Experimental result of a quasi-static test.

	Mean	Maximum difference	Variation coefficient
Force	9.8 N	1.3 N	3.33 %
Displacement	10.8 mm	4.6 mm	5.51 %

Table 8.5: Experimental results from the quasi-static tests and reproducibility.

One evolution of the vertical force obtained with these quasi-static tests is illustrated in Figure 8.4. As it can be seen, the raw experimental data (full blue curve) is affected by noise which is due to the large measuring range of the force plate spanning from 0 to 125 N, while the measured force is below 11 N. The impact of the noise is then reduced by filtering it with the `smooth` function from MATLAB. It consists of a moving average filter that replaces each value by a mean computed on the neighbouring data points defined within a span fixed here to 101, which corresponds to an elapsed time of 25.3 ms. The resulting curve is the red dashed one used in the remaining of this section. Compared to the general evolution of the bending moment with respect to the bending angle described in Figure 2.1, the same characteristic features are visible: the force reaches a maximum, which is then followed by a sudden drop caused by the buckling of the tape springs.

To assess the reproducibility of these quasi-static tests, the value of the maximum force and of its associated displacement are compared on 50 curves obtained with two different pairs of tape springs. The results are summarised in Table 8.5 where three features are computed: the mean value, the maximum difference noticed between the results and the associated variation coefficient (or relative standard deviation) which is defined as the ratio between the standard deviation and the mean. As the variation coefficients remain below 6 % in both cases, it can be concluded that these experimental tests show a good reproducibility, even though the motion was driven by hand.

Comparison with the finite element model A comparison between the results from these experimental quasi-static tests and the results from the finite element model described in Section 8.1 and characterised by the values of thickness and Young's modulus in Table 8.3 shows noticeable differences in terms of maximum vertical force before buckling (Table 8.6). Nonetheless, the associated vertical displacement is fairly captured. This evolution is confirmed qualitatively in Figure 8.5 where one experimental and the numerical results are superimposed, along with

	Experimental	Numerical	Δ [%]
Maximum force [N]	9.8	7.6	22.4
Displacement [mm]	10.8	10.1	6.48

Table 8.6: Comparison between the mean experimental and numerical results of the quasi-static tests.

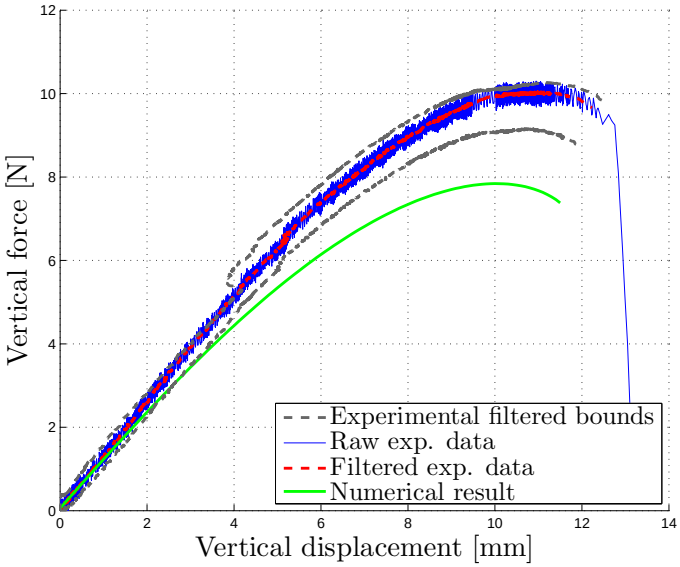

Figure 8.5: Comparison between one experimental quasi-static test and the numerical model.

the lowest and highest filtered experimental curves. Different attempts were made to refine the identification of the model by playing with other parameters, such as the radius of curvature, but they could not really improve the results.

Several elements could explain these differences. First of all, it was assumed that the material and the geometry, especially the thickness and the transverse curvature, are uniform along the tape springs. This represents a strong hypothesis since, in practice, these parameters are most likely not uniform and have a great influence on the quasi-static behaviour of the tape springs as shown in Chapter 3. Then, it was decided to represent the multi-layered tape springs as single-layered components characterised by equivalent values of thickness and Young's modulus. In this case, these equivalent parameters were identified based on an experimental test focusing on the post-buckling behaviour (Section 8.2.1), however, in this second type of tests, the response is mainly characterised by the pre-buckling behaviour. Since these behaviours (pre- and post-buckling) are clearly different, focusing on one part of the response curve to determine the parameters of the complete model turns out to be inappropriate to predict the second part of the response curve.

In order to further analyse the quasi-static behaviour of our tape springs, additional quasi-static experimental tests are performed and then numerically reproduced. For the finite element model, we shall try alternative methods to identify the parameters (thickness and Young's modulus), this time based on the pre-buckling behaviour. The results are then compared to the different experimental responses and to the previous numerical results.

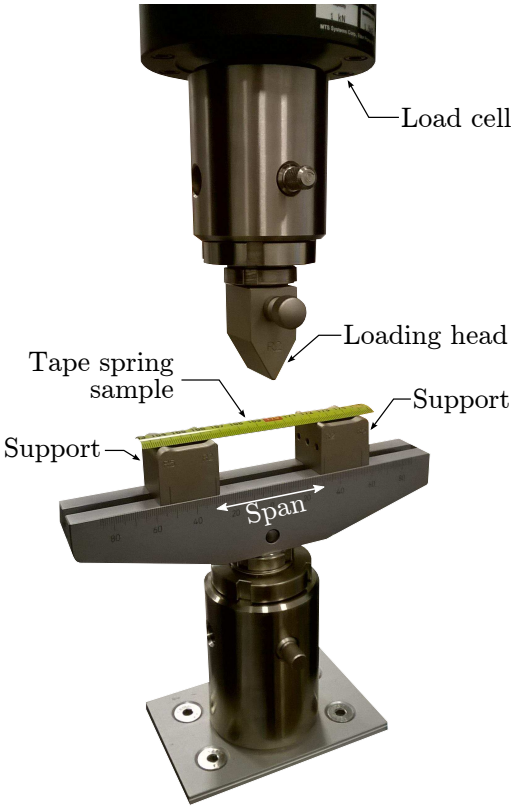

Figure 8.6: Experimental set-up for the three points bending tests.

8.2.3 Three points bending tests

Experimental tests Three points bending tests (TPBT) consist of a loading head coming into contact with a tape spring sample positioned on two supports separated by a chosen span (Figure 8.6). The loading machine is an MTS Criterion (Model 43) [28] available at the Mechanics of Biological and Bioinspired Materials Laboratory (`http://www.biomat.ulg.ac.be/`) at the University of Liège. A load cell of 1 kN is used, the tip of the loading head and the corners of the supports have a radius of 2 mm, and the span is set to 60 mm.

Preliminary tests were first performed in order to determine the most appropriate test rate (the amplitude of vertical displacement of the loading head in millimetre per second) in terms of accuracy. To have a point of comparison between several rates, a reference curve is measured at 0.05 mm/s. The mean differences in both senses of bending with respect to the reference are given in Table 8.7. As the differences remain small for all tests rates, a qualitative comparison of the resulting curves is given in Figure 8.7. Focusing on the buckling in opposite sense, it can be seen that the verticality of the curve is lost as the test rate increases. Furthermore, some odd behaviours can be encountered as, for example, for the test rate at 0.2 mm/s where a small increase in the force is noticed after the buckling phenomenon, while this region should be only characterised by a decreasing force. Based on this analysis, the following three points bending tests are performed with a rate of 0.1 mm/s.

Rate [mm/s]	0.1	0.2	0.5	1	2
Difference in opposite sense [%]	0.60	0.32	1.35	1.55	2.67
Difference in equal sense [%]	1.63	0.43	0.45	0.65	1.21

Table 8.7: Differences on the experimental three points bending curves obtained for several test rates with respect to the reference rate at 0.05 mm/s.

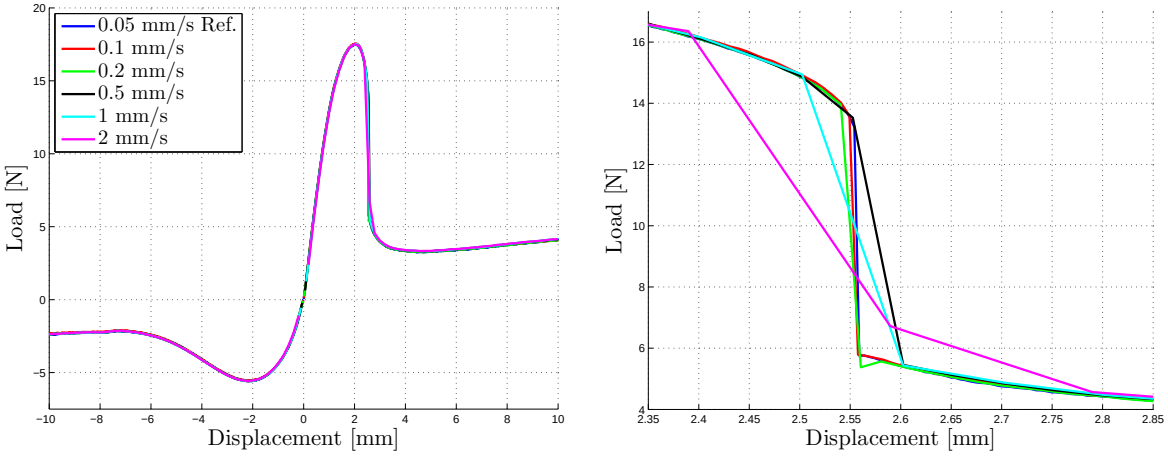

(a) Global evolution.

(b) Focus on the buckling phenomenon.

Figure 8.7: Qualitative comparison between the experimental three points bending curves obtained at several test rates.

For each tape spring, ten tests are performed in the two senses of bending. The results obtained on one sample are illustrated in Figure 8.8 where the 20 curves (10 in opposite sense and 10 in equal sense) are superimposed and show a good reproducibility. Notice that this evolution is different from the general one described in Figure 2.1, since three points bending tests give the relationship between the load and the displacement of the head, instead of the bending moment with respect to the bending angle. Nonetheless, the same main characteristics are identified: for small displacements, the evolution is first linear; then a maximum is reached, the amplitude being smaller in equal sense; it is followed by buckling which is sharper in opposite sense; and finally large displacements are associated to a residual load.

Regarding the reproducibility of the three points bending tests for different tape springs, the results are given in Tables 8.8 and 8.9 for the opposite and equal sense parts of the curves respectively. Three features are considered: the maximum load, the associated displacement of the loading head and the slope of the curve for small displacements. In each case, the mean value of all the tests (in total, 10 tape springs were used, so that each mean is computed on 100 values) is given, along with the largest difference noticed within the results and the associated variation coefficient (or relative standard deviation). As the variation coefficient remains below 5 % for almost all features except the slope in equal sense, it can be concluded that these experimental tests also show a good reproducibility from one tape spring to another. After analysis, it was discovered that the large variation coefficient of the slope in equal sense is due to a single tape spring sample for which a mean slope of 4.83 N/mm was measured. If that value is disregarded, a new variation coefficient of 4.14 % is found. Finally, the most noticeable sources of errors independent of the tape springs during the tests came from a bad alignment of the sample with respect to the loading head and the supports or a bad tightening of the loading head in the load cell, which can be both easily avoided by carefully preparing the set-up.

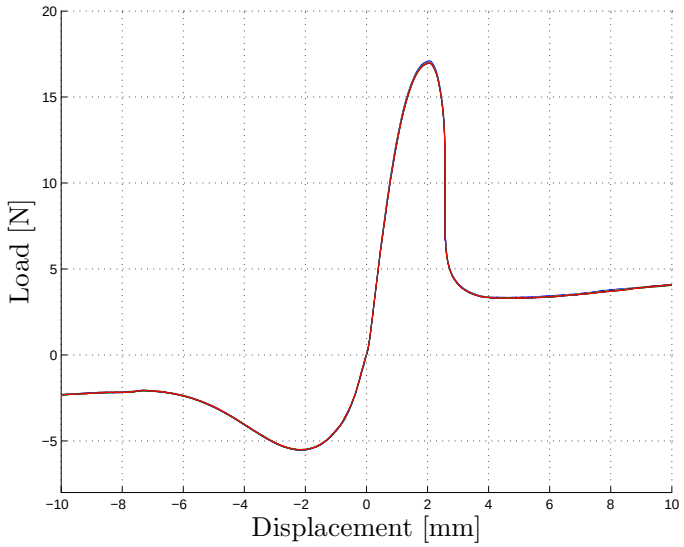

Figure 8.8: Experimental results of the three points bending tests for a single tape spring (10 curves in opposite sense and 10 curves in equal sense).

	Opposite sense		
	Mean	Maximum difference	Variation coefficient
Maximum load [N]	17.32	1.30	1.93 %
Displacement [mm]	2.01	0.35	3.75 %
Slope [N/mm]	12.71	0.96	1.56 %

Table 8.8: Experimental results from the three points bending tests in opposite sense.

	Equal sense		
	Mean	Maximum difference	Variation coefficient
Maximum load [N]	5.49	0.53	1.95 %
Displacement [mm]	2.16	0.35	3.49 %
Slope [N/mm]	6.69	2.68	10.15 %

Table 8.9: Experimental results from the three points bending tests in equal sense.

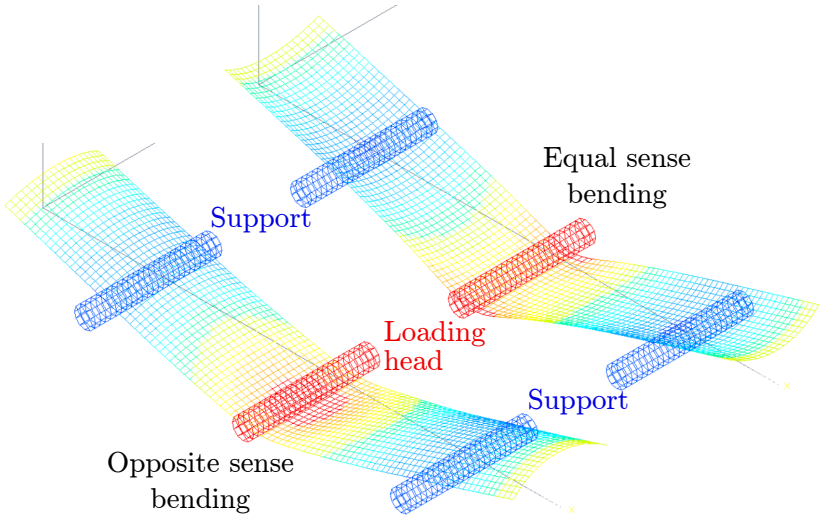

Figure 8.9: Finite element models for the three points bending tests (deformed configurations corresponding to a vertical displacement of 10 mm of the loading head).

Finite element model In order to determine new values for the Young's modulus E and the thickness t leading to a better fit of the pre-buckling behaviour of the tape springs, a model reproducing the three points bending tests is developed.

The specific modelling assumptions in this case are the following. The loading head and the supports are simplified as cylinders with a radius of 2 mm, which correspond to the local geometry of the tip and the corners of these components in the contact zone. Furthermore, these three elements are considered as rigid, while the tape spring is obviously flexible. Regarding the contact solver, a coupled iterations method is exploited, meaning that contact is treated as a nonlinearity and a kinematic constraint is active when contact occurs and inactive otherwise [89]. A Coulomb friction model is considered so that, in sliding conditions, the friction force is proportional to the force acting in the normal direction of the contact surface. Finally, the supports are considered as fixed, while the displacement of the loading head is controlled by imposing the same test rate as experimentally (0.1 mm/s). The resulting deformed configurations in both senses obtained with these models are given in Figure 8.9 where the Newmark method was exploited to solve this quasi-static nonlinear problem with an adaptive time stepping procedure.

Furthermore, it is interesting to see how the Von Mises stresses are distributed in these deformed configurations (Figure 8.10). While in opposite sense the largest stresses start at mid-width and propagate to the sides, the contrary happens in equal sense with the stresses remaining more localised at the sides.

In order to simplify the simulation of contact, the projections of the nodes of the cylinders on the tape spring and vice-versa have to be as close as possible. Due to this constraint, only three relevant mesh sizes allowed the convergence of the simulations and could be compared as illustrated in Figure 8.11. It can be seen that for a mesh size of 1.5 mm, unrealistic jumps occur in both senses around ± 8 mm, although less significant in equal sense. Between the mesh sizes 0.9 mm and 1 mm, the differences are minimal, however, the computation time is more than doubled in the first case compared to the second. From this analysis, a mesh size of 1 mm is selected for the following finite element models of three points bending tests.

Figure 8.11 also shows the limitations of the contact model: the buckling in opposite sense is not captured. Instead, the deformation of the tape spring is progressive and there is no sharp

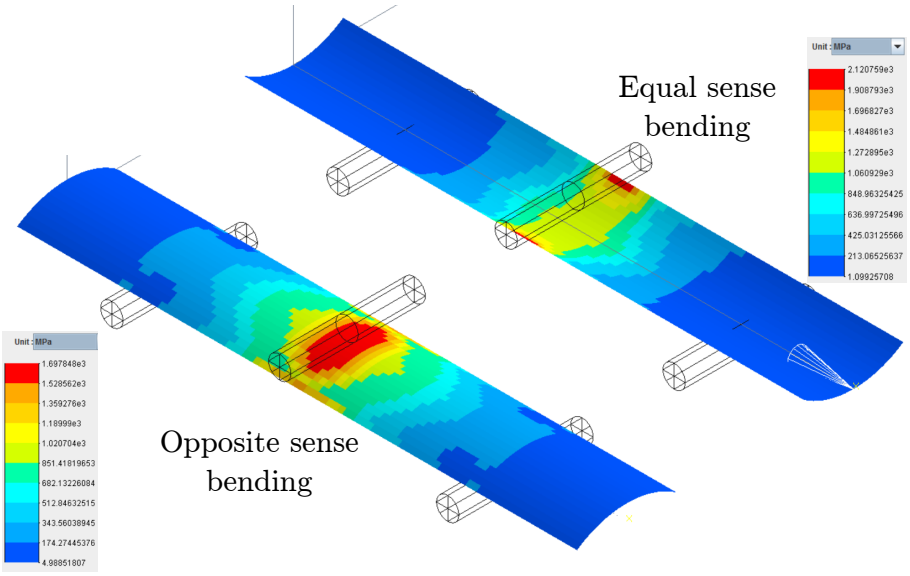

Figure 8.10: Distribution of the Von Mises stresses in three points bending tests reaching a displacement of 10 mm of the loading head.

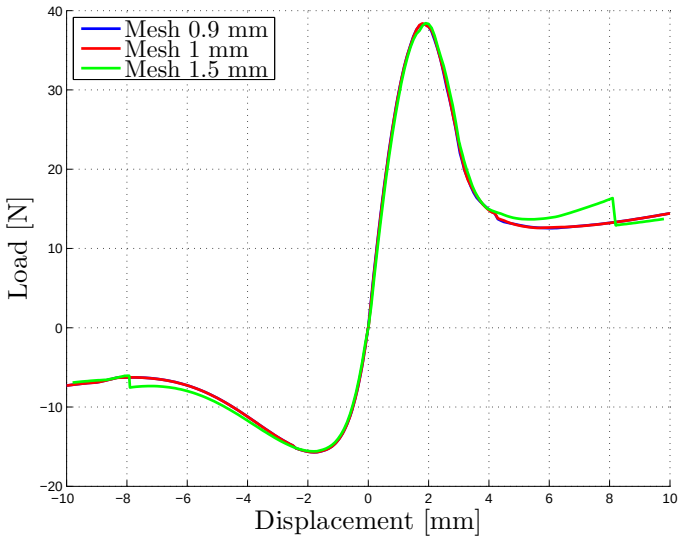

Figure 8.11: Comparison of numerical three points bending curves for three mesh sizes.

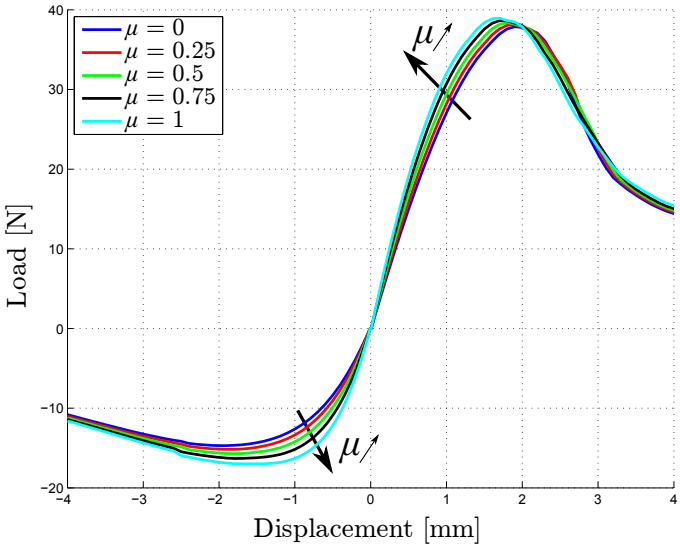

Figure 8.12: Impact of the friction coefficient μ on the results of the three points bending tests.

E [MPa]	t [mm]	μ [-]
196374	0.132	0.175

Table 8.10: Identified parameters based on the three points bending tests.

decrease of the load. Many tests were performed in order to find a more realistic contact model, however, the results presented here are the most representative ones that we could obtain using the SAMCEF software. The region between the maximum load and the residual load in opposite sense is then not taken into account in the following analyses. Regarding the rest of the curve, it is not possible at this stage to further evaluate the validity of the contact model.

Optimisation procedure An optimisation procedure similar to the one presented in Section 8.2.1 is then used to determine equivalent values for the thickness t and the Young's modulus E. The main difference comes from the existence of an additional uncertain variable to be evaluated: the friction coefficient μ between the loading head and the tape spring and between the supports and the tape spring. This latter affects the results of the three points bending tests as it can be seen in Figure 8.12. To simplify the problem, it is assumed that the friction coefficient μ is the same at the three contact locations and is between $\mu_{\min} = 0$ and $\mu_{\max} = 1$.

The optimisation problem is then expressed as:

$$\min_{E,t,\mu} f(E,t,\mu) \text{ such that } \begin{cases} E_{\min} \leq E \leq E_{\max} \\ t_{\min} \leq t \leq t_{\max} \\ \mu_{\min} \leq \mu \leq \mu_{\max} \end{cases} \tag{8.3}$$

where the objective function $f(E,t,\mu)$ compares the mean experimental three points bending curves to the numerical ones at 8 points (4 points in opposite sense and 4 points in equal sense) and the maximum and minimum bounds of E and t are defined in Table 8.2.

The results of the optimisation procedure are given in Table 8.10. Compared to the identification procedure based on the post-buckling behaviour (Table 8.3), the Young's modulus E has increased by almost 30 % and the thickness t has decreased of 4.35 %.

A comparison with the experimental results is illustrated in Figure 8.13 where it can be seen that, despite not capturing buckling, the finite element model with the new set of parameters

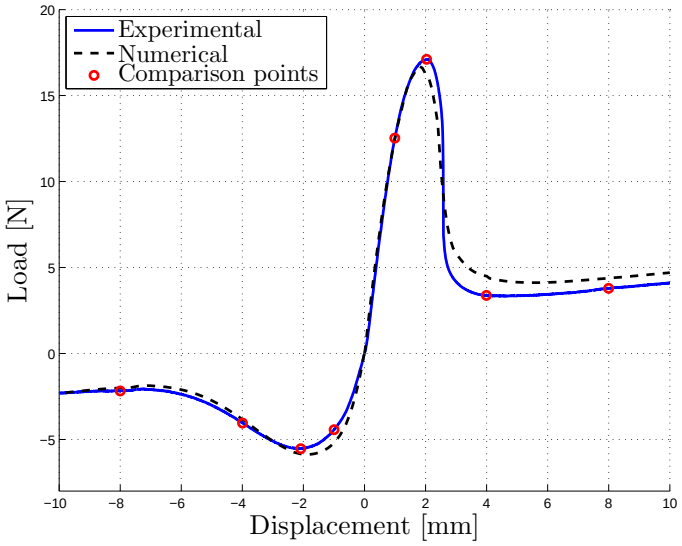

Figure 8.13: Comparison between the results of the optimisation procedure for the three points bending tests and one experimental curve.

	Opposite sense		
	Experimental	Numerical	Difference
Displacement	[N]	[N]	[%]
1 mm	12.55	12.53	0.14
2.01 mm	17.32	16.71	3.51
4 mm	3.36	4.50	34.00
8 mm	3.75	4.38	16.59

Table 8.11: Quantitative comparison between the experimental and the numerical results of the three points bending tests in opposite sense.

(Table 8.10) and the current contact model fairly respects the overall evolution of the experimental curve. Quantitative comparisons are computed in Tables 8.11 and 8.12 for the opposite and equal sense parts of the curve respectively. The main differences concern the residual load in opposite sense and the very small displacements in equal sense. For information, the second point in both tables is associated to the maximum experimental loads in absolute value in both senses.

If the Young's modulus and the thickness obtained with the three points bending tests (Table 8.10) are now used to reproduce the pre-buckling quasi-static evolution of the experimental set-up (Section 8.2.2), it can be seen in Figure 8.14 and Table 8.13 that the correlation between the experimental and numerical curves is better than previously, especially in terms of maximum load. The remaining main discrepancy is the instant of buckling. This analysis seems to show that with the current choice of design parameters and identification procedures used in this work, it is not possible to identify a model which numerically reproduces both the pre- and post-buckling parts of the quasi-static response.

8.2.4 Tip loading tests

Experimental tests The MTS Criterion machine was also used to perform a last type of quasi-static test: tip loading tests (Figure 8.15). An advantage of this set-up is that a single tape spring is clamped using the same interface as in the original set-up defined in Chapter 7 and submitted to an automated quasi-static loading. They consist in imposing the displacement

	Equal sense		
	Experimental	Numerical	Difference
Displacement	[N]	[N]	[%]
1 mm	4.34	5.20	19.95
2.16 mm	5.49	5.87	6.88
4 mm	4.02	3.83	4.61
8 mm	2.15	2.01	6.55

Table 8.12: Quantitative comparison between the experimental and the numerical results of the three points bending tests in equal sense.

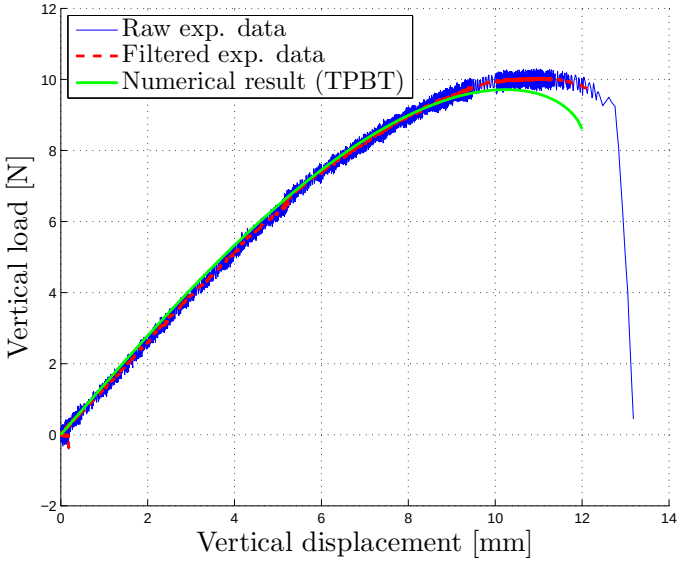

Figure 8.14: Comparison between one experimental quasi-static test and the numerical model obtained with the three points bending tests.

	Experimental	Numerical	Δ [%]
Maximum load [N]	9.8	9.71	0.92
Displacement [mm]	10.8	10.2	5.56

Table 8.13: Comparison between the mean experimental and numerical results obtained with the three points bending tests of the quasi-static tests.

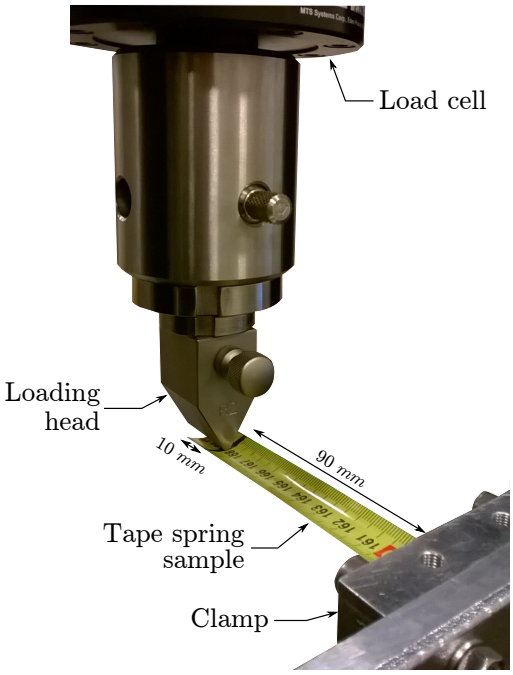

Figure 8.15: Experimental set-up for the tip loading tests.

	Load in opposite sense		
	Mean	Maximum difference	Variation coefficient
Displacement	[N]	[N]	[%]
2 mm	2.44	0.15	1.86
6 mm	6.39	0.29	1.06
9 mm	7.07	0.49	2.00
14 mm	0.78	0.19	6.07

Table 8.14: Experimental results from the tip loading tests in opposite sense.

rate of a loading head coming into contact with the tip of a tape spring sample rigidly clamped at its other extremity. The effective length of the tape spring measures 90 mm and the contact with the loading head occurs on an additional length of 10 mm. The test rate is fixed to the same value as the one used in the three points bending tests (1 mm/s).

In total, five different tape springs are used and ten tests are performed on each one of them. The results obtained on one sample are illustrated in Figure 8.16 with which the reproducibility of the tests is qualitatively validated. These experimental curves could be related to the general one (Figure 2.1) by collecting information on the bending angle of the tape spring induced by the loading head with the help, for example, of cameras. Quantitatively, the reproducibility of the tip load is checked at four displacements (Table 8.14) which are all characterised by a variation coefficient smaller than 7 %.

For this type of experimental tests, a good reproducibility could only be achieved by bending the tape springs in opposite sense. Regarding the behaviour in equal sense, it is too unstable and sensitive to the positioning of the tape spring sample with respect to the loading head. Indeed, even with the loading head perpendicular to the tape spring, the deformation is dominated by torsion and the tape spring tends to slide on the side of loading head loosing thus the symmetry of the loading (Figure 8.17).

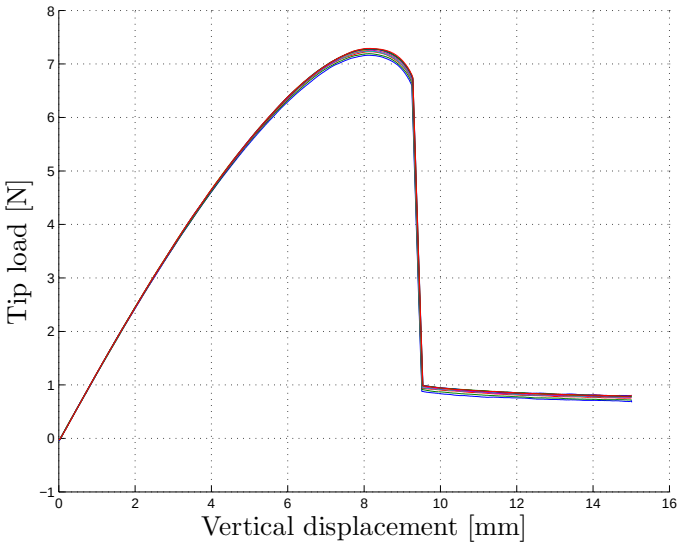

Figure 8.16: Experimental results of the tip loading tests in opposite sense for a single tape spring (10 superimposed curves).

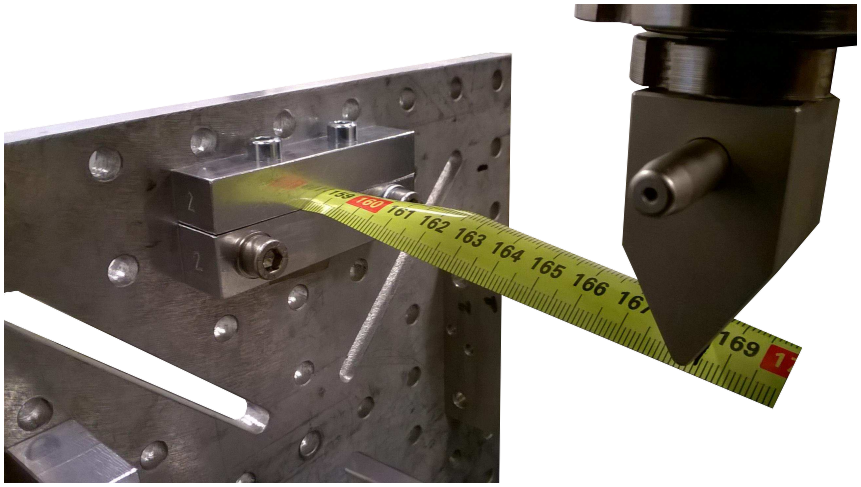

Figure 8.17: Experimental tip loading test in equal sense.

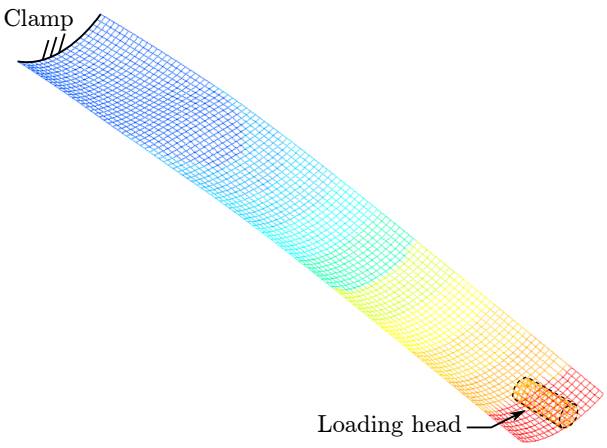

Figure 8.18: Finite element model for the tip loading tests (deformed configuration corresponding to a vertical displacement of 12 mm of the loading head).

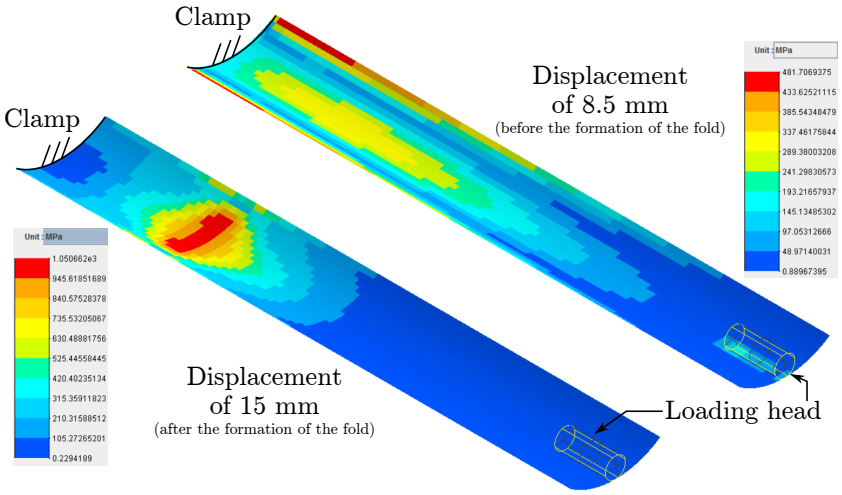

Figure 8.19: Distribution of the Von Mises stresses in the tip loading tests.

Finite element model In the finite element model, the loading head is simplified as a rigid cylinder with a radius of 2 mm and a length of 10 mm. Full contact between the head and the tape spring only occurs at the beginning of the test. The same contact model based on a coupled iteration method as for the three points bending tests is used, as well as the same mesh size (1 mm). The resulting deformed configuration is given in Figure 8.18 for a vertical displacement of 12 mm of the loading head.

Furthermore, regarding the distribution of the Von Mises stresses (Figure 8.19), it can be seen that before the formation of the fold, the largest stresses are encountered near the clamp, medium ones are visible in the region of contact with the loading head and, as the vertical displacement increases, the stresses propagate from the clamp extremity towards the loading head. For a specific value of displacement, buckling occurs and a fold is created in the tape spring. The largest Von Mises stresses are then localised at the fold and remain concentrated in that region as the structure is further deformed.

During the simulations, as the cylinder moves downwards, only one of its extremities stays in contact with the tape spring and it naturally slides on the surface of the tape spring. It was discovered that to ensure the convergence of the contact model, the sliding has to remain on the same elements of the mesh throughout the simulation. To this end, a line of elements along the

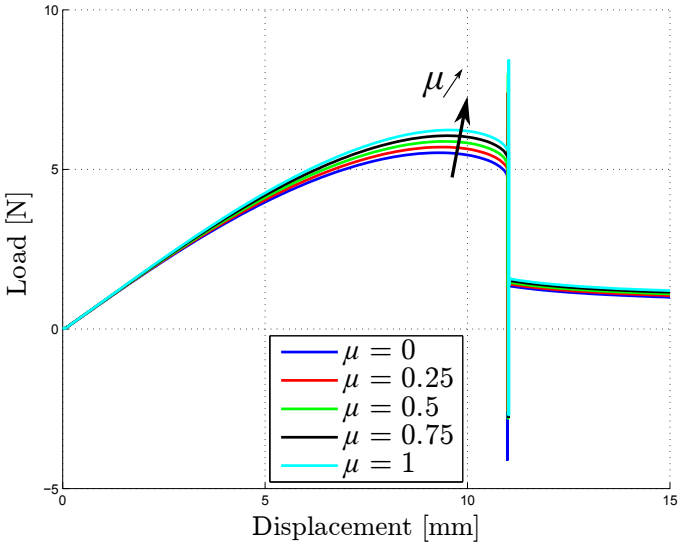

Figure 8.20: Impact of the friction coefficient μ in the numerical model of the tip loading tests.

	Load in opposite sense		
	Experimental	Numerical	Difference
Displacement	[N]	[N]	[%]
2 mm	2.44	2.67	9.25
6 mm	6.39	6.53	2.16
9 mm	7.07	1.31	81.42
14 mm	0.78	0.98	26.30

Table 8.15: Quantitative comparison between the experimental and the numerical results of the tip loading tests.

width have larger dimensions than the rest of the mesh as it is visible in Figure 8.18. Since the fold and the maximum Von Mises stresses are located near the clamp extremity and away from the loading head, the impact of this locally coarser discretisation on the results should be limited.

Finally, as in the three points bending tests, the friction coefficient defined in the contact model has an impact on the value of the loads. This behaviour is illustrated in Figure 8.20. Furthermore, it can also be seen on this figure that buckling is well captured by the finite element model.

Simplified finite element model The model can be simplified as a clamped tape spring of 90 mm in length on which the vertical displacement of the extremity is imposed instead of representing the loading head. Thus, the simulations are free of any contact model which seemed to be a source of inaccuracy in the three points bending tests.

Comparison To compare the numerical results of the finite element model to the experimental data, the model parameters in terms of Young's modulus, thickness and friction coefficient are fixed to the values obtained in the optimisation procedure of the three points bending tests (Table 8.10). Qualitative and quantitative comparisons are given in Figure 8.21 and Table 8.15 respectively. It can be clearly seen that, even though the first parts of the curves coincide, the model and the experiment diverge on the instant of buckling and the residual load.

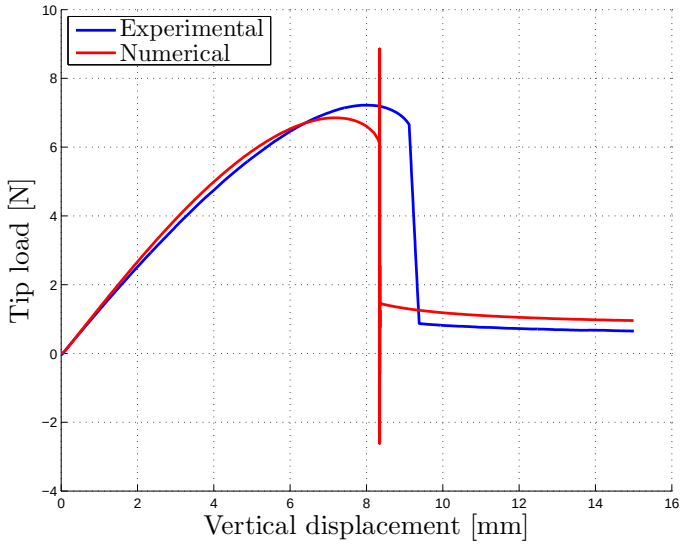

Figure 8.21: Comparison between the experimental and numerical results of the tip loading tests.

In this case, the poor correlation of the post-buckling response between the numerical and experimental results cannot be attributed to the contact model since similar results are obtained with the simplified model which is free from any friction model.

It can then be concluded from all these tests that experiments characterising the quasi-static behaviour of tape springs are hard to numerically reproduce based on a shell finite element model with a constant initial curvature, a constant thickness and an homogeneous material law relying on a constant Young's modulus. In order to develop a general finite element model able to represent different quasi-static experiments, either a more complex model should be considered or other tape springs with more uniform geometric and material parameters should be investigated. Regarding the second option, the manufacture of tape springs with highly controlled parameters appears as a non-trivial task, which is beyond the scope of the present thesis.

8.3 Summary

In order to develop a finite element model of the experimental set-up, equivalent values of the thickness and the Young's modulus of the tape springs have to be identified.

A first quasi-static experimental test is performed by comparing two equilibrium configurations. The required parameters are extracted by the means of an optimisation procedure. The robustness and the predictive capacity of the model are then evaluated in the case of a test which captures the evolution of the vertical force affecting the set-up while applying a vertical displacement at the tip of the tape springs. The comparison between the numerical and experimental results shows noticeable differences, which could be due to the assumption that the tape springs are characterised by a uniform geometry and a uniform material. In this case, the parameters of the model were identified based on an experimental test which focuses on the post-buckling behaviour of the tape springs, while in the second type of tests, the response is mainly characterised by the pre-buckling behaviour.

A third type of tests, consisting of three points bending tests, was then performed in order to investigate other identification procedures that allow capturing the pre-buckling behaviour with more accuracy. Finally, in the case of tip loading tests, the model with these new parameters could only capture a limited part of the pre-buckling response.

In conclusion, with the current assumptions, the complete quasi-static response of the experimental set-up is difficult to reproduce numerically. This issue could be further analysed in the future by improving either or both the numerical model and the experimental set-up. As this thesis mostly addresses dynamic deployments from a buckled folded configuration to an unfolded one, we propose to continue our investigations using the model identified from the post-buckling quasi-static test.

CHAPTER 9

DEPLOYMENT TESTS

The experimental set-up is now used to perform autonomous deployment tests in which the data are collected both in terms of displacements and forces. As in the quasi-static tests, the reproducibility of the experimental results is quantified by performing the tests a large number of times and on different pairs of tape springs.

In parallel, the deployment tests are reproduced with the finite element model of the set-up. The numerical parameters are determined based on the results from the previous chapter regarding the thickness and the Young's modulus, while the structural damping is identified by the means of small amplitude vibration tests. In the end, the experimental and numerical results are then compared in order to validate the model.

9.1 Experimental tests

The initial folded configuration is reached by pulling a rope attached in the middle of the rod until the small interfaces are in contact with stops attached to the fixation support (Figure 9.1). The initial folding leads thus to almost vertical deformed configurations which were assumed in the preliminary design of the set-up (Section 7.2). The mean initial bending angle reaches $95.5°$ and $-91.2°$ with respect to the horizontal in opposite and equal sense respectively. The deployment is then triggered by cutting the rope which leaves the structure free to oscillate. For each sense of bending, two different pairs of tape springs are used to perform the deployment tests. The evolution of the bending angle with respect to the horizontal obtained in 50 tests are superimposed in Figures 9.2 and 9.4 for an initial folding in opposite and equal sense respectively. For the statistical analysis below, the data from 100 tests are exploited in each sense.

9.1.1 Initial bending in opposite sense

The evolution of the bending angle with an initial folding in opposite sense (Figure 9.2) can be divided into three phases depending on the types of fold created by the motion, the frequency of the oscillations and the amount of damping affecting each phase. The presence or the absence of folds is visually confirmed during the deployment. Relevant snapshots from the recorded videos are given in Figure 9.3 and can be linked to the evolution of the bending angle in Figure 9.2. In phase I, the energy in the structure is able to create folds in both senses of bending associated to large motion amplitudes occurring at a low frequency (Figure 9.3, snapshots 2 and 3). Since distinct nonlinear behaviours appear whether the folds are in opposite or equal sense, this evolution is asymmetric. The significant damping between each peak is mainly due to the hysteresis phenomenon occurring in opposite sense every time that a fold disappears. As a reminder, the

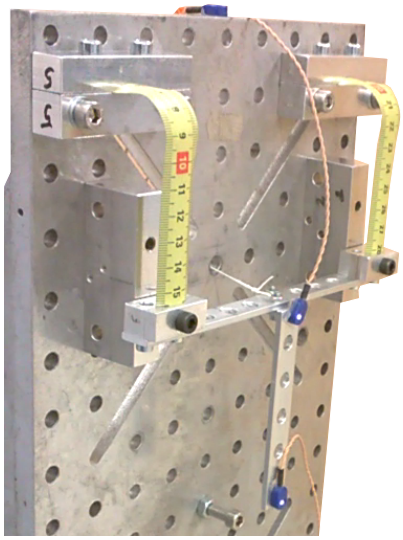

Figure 9.1: Initial folded configuration in equal sense of the experimental set-up.

relationship between the damping during the deployment and the hysteresis phenomenon was investigated in [41] and recalled in Section 6.3. Furthermore, as previously shown in Figure 2.11 and in Section 3.2, the quasi-static loading and unloading curves in equal sense are also not superimposed. It is then expected that during a dynamic deployment, this second hysteresis phenomenon is also responsible for some of the energy dissipation every time that a fold in equal sense disappears, but at a lower level than for folds in opposite sense.

In phase II, folds are only formed in equal sense (Figure 9.3, snapshots 4 and 5), the remaining energy being not sufficient to reach and go beyond the maximum bending moment $M_+^{\max}$ in opposite sense which can often be twice as large as in equal sense $M_-^{\max}$. It implies that positive bending angles remain small and that shocks and rebounds occur at each positive peak. As in phase I, the evolution is then again asymmetric, but the frequency of oscillation increases as the system stays closer to the deployed configuration characterised by a higher stiffness. This time, the damping is assumed to be caused by several phenomena: the hysteresis in equal sense, the shocks in opposite sense and the overall structural damping.

Finally in phase III, the tape springs vibrate without forming any folds as it can be seen by comparing the snapshots 4 and 6 in Figure 9.3. For small bending angles, a symmetric evolution of the motion is reached in which structural damping, drag effects and friction are predominant.

9.1.2 Initial bending in equal sense

In the case of an initial folding in equal sense (Figure 9.4), in phase I, the initial stored elastic energy is too small to induce the formation of folds in opposite sense. The motion is then characterised by an asymmetric evolution at low frequency with folds in equal sense only. The same type of folds are present in phase II, but they occur at a higher frequency and lower amplitudes. The transition between phase I and phase II is due to the different deformation patterns of the tape springs. In the first case, the folds are well formed which leads to the complete transverse flattening of the tape springs, however, in the second case, the folds are only partially formed which leaves the tape springs with a certain transversal curvature, increasing thus their stiffness. Finally, phase III is the same as the one in opposite sense.

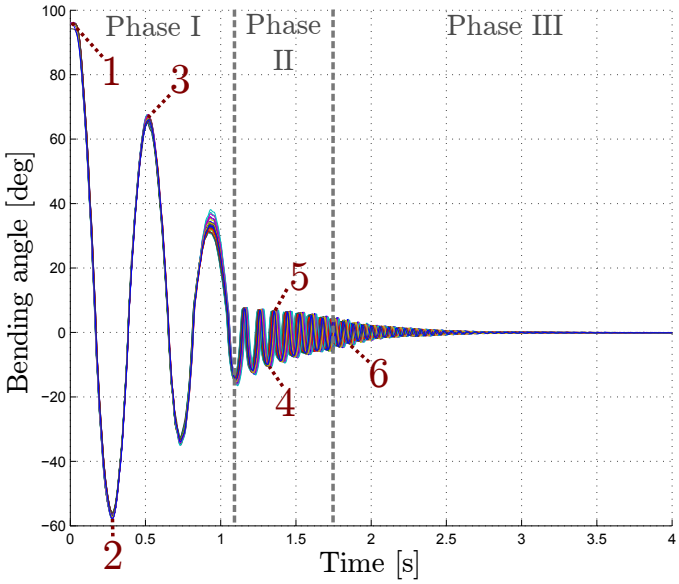

Figure 9.2: Experimental evolutions of the bending angle from the deployment tests in opposite sense.

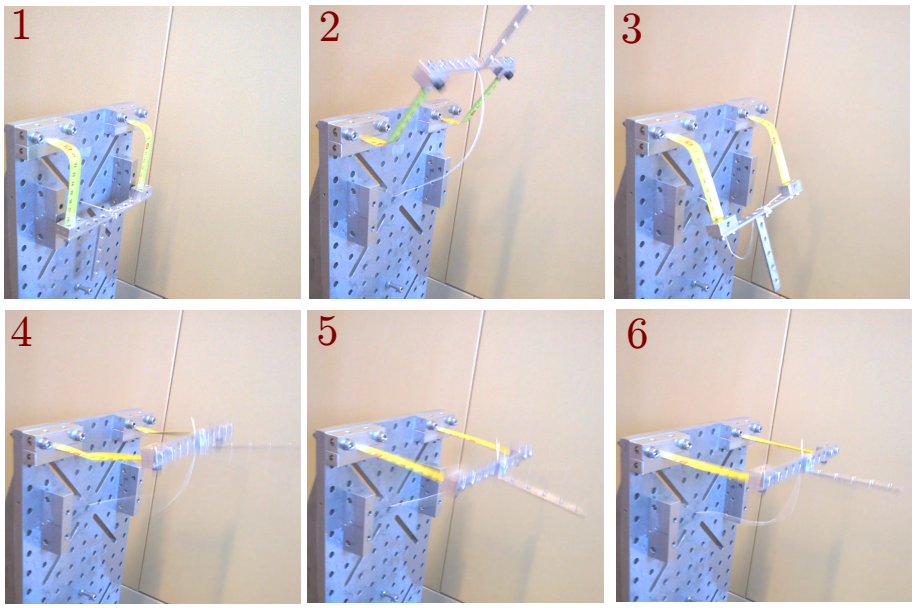

Figure 9.3: Deformed configuration of the experimental set-up in the different phases.

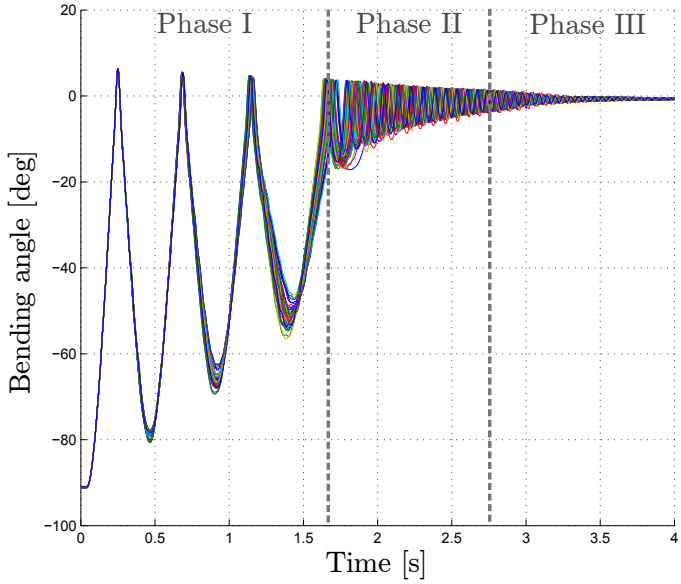

Figure 9.4: Experimental evolutions of the bending angle from the deployment tests in equal sense.

9.1.3 Reproducibility of the deployment tests

In order to assess the reproducibility of the experimental results, the variation coefficients (or relative standard deviations) of the peak amplitude and the peak time separation are computed for the first ten maximum and minimum peaks in Figure 9.5 obtained with two different pairs of tape springs in each sense (50 tests are performed on each pair, that is 100 tests in each sense). Regarding the peak time separation, it corresponds to the elapsed time between each peak.

The experimental tests show a good reproducibility for different tape springs and, as could be expected, the tests with an initial folding in equal sense are slightly less reproducible than the ones starting with a fold in opposite sense. It seems that the variability of these results is not dominated by the measurement uncertainties, but rather by the sensitivity of the mechanical response itself. Furthermore, the larger variation coefficients associated to the maximum amplitude peaks in equal sense are mostly due to their lower amplitudes, which are then more affected by small changes. Finally, the larger variations of the elapsed time between the peaks number 4 and 5 in equal sense are associated to the significant changes of amplitude between these peaks. This transition, at the beginning of phase II, is then harder to capture than the rest of the bending angle evolution.

Further information on the reproducibility of the tests can be found in Appendix B where the data are represented as histograms.

9.1.4 Evolution of the motion in the xz-plane

The deployments mainly remain in the xz-plane since the maximum lateral displacements reach amplitudes of 4.3 mm and 5.1 mm for initial foldings in opposite and equal sense respectively with respect to the equilibrium configuration. These values, measured at the tip of the appendix, correspond respectively to 1.82 % and 2.18 % of the longitudinal length of the set-up, without including the fixation support.

The trajectory of the appendix tip for a deployment with an initial folding in opposite sense in the xz-plane is illustrated in Figure 9.6 where the origin is centred on the equilibrium position.

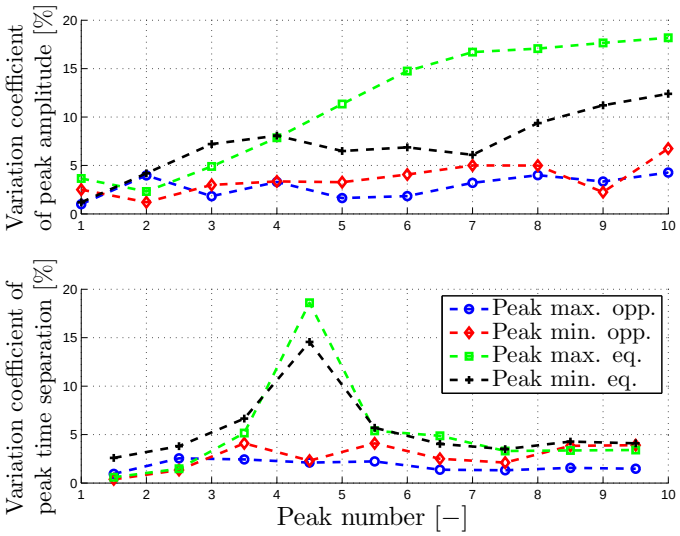

Figure 9.5: Variation coefficients of the first ten experimental peaks in amplitude and time separation of the bending angle for deployment tests.

The other marked points on the experimental curve correspond to the maximum and minimum peaks visible in Figure 9.2 during phase I, including the initial folded position. From this planar evolution, it can be seen that the oscillations remain close but are not perfectly superimposed and that, even if the trajectory looks circular at a first sight, it cannot be accurately captured by a single circular arc. Indeed, by fitting different sets of points, circles of different radii and centres are obtained. This behaviour can be explained by slight displacements of the folds along the tape springs.

9.1.5 Evolution of the vertical forces

Regarding the vertical forces measured at the base of the fixation support by the means of the force plate, the three phases defining the evolution of the associated bending angle are clearly visible (Figures 9.7 and 9.8 for an initial folding in opposite and equal sense respectively). Each large peak occurs when the bending angle is close to zero and is thus linked to the formation and the disappearance of folds or to rebounds depending on the phase. In phase I, the peaks are well separated since the motion frequency is low, in phase II, the frequency increases as well as the occurence of folds in equal sense, finally in phase III, the absence of large force peaks is in accordance with the absence of folds.

The complexity of the force curves hinders the development of a quantitative reproducibility analysis. However, qualitatively, the presence of all the characteristic features in the measured forces mentioned previously was confirmed visually in each individual test.

9.2 Finite element model

The finite element model used in the context of the deployment tests has the same characteristics as those described in Section 8.1. It implies thus that, in addition to the thickness and the Young's modulus, two numerical parameters have to be determined to define the model: the viscosity coefficient of the Kelvin-Voigt model η used to represent the structural damping of the set-up and the numerical damping ρ_∞ of the solver.

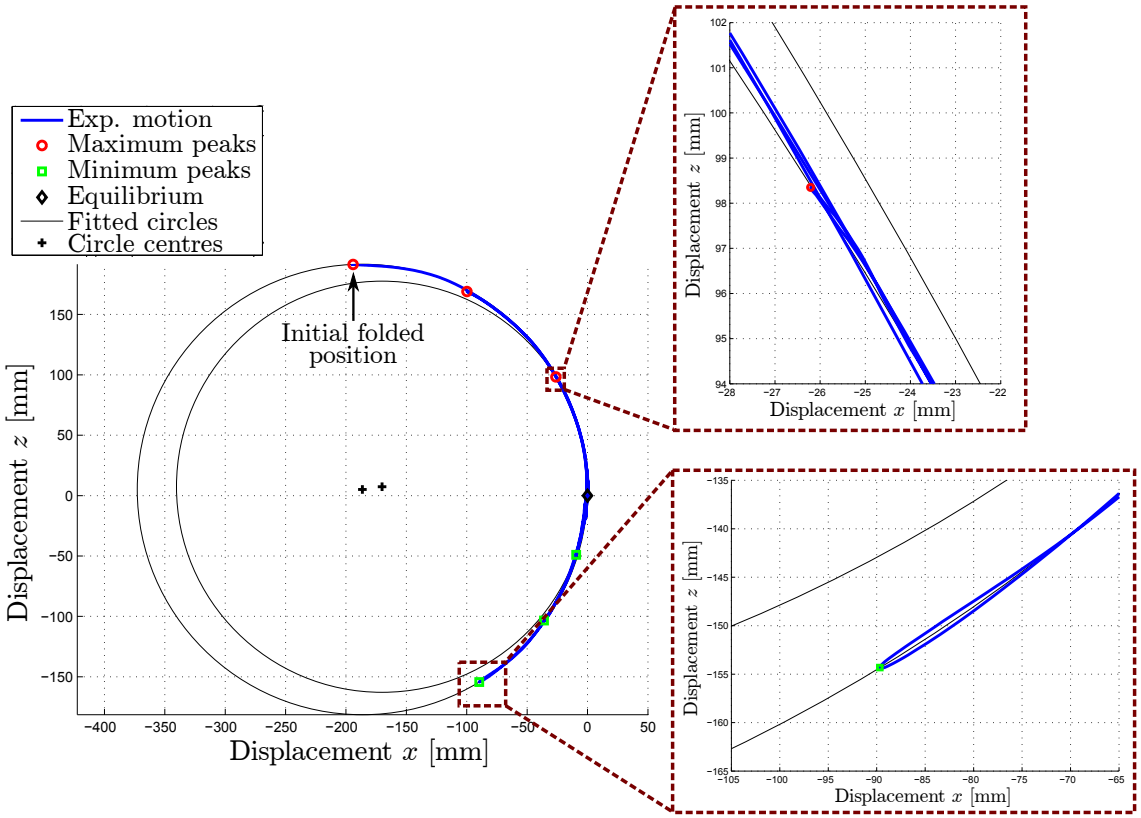

Figure 9.6: Experimental motion in the xz-plane of the appendix tip for an initial folding in opposite sense and fitted circles.

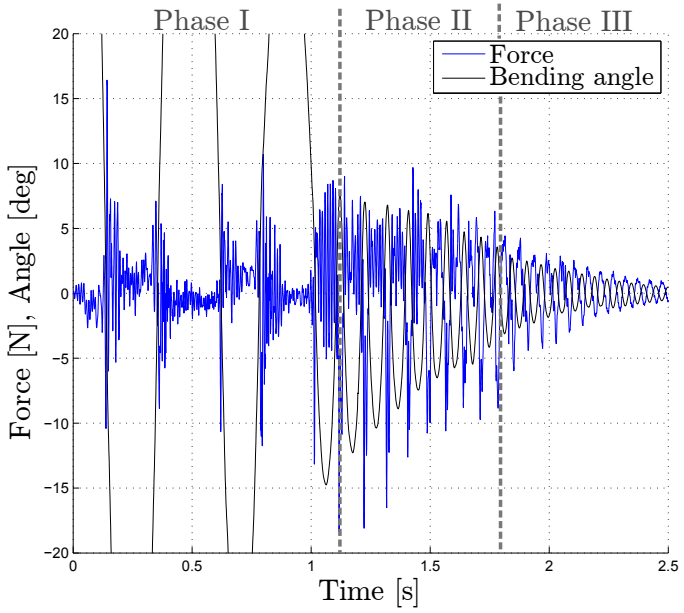

Figure 9.7: Experimental forces along the z-axis from the deployment tests with an initial folding in opposite sense, associated bending angle superimposed.

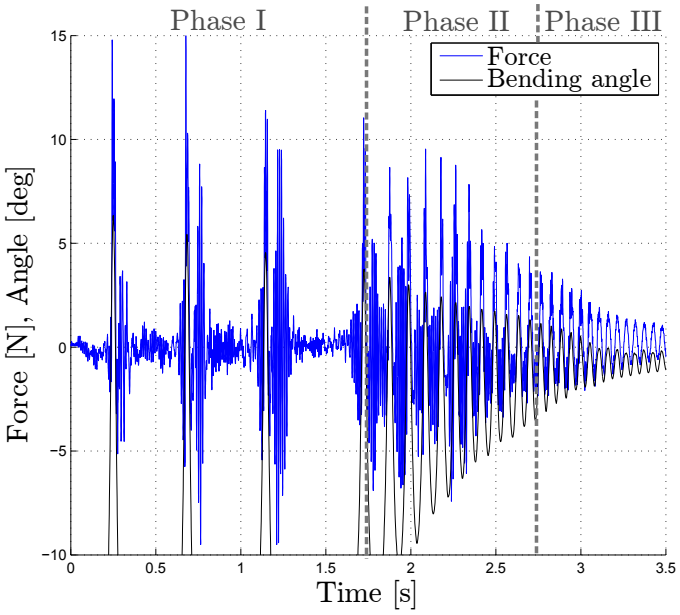

Figure 9.8: Experimental forces along the z-axis from the deployment tests with an initial folding in equal sense, associated bending angle superimposed.

9.2.1 Identification of the thickness and the Young's modulus

In the deployment tests, the whole motion is conditioned by the initial folded configuration and, most importantly, by the residual bending moment which triggers the passive deployment. It is then expected, based on the quasi-static analyses performed in the previous chapter, that the values of the thickness and the Young's modulus which should lead to the most accurate dynamic simulations are those which characterise the post-buckling behaviour of the tape springs. In the following finite element analyses, the parameters defined in Table 8.3 are then used.

9.2.2 Identification of the structural and numerical dampings

Experimental tests In order to evaluate the value of the viscosity coefficient η, the experimental set-up is submitted to small amplitude free vibrations at its free end. The displacements of the extremity are limited to small values to ensure that during the tests no fold is formed in the tape springs and their behaviour remains in the quasi-linear part described in Figure 2.1. Thus, it focuses on the phase III described in Section 9.1.1. As in the post-buckling quasi-static tests (Section 8.2.1), the dummy appendix is replaced by an additional weight (Figure 9.9) in order to reduce the frequency of these vibrations and improve the accuracy of the collected data.

Experimentally, the tests are performed with an initial vertical displacement around 8 mm reached by applying, manually, a vertical load on the additional weight, nevertheless, only the peaks belonging to the intervals $\pm[0.4; 4]$ mm are exploited. Indeed, displacements larger than 4 mm are too close to buckling and it cannot be assumed that the behaviour of the tape springs is still linear, while for displacements smaller than 0.4 mm, the experimental data are too altered by noise. One result of the small amplitude vibration tests is illustrated in Figure 9.10 in terms of displacements around the equilibrium configuration. It can be seen that the response is dominated by a single oscillation frequency and that the damping of the oscillations tends to follow an exponential decay.

Assuming that the system behaves as a damped single degree-of-freedom harmonic oscillator:

$$\ddot{z} + 2\varepsilon\omega_0\dot{z} + \omega_0^2 z = 0 \tag{9.1}$$

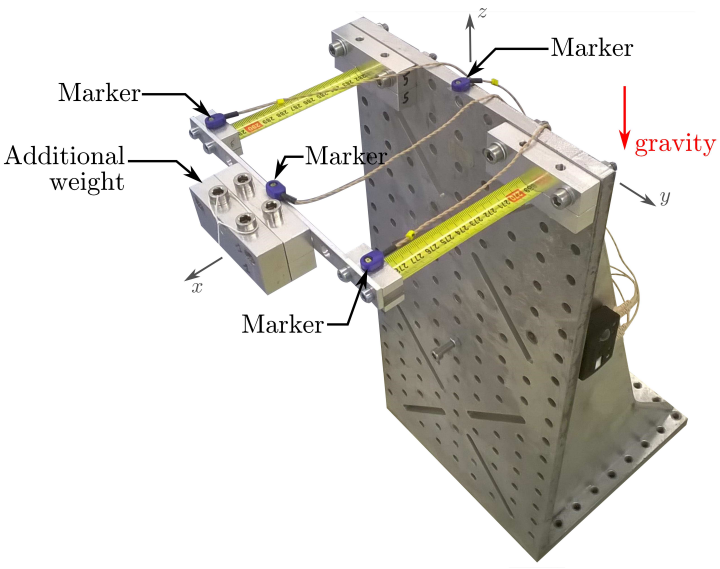

Figure 9.9: Experimental set-up used to perform small amplitude vibration tests and position of the markers.

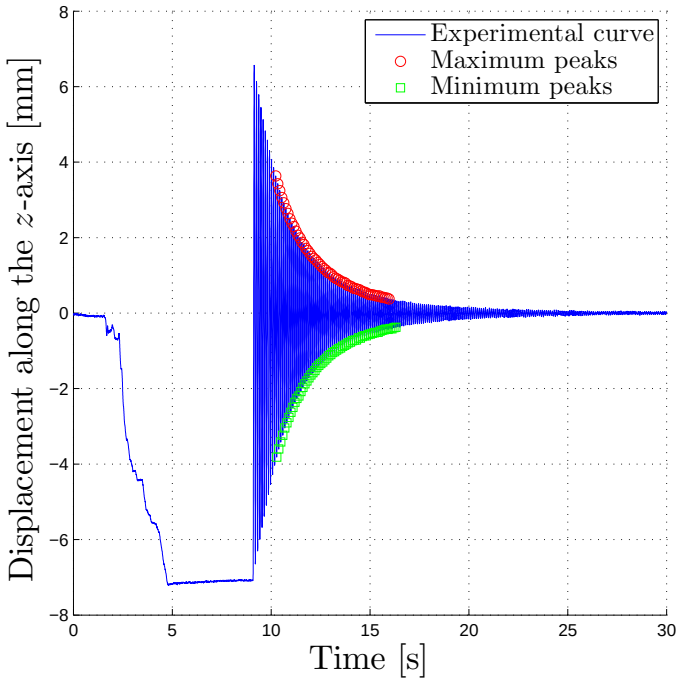

Figure 9.10: Experimental result of one small amplitude vibration test.

	Mean	Maximum difference	Variation coefficient
ε	0.509 %	0.288 %	20.67 %
Δt	0.100 s	0.003 s	0.919 %

Table 9.1: Experimental results from the small amplitude vibration tests with ε the structural damping and Δt the oscillation period.

the values of the natural pulsation ω_0 and the structural damping ε are fitted based on the peaks respecting the ranges previously mentioned and highlighted in Figure 9.10.

In total, 510 small amplitude vibration tests were performed on 4 different pairs of tape springs during 11 sessions of tests. After each session, mean values were determined for both the structural damping ε and the oscillation period Δt, this latter being used to solve the relationship:

$$\Delta t = \frac{2\pi}{\omega_0 \sqrt{1-\varepsilon^2}} \tag{9.2}$$

For information, it was not always possible to perform the same number of tests per session. The general mean on all the sessions is given in Table 9.1, along with the maximum difference noticed between sessions and the associated variation coefficient (or relative standard deviation).

It can be concluded from Table 9.1 that the experimental measurement of the structural damping ε is quite sensitive, its value experiencing significant changes from one session of tests to another. Several elements were identified to explain this lack of robustness. First of all, the structural damping is sensitive to the assembly of the set-up. Indeed, between sessions, disassembling and re-building the set-up with the same tape springs led to variations in the mean structural damping. Furthermore, changing the tape springs also impacts that parameter since the measuring tape from which they are cut out is probably not perfectly uniform. Finally, within a session of tests, the value of the structural damping tends to decrease as the number of tests increases as it can be seen in Figure 9.11. This behaviour is not clearly understood but is most likely due to thermal effects and unmodelled material phenomena.

Regarding the oscillation period Δt, this parameter is much less sensitive to all the disruptive elements mentioned previously and remains fairly stable between each session of tests.

Finally, as for the results of the deployment tests, histograms of the collected data on the structural damping and the oscillation period can be found in Appendix B.

Finite element model Numerically, the small amplitude vibration tests are performed on the finite element model illustrated in Figure 9.12. As it was done experimentally, a vertical load is applied on the additional weight to reach the initial vertical displacement, then the structure is left free to oscillate.

The solver used in this case is still the generalised-α method. In order to determine the most appropriate value of numerical damping ρ_∞ which has a limited impact on the results, but still allows the convergence of the solver and a reasonable computation time, a parametric study is performed for an arbitrary value of $\eta = 2.5e^{-4}$ s. In Figure 9.13, it can be seen that, as it was already shown in Chapter 6, an excessive increase of the amount of numerical damping (corresponding to a reduction of the value of ρ_∞) has a significant impact on the results of the small amplitude vibration tests, especially the structural damping. On the other hand, large values of ρ_∞ lead to larger computation time. In the following simulations, the value of the numerical damping ρ_∞ is then set to 0.7 which appears as a reasonable compromise.

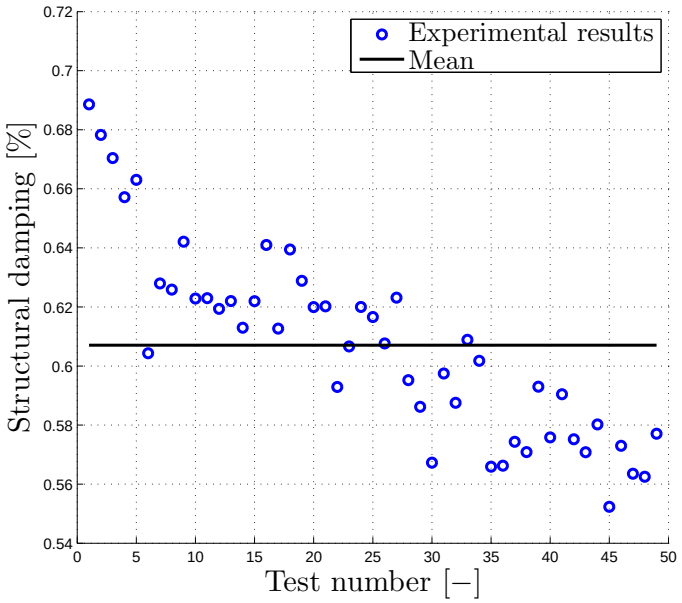

Figure 9.11: Evolution of the structural damping ε during the third session of small amplitude vibration tests.

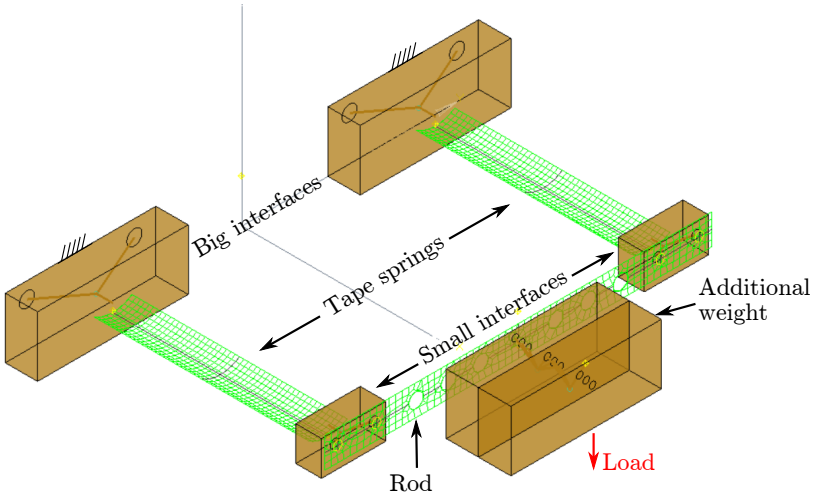

Figure 9.12: Finite element model used for the small amplitude vibration tests.

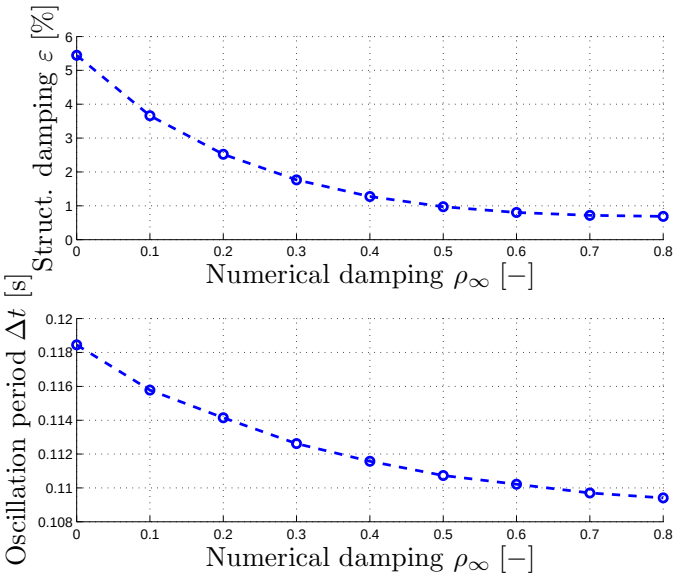

Figure 9.13: Impact of the numerical damping ρ_∞ on the structural damping ε and the oscillation period Δt for $\eta = 2.5e^{-4}$ s.

	Experimental	Numerical	Δ
ε	0.509 %	0.505 %	0.79 %
Δt	0.100 s	0.110 s	10 %
η	–	$1.73e^{-4}$ s	–

Table 9.2: Experimental and numerical results from the small amplitude vibration tests.

For a single degree of freedom system, the viscosity parameter η of the Kelvin-Voigt model is linearly related to the structural damping ε as:

$$\varepsilon = \frac{\eta}{2\omega_0 m} \tag{9.3}$$

where m is the mass. In the case of the finite element model in Figure 9.12, the linearity of the relationship is preserved under the small vibrations condition and the value of η can be adjusted to fit the exponential decay observed experimentally so that the experimental and numerical values of ε matched. For that purpose, the values of ε and Δt were extracted from the numerical results using the same procedure as the one developed to post-treat the experimental results, the correlation of Δt being verified *a posteriori*.

The final numerical results are given in Table 9.2 and compared to the experimental ones. It can be seen that there is a good agreement in the structural damping ε, but a bigger difference in the oscillation period Δt. This last observation can be explained by the fact that Δt mostly depends on the Young's modulus and the thickness which were here identified after a simplification of the tape springs definition (Section 8.2). Furthermore, the overestimation of Δt shows that, with the current parameters, the numerical model is less stiff than the experimental set-up as it was already the case in the quasi-static tests (Figure 8.5).

Estimation of air damping Knowing the global structural damping of the experimental set-up, the proportion of air damping can be estimated based on the equations introduced in Section 5.2. This estimation can be useful to adjust the model in order to better predict the response in vacuum. The mean logarithmic decrement in Eq. (5.1) is computed on the 510 small

amplitude vibration tests and is equal to:

$$\delta_{mean}^{global} = 0.029 \tag{9.4}$$

The variation coefficient of the experimental logarithmic decrement reaches 20.46 % which is logically similar to the variation coefficient of the structural damping (Table 9.1).

The amount of damping due to the surrounding air is evaluated based on Eq. (5.4) which represents a fair approximation of the logarithmic decrement in the case of low damping in thin cantilever beams. Since the structural damping is below 1 % and the tape springs behave like thin beams when they are submitted to small amplitude vibrations, Eq. (5.4) appears as a valid estimation of the air damping in the present case. The different parameters are fixed as follows:

- ▷ the air density ρ_f is 1.225 kg/m^3 at sea level and a temperature of 15° C;
- ▷ the drag coefficient C_D mainly depends on the shape of the moving body and is usually defined by a value lower than 2 [40]. Since the drag coefficient of the experimental set-up is unknown, its value is fixed to 3 in order to consider the worst case scenario;
- ▷ the surface area normal to the flow S measures 6.22 10^{-3} m^2 if the regions affected by the folds are considered as negligible;
- ▷ the tip amplitude X_n is fixed to its maximum value of 4 mm;
- ▷ the mass m is equal to 77 g;
- ▷ the mode shape contribution factor β_n is fixed to 1.473 since the set-up oscillates in its first bending mode (Table 5.1).

In the end, the logarithmic decrement due to air damping is:

$$\delta_{AD} = 0.0023 \tag{9.5}$$

This estimation represents 7.93 % of the global damping.

9.3 Correlation between the experimental and numerical results

After the identification of all the parameters required to build the finite element based in static and linear vibration tests, the dynamic deployment tests can be performed. At this level, no further calibration of the model was performed, *i.e.* the simulations are performed in a purely predictive manner.

In the finite element model, the deployment tests are divided into three phases: starting from the deployed configuration, the structure is folded by forcing the node representing marker 2 in Figure 7.7 to reach its initial position measured experimentally. This phase is performed at a displacement rate of less than 2 mm/s in order to have a quasi-static folding. Then the structure is stabilised in its folded configuration during 5 s. Finally, the deployment is triggered by removing the displacement constraint on marker 2.

Regarding deployment tests starting with an initial folding in opposite sense, the finite element model is able to correctly capture the three phases characterising the evolution of the bending angle as it can be seen in Figure 9.14 where the numerical simulation is superimposed on experimental results. The main discrepancy is an underestimation of the damping in phase III. In order to compare these results quantitatively, the difference, in absolute value, between the first ten maximum and minimum peaks in terms of amplitude and time separation is computed

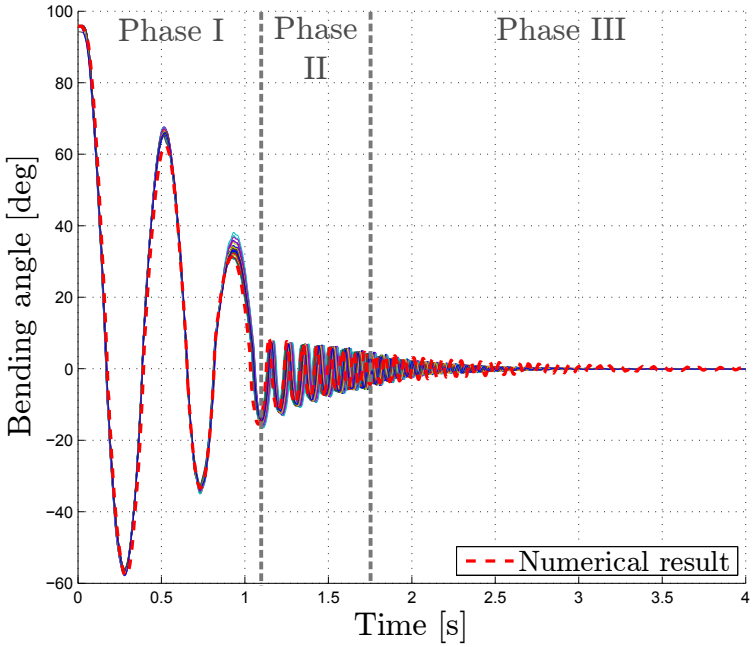

Figure 9.14: Qualitative comparison between the experimental and the numerical bending angles during the deployment tests in opposite sense.

(Figure 9.15). It can be seen that the differences mainly remain below 1.5° throughout the simulation without significant variation, except for the first maximum peak occurring around 0.5 s, while the elapsed time between the peaks is well captured. It can be concluded from this comparison that the behaviour of the finite element model deploying with an initial bending in opposite sense is validated.

In the case of an initial folding in equal sense (Figure 9.16), it can be seen that the finite element model is characterised by less damping than the experimental set-up, which results in an additional large amplitude peak around 2 s. Nonetheless, if that fourth peak is left aside, the quantitative comparison (Figure 9.17) shows that, in terms of amplitude, the main differences are encountered at the first three minimum peaks which are due to the underestimation of the damping. For the other minimum and all the maximum peaks, the differences remain stable and below 1.5°, as in the opposite sense case. Regarding the peak time separation, if the fourth peak is again discarded, it can be seen that the model is slightly less accurate for deployments in equal sense than in opposite sense.

Further investigations of the experimental set-up have shown that the motion triggered by an initial folding in equal sense is very sensitive to the initial conditions. For example, it is possible to recover a fourth large amplitude peak experimentally by changing the layout of the marker cables visible in Figure 7.7. The resulting evolution of the bending angle is given in Figure 9.18 with the associated numerical result. The finite element model shows a similar sensitivity. Indeed, by increasing the value of the damping parameter in the Kelvin-Voigt model to $\eta = 2.1e^{-4}$ s, it is possible to remove the fourth large amplitude peak (Figure 9.19).

Regarding the vertical forces that are experimentally measured at the base of the fixation support (Figure 9.20, blue curve) and numerically obtained at the clamped interface (Figure 9.20, red curve), disparities appear in terms of amplitude, but most importantly the high-frequency vibrations of small amplitude separating the experimental peaks are not captured numerically. However, by adding a flexible model of the support using a shell finite element mesh (Figure 9.21),

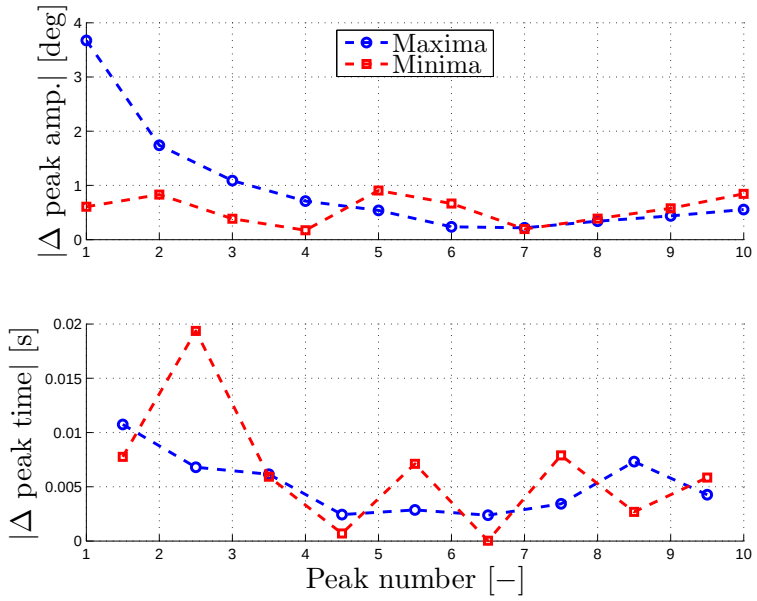

Figure 9.15: Quantitative comparison between the experimental and the numerical peak amplitude and peak time separation during the deployment tests in opposite sense.

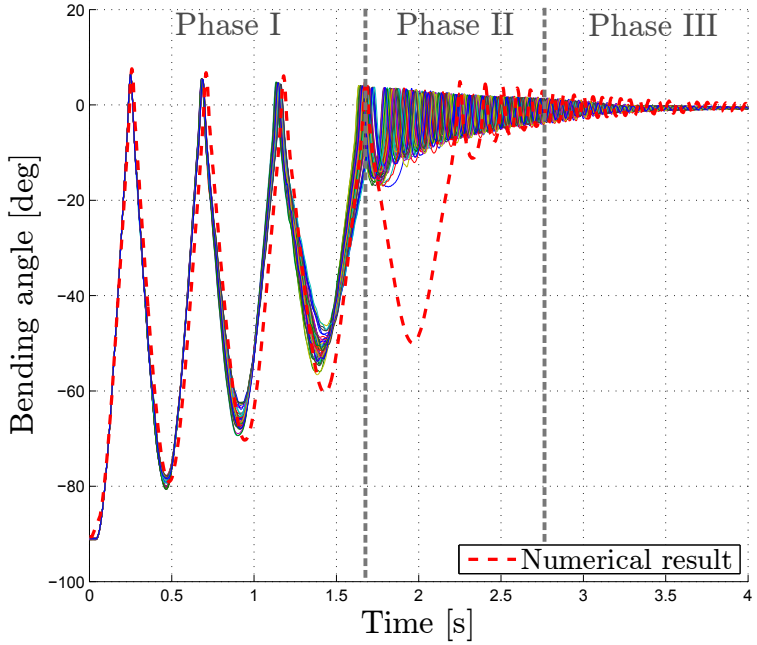

Figure 9.16: Qualitative comparison between the experimental and the numerical bending angles during the deployment tests in equal sense.

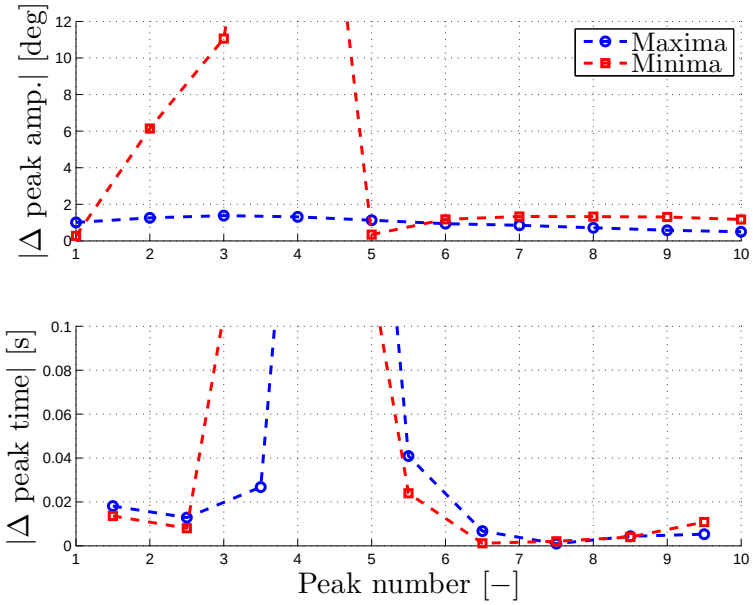

Figure 9.17: Quantitative comparison between the experimental and the numerical peak amplitude and peak time separation during the deployment tests in equal sense.

the high-frequency vibrations are recovered (Figure 9.20, green curve), but their amplitudes are overestimated and require more time to be damped out. A more detailed investigation of the flexibility of the support could be done in the future in order to better match the forces observed in the simulations and in the experiments. Alternatively, a stiffer support structure could be designed to reduce the influence of its flexibility.

9.4 Summary

Experimental deployment tests are performed to investigate the dynamic behaviour of tape springs. The post-processing shows that the evolution of the motion can be divided in three phases defined by different types of folds, frequencies of oscillation and damping behaviours, their characteristics being influenced by the initial sense of folding of the tape springs. These phases are also clearly visible in the evolution of the experimental loads affecting the structure. In the proposed set-up, this complex dynamic evolution remains mainly planar and shows a good reproducibility, especially for opposite sense motions.

In order to simulate the same tests with the finite element model of the set-up, the thickness and the Young's modulus extracted from a static analysis focusing on the post-buckling behaviour of the tape springs are used. Furthermore, the structural damping is evaluated based on small amplitude vibrations tests. They show that its value is subject to a high variability which is attributed to the assembly of the set-up, the non-uniformity of the tape springs, thermal effects and unmodelled material phenomena. Nonetheless, a simple material law defined by the Kelvin-Voigt model is sufficient to capture the essential nonlinear dynamic behaviours observed in the present tests.

For deployment tests with an initial folding in opposite sense, a good correlation between the experimental and numerical results is obtained. In the equal sense case, both the experimental set-up and the finite element model prove to be sensitive to the initial conditions and the system parameters. Finally, the transmitted forces experimentally measured at the base of the support are influenced by the flexibility of the support model.

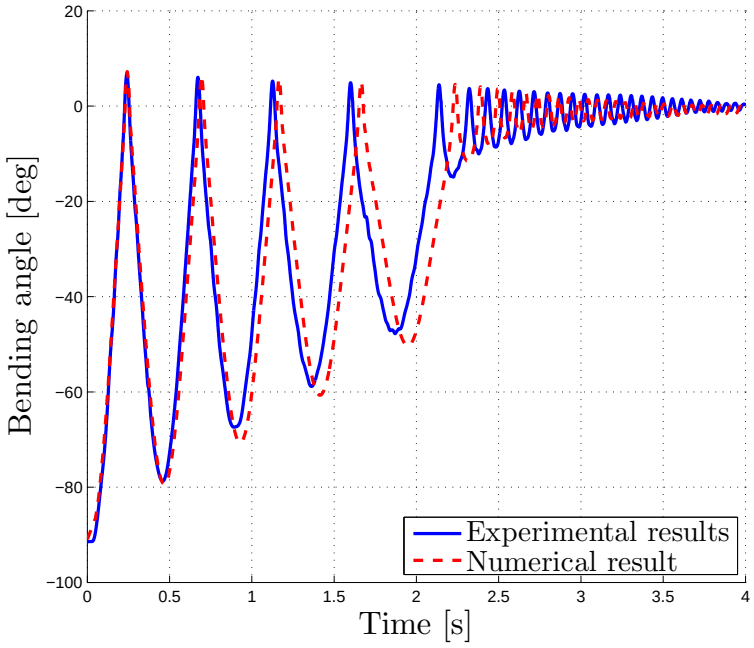

Figure 9.18: Deployment tests in equal sense: slightly disturbed experimental set-up.

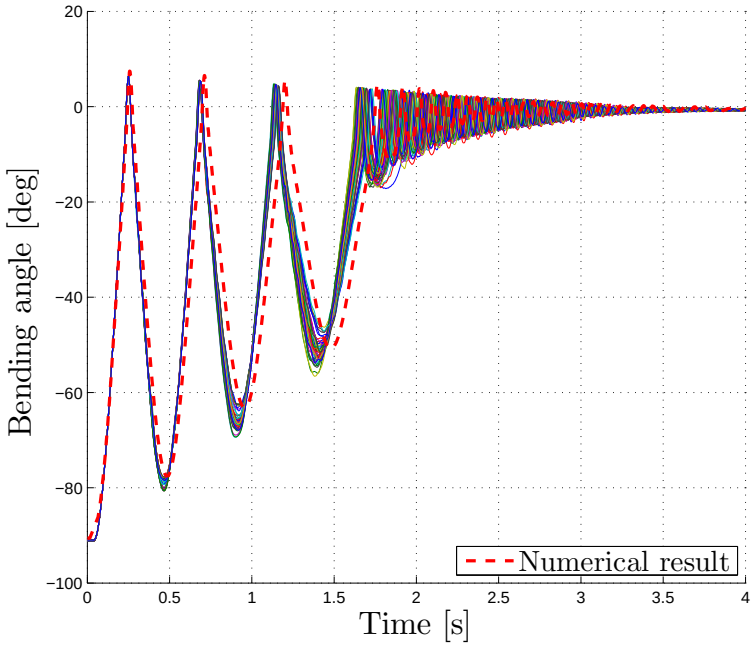

Figure 9.19: Deployment tests in equal sense: slightly disturbed finite element model.

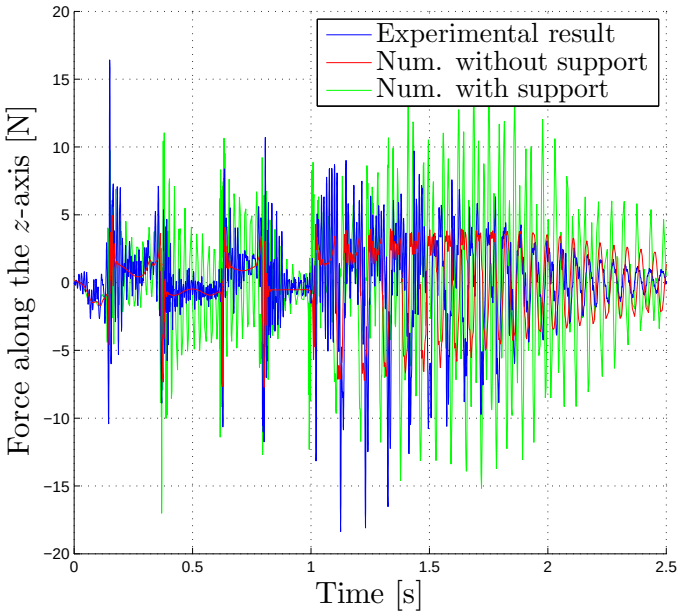

Figure 9.20: Qualitative comparison between the experimental and the numerical vertical forces during the deployment tests.

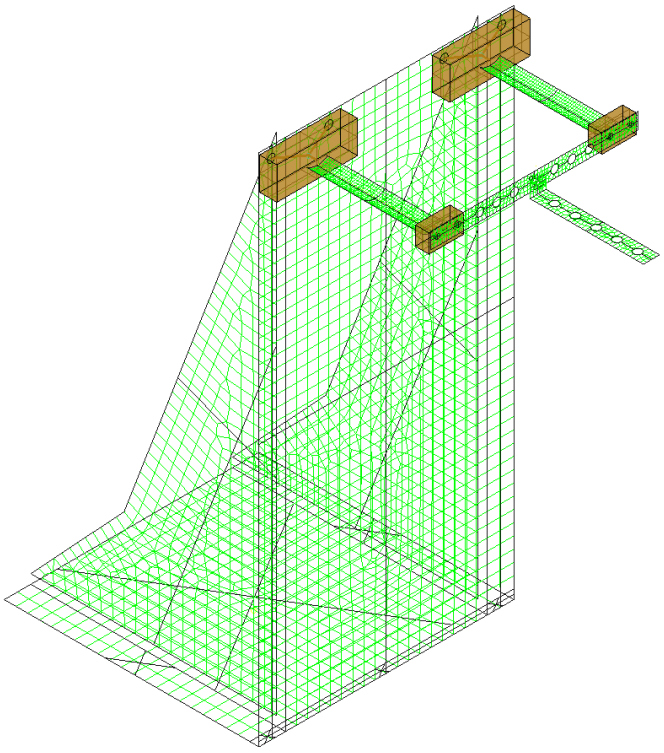

Figure 9.21: Finite element model of the experimental set-up with the fixation support modelled by shell elements.

CHAPTER 10

CONCLUSIONS AND PERSPECTIVES

10.1 Summary

In the present doctoral thesis, tape springs, belonging to the category of compliant mechanisms with major applications in deployable structures, have been studied in detail based on analytical models, numerical finite element simulations and experimental tests. Their static and dynamic responses are very rich and characterised by strongly nonlinear phenomena.

The nonlinear mechanical behaviour of tape springs was first defined based on fundamental concepts such as the dependence to the sense of bending, the formation of folds after buckling and the dissipation of energy by hysteresis. A large number of numerical analyses was then performed in order to evaluate the impact of each geometric parameter on the evolution of this behaviour and its characteristic features and on the modal content in terms of eigenfrequencies and mode shapes. These analyses highlighted the complexity of the nonlinear phenomena influencing the deformation of the tape springs and showed that their response is highly dependent on their geometry.

These models were then exploited for the design of a deployable reflector around a solar panel by the means of two tape springs. An optimisation procedure relying on finite element simulations was used to determine the geometric design variables, while respecting objective functions which combined the minimisation of the maximum Von Mises stress and of the maximum motion amplitude. The resulting optimised tape springs were then characterised by elastic deformations during the stages of folding and subsequent deployment and ensured a collision-free motion with the solar panel. These developments showed that the geometry of tape springs and the way they are combined to form a hinge can be designed to meet the specific requirements of the considered deployable structure.

The finite element models used in this application for the quasi-static folding of the tape springs and their dynamic deployments were further analysed in order to highlight the impact of the numerical damping needed for the convergence of the solver. It was shown that in quasi-static simulations, this parameter only has an impact on the time required to damp out the artificial oscillations after buckling, while all the other features remain stable. However, in dynamic analyses, if the model does not include any representation of the physical damping, the chosen amount of numerical damping clearly modifies the evolution of the deployments and reducing it does not lead to converged results.

A thorough analysis of the different physical forms of dissipation in structures and mechanical systems was then undertaken. A short review of physical damping phenomena showed that they can be found at several levels of a structure from phenomena occurring within the material to interactions between different components or with the environment. Based on a simple one-degree-of-freedom system, the impact of the structural and numerical dampings on the numerical solution was investigated. It was concluded that the numerical damping mainly filters high-frequency phenomena and guarantees the convergence of the solver, while on the other hand, the structural damping is dominant in the low-frequency domain where it is required to obtain a valid representation of the physical behaviour of the system. Regarding the dynamic behaviour of tape springs, it is necessary to include some structural damping in the model in order to ensure a correct representation of the damping of the oscillations after deployment and of the self-locking of the structure in its fully deployed state, as observed experimentally. Furthermore, it strongly reduces the dependence of the results on the numerical damping.

An experimental set-up was then designed in order to investigate the nonlinear phenomena present in the tape spring response, as well as to perform autonomous deployments despite the presence of the gravity field. The innovation for these tests came from the acquisition equipment which is able to triangulate the position of active markers in the 3D-space, while in the works found in the literature, the data are commonly collected in a 2D-space by the means of cameras. Furthermore, this motion analysis system was combined with a synchronised force plate which simultaneously captured the forces and moments affecting the structure.

The experimental tests were divided into two categories: quasi-static tests and dynamic deployment tests. In the first case, the main objective was the identification of equivalent values for the thickness and the Young's modulus in order to develop a finite element model of the experimental set-up. Different sets of parameters were determined whether the experimental tests focused on the pre- or post-buckling quasi-static behaviour which revealed a mitigated robustness and predictive capacity of the model. In the end, it was concluded that with the current modelling assumptions, the complete quasi-static response is difficult to reproduce numerically.

In experimental deployment tests, the post-processing showed that the evolution of the motion can be divided in three phases defined by different types of folds, frequencies of oscillation and damping behaviours, their characteristics being influenced by the initial sense of folding of the tape springs. These phases were also clearly visible in the evolution of the experimental loads affecting the structure. Furthermore, the experimental results showed a good reproducibility.

In order to numerically reproduce these tests, the thickness and the Young's modulus identified with a post-buckling quasi-static test were used and additional small amplitude vibration tests were performed to evaluate the structural damping of the set-up. For this last parameter, it was shown that the structural damping is subject to a high variability and is complex to evaluate accurately. Nonetheless, a simple material model defined by a single parameter was sufficient to capture the essential nonlinear dynamic behaviours observed in the present tests.

The comparison between the experimental and numerical results showed that for deployment tests with an initial folding in opposite sense, a good correlation was obtained without any additional fitting step. In the equal sense case, both the experimental set-up and the finite element model proved to be sensitive to the initial conditions and the system parameters. Regarding the transmitted forces at the base of the support, a significant dependency on the support flexibility defined in the model was uncovered.

10.2 Conclusions

The nonlinear mechanical behaviour of tape springs needs to be fully mastered for the design of deployable structures such as solar panels, antennas or masts which combine large amplitude self-actuated deployments, transient energy dissipation and the locking in a final configuration characterised by a large stiffness. This thesis has proposed a method to build reliable numerical models for that purpose.

The thorough analysis performed here on tape springs shows that these compliant elements can be modelled using nonlinear shell finite element models. Furthermore, the key parameters of the models can be identified based on a limited number of simple and reproducible experimental tests. For example, static post-buckling tests were performed to identify the thickness and the Young's modulus and small amplitude vibration tests were used to evaluate the structural damping. Thus, even if the studied components have a complex nonlinear behaviour, a numerical representation can be defined by following well-defined practical testing and identification procedures.

A comparison between the results from the finite element model and the experimental tests shows that, with the identified parameters, the model cannot reproduce all the quasi-static tests and that in most cases only a limited part of the quasi-static evolution, corresponding to either the pre- or post-buckling behaviour, is correctly simulated. However, with the parameters identified based on a post-buckling test, the dynamic model is shown to be predictive and the important transient characteristics are accurately captured.

The final dynamic model can then be exploited to evaluate and predict various quantities such as the trajectories of the structure during a deployment sequence and thus validate the absence of collision with the other components of the satellite, the vibrations and the shocks in order to check that they do not disrupt the effective operation of sensitive instruments and the stresses affecting the structure to confirm the absence of irreversible damage and ensure that, starting from a folded configuration, the sought deployed configuration will be recovered.

Finally, the study of a deployable reflector has demonstrated that dynamic models can be integrated in a design process in order to automatically determine the characteristics of the tape springs and validate the requirements of a specific application. Thus, a large number of designs can be simulated while limiting the number of time- and cost-consuming experimental tests.

10.3 Perspectives

Tape springs are mainly used to deploy appendices on satellites. The most common ones are solar panels, antennas and masts, but more complex structures are currently under study such as solar sails [46, 96], telescopes [11] or inflatable structures [26]. For each application, the geometric and material characteristics of the tape springs have to be determined, as well as their number, the location of their attachment points and their orientation. Both the experimental and numerical procedures introduced in this thesis could then be transposed to other experimental set-ups with different layouts of tape springs.

In the context of this thesis, the tape springs used in the experimental tests were cut out from a regular measuring tape and were thus made of a metallic core covered with plastic layers. However, other materials could also be considered such as purely metallic tapes, as for example in the case of Maeva hinges [33, 97], with well-controlled material and geometric properties or carbon fibre reinforced polymer (CFRP) which is a common alternative [11, 14, 18, 96, 112].

The increasing interest for this material is due to the higher stiffness-to-mass ratio compared to metallic tape springs, their higher flexibility and the larger number of customisation possibilities during their manufacturing [11].

Furthermore, as it was evaluated in Section 9.2.2, the tape springs studied in this work have a rather low level of structural damping while in practice, a higher level would present several advantages such as a reduction of the transmitted shocks and vibrations to the rest of the satellite components and in particular the sensitive instruments, and a reduction of the time lapse required to reach a stabilised deployed configuration. The structural damping in tape springs can be improved by adding a layer of non-metallic material with good dissipation properties such as polymers or cork and are currently under study in the industry. Finally, the improvements reached with these new elements could be measured by performing experimental tests analogous to those presented in this work.

In the end, whatever the number of tape springs used to deploy an appendix, their configuration and their characteristics, the final objective of the designers is often to validate the deployment sequence. In this thesis, the deployment tests performed with the experimental set-up led to limited transversal displacements and thus predominantly planar motions. Nonetheless, the acquisition equipment is suitable to acquire data during large three-dimensional motions with more complex initial folded configurations that could be required to fit in the available space inside the fairing of the launcher.

Finally, in practice, the deployments are performed in space, that is a vacuum zero-g environment. The resulting finite element models obtained here at the end of the identification procedures show a fair robustness, especially regarding the deployments with an initial folding in opposite sense. The model could then be extrapolated to simulate its evolution under these different conditions. Experimentally, a zero-g state could be approached by combining a gravity compensation system with the experimental set-up developed in this thesis. To this end, lines of inquiries and first elements of design were investigated based on kinematic and dynamic analyses in a master thesis [67] supervised during the achievement of this work. The proposed system still requires a more thorough design process, which could be efficiently supported by extended versions of the numerical models and experimental set-ups developed in this thesis.

APPENDIX A

DETAILED ANALYTICAL DEVELOPMENTS

A.1 Wüst's theory [111]

The main hypothesis of Wüst's theory is to consider that a tape spring with a small initial transversal curvature κ_t subtending an angle α smaller than 1 rad can be studied as the shell of an axisymmetric cylinder submitted to pure bending (Figure 2.2). Furthermore, the length L of the tape spring is considered infinitely long to be free of end effects by the principle of Saint-Venant. Finally, the deformed configuration is induced by two identical end moments M which create a uniform longitudinal curvature κ_l of corresponding radius r_l. The other parameters illustrated in Figure 2.2 are the transverse radius of curvature R, the thickness t, the height of the tape spring cross-section h and the width of the tape spring cross-section w.

Starting from the theory of shells from Calladine [19, 94], the bending moments per unit length can be linked to the variations of the transversal and longitudinal curvatures by the expressions:

$$m_{yx} = D[\kappa_t + \nu\kappa_l] \tag{A.1}$$

$$m_{xy} = D[\kappa_l + \nu\kappa_t] \tag{A.2}$$

where the subscripts of m_{yx} (resp. m_{xy}) means that the moment acts around the y-axis (resp. x-axis) on a face with a normal along the x-axis (resp. y-axis), D is the flexural rigidity which is given in the case of a plate by $D = \frac{Et^3}{12(1-\nu^2)}$, E is the Young's modulus and ν is the Poisson's ratio.

Initially, the transversal and longitudinal curvatures are respectively equal to $\kappa_t = -1/R$ and $\kappa_l = 0$. Due to the application of end bending moments, the curvatures change in the deformed configuration as follows:

$$\kappa_t = \frac{d^2u(y)}{dy^2} + \frac{1}{R} \tag{A.3}$$

$$\kappa_l = \frac{1}{r_l} \tag{A.4}$$

where $u(y)$ is the out of plane deflection in the z-direction measured from the undeformed configuration of the axisymmetric cylinder. Substituting these expressions in the bending moments per unit length, Eqs. (A.1) and (A.2), gives:

$$m_{yx} = \frac{Et^3}{12(1-\nu^2)}\left[\frac{d^2u(y)}{dy^2} + \frac{1}{R} + \nu\frac{1}{r_l}\right] \tag{A.5}$$

$$m_{xy} = \frac{Et^3}{12(1-\nu^2)}\left[\frac{1}{r_l} + \nu\left(\frac{d^2u(y)}{dy^2} + \frac{1}{R}\right)\right] \tag{A.6}$$

According to Calladine [19], the out of plane displacement $u(y)$ of an axisymmetric shell verifies an ordinary differential equation of the fourth order. The general solution of this equation can be expressed as the sum of four products between hyperbolic and trigonometric functions. In this particular case, $u(y)$ must be symmetric and two terms of the sum can be eliminated. The solution is then:

$$u(y) = C_1 \cosh\left(\frac{ny}{r_l}\right)\cos\left(\frac{ny}{r_l}\right) + C_2 \sinh\left(\frac{ny}{r_l}\right)\sin\left(\frac{ny}{r_l}\right) \tag{A.7}$$

where $n = \sqrt[4]{3(1-\nu)^2}\sqrt{\dfrac{r_l}{t}}$ to simplify the expression.

Two boundary conditions are required to identify the two integration constants C_1 and C_2. Based on how the bending moments are applied in Figure 2.2b, it can be seen that no force or moment is acting on the longitudinal sides of the tape spring. This corresponds to cancelling the shear force s_y on faces with a normal along the y-axis and the bending moment m_{yx} per unit length, or:

$$s_y = \frac{dm_{yx}}{dy} = 0 \quad \text{and} \quad m_{xy} = 0 \quad \text{for } y = \pm\frac{1}{2}\alpha R \tag{A.8}$$

Strictly speaking, these boundary conditions are only valid when the transversal curvature κ_t is equal to zero. Indeed, the edges of the plate representing the tape spring have a position in the y-direction of $\pm\frac{1}{2}\alpha R$ only when it is flat. Nevertheless, these values are used since the transversal curvature κ_t is considered relatively small and thus the boundary conditions do not differ much from the real values.

After solving the two equations in Eq. (A.8), one finds:

$$C_1 = -\frac{r_l^2}{2n^2}\left(\frac{1}{R} + \nu\frac{1}{r_l}\right)\frac{\cosh\beta\sin\beta - \sinh\beta\cos\beta}{\cosh\beta\sinh\beta + \cos\beta\sin\beta} \tag{A.9}$$

$$C_2 = \frac{r_l^2}{2n^2}\left(\frac{1}{R} + \nu\frac{1}{r_l}\right)\frac{\cosh\beta\sin\beta + \sinh\beta\cos\beta}{\cosh\beta\sinh\beta + \cos\beta\sin\beta} \tag{A.10}$$

with $\beta = \dfrac{nR\alpha}{2r_l}$.

Wüst finds then the following integral which links the applied bending moment to the longitudinal curvature of the tape spring:

$$M = \int_{-\frac{R\alpha}{2}}^{\frac{R\alpha}{2}} (m_{xy} - n_x u)\, dy \tag{A.11}$$

where n_x is the normal force per unit length along the x-axis such that $n_x = Et\kappa_l u$. As mentioned for the boundary conditions, the integral boundaries are also, in theory, only valid for a plate with no transversal curvature.

The resolution of the integral gives [76]:

$$M = \frac{\alpha R t^3 \kappa_l}{12}\frac{E}{1-\nu^2}\left[\left(1 + \nu\frac{1}{\kappa_l R}\right) - \nu\left(\frac{1}{\kappa_l R} + \nu\right)P_1 + \left(\frac{1}{\kappa_l R} + \nu\right)^2 P_2\right] \tag{A.12}$$

$$= \frac{\alpha R t^3}{12}\frac{E}{R(1-\nu^2)}\left[(\nu + R\kappa_l) - \nu(1+\nu R\kappa_l)P_1 + (1+\nu R\kappa_l)^2\frac{P_2}{\kappa_l R}\right] \tag{A.13}$$

with

- $P_1 = \dfrac{2}{\lambda}\dfrac{\cosh\lambda - \cos\lambda}{\sinh\lambda + \sin\lambda}$
- $P_2 = \dfrac{1}{2\lambda}\dfrac{\cosh\lambda - \cos\lambda}{\sinh\lambda + \sin\lambda} - \dfrac{\sinh\lambda \sin\lambda}{(\sinh\lambda + \sin\lambda)^2}$
- $\lambda = \sqrt[4]{3(1-\nu^2)}\sqrt{\dfrac{\kappa_l R^2 \alpha^2}{t}}$

This result is only valid in opposite sense bending since it is only characterised by flexural deformations. Indeed, this analytical model does not take into account torsional deformations which appear in the case of equal sense bending.

A.2 Mansfield's theory [66]

The theory developed by Mansfield [66] exploits the non-linear equations describing the behaviour of large deflections in long strips either of lenticular or constant thickness. Only the second situation is of interest in the case of the tape springs considered in this work. This theory also captures the bending and, unlike Wüst's theory, the torsion characterising the deformation of tape springs.

The hypotheses that guarantee the validity of this theory are the following. First of all, the rotations and the slopes are assumed small everywhere as it is commonly done in the theory of plates submitted to large deflections. The *everywhere* condition can be relaxed to *a length equal to the width of the plate* in particular cases when all the sections behave in the same manner. Furthermore, as in the theory developed by Wüst, the tape spring is considered infinitely long in order to avoid taking into account end effects. Finally, the reference coordinate system and the characteristics of the tape spring used in these developments are given in Figure 2.3.

In the case of tape springs, the longitudinal, transversal and torsional curvatures are respectively:

$$\kappa_{x,0} = 0 \qquad \kappa_{y,0} \neq 0 \qquad \kappa_{xy,0} = 0 \tag{A.14}$$

in the undeformed configuration. Then, in a stress-free state, the out of plane deflection in the w-direction is given by:

$$w_0 = \frac{1}{2}\kappa_{y,0} y^2 \tag{A.15}$$

On the contrary, when the plate is submitted to end moments and torques, the deflection becomes:

$$w = \frac{1}{2}\kappa_x x^2 + \kappa_{xy} xy + w^*(y) \tag{A.16}$$

where κ_x and κ_{xy} are respectively the current longitudinal and torsional curvature and $w^*(y)$ is the chordwise distortion of the tape spring for which a differential equation can be derived through a variational method.

Starting from a flat state for which $w = 0$, the longitudinal strains can be determined as:

$$\varepsilon_x = \frac{1}{2} y^2 \kappa_{xy}^2 - \kappa_x w^*(y) + A + By \tag{A.17}$$

where A and B are constants such that the equilibrium in the plane of the tape spring is verified. For a tape spring of constant thickness t, one finds:

$$\begin{cases} A &= -\dfrac{1}{24}\, a^2 \kappa_{xy}^2 \\ B &= 0 \end{cases} \tag{A.18}$$

The total strain energy per unit length can then be decomposed into two terms. The first one represents the strain energy per unit length due to the longitudinal stresses in the neutral surface which is given by:

$$V_m = \frac{1}{2}\int_{-\frac{1}{2}a}^{\frac{1}{2}a} Et\varepsilon_x^2 \, dy \tag{A.19}$$

while the second term is the flexural strain energy per unit length whose expression is:

$$V_f = \frac{1}{2}\int_{-\frac{1}{2}a}^{\frac{1}{2}a} D\left[\left(\frac{d^2w^*}{dy^2}+\kappa_x\right)^2 - 2(1-\nu)\left(\kappa_x\left(\frac{d^2w^*}{dy^2}-\kappa_{y,0}\right)-\kappa_{xy}^2\right)\right] dy \tag{A.20}$$

The total strain energy per unit length is finally:

$$V = V_m + V_f \tag{A.21}$$

The deformed configuration must be associated to a total strain energy that is minimum with respect to w^*. This condition implies that w^* must respect the following differential equation in the case of a general strip:

$$\frac{d^2}{dy^2}\left[D\left(\frac{d^2w^*}{dy^2}-\kappa_{y,0}+\nu\kappa_x\right)\right] - Et\kappa_x\left[\frac{1}{2}y^2\kappa_{xy}^2 - \kappa_x w^* - \frac{1}{24}a^2\kappa_{xy}^2\right] = 0 \tag{A.22}$$

This differential equation is of the fourth order and characterised by four boundary conditions. As it can be seen in Figure 2.3, only the extremities of the tape spring are submitted to moments, the rest of the structure being stress-free. This configuration is then expressed as:

$$\left[D\left(\frac{d^2w^*}{dy^2}-\kappa_{y,0}+\nu\kappa_x\right)\right]_{y=\pm\frac{1}{2}a} = 0 \tag{A.23}$$

$$\left[\frac{d}{dy}\left(D\left(\frac{d^2w^*}{dy^2}-\kappa_{y,0}+\nu\kappa_x\right)\right)\right]_{y=\pm\frac{1}{2}a} = 0 \tag{A.24}$$

In the particular situation of a tape spring with constant thickness, the differential equation Eq. (A.22) becomes:

$$\frac{1}{4k^4}\frac{d^4w^*}{dy^4} + w^* = Q\left(y^2 - \frac{a^2}{12}\right) \tag{A.25}$$

with $k^4 = \frac{Et\kappa_x^2}{4D}$ and $Q = \frac{\kappa_{xy}^2}{2\kappa_x}$. The solution to this equation that satisfies the four boundary conditions is after calculations:

$$w^*(y) = Q\left(y^2 - \frac{a^2}{12}\right) + C_1\cosh(ky)\cos(ky) + C_2\sinh(ky)\sin(ky) \tag{A.26}$$

with

- $C_1 = P\dfrac{\cos\phi\sinh\phi - \cosh\phi\sin\phi}{\cosh\phi\sinh\phi + \cos\phi\sin\phi}$
- $C_2 = P\dfrac{\cos\phi\sinh\phi + \cosh\phi\sin\phi}{\cosh\phi\sinh\phi + \cos\phi\sin\phi}$
- $P = \dfrac{\kappa_{y,0} - \nu\kappa_x - 2Q}{2k^2}$
- $\phi = \dfrac{1}{2}ka$

To get a simplified expression of the relation linking the bending moment M to the curvature and the torque T to the twist, Mansfield introduced non-dimensional parameters:

$$\{\bar{\kappa}_{y,0}, \bar{\kappa}_x, \bar{\kappa}_{xy}\} = \frac{a^2\sqrt{3(1-\nu^2)}}{4t}\{\kappa_{y,0}, \kappa_x, \kappa_{xy}\} \tag{A.27}$$

$$\bar{M} = \frac{3a\sqrt{3(1-\nu^2)}}{Et^4}M \tag{A.28}$$

$$\bar{T} = \frac{6a(1+\nu)\sqrt{3(1-\nu^2)}}{4Et^4}T \tag{A.29}$$

$$\bar{V} = \frac{9a^3(1-\nu^2)}{4Et^5}V \tag{A.30}$$

Starting from Eq. (A.21), substituting the expression of $w^*(y)$ of Eq. (A.26) and making use of the non-dimensional parameters, the new formulation of the strain energy per unit length can be found as:

$$\bar{V} = \frac{1}{2}\bar{\kappa}_x^2 + \frac{\bar{\kappa}_{xy}^2}{1+\nu} + \frac{\lambda^2\Phi_1(\bar{\kappa}_x)}{2(1-\nu^2)} \tag{A.31}$$

which leads to the expression of the non-dimensional bending moment:

$$\bar{M} = \frac{\partial V}{\partial \kappa_x} \tag{A.32}$$

$$= \bar{\kappa}_x + \frac{\lambda}{1-\nu^2}\left(\mu\Phi_1(\bar{\kappa}_x) - \lambda\bar{\kappa}_x\Phi_2(\bar{\kappa}_x)\right) \tag{A.33}$$

and of the non-dimensional torque:

$$\bar{T} = \frac{1+\nu}{2}\frac{\partial V}{\partial \kappa_{xy}} \tag{A.34}$$

$$= \kappa_{xy} - \kappa_{xy,0} + \frac{\lambda\kappa_{xy}\Phi_1(\kappa_x)}{1-\nu} \tag{A.35}$$

with the following parameters:

- $\lambda = \bar{\kappa}_{xy}^2 + \bar{\kappa}_x(\nu\bar{\kappa}_x - \bar{\kappa}_{y,0})$
- $\mu = 2\nu\bar{\kappa}_x - \bar{\kappa}_{y,0}$
- $\Phi_1(\bar{\kappa}_x) = \dfrac{1}{\bar{\kappa}_x^2}\left[1 - \dfrac{1}{\sqrt{\bar{\kappa}_x}}\dfrac{\cosh(2\sqrt{\bar{\kappa}_x}) - \cos(2\sqrt{\bar{\kappa}_x})}{\sinh(2\sqrt{\bar{\kappa}_x}) + \sin(2\sqrt{\bar{\kappa}_x})}\right]$
- $\Phi_1(\bar{\kappa}_x = 0) = \dfrac{4}{45}$
- $\Phi_2(\bar{\kappa}_x) = \dfrac{1}{\bar{\kappa}_x^4}\left[1 + \dfrac{\sinh(2\sqrt{\bar{\kappa}_x})\sin(2\sqrt{\bar{\kappa}_x})}{(\sinh(2\sqrt{\bar{\kappa}_x}) + \sin(2\sqrt{\bar{\kappa}_x}))^2} - \dfrac{5}{4\sqrt{\bar{\kappa}_x}}\dfrac{\cosh(2\sqrt{\bar{\kappa}_x}) - \cos(2\sqrt{\bar{\kappa}_x})}{\sinh(2\sqrt{\bar{\kappa}_x}) + \sin(2\sqrt{\bar{\kappa}_x})}\right]$
- $\Phi_2(\bar{\kappa}_x = 0) = \dfrac{32}{2835}$

Contrary to Wüst's theory, an expression of the torque due to the torsional deformations of the tape spring is then obtained.

APPENDIX B

HISTOGRAMS OF THE EXPERIMENTAL DATA

This appendix presents the histograms of the experimental data collected during the deployment tests described in Section 9.1 and the small amplitude vibration tests in Section 9.2.2.

A histogram is a graphical representation of data which shows how they are distributed on non-overlapping intervals called *bins*. The choice is made for the deployment tests to use the following definition to define the width of the bins:

$$k = \frac{n}{3} \tag{B.1}$$

where k is the number of equal width bins and n the number of data, and for the small amplitude vibration tests to use:

$$k = \sqrt{n} \tag{B.2}$$

Other definitions for the bin width and more information on histograms can be found in [99].

B.1 Deployment tests

It can be seen from Figures B.1 and B.2, which respectively show some histograms of the peak amplitudes in the case of an initial folding in opposite and equal sense, that various evolutions are encountered. For example in Figure B.1, for the third maximum peak and the second minimum peak, the histograms appear to be closer to Gaussian distributions than the other represented results. A second interesting type of histograms is visible for the first minimum peak in opposite sense and the first maximum peak in equal sense where the data are clearly separated in two groups. It can be seen that 50 occurrences are present in each group which can be explained by the fact that two series of 50 tests were performed with two different pairs of tape springs. Changing the tape springs has then a clear impact on the results for these two peaks. However, in general, more complex patterns are visible and should be put in parallel with the variation coefficients given in Figure 9.5 to validate the reproducibility of the experimental tests.

B.2 Small amplitude vibration tests

Regarding the results extracted from the small amplitude vibration tests (Section 9.2.2), the histograms for the structural damping (Figure B.3) and the oscillation period (Figure B.4) lead to the same conclusions that were summarised in Table 9.1, that is that the collected values of the structural damping are subject to large variations, while the values of the oscillation period remain inside a small interval.

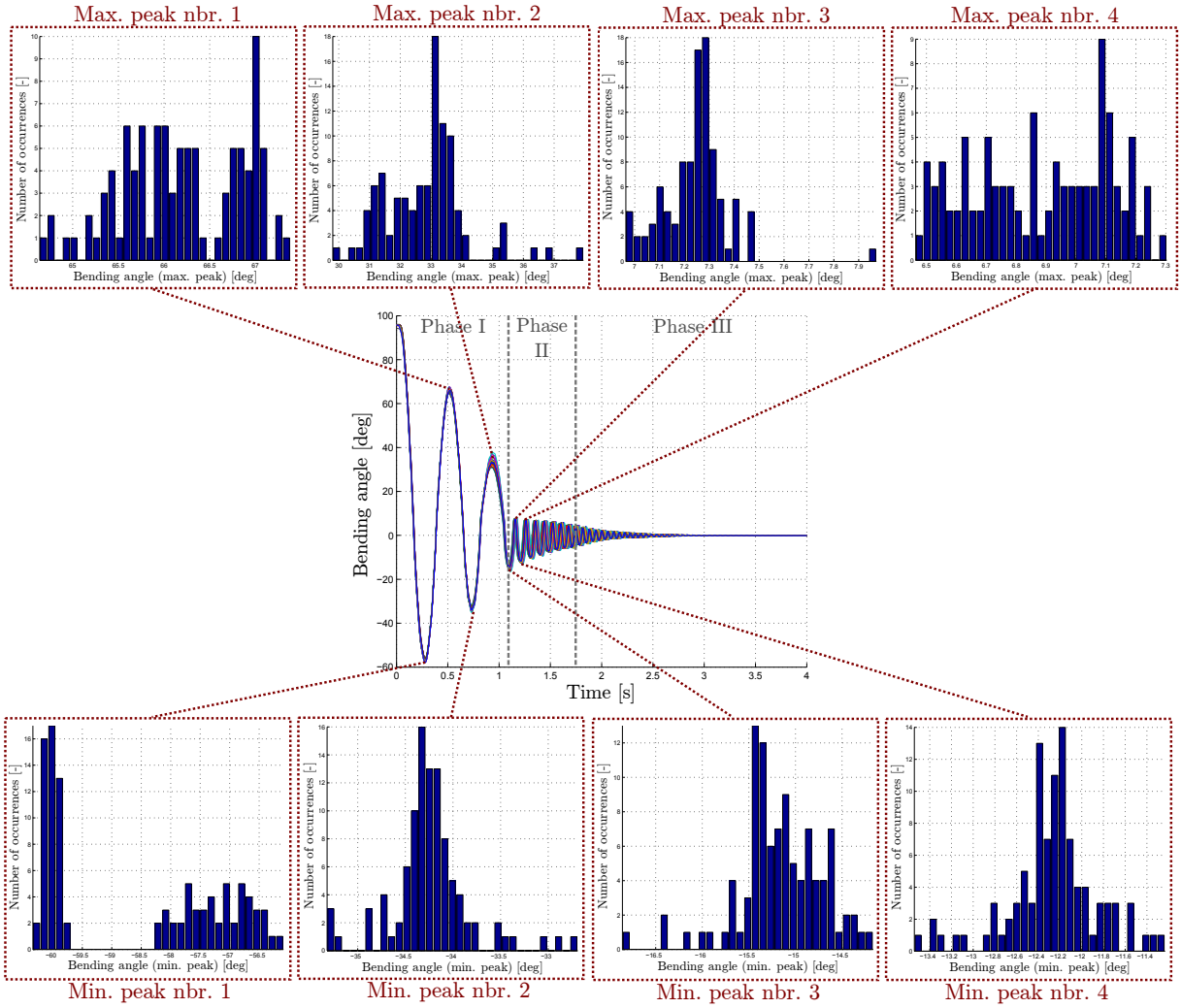

Figure B.1: Histograms of some peak amplitudes for an initial folding in opposite sense.

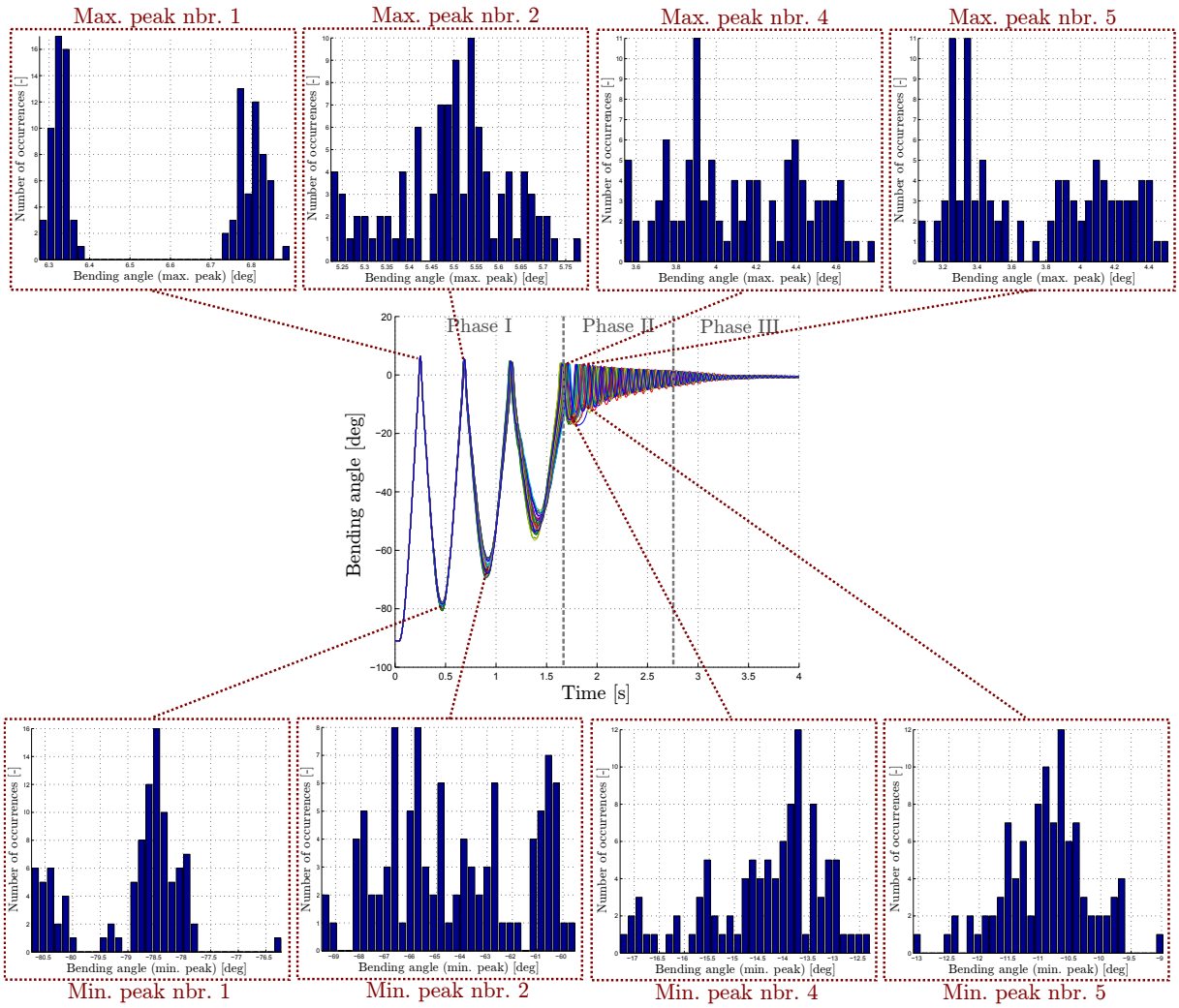

Figure B.2: Histograms of some peak amplitudes for an initial folding in equal sense.

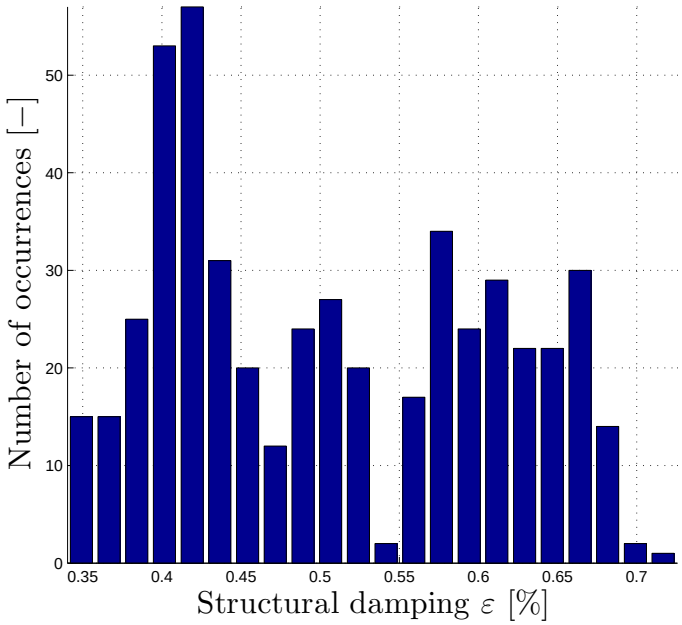

Figure B.3: Histogram of the structural damping obtained with small vibration tests.

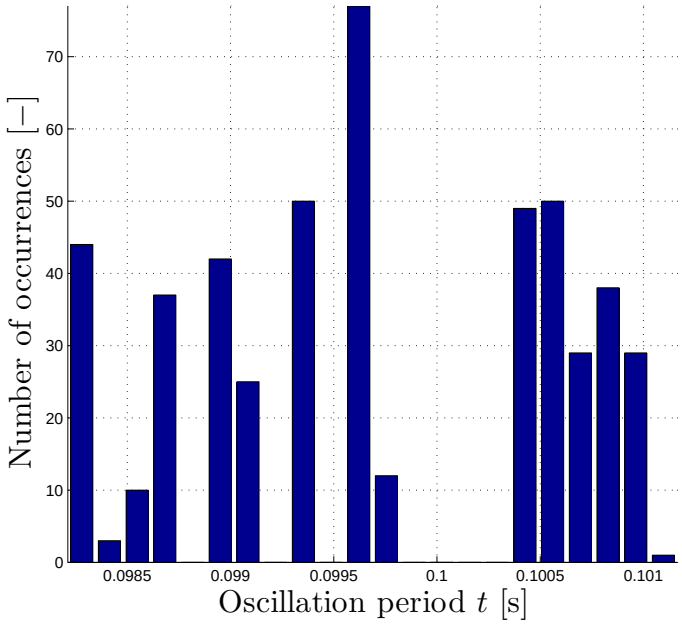

Figure B.4: Histogram of the oscillation period of the small amplitude vibration tests.

APPENDIX C

PUBLICATIONS AND CONFERENCES

This appendix presents the list of papers published in scientific journals and conferences attended during the achievement of this Ph.D. thesis.

C.1 Journal publications

- Florence Dewalque, Pierre Rochus, Olivier Brüls, Importance of structural damping in the dynamic analysis of compliant deployable structures, *Acta Astronautica* **111**, 2015, 323–333.
- Florence Dewalque, Jean-Paul Collette, Olivier Brüls, Mechanical behaviour of tape springs used in the deployment of reflectors around a solar panel, *Acta Astronautica* **123**, 2016, 271–282.
- Florence Dewalque, Cédric Schwartz, Vincent Denoël, Jean-Louis Croisier, Bénédicte Forthomme, Olivier Brüls, Experimental and numerical investigation of the nonlinear dynamics of compliant mechanisms for deployable structures, *Mechanical Systems and Signal Processing Journal* **101**, 2018, 1–25.

C.2 Conference publications (full papers)

- Florence Dewalque, Pierre Rochus, Olivier Brüls, Importance of structural damping in the dynamic analysis of compliant deployable structures, in: *The Proceedings of the 65th International Astronautical Congress (IAC)*, Toronto, Canada, 29 September – 3 October 2014.
- Florence Dewalque, Olivier Brüls, Experimental validation of structural damping models for tape springs, in: *The Proceedings of the 6th European Conference for Aeronautics and Space Sciences (EUCASS)*, Krakòw, Poland, 29 June – 3 July 2015.
- Florence Dewalque, Jean-Paul Collette, Olivier Brüls, Mechanical behaviour of tape springs used in the deployment of reflectors around a solar panel, in: *The Proceedings of the 6th International Conference on Mechanics and Materials in Design (M2D)*, Ponta Delgada, Azores, Portugal, 26–30 July 2015.
- Florence Dewalque, Olivier Brüls, Design of an experimental set-up to analyse compliant mechanisms used for the deployment of a panel, in: *The Proceedings of the 14th European Conference on Spacecraft Structures, Materials and Environmental Testing (ECSSMET)*, Toulouse, France, 27–30 September 2016.

C.3 Presentations in conferences

- ▷ Florence Dewalque, Valentin Sonneville, Olivier Brüls, Nonlinear analysis of tape springs: Comparison of two geometrically exact finite element formulations, *Oral presentation at the 11th World Congress on Computational Mechanics (WCCM)*, Barcelona, Spain, 20–25 July 2014.
- ▷ Florence Dewalque, Olivier Brüls, Nonlinear analysis of compliant mechanisms: application to tape springs, *Poster at the 6th International Conference on Nonlinear Vibrations, Localization and Energy Transfer (NNM)*, Liège, Belgium, 4–8 July 2016.
- ▷ Florence Dewalque, Cédric Schwartz, Vincent Denoël, Jean-Louis Croisier, Bénédicte Forthomme, Olivier Brüls, Experimental characterisation of tape spring nonlinear compliant mechanisms, *Oral presentation at the 9th European Nonlinear Dynamics Conference (ENOC)*, Budapest, Hungary, 25–30 June 2017.

BIBLIOGRAPHY

[1] Arianespace. GSAT-10 "spreads its wings" in preparation for Arianespace's next Ariane 5 launch. Online, August 2012. `http://www.arianespace.com/mission-update/gsat-10-spreads-its-wings-in-preparation-for-arianespaces-next-ariane-5-launch-2/`.

[2] G. Aridon, L. Blanchard, A. Allezy, D. Rémond, and R. Dufour. On the correction capability of a deployed tape-spring hexapod. *Mechanism and Machine Theory*, 43:1009–1023, 2008.

[3] B. Armstrong-Hélouvry, P. Dupont, and C. Canudas de Wit. A survey of models, analysis tools and compensation methods for the control of machines with friction. *Automatica*, 30(7):1083–1138, 1994.

[4] M. Arnold and O. Brüls. Convergence of the generalized-alpha scheme for constrained mechanical systems. *Multibody System Dynamics*, 18(2):185–202, 2007.

[5] W.E. Baker, W.E. Woolam, and D. Young. Air and internal damping of thin cantilever beams. *International Journal of Mechanical Sciences*, 9:743–766, 1967.

[6] E. Balmès. High modal density, curve veering, localization - a different perspective on the structural response. *Journal of Sound and Vibration*, 161(2):358–363, 1993.

[7] M. Bao and H. Yang. Squeeze film air damping in MEMS. *Sensors and Actuators A: Physical*, 136:3–27, 2007.

[8] N. Bay, D.D. Olsson, and J.L. Andreasen. Lubricant test methods for sheet metal forming. *Tribology International*, 41(9):844–853, 2008.

[9] G. Binnig, C.F. Quate, and C. Gerber. Atomic force microscope. *Physical Review Letters*, 56(9):930–933, 1986.

[10] J. Blaauwendraad. *Plates and FEM: Surprises and Pitfalls*. Springer (Netherlands), 2010.

[11] J.T. Black, J.A. Whetzal, B.J. deBlonk, and J.J. Massarello. Deployment repeatability testing of composite tape springs for space optics applications. In *Proceedings of the 47th AIAA/ASME/ASCE/AHS/ASC Structures, Structural Dynamics, and Materials Conference*, Newport, Rhode Island, USA, 1–4 May 2006.

[12] M.S. Blanter, I.S. Golovin, H. Neuhäuser, and H.-R. Sinning. *Internal Friction in Metallic Materials A Handbook*. Springer (Berlin Heidelberg), 2007.

[13] J.M. Bodeau. Root cause of the BSS 702 concentrator array anomaly. *Space Power Workshop*, 2003.

[14] C. Boesch, C. Pereira, R. John, T. Schmidt, K. Seifart, H. Sparr, J.M. Lautier, and T. Pyttel. Ultra light self-motorized mechanism for deployment of light weight space craft appendages. In *Proceedings of the 39th Aerospace Mechanisms Symposium*, NASA Marshall Space Flight Center, USA, 7–9 May 2008.

[15] F.P. Bowden and L. Leben. The nature of sliding and the analysis of friction. *Proceedings of the Royal Society of London, Series A, Mathematical and Physical Sciences*, 169:371–391, 1939.

[16] C. Boyle, L.L. Howell, S.P. Magleby, and M.S Evans. Dynamic modeling of compliant constant-force compression mechanisms. *Mechanism and Machine Theory*, 38:1469–1487, 2003.

[17] D. Braun, H. Cherdron, M. Rehahn, H. Ritter, and B. Voit. *Polymer synthesis: Theory and practice (Fifth Edition)*. Springer (Berlin Heidelberg), 2013.

[18] A. Brinkmeyer, S. Pellegrino, and P.M. Weaver. Effects of long-term stowage on the deployment of bistable tape springs. *ASME Journal of Applied Mechanics*, 83(1):1–11, 2016.

[19] C. Calladine. *Theory of shell structures*. Cambridge University Press, 1983.

[20] C. Calladine. The theory of thin shell structures. *Proceedings of the Institution of Mechanical Engineers, Part A: Journal of Power and Energy*, 202(3):141–149, 1988.

[21] A.C. Capelo, L. Ironi, and S. Tentoni. An algorithm for the automated generation of rheological models. *Applications of Artificial Intelligence in Engineering*, 6:963–979, 1991.

[22] E. Chater and J.W. Hutchinson. On the propagation of bulges and buckles. *Journal of Applied Mechanics*, 51:269–277, 1984.

[23] R.M. Christensen. *Theory of Viscoelasticity: An Introduction*. Academic Press (New York), 1971.

[24] J. Chung and G. Hulbert. A time integration algorithm for structural dynamics with improved numerical dissipation: the generalized-α method. *ASME Journal of Applied Mechanics*, 60:371–375, 1993.

[25] Codamotion. Charnwood dynamics Ltd., Rothley, United Kingdom. `www.codamotion.com`.

[26] A.J. Cook and S.J.I. Walker. Experimental research on tape spring supported space inflatable structures. *Acta Astronautica*, 118:316–328, 2016.

[27] C.A. Coulomb. *Théorie des machines simples ayant égard au frottement de leurs parties et à la roideur des cordages*. Bachelier (Paris), 1821.

[28] MTS. Criterion. MTS Systems Corporation, USA. `www.mtsmonotonic.com`.

[29] J.P. Den Hartog. Forced vibrations with combined coulomb and viscous damping. *Transactions of the American Society of Mechanical Engineering*, 53:107–115, 1931.

[30] F. Dewalque, J.-P. Collette, and O. Brüls. Mechanical behaviour of tape springs used in the deployment of reflectors around a solar panel. *Acta Astronautica*, 123:271–282, 2016.

[31] A. Fischer. Bending instabilities of thin-walled transversely curved metallic springs. Technical Report CUED/D-STRUCT/TR 154, Department of Engineering, University of Cambridge, 1995.

[32] J. Fréne and T. Cicone. *Handbook of Material Behavior Models*, chapter Friction in lubricated contacts, pages 760–767. Academic Press Cambridge, 2001.

[33] D. Givois, J. Sicre, and T. Mazoyer. A low cost hinge for appendices deployment: design, test and application. In *Proceedings of the 9th European Space Mechanisms and Tribology Symposium*, Liège, Belgium, 19–21 September 2001.

[34] M. Géradin and A. Cardona. *Flexible Multibody Dynamics, A Finite Element Approach.* Wiley (New York), 2001.

[35] E. Groskopfs. Storable tubular extendible member device. *U.S. Patent* 3434674 A, 1969.

[36] F.L. Guan, X.Y. Wu, and Y.W. Wang. The mechanical behavior of the double piece of tape spring. *Advanced Intelligent Computing Theories and Applications*, pages 102–110, 2010.

[37] F. Guinot, S. Bourgeois, B. Cochelin, and L. Blanchard. A planar rod model with flexible thin-walled cross-sections. Application to the folding of tape springs. *International Journal of Solids Structures*, 49(1):73–86, 2012.

[38] G. Höhler. *Point defects in metals I. Introduction to the theory.* Springer-Verlag (Berlin), 1977.

[39] H. Hilber, T. Hughes, and R. Taylor. Improved numerical dissipation for time integration algorithms in structural dynamics. *Earthquake Engineering and Structural Dynamics*, 5:283–292, 1977.

[40] S.F. Hoerner. *Fluid-dynamic drag: practical information on aerodynamic drag and hydrodynamic resistance.* Midland Park, 1958.

[41] S. Hoffait, O. Brüls, D. Granville, F. Cugnon, and G. Kerschen. Dynamic analysis of the self-locking phenomenon in tape-spring hinges. *Acta Astronautica*, 66:1125–1132, 2010.

[42] L.L. Howell. *Compliant Mechanisms.* John Wiley & Sons (New York), 2001.

[43] S. Hussain, S.Q. Xie, P.K. Jamwal, and J. Parsons. An intrinsically compliant robotic orthosis for treadmill training. *Medical Engineering & Physics*, 34:1448–1453, 2012.

[44] L.S. Jacobsen. An approximate solution of the steady forced vibration of a system of one degree of freedom under the influence of various types of damping. *Bulletin of the Seismological Society of America*, 20(3):196–223, 1930.

[45] J.W. Jeong, Y.I. Yoo, D.K. Shin, J.H. Lim, K.W. Kim, and J.J. Lee. A novel tape spring hinge mechanism for quasi-static deployment of a satellite deployable using shape memory alloy. *Review of Scientific Instruments*, 85(2), 2014.

[46] L. Johnson, M. Whorton, A. Heaton, R. Pinson, G. Laue, and C. Adams. NanoSail-D: A solar sail demonstration mission. *Acta Astronautica*, 68:571–575, 2011.

[47] R.A. Johnston and A.D.S. Barr. Acoustic and internal damping in uniform beams. *Journal of Mechanical Engineering Science*, 11:117–127, 1969.

[48] A. Kainz, W. Hortschitz, J. Schalko, A. Jachimowicz, and F. Keplinger. Air damping as design feature in lateral oscillators. *Sensors and Actuators A: Physical*, 236:357–363, 2015.

[49] A. Kainz, W. Hortschitz, H. Steiner, J. Schalko, A. Jachimowicz, and F. Keplinger. Accurate analytical model for air damping in lateral MEMS/MOEMS oscillators. *Sensors and Actuators A: Physical*, 255:154–159, 2017.

[50] K. Kato. Wear in relation to friction - a review. *Wear*, 241(2):151–157, 2000.

[51] E. Kebadze, S.D. Guest, and S. Pellegrino. Bistable prestressed shell structures. *International Journal of Solids and Structures*, 41:2801–2820, 2004.

[52] C. Kim, M.-G. Song, Y.-J. Kim, N.-C. Park, K.-S. Park, Y.-P. Park, K.S. Shin, J.G. Kim, and G.S. Lee. Design of an auto-focusing actuator with a flexure-based compliant mechanism for mobile imaging devices. *Microsystem Technologies*, 19:1633–1644, 2013.

[53] K.-W. Kim and Y. Park. Solar array deployment analysis considering path-dependent behavior of a tape spring hinge. *Journal of Mechanical Science and Technology*, 29(5):1921–1929, 2015.

[54] K.-W. Kim and Y. Park. Systematic design of tape spring hinges for solar array by optimization method considering deployment performances. *Aerospace Science and Technology*, 46:124–136, 2015.

[55] Kistler. Kistler Holding AG, Winterthur, Switzerland. `www.kistler.com`.

[56] I. Kovács and H. El Sayed. Point defects in metals. *Journal of Materials Science*, 11:529–559, 1976.

[57] M.K. Kwak, S. Heo, and H.B. Kim. Dynamics of satellite with deployable rigid solar arrays. *Multibody System Dynamics*, 20(3):271–286, 2008.

[58] K. Kwok and S. Pellegrino. Viscoelastic effects in tape-springs. In *Proceedings of the 52nd AIAA/ASME/ASCE/ AHS/ASC Structures, Structural Dynamics and Materials Conference*, Denver, USA, 4–7 April 2011.

[59] E.S. Levitan. Forced oscillation of a spring-mass system having combined coulomb and viscous damping. *The Journal of the Acoustical Society of America*, 32(10):1265–1269, 1960.

[60] A.E.H. Love. The small free vibrations and deformation of a thin elastic shell. *Philosophical Transactions of the Royal Society A: Mathematical, Physical and Engineering Sciences*, 179(0):491–546, 1888.

[61] K.J. Lu and S. Kota. Design of compliant mechanisms for morphing structural shapes. *Journal of Intelligent Material Systems and Structures*, 14:379–391, 2003.

[62] G. Maidanik. Energy dissipation associated with gas-pumping in structural joints. *Journal of the Acoustical Society of America*, 40(5):1064–1072, 1966.

[63] H.M.Y.C. Mallikarachchi and S. Pellegrino. Quasi-static folding and deployment of ultrathin composite tape-spring hinges. *Journal of Spacecraft and Rockets*, 48(1):187–198, 2011.

[64] H.M.Y.C. Mallikarachchi and S. Pellegrino. Deployment dynamics of ultrathin composite booms with tape-spring hinges. *Journal of Spacecraft and Rockets*, 51(2):604–613, 2014.

[65] H.M.Y.C. Mallikarachchi and S. Pellegrino. Design of ultrathin composite self-deployable booms. *Journal of Spacecraft and Rockets*, 51(6):1811–1821, 2014.

[66] E.H. Mansfield. Large-deflexion torsion and flexure of initially curved strips. *Proceedings of the Royal Society of London*, A 334:1125–1132, 1973.

[67] A. Marchand. Analysis of a gravity compensation system for deployment tests. Master's thesis, University of Liège, Belgium, 2016.

[68] F. Marques, P. Flores, J.C. Pimenta Claro, and H.M. Lankarani. A survey and comparison of several friction force models for dynamic analysis of multibody mechanical systems. *Nonlinear Dynamics*, 86(3):1407–1443, 2016.

[69] S.P.C. Marques and G.J. Creus. *Computational Viscoelasticity*. Springer (Berlin Heidelberg), 2012.

[70] MathWorks. *Matlab, Version 7.9.0 (R2009b)*, 2009.

[71] J.C. Meaders and C.A. Mattson. Optimization of near-constant force spring subject to mating uncertainty. *Structural and Multidisciplinary Optimization*, 41:1–15, 2010.

[72] P.L. Menezes, Kishore, and S.V. Kailas. Influence of surface texture on coefficient of friction and transfer layer formation during sliding of pure magnesium pin on 080 M40 (EN8) steel plate. *Wear*, 261(5):578–591, 2006.

[73] R.D. Mindlin. Influence of rotary inertia and shear on flexural motions of isotropic, elastic plates. *Journal of Applied Mechanics, Transaction of American Society of Mechanical Engineers*, 18(1):31–38, 1951.

[74] M. Mobrem and D. Adams. Deployment analysis of lenticular jointed antennas onboard the Mars Express spacecraft. *Journal of Spacecraft and Rockets*, 46:394–402, 2009.

[75] A.J. Morin. New friction experiments carried out at Metz. *Proceedings of the French Royal Academy of Sciences*, 4:1–128, 1833.

[76] A. Moxhet. Dimensionnement et caractérisation de joints de carpentier par la méthode des éléments-finis, Application au déploiement des panneaux solaires du satellite ESEO. Master's thesis, University of Liège, Belgium, 2007.

[77] A.D. Nashif and D.I.G. J. ans J.P Henderson. *Vibration Damping*. John Whiley (New York), 1985.

[78] M.A. Neto, A. Amaro, L. Roseiro, J. Cirne, and R. Leal. *Engineering Computation of Structures: The Finite Element Method*. Springer (International Publishing), 2015.

[79] N. Newmark. A method of computation for structural dynamics. *ASCE Journal of the Engineering Mechanics Division*, 85:67–94, 1959.

[80] S. Pellegrino. *Deployable Structures*, volume 412, chapter Deployable Structures in Engineering. CISM Courses and Lectures, Springer (Wien), 2001.

[81] E. Picault, P. Marone-Hitz, S. Bourgeois, B. Cochelin, and F. Guinot. A planar rod model with flexible cross-section for the folding and the dynamic deployment of tape springs: Improvements and comparisons with experiments. *International Journal of Solids Structures*, 51(18):3226–3238, 2014.

[82] L. Priester. *Grain boundaries: From theory to engineering*. Springer (Netherlands), 2013.

[83] V. Randle, H. Davies, and I. Cross. Grain boundary misorientation distributions. *Current Opinion in Solid State and Materials Science*, 5(1):3–8, 2001.

[84] E. Reissner. The effect of transverse shear deformation on the bending of elastic plates. *Journal of Applied Mechanics, Transaction of American Society of Mechanical Engineers*, 12(A):68–77, 1945.

[85] O. Reynolds. On the theory of lubrication and its application to Mr. Beauchamp Tower's experiments, including an experimental determination of the viscosity of olive oil. *Philosophical Transactions of the Royal Society of London*, 177:157–234, 1886.

[86] F.P.J. Rimrott. Querschnittsverformung bei Torsion offener Profile. *Zeitschrift für Angewandte Mathematik und Mechanik*, 50:775–778, 1970.

[87] D. Rodney and J. Bonneville. *Physical Metallurgy (Fifth Edition)*, chapter 16: Dislocations. Elsevier, 2014.

[88] H. Saito et al. Small satellite REIMEI for auroral observations. *Acta Astronautica*, 69:499–513, 2011.

[89] S.A. Samcef. *SAMCEF User Manual, Version 8.4*, 2013.

[90] C. Schwartz, V. Denoël, B. Forthomme, J.-L. Croisier, and O. Brüls. Merging multi-camera data to reduce motion analysis instrumental errors using kalman filters. *Computer Methods in Biomechanics and Biomedical Engineering*, 18(9):952–960, 2015.

[91] K.A. Seffen. *Analysis of structures deployed by tape-springs*. PhD thesis, Cambridge University, United-Kingdom, 1997.

[92] K.A. Seffen. On the behaviour of folded tape-springs. *ASME Journal of Applied Mechanics*, 68:369–375, 2001.

[93] K.A. Seffen and S. Pellegrino. Deployment of a rigid panel by tape-springs. Technical Report CUED/D-STRUCT/TR168, Department of Engineering, University of Cambridge, 1997.

[94] K.A. Seffen and S. Pellegrino. Deployment dynamics of tape springs. *Proceedings of the Royal Society of London: Mathematical, Physical and Engineering Sciences*, A 455:1003–1048, 1999.

[95] K.A. Seffen, Z. You, and S. Pellegrino. Folding and deployment of curved tape springs. *International Journal of Mechanical Sciences*, 42:2055–2073, 2000.

[96] C. Sickinger and L. Herbeck. Deployment strategies, analyses and tests for the CFRP booms of a solar sail. In *Proceedings of the European Conference on Spacecraft Structures, Materials & Mechanical Testing*, Toulouse, France, 11–13 December 2002.

[97] J. Sicre, D. Givois, and E. Emerit. Application of Maeva hinge to Myriade microsatellites deployments needs. In *Proceedings of the 11th European Space Mechanisms and Tribology Symposium*, Lucerne, Switzerland, 21–23 September 2005.

[98] O. Sigmund. On the design of compliant mechanisms using topology optimization. *Mechanics of Structures and Machines*, 25(4):493–524, 1997.

[99] F.J. Sigworth and S.M. Sine. Data transformations for improved display and fitting of single-channel dwell time histograms. *Biophysical Journal*, 52(6):1047–1054, 1987.

[100] R.E. Smallman and A.H.W. Ngan. *Modern Physical Metallurgy (Eight Edition)*, chapter 4: Introduction to Dislocations. Butterworth-Heinemann (Tokyo), 2014.

[101] I. Sokolsky and M.A. Brown. Naval research laboratory solar concentrator program. *AIP Conference Proceedings*, 420:282–287, 1998.

[102] Ö. Soykasap. Analysis of tape spring hinges. *International Journal of Mechanical Sciences*, 49:853–860, 2007.

[103] K. Steele, E. Linder, and J. Renshall. High specific power solar concentrator array for low cost commercial satellite. In *Proceedings of the 5th European Power Conference*, Tarragona, Spain, 1998.

[104] R. Stribeck. Die Wesentlichen Eigenschaften der Gleit- und Rollenlager. *Zeitschrift des Vereines Deutscher Ingenieure*, 46(38):1342–1348, 1902.

[105] K.A. Tolman, E.G. Merriam, and L.L. Howell. Compliant constant-force linear-motion mechanism. *Mechanism and Machine Theory*, 106:68–79, 2016.

[106] S.J.I. Walker and G. Aglietti. Study of the dynamics of three-dimensional tape spring folds. *AIAA Journal*, 42:850–856, 2004.

[107] S.J.I. Walker and G. Aglietti. Experimental investigation of tape springs folded in three dimensions. *AIAA Journal*, 44:151–159, 2006.

[108] C.M. Wang, G.T. Lim, J.N. Reddy, and K.H. Lee. Relationships between bending solutions of Reissner and Mindlin plate theories. *Engineering Structures*, 23(7):838–849, 2001.

[109] M. Wesolowski and E. Barkanov. Air damping influence on dynamic parameters of laminated composite plates. *Measurement*, 85:239–248, 2016.

[110] W.E. Woolam. Drag coefficients for flat square plates oscillating normal to their planes in air. Technical Report NASA CR-66544, NASA, 1968.

[111] W. Wüst. Einige Anwendungen des Theorie der Zylinderschale. *Zeitschrift für Angewandte Mathematik und Mechanik*, 34:444–454, 1954.

[112] J.C.H. Yee, O. Soykasap, and S. Pellegrino. Carbon Fibre Reinforced Plastic tape springs. In *Proceedings of the 45th AIAA/ASME/ASCE/AHS/ASC Structures, Structural Dynamics, and Materials Conference*, Palm Springs, CA, USA, 19–22 April 2004.

[113] K. Zajac, T. Schmidt, M. Schiller, K. Seifart, M. Schmalbach, and L. Scolameiro. Verification test for ultra-light deployment mechanism for sectioned deployable antenna reflectors. In *Proceedings of the 15th European Space Machanisms and Tribology Symposium*, Noordwijk, The Netherlands, 25–27 September 2013.

[114] C. Zhang, G. Xu, and Q. Jiang. Analysis of the air-damping effect on a micromachined beam resonator. *Mathematics and Mechanics of Solids*, 8:315–325, 2003.